High-power properties of lead-based and lead-free ferroelectric ceramics

Fachbereich Material- und Geowissenschaften, Technische Universität Darmstadt

Dissertation zur Erlangung des akademischen Grades Doktor-Ingenieur (Dr.-Ing.)
von Mihail Slabki

Erstgutachter: Assist. Prof. Dr. Jurij Koruza
Zweitgutachter: Prof. Dr. Wolfgang Donner

Darmstadt 2022

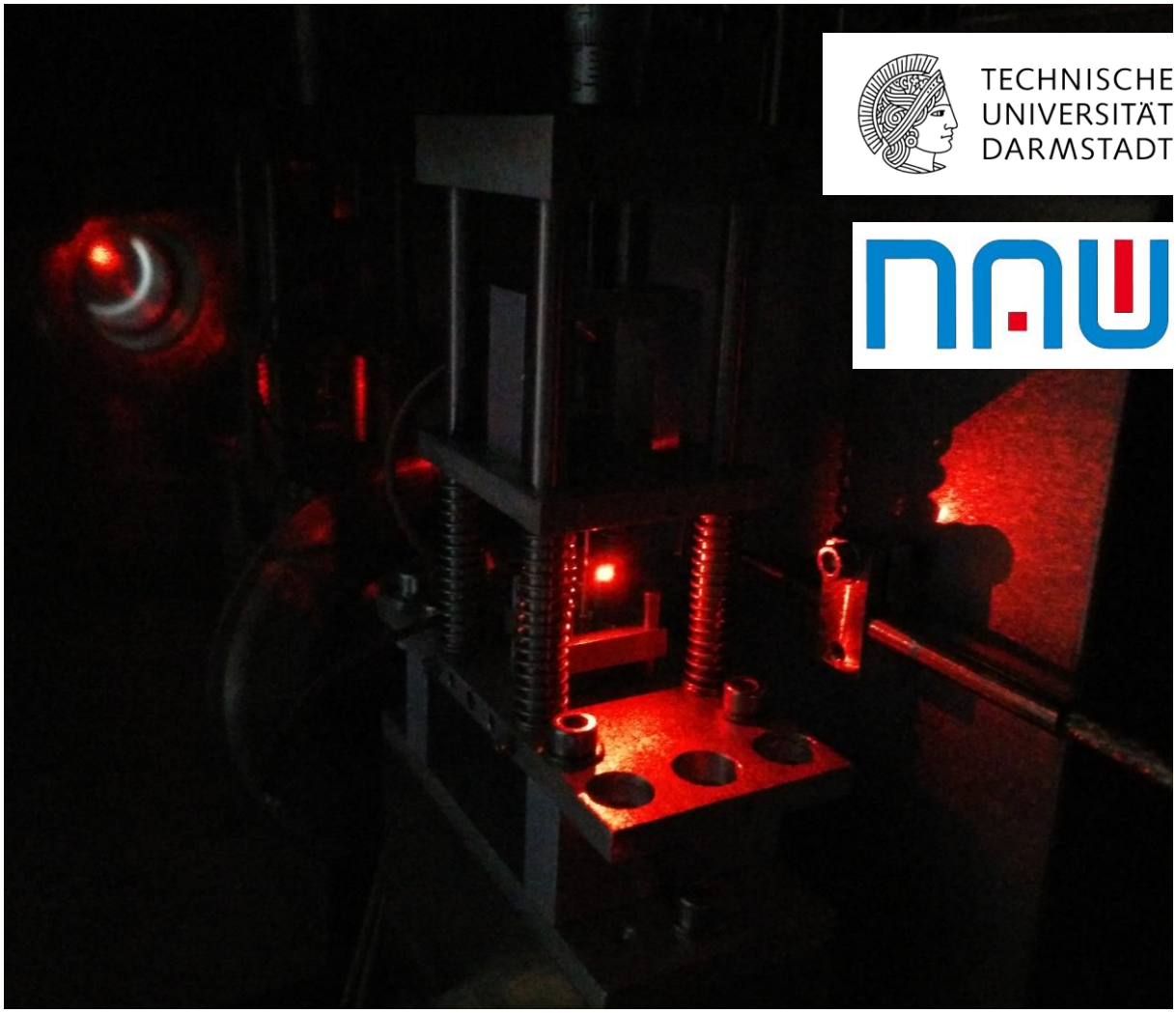

Dissertation

High-power properties of lead-based and lead-free ferroelectric ceramics

von Mihail Slabki, M. Sc.

Erstgutachter: Assist. Prof. Dr. Jurij Koruza

Zweitgutachter: Prof. Dr. Wolfgang Donner

Beisitzer: Prof. Dr. Robert Stark

Beisitzer: Prof. Dr. Mario Kupnik

Tag der Prüfung: 8. Juli 2022

Jahr der Veröffentlichung der Dissertation auf TUprints: 2022

Fachbereich Material- und Geowissenschaften

Technische Universität Darmstadt

Alarich-Weiss-Straße 2

64287 Darmstadt

Veröffentlicht unter CC BY-SA 4.0 International

https://creativecommons.org/licenses/

Declaration of Authorship

Thesis Statement pursuant to § 22 paragraph 7 and § 23 paragraph 7 of APB TU Darmstadt

I hereby formally declare that I, Mihail Slabki, have written the submitted thesis independently pursuant to §22 paragraph 7 of APB TU Darmstadt. I did not use any outside support except for the quoted literature and other sources mentioned in the thesis. Furthermore, I state that all passages which have been taken out of publications of all means or unpublished material either whole or in part, in words or ideas, have been marked as quotations in the relevant passage. This thesis has not been handed in or published before in the same or similar form.

In the submitted thesis the written copies and the electronic version for archiving are pursuant to § 23 paragraph 7 APB identical in content.

Darmstadt, 17. Mai 2022

Abstract

Hard-type ferroelectric ceramics are increasingly demanded as indispensable parts in numerous high-power applications, ranging from ultrasonic welding, over voltage transformers, to miniaturized ultrasonic motors in robotics. In these devices, the ferroelectric resonator is driven at or near its piezoelectric resonance frequency, which is a unique constitution that enables the generation of large oscillating displacement/strain at comparably small driving electric fields. The resonance amplification is thereby determined by the energy dissipation and induced hysteretic loss, usually represented by the resonators quality factor, i.e., the strain generation does not require exceptionally large piezoelectric coefficients but relies on the combination of moderate electromechanical coupling and minimal loss generation. However, state-of-the-art lead-based ferroelectrics are hitting their operational limits and are restricted to low output power densities due to rapidly evolving loss. This sets a natural boundary to the maximum achievable vibration velocities and terminates into overheating, depolarization, fracture, and ultimately device failure. Recently-emerged lead-free ferroelectrics demonstrated promising high-power properties and are discussed as potential alternatives, enabling to push the vibration limits to higher velocities. However, outperforming their lead-based counterparts in terms of reduced loss generation, they generally fall short on the poor electromechanical coupling and the narrow operational temperature window. In both cases, a consistent rationalization of the underlying resonance mechanisms and a systematic study of the decisive impact parameters are missing. This hampers the development of future high-power ferroelectrics.

The present study investigates and compares the high-power properties and mechanistic processes of several $Pb(Zr,Ti)O_3$-based and $(Na_{1/2}Bi_{1/2})TiO_3$-$BaTiO_3$-based ferroelectric compositions in piezoelectric resonance. Pulse drive measurements with burst excitation were utilized to determine piezoelectric, mechanical, and dielectric coefficients, as well as quality factors in a broad vibration velocity, temperature, and frequency range and under various vibration modes. The resonance performance is thereby best expressed by accumulating several of the coefficients to a high-power figure of merit; however, the properties are predominantly dictated by the values and the relative stability of the piezoelectric coefficients and the quality factors which are subjected to significant variation. The largest combination of both was determined in acceptor-doped $Pb(Zr,Ti)O_3$ compositions. However, while the piezoelectric coefficients slightly increase with increasing vibration velocity, the quality factors reveal a rapid decrease by more than 80 % already in the range below 1 m/s, which is the detrimental limitation for the vibration velocity generation. The massive decrease appears qualitatively equivalent in all $Pb(Zr,Ti)O_3$ compositions, irrespective of the doping element and concentration (acceptor/donor), crystal structure (Zr/Ti ratio), or grain size (domain size), i.e., an increase of the quality factor values does not result in improved relative stability. Moreover, normalizing the vibration velocity dependence of the quality factor to the small-field values revealed a clustering of all compositions, which manifests that the poor stability is primarily determined by the inherent properties of the ferroelectric matrix and mostly independent of chemical doping or other modifications. $(Na_{1/2}Bi_{1/2})TiO_3$-$BaTiO_3$ compositions possess, in general, inferior piezoelectric coefficients and quality factors, but can compete with $Pb(Zr,Ti)O_3$ if morphotropic phase boundary compositions (large piezoelectric coefficients) are ferroelectrically hardened (increasing quality factor) by Zn^{2+} acceptor-doping or composite formation with ZnO inclusions. The compositions reveal inherently superior stability, i.e., the piezoelectric coefficients are almost constant up to considerably large vibration velocities, while

the quality factors exhibit only a moderate decrease. The pronounced stability in combination with profound fracture toughness and heat conductivity transforms into excellent high-power performance and enables the generation of large vibration velocities beyond 4 m/s with an essentially reduced self-heating, while state-of-the-art $Pb(Zr,Ti)O_3$ already fail below 2.6 m/s.

The mechanistic origin of the stability difference was identified by synchronizing the pulse drive measurements with in-situ synchrotron x-ray diffraction. The quality factor decrease in $Pb(Zr,Ti)O_3$ was directly associated with increased non-180° domain wall motion, which is a loss-afflicted strain-generating process driven by the evolving dynamic mechanical stress. A general relation between the microstructural strain contributions and macroscopic electromechanical behavior was established, which is suggested to predict the inherent high-power stability of ferroelectric systems. Moreover, the stability of $(Na_{1/2}Bi_{1/2})TiO_3$-$BaTiO_3$ was found to correlate with a significantly lower domain wall contribution to the generated strain. The strain has a predominantly intrinsic nature and results from lattice distortion, which is the consequence of a significant coercive stress in these materials. However, the yet smaller quality factors indicate a substantial intrinsic loss in addition to the usually-dominant extrinsic loss. The intrinsic loss was rationalized to originate from a pronounced lattice polarization rotation compared to the polarization extension, exhibiting only weak vibration velocity dependence. The results confirmed that the modifications and hardening mechanisms influence the absolute values while the high-power stability is predominantly related to the basic ferroelectric material.

Furthermore, the above-mentioned relative stability and clustering were determined to be temperature independent. On the other hand, the values reveal a pronounced temperature dependence. Especially acceptor-doped compositions exhibit a severe discontinuous temperature alternation, which was found to originate from evolving dielectric loss associated with the generated oxygen vacancies and the thermally-activated ionic hopping conductivity. This leads to the ambiguity that heavily acceptor-doped compositions reach exceptionally large quality factors, but only in a narrow temperature window and are prone to substantial temperature variance. A promising alternative is the second phase hardening approach demonstrated upon ZnO inclusions in $(Na_{1/2}Bi_{1/2})TiO_3$-$BaTiO_3$. These ceramic-ceramic composites possess enhanced quality factors, delayed thermal depolarization, and almost temperature-independent properties, since the introduced mismatch stress does not contribute to conductivity. In combination with the inherent relative stability, the composites retain a broader temperature-velocity operation window and are suggested to be better suitable for high-power applications under thermal load and/or pronounced self-heating.

A further approach based on ferroelectric property manipulation through DC bias superposition was suggested and examined. To this end, a piezoelectric resonance impedance spectrometer capable of superimposing excitation AC voltages with high-voltage DC bias has been designed. Intriguing effects were determined in acceptor-doped $Pb(Zr,Ti)O_3$, where a six-fold increase of the quality factors at DC bias fields of 2 kV/mm was found to overcompensate the decrease of the piezoelectric coefficient, resulting in a substantial increase of the high-power figure of merit. The results suggest that the replacement of acceptor-doping with DC bias hardening has the potential to enhance high-power properties and temperature stability simultaneously, and reduce parasitic conductivity in extrinsic loss dominated ferroelectrics.

Kurzfassung

Hart-ferroelektrische Keramiken wurden in den letzten Jahren als das am schnellsten wachsende Segment des Elektrokeramikmarktes identifiziert, da sie eine Reihe moderner Technologien in der industriellen Automatisierung, Unterhaltungselektronik, intelligenten Fahrzeugen, Mikrorobotik und Medizin ermöglichen. Sie sind Kernelemente zahlreicher Hochleistungsanwendungen (*engl.* high-power applications) die vom Ultraschallschweißen über Spannungstransformatoren bis hin zu Ultraschallmotoren in der Robotik reichen. In diesen Anwendungen wird ein ferroelektrischer Resonator bei oder nahe seiner piezoelektrischen Resonanzfrequenz angetrieben, was eine einzigartige Konstellation darstellt, die die Erzeugung einer großen oszillierenden Verschiebung/Dehnung bei vergleichsweise kleinen elektrischen Antriebsfeldern ermöglicht. Die Dehnungsamplifikation in Resonanz hängt dabei von der Energiedissipation und den induzierten Hystereseverlusten ab, die üblicherweise im Qualitätsfaktor des Resonators zusammengefasst werden, d. h. die Spannungserzeugung erfordert keine außergewöhnlich großen piezoelektrischen Koeffizienten, sondern stützt sich auf die Kombination aus moderater elektromechanischer Kopplung und minimaler Verlusterzeugung. Bleibasierte Ferroelektrika stoßen jedoch bereits an ihre Belastungsgrenzen und sind aufgrund der sich schnell entwickelnden Verluste auf niedrige Leistungsdichten beschränkt. Dies setzt den maximal erreichbaren Vibrationsgeschwindigkeiten eine Grenze und führt zu Überhitzung, Depolarisation, mechanischem Bruch und schließlich Geräteversagen. Kürzlich entwickelte bleifreie Ferroelektrika zeigten vielversprechende Hochleistungseigenschaften und werden als potenzielle Alternativen gehandelt, die es ermöglichen, die Vibrationsgrenzen zu höheren Geschwindigkeiten zu verschieben. Sie übertreffen ihre bleibasierte Konkurrenz in Bezug auf verringerte Verlusterzeugung, sind jedoch im Allgemeinen durch die geringere elektromechanische Kopplung und engere Betriebstemperaturfenster limitiert. In beiden Fällen fehlen jedoch noch immer eine konsistente Beschreibung der den Resonanzeigenschaften zugrunde liegenden Mechanismen und eine systematische Untersuchung der entscheidenden Einflussfaktoren. Dies behindert die Entwicklung zukünftiger Hochleistungs-Ferroelektrika.

Diese Arbeit untersucht und vergleicht die Hochleistungseigenschaften und die mechanistischen Prozesse mehrerer $Pb(Zr,Ti)O_3$-basierter und $(Na_{1/2}Bi_{1/2})TiO_3$-$BaTiO_3$-basierter ferroelektrischer Zusammensetzungen in piezoelektrischer Resonanz. Unter Verwendung gepulster Messungen werden piezoelektrische, mechanische, dielektrische Koeffizienten und Qualitätsfaktoren in einem breiten Vibrations-, Temperatur- und Frequenzbereich und in verschiedenen Schwingungsmodi bestimmt. Die Performance wird dabei am genausten durch einen Hochleistungs-Gütefaktor repräsentiert, der gleichzeitig mehrere der Koeffizienten akkumuliert darstellt. Dabei fällt auf, dass vor allem die Werten und die relative Stabilität der piezoelektrischen Koeffizienten und der sich erheblich ändernden Qualitätsfaktoren den Gütefaktor dominieren. Die höchsten Gütewerte werden in Akzeptor-dotierten $Pb(Zr,Ti)O_3$-Zusammensetzungen erreicht. Doch während die piezoelektrischen Koeffizienten dieser Kompositionen mit zunehmender Vibrationsgeschwindigkeit leicht ansteigen, zeigen die Qualitätsfaktoren bereits im Bereich unter 1 m/s einen rapiden Abfall um mehr als 80 %, was sich als Hauptlimitierung für die Geschwindigkeitserzeugung darstellt. Die massive Abnahme erscheint qualitativ äquivalent in allen $Pb(Zr,Ti)O_3$-Zusammensetzungen, ungeachtet der verwendeten Dotierelementen und -konzentrationen (Akzeptor/Donor), Kristallstruktur (Zr/Ti-Verhältnis) oder Korngröße (Domänengröße), d. h. eine Erhöhung der Qualitätsfaktorwerte führt nicht zu einer verbesserten relativen Stabilität bei hohen Geschwindigkeiten. Darüber hinaus, werden

die Qualitätsfaktors in Abhängigkeit von der Vibrationsgeschwindigkeit auf die Kleinfeldwerte normiert, zeigen aller Zusammensetzungen eine Überlagerung, was darauf hindeutet, dass die geringe Stabilität in erster Linie durch die inhärenten Eigenschaften der ferroelektrischen Matrix bestimmt wird und weitgehend unabhängig von chemischer Dotierung oder anderen Modifikationen ist. $(Na_{1/2}Bi_{1/2})TiO_3$-$BaTiO_3$ Zusammensetzungen weisen im Allgemeinen geringere piezoelektrische Koeffizienten und Qualitätsfaktoren auf, können jedoch mit $Pb(Zr,Ti)O_3$ konkurrieren, wenn Zusammensetzungen an der morphotropen Phasengrenze (große piezoelektrische Koeffizienten) durch Zn^{2+}-Akzeptordotierung oder Kompositbildung mit ZnO-Einschlüssen ferroelektrisch gehärtet werden (steigende Qualitätsfaktoren). Die Zusammensetzungen weisen eine deutlich bessere inhärent Stabilität auf, d. h. die piezoelektrischen Koeffizienten sind bis zu großen Vibrationsgeschwindigkeiten nahezu konstant, während die Qualitätsfaktoren nur eine mäßige Abnahme aufweisen. Die ausgeprägte Stabilität in Kombination mit einer hohen Bruchzähigkeit und Wärmeleitfähigkeit resultiert in einer hervorragende Hochleistungs-Performance und ermöglicht die Erzeugung großer Vibrationsgeschwindigkeiten jenseits von 4 m/s bei wesentlich reduzierter Eigenerwärmung, während modernstes $Pb(Zr,Ti)O_3$ Zusammensetzungen bereits unterhalb von 2,6 m/s versagen.

Der mechanistische Ursprung des Stabilitätsunterschiedes wurde identifiziert, indem die Impulsantriebsmessungen mit Synchrotron-Röntgenbeugung synchronisiert wurden. Die Abnahme des Qualitätsfaktors in $Pb(Zr,Ti)O_3$ ist direkt verbunden mit einer erhöhten Bewegung von nicht-180° Domänenwänden. Die Domänenwandbewegung ist ein verlustbehafteter dehnungserzeugender Prozess, der durch die sich entwickelnden dynamischen mechanischen Spannungen im Resonator angetrieben wird. Es konnte eine allgemeine Beziehung zwischen den mikrostrukturellen Dehnungsbeiträgen und dem makroskopischen elektromechanischen Verhalten hergestellt werden. Es wird vorgeschlagen, dass die so extrahierten Parameter die inhärente Hochleistungsstabilität ferroelektrischer Systeme vorherzusagen können. Darüber hinaus wurde festgestellt, dass die Stabilität von $(Na_{1/2}Bi_{1/2})TiO_3$-$BaTiO_3$ mit einem signifikant geringeren Beitrag der Domänenwände zur erzeugten Dehnung zusammenhängt. Die Dehnung ist überwiegend von intrinsischer Natur und resultiert vorwiegend aus der Gitterverzerrung, was die Folge erheblich höherer Koerzitivspannungen in diesen Materialien ist. Die dennoch kleineren Qualitätsfaktoren weisen jedoch darauf hin, dass neben den normalerweise dominierenden extrinsischen Verlusten auch erhebliche intrinsische Verluste vorhanden sind. Die intrinsischen Verluste entwickeln sich höchstwahrscheinlich aus einer ausgeprägten Rotation der Gitterpolarisation, diese weist jedoch nur eine schwache Abhängigkeit von der Vibrationsgeschwindigkeit aufweist. Die Ergebnisse bestätigten, dass die Modifikationen und Härtungsmechanismen die Werte beeinflussen, während die Stabilität überwiegend von den grundlegenden Eigenschaften der Materialgruppe abhängt.

Weiterhin wurde festgestellt, dass die oben genannte relative Stabilität und Überlagerung temperaturunabhängig sind. Die absoluten Werte weisen hingegen eine ausgeprägte Temperaturabhängigkeit auf. Insbesondere Akzeptor-dotierte Zusammensetzungen zeigen eine starke nicht kontinuierliche Temperaturänderung. Es wurde festgestellt, dass diese mit den dielektrischen Verlusten in Verbindung steht, welche von den erzeugten Sauerstoffleerstellen und der thermisch aktivierten Ionenleitfähigkeit herrührt. Dies führt zu der Ambivalenz, dass stark Akzeptor-dotierte Zusammensetzungen äußerst hohe Qualitätsfaktoren erreichen, dies aber nur in einem schmalen Temperaturfenster und bei zugleich erheblicher Neigung zur Temperaturabhängigkeit. Eine vielversprechende Alternative ist deshalb der Zweitphasen-basierte

Härtungsansatz, der anhand von ZnO-Einschlüssen in $(Na_{1/2}Bi_{1/2})TiO_3$-$BaTiO_3$ demonstriert wurde. Diese Keramik-Keramik-Verbundwerkstoffe besitzen erhöhte Qualitätsfaktoren, hinausgezögerte Depolarisationstemperaturen und nahezu temperaturunabhängige Eigenschaften, da die eingeführte Fehlpassungsspannung nicht zur Leitfähigkeit beiträgt. In Kombination mit der inhärenten relativen Stabilität weisen die Verbundwerkstoffe ein viel breiteres Temperatur-Geschwindigkeits-Betriebsfenster auf und sind voraussichtlich besser geeignet für Hochleistungsanwendungen unter thermischer Belastung und/oder ausgeprägter Selbsterwärmung.

Ein weiterer vorgeschlagener und untersuchter Härtungsansatz basiert auf der Manipulation ferroelektrischer Eigenschaften durch DC-Spannungs-Überlagerung. Zu diesem Zweck wurde ein piezoelektrisches Resonanz-Impedanz-Spektrometer entwickelt, das in der Lage ist, Anregungs-Wechselspannungen mit einer hohen Gleichspannung zu überlagern. Signifikante Effekte wurden vor allem in Akzeptor-dotiertem $Pb(Zr,Ti)O_3$ festgestellt, wo ein sechsfacher Anstieg der Qualitätsfaktoren bei DC-Feldern von 2 kV/mm die gleichzeitige Abnahme des piezoelektrischen Koeffizienten überkompensierte und zu einer erheblichen Erhöhung der Gütefaktoren führt. Die Ergebnisse legen nahe, dass der Ersatz der Akzeptor-Dotierung durch DC-Härtung das Potenzial hat, die Hochleistungseigenschaften und die Temperaturstabilität gleichzeitig zu verbessern und die parasitäre Leitfähigkeit in Ferroelektrika zu reduzieren.

Content

Symbols and abbreviations

A_{ij}, B_{ij}	Force factors	$\left[\frac{As}{m}\right]$ and $\left[\frac{V}{m}\right]$
B_0, B_{max}	Exponential fitting parameters	$[-]$
C_0, C_d	Static and dynamic capacity	$[F]$
D_i	Dielectric displacement	$\left[\frac{C}{m^2}\right]$
E_i, E_c, E_{ib}	Electric field, coercive field, internal bias field	$\left[\frac{V}{m}\right]$
G	Gibbs free energy	$[J]$
H	Energy loss	$[J]$
I_i	Electric current	$[A]$
I_{hkl}	Diffraction intensity of hkl lattice plane	$[-]$
L_d	Dynamic inductivity	$[H]$
N_i	Dimension normalized resonance frequency	$[Hz \cdot m]$
P_i, P_r, P_{max}	Polarization, remanent polarization, maximum polarization	$\left[\frac{C}{m^2}\right]$
Q_{ij}^R, Q_{ij}^{AR}	Resonance and antiresonance quality factor	$[-]$
R_0, R_d	Static and dynamic resistance	$[\Omega]$
S_{ij}	Elastic strain	$[-]$
T_{ij}	Mechanical stress	$\left[\frac{N}{m^2}\right]$
V_i	Voltage	$[V]$
W	Stored energy	$[J]$
Y	Admittance	$\left[\frac{1}{\Omega}\right]$
Z	Impedance	$[\Omega]$
a, b, c	Lattice constants	$[m]$
d_{ij}	Piezoelectric coefficient	$\left[\frac{m}{V}\right]$ or $\left[\frac{C}{N}\right]$
e	Exponential decay constant	$[Hz]$
f_R, f_{AR}	Resonance and antiresonance frequency	$[Hz]$
h	Height	$[m]$
j	Complex number	$[-]$
k_{ij}	Coupling coefficient	$[-]$
l	Length	$[m]$
m_{hkl}	Multiplicity factor	$[-]$
p_{hkl}	Texture factor	$[-]$
q	Spring constant	$\left[\frac{N}{m}\right]$
r	Phase ratio	$[-]$
s_{ij}^E	Elastic compliance	$\left[\frac{m^2}{N}\right]$

t	Time	$[s]$
u_i	Displacement	$[m]$
v_i	Vibration velocity	$\left[\frac{m}{s}\right]$
w	Width	$[m]$
x_i	Direction	$[m]$
y	Average grain size	$[m]$
Γ	Non-linear power constant	$[-]$
Δ_{ij}	Kronecker delta	$[-]$
Θ	Impedance phase angle	$[°]$
Υ_{ij}^{m}	Mechanical energy density	$\left[\frac{J}{m^3}\right]$
Ψ^{m}	Mechanical power density	$\left[\frac{W}{m^3}\right]$
Ω	Volume element	$[m^3]$
α	Azimuthal diffraction angle	$[°]$
α_R	Rayleigh coefficient	$[-]$
β	Rhombohedral tilt angle	$[°]$
γ_{ij}	Mechanical loss angle	$[°]$
δ_{ij}	Dielectric loss angle	$[°]$
ε_0	Vacuum permittivity	$\left[\frac{As}{Vm}\right]$
ε_{ij}^{T}	Relative permittivity	$[-]$
ζ	Grain size variance	$[m]$
η	Domain switching fraction	$[-]$
θ	Diffraction angle	$[°]$
ϑ	Parabolic fitting parameter	$\left[\frac{s^2}{m^2}\right]$
λ	X-ray wavelength	$[m]$
μ_{ij}	Total loss angle	$[°]$
ξ	Linear fitting parameter	$\left[\frac{s}{m}\right]$
ρ	Density	$\left[\frac{kg}{m^3}\right]$
ϱ	Viscosity	$\left[\frac{Ns}{m^2}\right]$
σ	Poisson's ratio	$[-]$
ς_{ij}	Susceptibility	$[-]$
τ, τ_d, τ_{FR}, τ_c	Temperature, depolarization temperature, ferroelectric-to-relaxor transition temperature, Curie temperature	$[°C]$
υ_i^E	Wave velocity	$\left[\frac{m}{s}\right]$
φ	Angle between lattice vector and polar axis	$[°]$

ϕ_{ij}	Piezoelectric loss angle	[°]
χ	Exponential fitting parameter	$\left[\frac{s}{m}\right]$
ψ	Logarithmic fitting parameter	$[-]$
ω_R, ω_{AR}	Resonance and antiresonance angular frequency	$[Hz]$
$\Re$	Real number	
$\Im$	Imaginary number	
BFO	$BiFeO_3$	
BSE	Backscattered secondary electron	
BT	$BaTiO_3$	
DUT	Device under test	
FEM	Finite element modeling	
KNN	$(K_{1/2}Na_{1/2})NbO_3$	
MPB	Morphotropic phase boundary	
NBT-BT	$(1\text{-}x)(Na_{1/2}Bi_{1/2})TiO_3\text{-}xBaTiO_3$	
PCB	Printed circuit board	
PZT	$Pb(Zr_xTi_{1\text{-}x})O_3$	
SEM	Scanning electron microscopy	
TEM	Transmission electron microscopy	
XRD	X-ray diffraction	

1. Introduction

Piezoelectrics transform electric energy into mechanical energy and vice versa without the necessity for moving parts like a motor or generator. Moreover, size-independent energy density and minimal electromagnetic noise make them well-suitable for device miniaturization [1]. In recent years, they have been identified as the fastest-growing segment of the electroceramics market [2, 3], enabling a range of modern technologies in industrial automation, consumer electronics, smart vehicles, microrobotics, and medicine [4, 5]. Piezoelectric ceramics are indispensable components in a variety of high-power devices ranging from ultrasonic motors, welders, cutters, and cleaners to voltage transformers [5-9]. “High-power” excitation, operation, or drive are thereby established terms denoting the electric excitation of a piezoelement at its first- or higher-order mechanical resonance frequency [10]. Due to the electromechanical coupling, it might be more explicit to depict the condition as piezoelectric or electromechanical resonance. The unique feature of the resonance is the generation of largely amplified oscillating strain amplitudes, vibration velocities, and output power at relatively low applied electric fields.

The amplification is determined by the material’s piezoelectric, mechanical, and dielectric properties as much as by the energy dissipation and generated loss, which is a distinct difference from the off-resonance conditions. The strain amplitude (S_i) is expressed as [10]

$$S_i = \frac{8}{\pi^2} Q_{ij}^R \cdot d_{ij} \cdot E_j. \tag{1.1}$$

While the piezoelectric coefficient (d_{ij}) and applied field amplitude (E_j) assign the piezoelectric strain at off-resonance frequencies ($S_i = d_{ij} \cdot E_j$), the resonance quality factor (Q_{ij}^R) determines the strain enhancement by $(8Q_{ij}^R)/\pi^2$ particularly at the resonance frequency [11]. This factor is inversely proportional to the intrinsic and extrinsic vibrational loss in the material, which cause self-heating and failure of the resonator [12]. It dictates the piezoceramics' resonance properties and stability, usually exhibiting a significantly more pronounced variation than other coefficients upon internal and external condition changes, such as composition, vibration velocity, and temperature [13, 14]. Therefore, it is surprising that despite its decisive role, the quality factor has been subjected to consolidate investigations significantly fewer than the piezoelectric coefficient.

Piezoelectric materials presently used in most high-power devices are poly-crystalline hard-type ferroelectric ceramics. Formerly utilized piezoelectric single-crystals such as quartz or Rochelle salt have been displaced largely, since competing favorably with the ceramics on one count, they generally fall far short on others. Thereby, crucial requirements in addition to large electromechanical coupling (for strain generation and broad bandwidth) and quality factor (for amplification), are a large permittivity (low impedance), mechanical strength, heat conduction, and perseverance to ambient conditions (temperature, pressure, humidity) [6, 10]. However, also state-of-the-art ferroelectrics subjected to the harsh conditions in resonance reveal detrimental shortcomings and limitations, which calls for next-generation high-power materials.

This work provides a systematic understanding of the resonance properties of state-of-the-art ferroelectrics and potential descendants. It is attempted to bridge phenomenological descriptions, fundamental mechanisms, and applicational aspects. The work is divided into

three main parts, aiming to enlighten some of the open questions and contribute to the development of next-generation high-power ferroelectrics.

The first part introduces the approaches and methodologies developed to experimentally investigate the properties of ferroelectric materials under piezoelectric resonance. Piezoelectric, mechanical, and dielectric properties as well as the quality factors are usually determined at small excitation fields and are then extrapolated linearly to large vibration velocities, leading to significant deviation from reality. The aim was to establish an experimental route using pulse drive excitation to measure the electromechanical coefficients at large strain amplitudes in different resonance modes and distinguish vibrational and thermal impacts. The results should be referenced to standardized small-field measurements on the low strain end as well as continuous measurements mimicking device driving conditions. Bridging the different measurement approaches was expected to enable a generalized property description. Moreover, combining the measurements with time-resolved in-situ diffraction studies should allow to observe microstructural changes direct under high-power loading. In addition, it was targeted to employ an equipment for resonance impedance spectroscopy under an AC measurement voltage superimposed with a high-voltage DC bias. It was expected to deconvolute intrinsic and extrinsic material contributions by manipulating the ferroelectric properties with the DC bias.

The second part focuses on the currently most dominant ferroelectric material system, integrated into the majority of all high-power devices – $Pb(Zr,Ti)O_3$. Despite the vast application range, a rapid decrease of the quality factor along with a severe self-heating have been reported as detrimental limitations of these compositions for the use at large vibration velocities. A long-standing hypothesis relates the observed degradation to increasing displacement of ferroelectric domain walls, which is a loss-affected process. The above-mentioned experimental methodology should be used to provide a novel insight into the motion of domain walls and their evolution, for the first time directly under high-power conditions. Moreover, measurements of selected $Pb(Zr,Ti)O_3$-based compositions should reveal the impact of internal (chemical modification or crystal structure) and external (temperature, frequency, DC bias) parameters on the high-power electromechanical coefficients. The main target was to implement a systematic understanding of this ferroelectric system´s advantages and (even more) shortcomings, be it the loss from domain wall motion or other strain generation processes.

The third part is dedicated to the resonance properties of lead-free ferroelectric alternatives to $Pb(Zr,Ti)O_3$. Particularly $(Na_{1/2}Bi_{1/2})TiO_3$-$BaTiO_3$-based compositions were subjected to the above-introduced characterization procedure. Recent reports indicated superior high-power properties of this material group, which already resulted in first patents and commercial applications, although the origin of this behavior is not understood yet. Therefore, it was first aimed to examine the macro- and microscale properties of unmodified compositions to trace the strain generation mechanisms and their contribution in resonance. Subsequently, modified compositions were inspected, comparing the property tailoring (ferroelectric hardening) by the state-of-the-art doping approach with the recently-introduced second phase approach. The latter is considered a generic hardening strategy and expected to conduct superior high-power properties, since it does not require a chemical modification of the ferroelectric matrix material; however, it requires the inclusion of a tailored second phase and the mechanisms are poorly understood yet. Using internal and external parameters, it was attempted to separate and elucidate these mechanisms. The results should highlight the benefits and drawbacks of these

lead-free compositions for high-power use. Together with the findings and general conclusions from the previous part, it was intended to formulate the requirements and provide guidance for the development of next-generation high-power ferroelectrics with larges efficiency and output power potential.

2. Review on piezoelectricity, ferroelectricity, and high-power properties

The following review introduces physical concepts and mechanistic processes, which are considered necessary to describe and interpret the results of the present research study. The chapter is divided into four parts: The first part provides a brief overview of dielectric materials and their piezo-, pyro-, and ferroelectrics subgroups. The second part introduces the basic definition and *phenomenological* treatment of piezoelectricity and piezoelectric resonance vibration. The third part covers the *mechanistic* description of piezoelectricity in ferroelectrics and relaxor-ferroelectrics. The last part focuses on the ferroelectric materials investigated in the study, summarizing the current understanding of their high-power properties. It is important to note that in literature, phenomenological and mechanistic descriptions are often convoluted using the same terminology, which is prone to misunderstanding and misinterpretation. It is attempted in the review and throughout the entire report to separate these approaches.

2.1. Electroceramics – from dielectrics to ferroelectrics

Dielectrics are electrically isolating materials that react to an applied electric field by a short-range charge displacement instead of a long-range charge transport [15]. The short-range charge displacement (D_i) is the sum of the electric field-induced (E_i) vacuum displacement and polarization (P_i), represented in tensor notation by

$$D_i = \varepsilon_0 E_i + P_i, \tag{2.1}$$

where ε_0 is the dielectric permittivity of vacuum. Polarization is defined as the amount of induced electric dipole moments per unit volume expressed as

$$P_i = \varsigma_{ij} \varepsilon_0 E_j, \tag{2.2}$$

with ς_{ij} being the dielectric susceptibility. The dielectric displacement is therefore proportional to the applied electric field

$$D_i = \left(\Delta_{ij} + \varsigma_{ij}\right)\varepsilon_0 E_j = \varepsilon_{ij}\varepsilon_0 E_j, \tag{2.3}$$

with the relative dielectric permittivity (ε_{ij}) as the material-specific proportionality constant (Δ_{ij} is the Kronecker-delta). Four types of polarization contributions are usually distinguished, including atomic polarization (displacement of nucleus and electron shell), ionic polarization (displacement of anion and cation sub-lattices), dipole reorientation (rotation of dipole vector), and space charge polarization (migration of charges) [15].

Subgroups of dielectrics are piezo-, pyro-, and ferroelectrics. In first approximation, the subgroups are determined by the crystallographic structure, which directly influences the physical properties. Only crystals belonging to 20 of the 32 possible symmetry point groups can be piezoelectric, i.e., those which are not centrosymmetric (**Figure 2.1**). *Piezoelectricity* denotes thereby the electromechanical property of the crystal to convert mechanical energy into electric energy (direct effect) and vice versa (indirect effect). Hence, applying an electric field or mechanical stress results simultaneously in strain and polarization. In purely piezoelectric

crystals only the linear reversible piezoelectric effect contributes to the electromechanical coupling, i.e., generated strain and polarization are attributed to the relative displacement of the ionic sub-lattices under formation of a dipole moment. The process is known as the intrinsic effect [1].

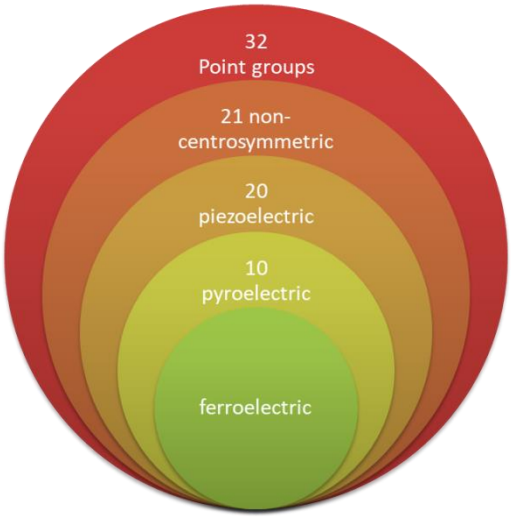

Figure 2.1: Relationship between crystal symmetry (point groups) and dielectric properties. 20 non-centrosymmetric point groups reveal a polarization vector upon external perturbation. In 10 point groups the polar vector is permanent also in the unloaded state. The crystal is ferroelectric if the polar vector can be switched between crystallographic orientations.

Pyroelectricity appears in 10 of the 20 piezoelectric point group crystals (**Figure 2.1**), featuring a spontaneous polarization along one crystallographic direction, which appears already in the unloaded state. Temperature variations induce changes in polarization and charge generation. In non-pyroelectric crystals, only an inhomogeneous temperature distribution and the thereby induced mechanical stress would result in polarization change [1].

Ferroelectrics are a subgroup of pyroelectrics. However, ferroelectricity cannot be directly attributed to a crystal structure and requires additional thermodynamic preconditions. The spontaneous polarization arises along multiple crystallographic orientations, which are energetically equivalent. The polarization direction can be switched reversibly between the orientations applying an external load. This breaks the linear relation between polarization or strain and electric field or mechanical stress, leading to a hysteretic behavior. Focus of this study is the class of poly-crystalline ferroelectric ceramics with the perovskite ABO_3 structure. The nomenclature denotes cations of +1 to +3 valence on the A-site and cations of +3 to +5 valence on the B-site located at the corners and in the body-center of an essentially cubic unit cell, respectively. Core feature of the cell is a face-centered oxygen octahedron enclosing the B-site [16]. The term “ferroelectricity” evolves from the phenomenological similarity to ferromagnetism.

2.2. Piezoelectricity

The following phenomenological description of the electromechanical energy conversion addresses the constitutive equations, boundary conditions, anisotropy, resonance vibration, and loss utilizing the terminology established in the literature. Therefore, it should be noted that the term “piezoelectricity” refers here to the macroscopic effect of electromechanical coupling. The term does not denote mechanistic processes. For instance, in the case of ferroelectrics,

several processes contribute to the electromechanical coupling, including lattice distortion (intrinsic piezoelectric effect in its original sense), but also other extrinsic contributions like domain wall motion (sometimes called extrinsic piezoeffect [1]). Hence, the introduced concepts should be considered independent of any material characteristics, the underlying processes will be distinguished in the subsequent section.

2.2.1. Constitutive equations

The piezoelectric effect (electromechanical coupling) follows from the thermodynamic description of a linearly coupled system [17, 18]. The Gibbs free energy (G) of the system under isothermal conditions[i] is expressed as

$$G = U - T_{ij}S_{ij} - E_n D_n. \tag{2.4}$$

The first derivatives of G govern the variables mechanical stress (T_{ij}), elastic strain (S_{ij}), electric field (E_n), and dielectric displacement[ii] (D_n). The second derivatives of G determine the electromechanical coefficients, like the elastic compliance (s_{ijkl}), dielectric permittivity (ε_{nm}), and piezoelectric charge coefficient (d_{nij}) in terms of

$$s_{ijkl}^E = \left(\frac{\partial S_{ij}}{\partial T_{kl}}\right)_E = -\left(\frac{\partial^2 G}{\partial T_{ij}\partial T_{kl}}\right)_E, \tag{2.5}$$

$$\varepsilon_{nm}^T = \left(\frac{\partial D_n}{\partial E_m}\right)_T = -\left(\frac{\partial^2 G}{\partial E_n \partial E_m}\right)_T, \text{ and} \tag{2.6}$$

$$d_{nij} = \left(\frac{\partial S_{ij}}{\partial E_n}\right)_T = \left(\frac{\partial D_n}{\partial T_{ij}}\right)_E = \left(\frac{\partial^2 G}{\partial E_n \partial T_{ij}}\right). \tag{2.7}$$

The superscripts indicate that the electromechanical coefficients are valid only if the corresponding variables are constant. These boundary conditions will be described in more detail below. The subscripts specify that the variables and the coefficients are tensors of different ranks, representing the anisotropy and direction dependence of the coupling. The tensor notation is commonly converted into a simpler matrix expression utilizing an index abbreviation according to the Voigt notation [19]. The fundamental constitutive piezoelectric (electromechanical) relations are expressed as

$$S_i = s_{ij}^E T_j + d_{ij}E_j \text{ and} \tag{2.8}$$

$$D_i = \varepsilon_{ij}^T E_j + d_{ij}T_j. \tag{2.9}$$

Note that the constitutive equations conjecture a uniform distribution of mechanical stress and electric field. They are confined to the linear regime at relatively low levels of applied electric field and stress, but become increasingly inaccurate as the field and stress levels increase. In case of non-linearity, additional cross-coupled terms need to be considered. The Einstein tensor convention was used to express the equations.

The matrix representation can be further tailed off considering the tensor and crystal symmetry. Some of the matrix elements become exchangeable or zero due to symmetry arguments [19].

[i] Isothermal condition disposes the electrocaloric and pyroelectric effects.

[ii] Strictly speaking polarization (P_n) instead of electric displacement (D_n) should be employed in the energy formulation. However, for materials where $\varepsilon_{ij} \gg 1$, like those used in this study, the approximation $P_n \approx D_n$ can be applied.

In the simplest but also most applied case of ∞m symmetry (poly-crystalline piezoelectric), the constitutive equations are represented by

$$\begin{pmatrix} S_1 \\ S_2 \\ S_3 \\ S_4 \\ S_5 \\ S_6 \\ D_1 \\ D_2 \\ D_3 \end{pmatrix} = \begin{pmatrix} s_{11}^E & s_{12}^E & s_{13}^E & 0 & 0 & 0 & 0 & 0 & d_{31} \\ s_{12}^E & s_{11}^E & s_{13}^E & 0 & 0 & 0 & 0 & 0 & d_{31} \\ s_{13}^E & s_{13}^E & s_{33}^E & 0 & 0 & 0 & 0 & 0 & d_{33} \\ 0 & 0 & 0 & s_{55}^E & 0 & 0 & 0 & d_{15} & 0 \\ 0 & 0 & 0 & 0 & s_{55}^E & 0 & d_{15} & 0 & 0 \\ 0 & 0 & 0 & 0 & 0 & s_{66}^E & 0 & 0 & 0 \\ 0 & 0 & 0 & 0 & d_{15} & 0 & \varepsilon_{11}^T & 0 & 0 \\ 0 & 0 & 0 & d_{15} & 0 & 0 & 0 & \varepsilon_{11}^T & 0 \\ d_{31} & d_{31} & d_{33} & 0 & 0 & 0 & 0 & 0 & \varepsilon_{33}^T \end{pmatrix} \times \begin{pmatrix} T_1 \\ T_2 \\ T_3 \\ T_4 \\ T_5 \\ T_6 \\ E_1 \\ E_2 \\ E_3 \end{pmatrix}, \tag{2.10}$$

including two independent dielectric, five[iii] elastic, and three piezoelectric coefficients [16]. To describe the properties of a piezoelectric resonator entirely, it is necessary to determine all independent matrix elements, i.e., electromechanical coefficients. Specific sample geometries are required to distinguish the coefficients experimentally (**Table 2.1**).

Electromechanical coupling

The constitutive equations express the linear electromechanical coupling, i.e., applied mechanical stress induces elastic strain and generates additionally surface charges, which is denoted as the direct piezoelectric effect. Vice versa, applied electric fields cause an electric displacement inducing additionally elastic strain[iv], which is denoted as the indirect piezoelectric effect. The conversion ratio between mechanical and electric energy is quantified by the electromechanical coupling coefficient (k_{ij}) [15]

$$k_{ij}^2 = \frac{output\ mechanical\ energy}{input\ electric\ energy} = \frac{output\ electric\ energy}{input\ mechanical\ energy}. \tag{2.11}$$

k_{ij} is also a tensor quantity with elements in the theoretical limits between 0 and 1. Note that k_{ij} does not directly represent conversion efficiency or conversion loss. For example, if $k_{ij} < 1$, more energy is provided during an energy cycle than converted; however, part of the excess energy returns to the source after the cycle is completed [11]. k_{ij} is determined by the electromechanical coefficients as

$$k_{ij}^2 = \frac{d_{ij}^2}{s_{ij}^E \varepsilon_{ij}^T}. \tag{2.12}$$

Equations (2.8)-(2.12) are given in the intensive or (T, E)-type form. The relations can be equivalently represented in the extensive or (S, D)-type form, which is summarized in the supplemental material (**Equations (7.1)-(7.7)**). The intensive and extensive forms are related through the coupling coefficient [11]

$$1 - k_{ij}^2 = \frac{s_{ij}^D}{s_{ii}^E} = \frac{\varepsilon_{ij}^S}{\varepsilon_{ii}^T}. \tag{2.13}$$

[iii] $s_{66}^E = 2(s_{11}^E - s_{12}^E)$ is not independent.

[iv] Strain can also be induced by an external field through non-linear coupling. This effect is called *electrostriction* and will be neglected here, since in ferroelectrics the magnitude is typically much lower compared to the piezoelectric effect.

Electric and mechanical boundary conditions

The applied boundary conditions determine whether the intensive or extensive form is applied and are essential in order to derive the electromechanical coefficients accurately. For example, when mechanical stress is applied under zero electric field condition (**Figure 2.2b**), the elastic strain is derived according to **Equation (2.8)** as (direction dependency is neglected for simplicity)

$$S = s^E T. \tag{2.14}$$

Under zero dielectric displacement (**Figure 2.2c**), an additional internal electric field (E') arises according to **Equation (2.9)** to fulfill the condition

$$D = 0 \rightarrow \varepsilon^T E' = -dT. \tag{2.15}$$

Inserting the internal electric field into **Equation (2.8)**, the generated strain is determined by

$$S = s^E T - \frac{d^2}{\varepsilon^T} T = \left(s^E - \frac{d^2}{\varepsilon^T}\right) T = s^D T. \tag{2.16}$$

Obviously, the elastic compliance depends on the electric boundary conditions, which are denoted by the superscripts as mentioned above. The intensive and extensive coefficients are related through the coupling coefficient. Constant electric field and constant dielectric displacement conditions are experimentally achieved by short-circuiting or open-circuiting the surface electrodes of the piezoelectric resonator, respectively [11].

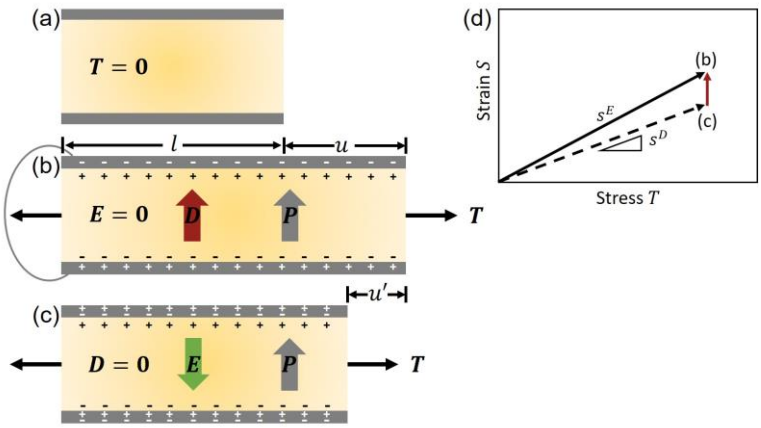

Figure 2.2: Schematic of elastic strain ($S = \frac{u}{l}$ or $S = \frac{u-u'}{l}$) generated by an applied mechanical stress (T) perpendicular to the polarization (P) direction of a piezoelectric element under (b) constant electric field (E) and (c) constant dielectric displacement (D) conditions. The elastic compliance, which is the proportionality constant between (d) S and T, depends on the electric boundary conditions.

Non-linear constitutive equations

The constitutive relations (**Equations (2.8)-(2.9)**) become increasingly inaccurate as the field and stress levels increase, which is attributed to the non-linearity of the coefficients [20, 21]. The non-linearity can be accounted by higher-order coefficients and additional cross-coupled terms

$$S_i = s_{ij}^E T_j + s_{ijk}^E T_j T_k + s_{ijkl}^E T_j T_k T_l + d_{ij} E_j + d_{ijk} E_j E_k + \cdots \text{ and} \tag{2.17}$$

$$D_i = d_{ij} T_j + d_{ijk} T_j T_k + d_{ijkl} T_j T_k T_l + \varepsilon_{ij}^T E_j + \varepsilon_{ijk}^T T_j T_k + \cdots. \tag{2.18}$$

The appearance of higher-order dependencies requires to treat the piezoelectric, mechanical, and dielectric coefficients as functions of field and stress amplitudes instead of constants. Accounting only the quadratic terms, the non-linear expressions associate with the empirical Rayleigh relations (**Equations (2.53)-(2.55)**) [22]. Moreover, the non-linear coefficients represent the appearance of higher-harmonics under harmonic dynamic load [23, 24] and the resonance peak distortion [25, 26] (discussed in next section). It is necessary to decouple the impacts of field and stress, as well as temperature, bias, and other variables, in order to identify the underlying mechanisms determining the coefficients.

2.2.2. Piezoelectric resonance vibration

The above-derived constitutive equations are equivalently valid under static as well as dynamic loading. Dynamic loading in terms of a harmonic electric excitation at specific frequencies allows thereby to generate an amplified mechanical response. This condition is denoted as piezoelectric resonance or high-power drive and describes the initiation of a mechanical resonance vibration through electrical excitation and electromechanical coupling [10]. The amplified response is used in a variety of piezoelectric applications introduced above. The resonance characteristics (e.g., frequency range, amplification factor) are determined by the electromechanical coefficients and loss of the piezoelectric resonator. In turn, the evaluation of the recorded resonance can be utilized to determine the electromechanical properties. To this end, the phenomenological description of piezoelectric resonance is derived here.

Three different resonance vibration modes have been investigated in this study to determine the tensor elements of the electromechanical coefficients. These include the transverse length mode (k_{31} coupling), the longitudinal length mode (k_{33} coupling), and the transverse radial or planar mode (k_p coupling). The corresponding geometries of the piezoelectric resonators are demonstrated in **Table 2.1**. The modes denote the directional relation between the polarization, applied electric field, and strain [11]. The considerations in the following focus on the transverse length mode, which is the predominantly utilized mode in the study. Derivations for the other modes are summarized in the supplemental material (Section 7.1).

Table 2.1 displays a bar-shaped resonator with its length along the x_1-direction and electroded faces normal to the x_3-direction. Polarization and the applied electric field are parallel to the x_3-direction. Length is much greater than width and height, therefore, in first approximation, strain and vibration can be assumed to occur only in the x_1-direction. In this case, the bar-shaped resonator can essentially be treated as a one-dimensional problem. Moreover, the resonator can be considered by a simple vibration model of coupled spring and mass, usually called a discrete or lumped mechanical model [10].

Along the x_2- and x_3-directions, the bar is free to expand; the electroded faces form equipotential surfaces in the direction of strain (x_1-direction). The electric and mechanical boundary conditions are consequently represented by [10]

$$T_2 = T_3 = T_4 = T_5 = T_6 = 0, \tag{2.19}$$

$$E_1 = E_2 = 0, \text{ and} \tag{2.20}$$

$$\frac{\partial E_3}{\partial x_1} = \frac{\partial E_3}{\partial x_2} = 0. \tag{2.21}$$

Table 2.1. Electroded resonators vibrating in the transverse mode (31), longitudinal mode (33), and radial mode (p), with l, d, w, and h denoting the length, diameter, width, and height. In all cases, electric field (E) and polarization (P) vectors are parallel to the x_3-direction. The main strain directions are represented by the dashed arrows. Summarized equations to calculate the coupling (k_{ij}), mechanical (s_{ij}^E), piezoelectric (d_{ij}), dielectric (ε_{ij}^T) coefficients and the Poison's ratio (σ) of a piezoelectric resonator in one of the three different vibration modes from the characteristic resonance (f_R), antiresonance (f_{AR}) frequency, and force factors (A_{ij} and B_{ij}) [27-29].

Modes	Transverse (31) mode	Radial (p)	Longitudinal (33)
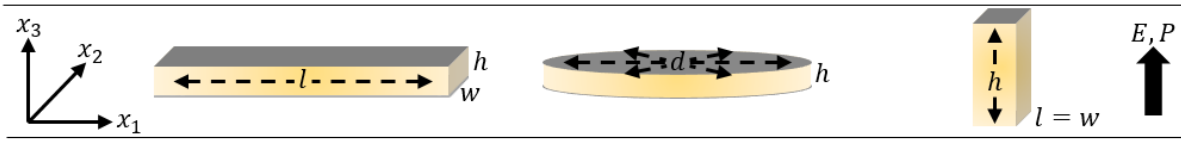			
	$l \geq 5w, 5h$	$d \geq 10h$	$h \geq 2.5l, 2.5w$
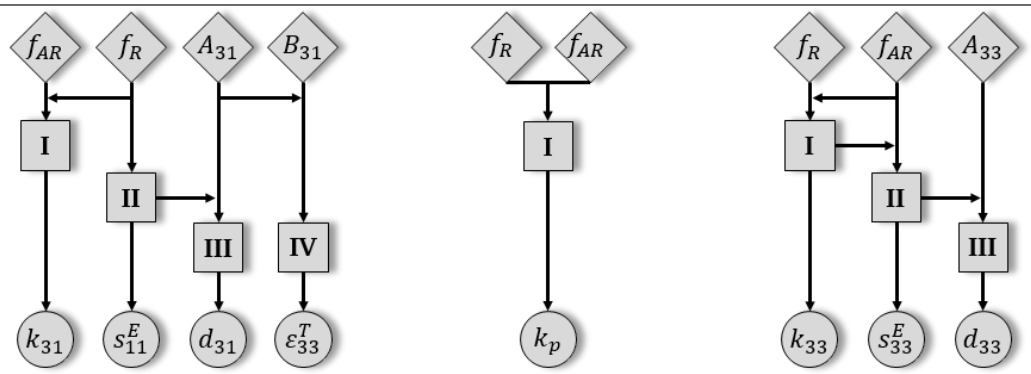			
I	$k_{31}^2 = \frac{\pi}{2}\frac{f_{AR}}{f_R}\frac{1}{\frac{\pi}{2}\frac{f_{AR}}{f_R} - tan\left(\frac{\pi}{2}\frac{f_{AR}}{f_R}\right)}$	$k_p^2 \cong 2.51\frac{f_{AR}-f_R}{f_R} - \left(\frac{f_{AR}-f_R}{f_R}\right)^2$	$k_{33}^2 = \frac{\pi}{2}\frac{f_R}{f_{AR}}\cot\left(\frac{\pi}{2}\frac{f_R}{f_{AR}}\right)$
II	$s_{11}^E = \frac{1}{4\rho f_R^2 l^2}$		$s_{33}^E = \frac{1}{4\rho f_{AR}^2 t^2}\frac{1}{1-k_{33}^2} = \frac{s_{33}^D}{1-k_{33}^2}$
III	$d_{31} = \frac{A_{31}s_{11}^E}{2w}$		$d_{33} = A_{33}s_{33}^E\frac{t}{2w^2}$
IV	$\varepsilon_{33}^T = \frac{A_{31}}{B_{31}}\frac{t}{lw}\frac{1}{1-k_{31}^2} = \frac{d_{31}^2}{s_{11}^E k_{31}^2}$		
V		$\sigma = 1 - 2\frac{k_{31}^2}{k_p^2} = -\frac{s_{12}^E}{s_{11}^E}$	

Therefore, the constitutive piezoelectric relations (**Equations (2.8)** and **(2.9)**) reduce to

$$S_1 = s_{11}^E T_1 + d_{31}E_3 \text{ and} \tag{2.22}$$

$$D_3 = \varepsilon_{33}^T E_3 + d_{31}T_1, \tag{2.23}$$

where superscripts indicate the independent variable held constant, while subscripts denote the tensor element. The time- and spatial displacement (u_1) of the resonator's elemental volume $dx_1dx_2dx_3$ can be expressed by Newton's wave equation as

$$\rho\frac{\partial^2 u_1}{\partial t^2}dx_1dx_2dx_3 = \frac{\partial T_1}{\partial x_1}dx_1dx_2dx_3. \tag{2.24}$$

Substituting **Equation (2.22)** into **Equation (2.24)** under consideration that $S_1 = {\partial u_1}/{\partial x_1}$ and ${\partial E_3}/{\partial x_1} = 0$, the wave equation becomes

$$\frac{\partial^2 u_1}{\partial t^2} = \frac{1}{\rho s_{11}^E}\frac{\partial^2 u_1}{\partial x_1^2} = (v_1^E)^2 \frac{\partial^2 u_1}{\partial x_1^2}, \tag{2.25}$$

where v_1^E is the wave velocity in the bar under constant electric field conditions. Under harmonic excitation $E_3 = E_0 e^{j\omega t}$ with an angular frequency ω, the differential equation is solved by

$$u_1 = \frac{v_1^E}{\omega}\left(\sin\left(\frac{\omega x_1}{v_1^E}\right) + \frac{\cos\left(\frac{\omega l}{v_1^E}\right)-1}{\sin\left(\frac{\omega l}{v_1^E}\right)}\sin\left(\frac{\omega x_1}{v_1^E}\right)\right) d_{31} E_0 e^{j\omega t}. \tag{2.26}$$

Substitution of **Equations (2.22)** and **(2.26)** into **Equation (2.23)** yields the dielectric displacement

$$D_3 = \left(\varepsilon_{33}^T(1-k_{31}^2) + \varepsilon_{33}^T k_{31}^2\left(\cos\left(\frac{\omega x_1}{v_1^E}\right) + \frac{\cos\left(\frac{\omega l}{v_1^E}\right)-1}{\sin\left(\frac{\omega l}{v_1^E}\right)}\sin\left(\frac{\omega x_1}{v_1^E}\right)\right)\right) E_0 e^{j\omega t}, \tag{2.27}$$

where the coupling coefficient is given as $k_{31}^2 = {d_{31}^2}/{s_{11}^E \varepsilon_{33}^T}$. It follows that the admittance of the vibrating bar is given by

$$Y = \frac{1}{Z} = \frac{I}{V} = \frac{w\int_0^l \dot{D}_3 dx_1}{\int_0^h E_3 dx_3} = j\omega \frac{lw}{h}\varepsilon_{33}^T\left((1-k_{31}^2) + k_{31}^2 \frac{tan\left(\frac{\omega l}{2v_1^E}\right)}{\left(\frac{\omega l}{2v_1^E}\right)}\right). \tag{2.28}$$

The admittance exhibits two characteristic frequencies, the resonance (f_R, maximum) and the antiresonance (f_{AR}, minimum) frequency, where the admittance becomes infinite or zero, respectively. The frequencies are determined by

$$f_R = \frac{v_1^E}{2l} \text{ and} \tag{2.29}$$

$$\frac{\tan\left(\frac{\pi f_{AR}}{2\, f_R}\right)}{\left(\frac{\pi f_{AR}}{2\, f_R}\right)} = \frac{k_{31}^2-1}{k_{31}^2}. \tag{2.30}$$

In the case of a free resonator, the frequency evolution of the admittance in the resonance-antiresonance range can be equivalently represented by a modified Butterworth-Van Dyke (BVD) [30] electric circuit (**Figure 2.3**). The dynamic branch of the circuit consists of a capacitance (C_d) and an inductance (L_d) and represents the vibration of the resonator (the resistors will be introduced later). Ideally, only the dynamic branch is active in resonance. Hence, it is the counterpart to the lumped mechanical spring-mass model. Both are interconnected through the force factor (A_{31}), which correlates the induced electric current (I_3) with the generated vibration velocity (v_1) in resonance by [11]

$$A_{31} = \frac{I_3}{v_1}. \tag{2.31}$$

An extension of the model also derives the force factor B_{31}, which correlates the applied voltage (V_3) with the generated displacement (u_1) in antiresonance by [27]

$$B_{31} = \frac{V_3}{u_1}. \tag{2.32}$$

However, the bar-shaped configuration requires to consider the resonator as a parallel plated capacitor. The off-resonance "clamped" capacitance (C_0) is represented by the parallel branch.

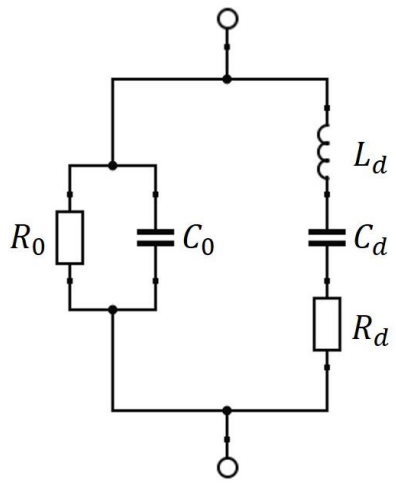

Figure 2.3. Equivalent circuit representing a piezoelectric resonator in transverse (31) vibration mode with two parallel dynamic ($L_d C_d R_d$) and static ($C_0 R_0$) branches.

Representing the resonator impedance by the equivalent electric circuit is a convenient approach to determine its electromechanical coefficients by purely electrical measurements (e.g., resonance impedance spectroscopy) or combined electromechanical measurements (e.g., pulse drive method with burst excitation). Thereby, measured "circuit components" are directly correlated with the electromechanical coefficients of the resonator (**Supplemental Equations (7.13)-(7.15)**). Coefficients k_{ij}, s_{ij}^E, and d_{ij} are calculated from the measured quantities f_R, f_A, A_{ij}, and B_{ij}. **Table 2.1** summarizes the resonator configurations and the corresponding equations for the transverse vibration mode with k_{31} coupling, as well as for the longitudinal vibration mode with k_{33} coupling and the radial vibration mode with k_{p} coupling [27-29].

In summary, a piezoelectric resonator exhibits the frequency-dependent admittance of a parallel-plate capacitor superimposed with two anomalies at the characteristic resonance and antiresonance frequencies, where the admittance deviates toward infinity or zero, respectively (**Figure 3.1**). Due to the piezoelectric (electromechanical) coupling, the anomalies coincide with the mechanical resonance of the resonator and an infinite amplification of the induced strain amplitude, which is otherwise constant at frequencies away from the anomalies. This effect is denoted as piezoelectric resonance and is characterized by the piezoelectric, mechanical, and dielectric coefficients and the corresponding resonator dimensions and vibration mode.

2.2.3. Loss in piezoelectric resonance

The admittance of the resonator determined in **Equation (2.28)** exhibits a divergence to infinite or zero at the characteristic resonance and antiresonance frequencies, respectively, since dissipative sources or loss have not been introduced yet. Loss generally reflects the delayed responses to a corresponding external stimulus, which is usually related to the friction and

inertia of the underlying processes. In order to consider dissipation, it is required to treat the electromechanical coefficients as complex quantities[v]

$$(s_{11}^E)^* = (s_{11}^E)' + j(s_{11}^E)'', \tag{2.33}$$

$$(\varepsilon_{33}^T)^* = (\varepsilon_{33}^T)' + j(\varepsilon_{33}^T)'', \text{ and} \tag{2.34}$$

$$(d_{31})^* = (d_{31})' + j(d_{31})''. \tag{2.35}$$

The phase angle is thereby determined by the ratio of the real and imaginary part

$$tan\,\gamma_{11} = \frac{(s_{11}^E)''}{(s_{11}^E)'}, \tag{2.36}$$

$$tan\,\delta_{33} = \frac{(\varepsilon_{33}^T)''}{(\varepsilon_{33}^T)'}, \text{ and} \tag{2.37}$$

$$tan\,\phi_{31} = \frac{(d_{31})''}{(d_{31})'}. \tag{2.38}$$

It turns out that the energy stored (W) and dissipated (H) in a volume element ($d\Omega$) of an electrically and mechanically loaded resonator can be expressed as [31]

$$W(\vec{r}) = 0.5\,\Re\left(D_i^* \cdot E_i + S_{ij}^* \cdot T_{ij}\right) \text{ and} \tag{2.39}$$

$$H(\vec{r}) = 0.5\omega\,\Im\left(D_i^* \cdot E_i + S_{ij}^* \cdot T_{ij}\right). \tag{2.40}$$

For the one-dimensional transverse (31) vibration, the expression reduces to [32]

$$W(x_1) = 0.5\,((\varepsilon_{33}^T)'E_3^2 + (s_{11}^E)'T_1^2 + (d_{31})'E_3^2 + (d_{31})'T_1^2) \text{ and} \tag{2.41}$$

$$H(x_1) = 0.5\omega\,((\varepsilon_{33}^T)'E_3^2\,tan\,\delta_{33} + (s_{11}^E)'T_1^2\,tan\,\gamma_{11} + (d_{31})'E_3^2\,tan\,\phi_{31} + (d_{31})'T_1^2\,tan\,\phi_{31}). \tag{2.42}$$

The loss is usually accounted for by a reciprocal quantity, referred to as quality factor (Q). In case of vibration, the quality factor determines the ratio between the stored energy and the energy loss within one complete vibration cycle and is expressed in the most general form as [33]

$$Q = 2\pi\frac{\int_\Omega W(\vec{r})d\Omega}{\int_\Omega H(\vec{r})d\Omega}. \tag{2.43}$$

Q is often denoted as the "mechanical" quality factor (Q_m), in order to emphasize its origin from mechanical vibration. Sometimes the more accurate expression "electromechanical" quality factor is used to highlight the coupling of electrical and mechanical loss in the case of piezoelectrically generated vibration. Throughout this study, Q will be simply denoted as "quality factor", since no other scenario apart from piezoelectric vibration is considered.

To account for the dissipation, the complex quantities need to be included in the wave equation (**Equation (2.24)**), which is then expressed for the transverse (31) vibration as [10]

$$\frac{\partial^2 u_1}{\partial t^2} = q^*\frac{\partial^2 u_1}{\partial x_1^2}, \tag{2.44}$$

[v] Strictly speaking, the consideration of loss requires the introduction of dissipation functions into the fundamental thermodynamic relations (**Equations (2.5)-(2.7)**). However, small loss that can be treated as perturbation, can also be accounted by introducing complex physical coefficients into the constitutive **Equations (2.8)-(2.9)**.

where $q^* = ((v_1^E)^*)^2 = q + j\omega\varrho$ and $\partial/_{\partial t} \rightarrow j\omega$. Thereby, q denotes the elastic constant of the spring, while ϱ adds a viscosity element and thus a delay and loss to the lumped mechanical model. Following the procedure described above, the admittance of the resonator is derived in the same form as given in **Equation (2.28)**, including the complex expressions of the electromechanical coefficients [34]. The evolution of the admittance as a function of frequency reveals finite values at the characteristic resonance and antiresonance frequencies, which is schematically displayed in **Figure 3.1**.

In the equivalent electrical circuit, the dissipation is accounted for by introducing additional resistive elements. In the simplest case, where only elastic loss ($tan\,\gamma_{11} = (s_{11}^E)''/(s_{11}^E)'$) is considered [1], a resistive element (R_d) is added to the dynamic branch (**Figure 2.3**). The dielectric loss ($tan\,\delta_{33} = (\varepsilon_{33}^T)''/(\varepsilon_{33}^T)'$) of the clamped capacity is represented by a parallel resistor R_0. An additional LCR branch can be added to address the piezoelectric loss ($tan\,\phi_{31} = (d_{31})''/(d_{31})'$) [34]. In general, a considerable amount of different equivalent electrical circuit layouts have been reported to resemble the observed admittance of a real resonator, to account for different types of loading and boundary conditions, or to consider the coupling between the different types of loss [10, 11, 34-36]. However, for a free unloaded piezoelectric resonator, it is often approximated that the elastic loss has a paramount contribution to the total loss or quality factor, respectively [1]. From the equivalent circuit displayed in **Figure 2.3** it is then derived that the quality factor in resonance is equal to the elastic loss, while the quality factor in antiresonance incorporates contributions of all three electromechanical loss [31, 37]

$$Q_{31}^R = \frac{1}{tan\,\gamma_{11}} \text{ and} \tag{2.45}$$

$$\frac{1}{Q_{31}^{AR}} = tan\,\gamma_{11} - \frac{k_{31}^2}{1-k_{31}^2}(tan\,\gamma_{11} + tan\,\delta_{33} - 2tan\,\phi_{31}). \tag{2.46}$$

Similar expressions are also derived for other vibration modes [38, 39]. However, note that it has also been stressed out that the dielectric and piezoelectric loss often substantially impact the resonance quality factor and are eventually even larger than the elastic loss [34, 36, 40]. Thus, for an accurate reconstruction of the resonator properties, it is inevitable to consider all three loss contributions and their coupling, particularly in the case of ferroelectric resonator material, where the different contributions to the piezoelectric/electromechanical response (intrinsic/extrinsic) are known to have an inherently lossy nature. Procedures to measure the resonator properties, the quality factors, and the corresponding loss contributions based on the equivalent circuit concept will be introduced in Section 3.1.

2.2.4. Resonance vibration velocity

Vibration velocity (v_i) is in general form the product of edge displacement and angular frequency ($v_i = \omega \cdot u_i$). In resonance, the vibration velocity can also be expressed independently of the resonator's dimensions as (modified after [10])

$$v_i = 2\pi f_R \frac{x_i}{2}\frac{2u_i}{x_i} = \pi N_i S_i, \tag{2.47}$$

where x_i is the resonator dimension in the main vibration direction, N_i is the dimension-normalized resonance frequency of the corresponding mode, and S_i the strain (**Equation (1.1)**). Utilizing the electromechanical coefficients, the expression transforms into (modified after [41])

$$v_i = \frac{4}{\pi}\frac{d_{ij}}{\sqrt{s_{ij}^E \cdot \rho}} \cdot Q_{ij}^R \cdot E_j = \frac{4}{\pi}\sqrt{\frac{\varepsilon_{ij}^T}{\rho}} \cdot k_{ij} \cdot Q_{ij}^R \cdot E_j, \tag{2.48}$$

convoluting the piezoelectric, mechanical, dielectric coefficients, the resonator density, the resonance loss (quality factor), and the driving electric field amplitude. It indicates a linear correlation between the induced vibration and the applied field. However, the coefficients usually reveal a significant field and vibration velocity dependence (Sections 2.4.2 and 2.4.4) leading to a non-linear correlation. In contrast to off-resonance conditions, it is common to determine the coefficients as a function of vibration velocity instead of electric field, since it is a dimension-independent variable, i.e., it represents equivalent strain states independent of the resonator size.

The spatial distribution and time dependence of the displacement or vibration velocity according to **Equation (2.26)** reduce in the resonance of the transverse (31) mode to

$$v_1(x_1) = v_{1,0} \sin\left(\frac{\pi}{l} x_1\right) \text{ and} \tag{2.49}$$

$$v_1(t) = v_{1,0} \sin(\omega t), \tag{2.50}$$

with $\frac{\omega}{v_1^E} = \frac{\pi}{l}$ (**Figure 2.4a,b**). The maximum mechanical energy density ($\Upsilon_0^{m,31}$) is given in that case as

$$\Upsilon_0^{m,31} = \int_{-l/2}^{l/2} \frac{1}{2}\rho v_1^2(x_1) dx_1 = \frac{1}{4}\rho v_{1,0}^2. \tag{2.51}$$

The power density ($\Psi^{m,31}$) follows from the time-average of the mechanical energy density as

$$\Psi_0^{m,31} = \frac{1}{16}\sqrt{\frac{\rho}{s_{11}^E l^2}} v_{1,0}^2. \tag{2.52}$$

Current commercial lead-based resonator materials are limited to a power density of about 10-50 W/cm³ [1, 5, 42], which corresponds to a maximum mechanical energy density of 1-5 mJ/cm³ and a vibration velocity in the range of 1 m/s.

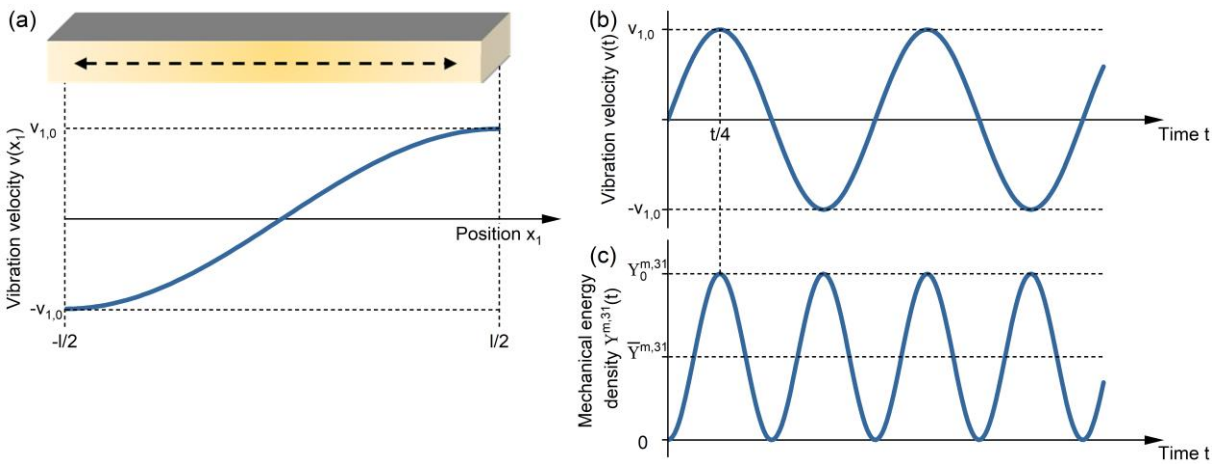

Figure 2.4. (a) Spatial distribution (**Equation (2.49)**) of the vibration velocity ($v_1(x_1)$; equivalent for displacement) along the length (x_1) of a transverse mode resonator bar at $t/4$. The vibration maxima ($v_{1,0}$) are at the edges of the bar; the nodal point is in the center. (b) Time (t) dependence (**Equation (2.50)**) of the (b) edge vibration velocity and (c) integrated mechanical energy density ($\Upsilon^{m,31}$; **Equation (2.51)**) assuming a harmonic electric excitation. $\overline{\Upsilon}^{m,31}$ denotes the time-average of the energy density.

2.3. Ferroelectricity

Poly-crystalline piezoelectric ceramic resonators are by necessity ferroelectric materials, exhibiting, among others, large electromechanical coefficients, extensive property variability, and ease to produce. Essential precondition is the ability to pole the ferroelectric material, which is isotropic after processing, i.e., to induce a preferred direction of polarization and imprint a macroscopic anisotropy that is mandatory to achieve piezoelectric activity. Non-ferroelectric materials cannot be piezoelectric, unless they are single crystalline or textured [43]. The following mechanistic considerations were predominantly derived from theoretical and experimental data of $BaTiO_3$- and $Pb(Zr,Ti)O_3$-based proper ferroelectrics. However, it has been evidenced that the considerations apply qualitatively to other ferroelectric systems as well; fundamental differences will be emphasized explicitly.

2.3.1. Large field characteristic – ferroelectric hysteresis

Virgin ferroelectrics exhibit no piezoelectric (electromechanical) activity despite having a spontaneous polarization. Every single-crystal (ceramic grain) is divided into regions of homogeneous polarization, i.e., the dipole moment of every unit cell within a region is aligned along one of the energetically equivalent crystallographic orientations accumulating to a polarization vector (**Figure 2.5c;** A). These regions are denoted as domains. The orientations of the polarization vectors between the domains are statistically distributed and sum up to zero macroscopic polarization [1]. Driving force for domain formation is the minimization of the depolarizing field (electrostatic energy) and mechanical stress (elastic energy). The domain size is balanced between the gained electrostatic and elastic energy and the contributed domain wall energy [18]. Boundaries between domains are depicted as domain walls. They are grouped into 180° and non-180° domain walls [44]. 180° walls separate domains with antiparallel polarization vectors; non-180° walls separate domains with a polarization vector angle smaller 180°. In ferroelectrics with tetragonal symmetry, for example, they separate domains with perpendicular (90°) polarization vectors (**Figure 2.5c;** A).

External disturbance, either electric or mechanical, induce the characteristic hysteretic behavior. Two processes are convoluted (**Figure 2.5a**): The increasing electric field induces ionic polarization in terms of an opposite displacement of the cation and anion sub-lattices. Additionally, above the poling field (B) the domains change in size and shape. Domains with a favorable polarization direction with respect to the field direction nucleate and/or grow to the expense of the unfavorable oriented domains (B-C). The process is referred to as domain switching, indicating an irreversible long-range translation of domain walls that breaks the linearity of the polarization response. Driving force is the reduced Gibbs free energy for polarization directions along the electric field according to the Landau–Ginsburg–Devonshire theory [45, 46]. Above a threshold field (C), the domain configuration is saturated (poly-crystals), ideally a monodomain state with the polarization vector parallel to the applied field is established (single-crystal). A further field increase (C-D) associates with a linear polarization increase (**Equation (2.2)**) due to ionic polarization. The processes are designated as *intrinsic* or lattice contribution (ionic displacement) and *extrinsic* contribution (domain wall displacement). Other processes like electrostriction (intrinsic) or induced phase transition and interphase boundary displacement (extrinsic) usually have a subordinated effect [47]. Decreasing the field to zero (D-E) diminishes the ionic polarization and allows partial domain back-switching, terminating at the remanent polarization (P_{rem}). The back-switching is initiated

by internal electric fields or mechanical stress (poly-crystal) and entropy arguments (single-crystal) [18]. The half-cycle is declared as poling, emphasizing the non-zero macroscopic polarization in the remanent state and the induced electromechanical activity. A field increase opposite to the polarization direction induces the reverse processes (E-G). However, since the starting point is shifted along the polarization axis (A-E), the polarization crosses the zero state at the coercive field (E_c), dedicated as field-induced depolarization (F). The ferroelectric remains in the remanent state along the negative direction after removing the field (H).

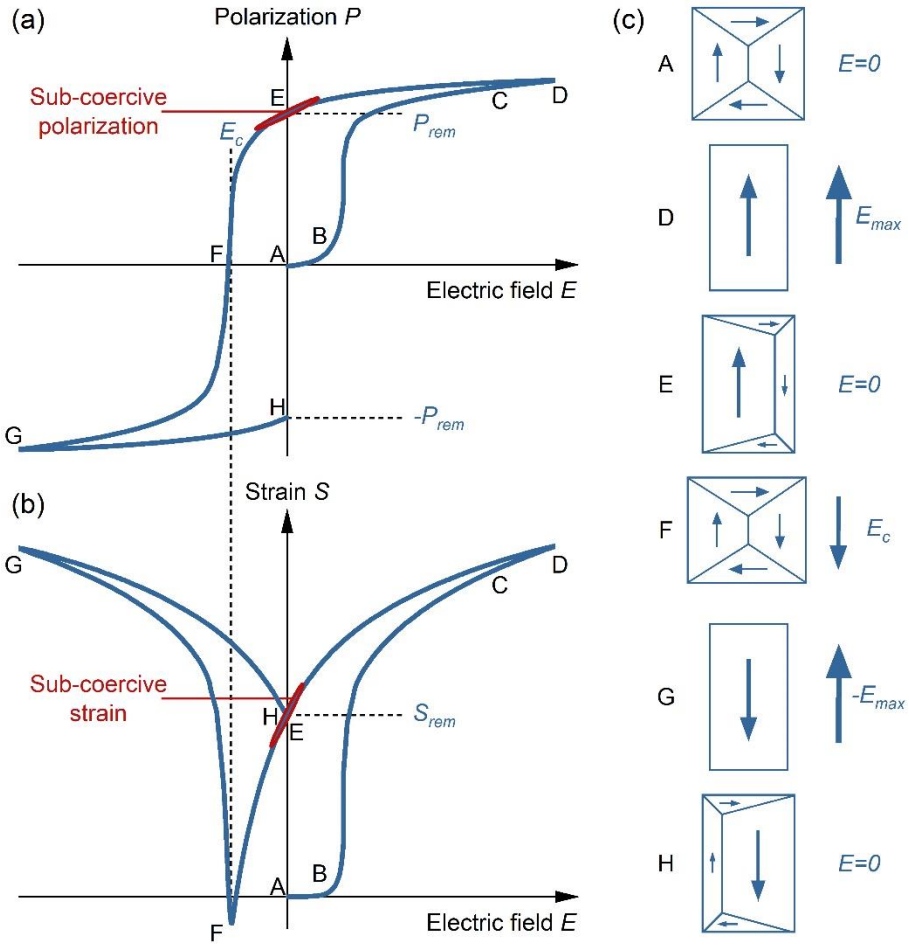

Figure 2.5: Schematic of ferroelectric (a) polarization (P) and (b) strain (S) hysteresis under bipolar electric field (E) starting from the unpolarized state (blue lines); marked are the coercive electric field (E_c) and the remanent polarization (P_{rem}) and strain (S_{rem}). Sub-coercive linear hysteresis is inserted (red lines). (c) Idealized domain configurations at selected states (A-H) of a crystal (grain) with tetragonal crystal structure. Arrows within the domains represent the polarization vector, the field vectors are denoted outside (modified after [48]).

The applied electric field induces simultaneously a strain hysteresis due to the electromechanical coupling, usually called "butterfly" loop (**Figure 2.5b**). The strain hysteresis is associated with the same mechanistic processes as the polarization hysteresis: The domain switching upon increasing field induces a non-linear elongation along and shrinkage perpendicular to the field direction (B-C). The strain is determined by the lattice distortion in the polarization direction (e.g., tetragonal c/a lattice constants ratio) and the volume of domain switching. The response becomes linear above the threshold field (C-D), correlated with the field-induced lattice stain, i.e., pure intrinsic (indirect) piezoeffect. The strain is non-zero in the remanent state upon removal of the field due to modified domain configuration (D-E). Negative fields reduce the strain to a minimum at the coercive field due to depolarization (E-F). Beyond

the coercive field the strain increases again (F-G) and returns to the same remanent strain state but opposite polarization direction (G-H). Note that the polarization hysteresis results from the long-range translation of 180° as well as non-180° domain walls, while stain hysteresis originates solely from non-180° domain wall displacement (domains with antiparallel polarization exhibit the same lattice distortion). Hence, 180° domain walls are ferroelectric, while non-180° domain walls are also ferroelastic. Therefore, the intrinsic and extrinsic contributions and the domain wall properties can be distinguished by considering their variations as a function of externally controlled variables, mostly field, stress, temperature, frequency, time, or others [49].

Ferroelasticity is also the origin of polarization and strain hysteresis under mechanical load (**Figure 2.6a,b**). Compressive stress on a ferroelectric/ferroelastic material in the remanent state induces linear polarization and strain response according to the intrinsic (direct) piezoelectric effect and lattice elasticity (**Equations (2.8)-(2.9)**). Above the coercive stress (T_c) it initiates additional non-linear ferroelastic domain switching in terms of long-range translation of non-180° domain walls (B-C). The responses return to a linear regime beyond a threshold stress where the domain configuration is saturated (C-D). The material remains in a remanent state after unloading and back-switching (D-E). Note that large electric fields align the polarization vectors parallel to the field vector, while compressive stress aligns them in a plane perpendicular to the loading direction (D). Thereby, the macroscopic polarization vanishes due to the formation of 180° domain walls that minimize the electrostatic energy but do not couple to the mechanical stress, leading to a stress-induced depolarization [50, 51].

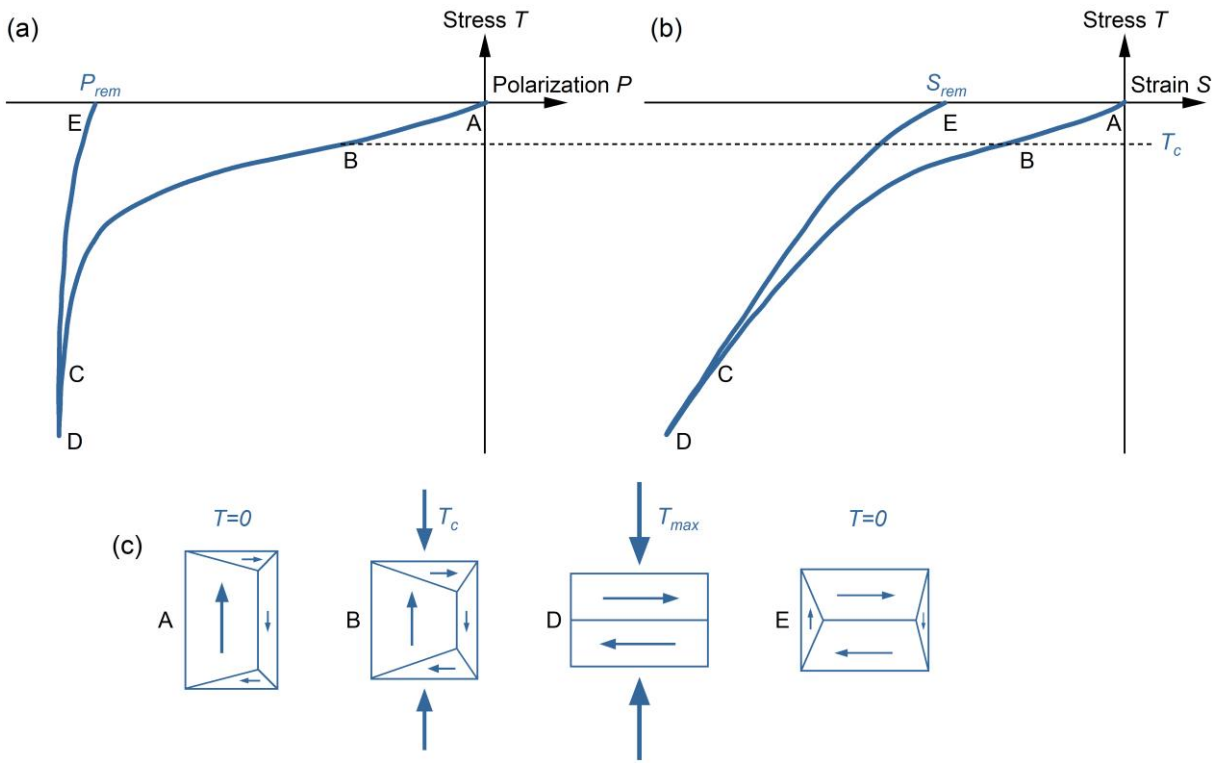

Figure 2.6. Schematic of ferroelastic (a) polarization (P) and (b) strain (S) hysteresis under uniaxial compressive stress (T) starting from the polarized state; marked are the coercive stress (T_c) and the remanent polarization (P_{rem}) and strain (S_{rem}). (c) Idealized domain configurations at selected states (A-E) of a crystal (grain) with tetragonal crystal structure. Arrows within the domains represent the polarization vector, the stress vectors are denoted outside (modified after [51]).

2.3.2. Soft and hard ferroelectrics

Ferroelectrics are classified into *soft-type* and *hard-type* (in analogy to soft/hard ferromagnetism). Ferroelectrically soft compositions are characterized by rectangular polarization loops, low coercive fields and coercive stress, large maximum and remanent polarizations and strains, but also a broad hysteresis (loss) and significant amount of back-switching. Moreover, they reveal large piezoelectric, mechanical, and dielectric coefficients and do not exhibit a pronounced time dependence (aging) or significant difference in the large-field characteristics before and after poling [43]. In contrast, ferroelectrically hard compositions expose large coercive fields and stress, low strain and polarization responses, but slim hysteresis loops. The loops often reveal a pinching and a strong back-switching to almost zero remanent polarization and strain. However, the properties are usually diffusion-controlled and time-dependent. After poling and aging, the pinching transforms into an internal bias field, i.e., the polarization and strain loops are shifted along the abscissa, indicating larger coercive field and stress opposite the poling direction. Moreover, the responses along the poling direction become considerably more linear (examples in **Figure 4.3**) [49].

The differences originate mainly from the extrinsic contributions, particularly from the domain properties (in the absence of phase transformations). In hard ferroelectrics, the domain configuration is stable and the domain walls are pinned to their positions. Therefore, large driving forces are required to induce a reordering. In contrast, the energy potential of domains in soft ferroelectrics is comparably flat and large domain wall displacement can be induced easily [18, 52, 53].

Various internal and external conditions determine the ferroelectric hardening or softening, including microstructure, crystal structure, chemical modifications, temperature, or static fields/stress. Small domain size, usually induced by small grain size, hinders domain wall motion due to self-clamping effects [54-56]. Different crystal structures, although of same chemical compositions, exhibit distinct differences [57, 58]. A larger ferroelectric distortion of the unit cell induces hardening, while softening appears in the vicinity of the Morphotropic Phase Boundary (MPB) [13, 59].

However, the most significant internal impact arises from isovalent and aliovalent doping [43, 60]. Donor-doping denotes the employment of ions with larger positive valance on the A- or B-site of a perovskite crystal lattice. The charge is compensated by the formation of A- or B-site vacancies during calcination or sintering to retain charge neutrality. The introduced lattice defects usually remain isolated due to the low diffusion coefficients [61], but significantly increase the domain wall mobility and induce ferroelectric softening (the mechanism is still under dispute) [62]. Acceptor-doping depicts the employment of ions with lower positive valance usually on the perovskite B-site, which is compensated by the formation of oxygen vacancies. It was proven that the oxygen vacancies are able to diffuse toward the dopants (aging), forming polar defect complexes [61, 63]. Moreover, the formed defect dipoles orient along the polarization vector and retain only limited mobility, stabilizing the domain configuration, which manifests in ferroelectric hardening [64-66]. Driving force for the orientation is the minimization of the electrostatic and elastic energies associated with the dipole moment and lattice deformation [52, 67]. Still debated is the effective length scale of the defect influence, i.e., whether the impact is most significant upon defect accumulation in the bulk [52, 68], at the domain walls [69], or at the grain boundaries [70] (**Figure 2.7a**).

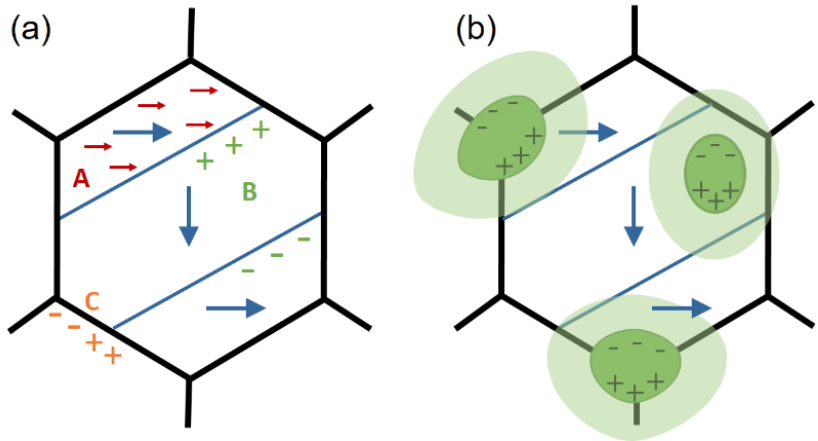

Figure 2.7. Schematic representation of hardening mechanisms in (a) acceptor-doped and (b) second phase hardened ferroelectrics. In (a) the ferroelectric domains (blue) are stabilized either by defect complexes in the bulk (A), or defect charge accumulation at domain walls (B) or grain boundaries (C). In (b) second phases at grain boundaries or precipitations within the grains stabilize the domain configuration introducing mismatch stress or free charges.

Comparatively novel is the ferroelectric hardening arising from targeted introduction of non-ferroelectric inclusions [71-73] or precipitation of secondary phases [74] in the ferroelectric matrix, forming 0-3 ceramic-ceramic composites (**Figure 2.7b**). The effect is based on inter- and intragranular stress, i.e., the generation of strain incompatibilities and mismatch stress between the phases, hindering domain wall displacement [75]. The deformation of a grain in a poly-crystalline ceramic upon application of a DC (poling) or AC (excitation) electric field occurs in cooperation with the surrounding grains [76, 77]. The grain-to-grain interactions result in strain incompatibilities due to their orientation mismatch, exerting clamping effects on the domain walls due to constrained deformation [78, 79]. This strain/stress is amplified by the presence of inclusions that exhibit inferior piezoelectric response but are elastically rigid (e.g., ZnO grains [80]). The process is schematically illustrated utilizing the Eshelby approach in **Figure 2.8**, assuming a single spheric particle in an infinite isotropic matrix [81]. The inclusion is removed from the matrix (**Figure 2.8a**) to allow an unconstrained deformation upon field application (**Figure 2.8b**). Subsequent refitting under consideration of the residual stress (**Figure 2.8c**) evolves in a reduced matrix strain (**Figure 2.8d**) with compressive matrix stress parallel and tensile matrix stress perpendicular to the field direction, respectively. The correlation reverses upon negative electric field application with respect to the matrix polarization direction. The induced residual stress decreases with increasing distance to the matrix/inclusion interface proportional to $^{1}/_{r^3}$, i.e., the effect is most pronounced in the close vicinity of the interface. The constraints largely affect the extrinsic strain mechanisms, but also impact the intrinsic processes [82].

The initial and alternative explanation based on introduced trapped charges at the interphase (in case of semiconducting inclusion) compensating for the depolarization fields is mostly withdrawn [83]. However, note that it cannot be disregarded that second phase ions can possibly enter the matrix lattice through interdiffusion during sintering, leading to, at least, additional doping effects. This has been enlighted by transmission electron microscopy with energy dispersive spectroscopy [84] and is indicated by the reduced sintering temperatures (second phase acts as sintering aid) [72]. Nevertheless, permittivity studies (charge hopping) [75], ferroelectric and piezoelectric characterization [74, 75], and phase transformation [85, 86] reveal distinct differences between compositions modified following one of the two

concepts. It requires further clarification and deconvolution of the contributions. Since the interdiffusion and residual stress are co-located at the matrix/inclusion interface, it is not trivial to distinguish the effects.

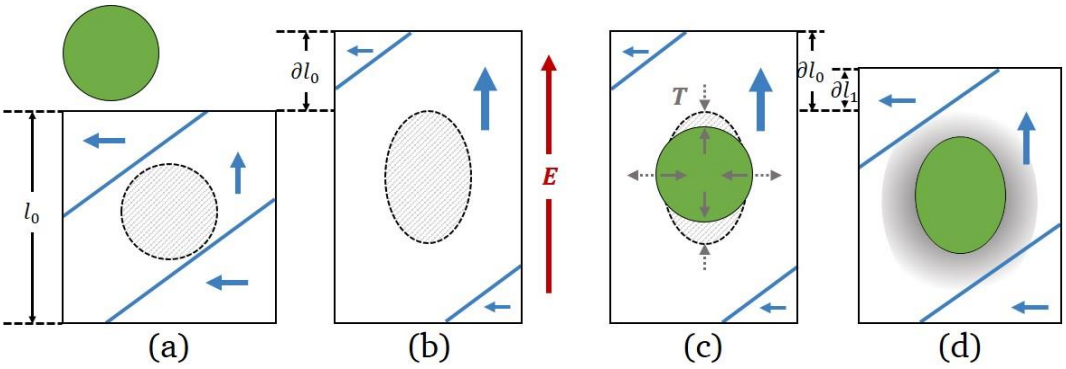

Figure 2.8. Eshelby description of strain incompatibility between an isotropic ferroelectric matrix (blue arrows denote the domain polarization) and a spheric non-ferroelectric inclusion (green). (a) The inclusion is cut out from the matrix, (b) which is strained upon electric field application (E, red arrow). (c) To fit the inclusion into the strained matrix, tensile and compressive stress (T; gray arrows) are applied to the matrix and the inclusion. Note that only the main stress components parallel and perpendicular to the field direction are denoted. (d) The evolving misfit stress at the matrix/inclusion interface reduce elongation along the field direction and imply reduced domain wall displacement.

Temperature is an important external condition as thermal energy activates domain wall motion [68]. Therefore, temperature increase is usually associated with ferroelectric softening [58]. However, the temperature dependence is not continuous, temperature-induced phase transitions can lead to rapid and hysteretic property changes in either direction (softening or hardening) [58]. A DC bias electric field or static mechanical stress superimposed with the driving field or stress induce hardening or softening if applied with the polarity parallel or opposite to the polarization vector, respectively [87]. According to the Landau–Ginsburg–Devonshire theory, the external bias stabilizes a polarization direction. Further external conditions that contribute to ferroelectric hardening or softening include other energy sources (e.g., light [88]). Note that the introduced internal and external conditions will always simultaneously impact the intrinsic contributions, however, usually to a significantly minor extent.

2.3.3. Small-field characteristics – piezoelectric, mechanical, and dielectric properties

Intrinsic and extrinsic contributions also determine the small-field response of ferroelectrics, i.e., the polarization and strain generation under sub-coercive loading. Also in this case, lattice distortion and domain wall displacement are the major contributions [89]. While the intrinsic response is linear in a wide loading magnitude range and does not exhibit a threshold, the sub-coercive displacement of domain walls is complex and not unambiguous. The displacement is commonly denoted as short-range domain wall motion or vibration [62, 89], to be distinguished from the long-range translation or switching (also called micro-hysteresis and macro-hysteresis [90]). Moreover, reversible and irreversible motions are differentiated [91-93]. An established model to describe the motion is based on a potential landscape around the equilibrium domain wall position (**Figure 2.9**). The potential is generated by a quadratic function representing the long-range elastic restoring force acting on the domain wall, superimposed by an empiric local periodic potential (exact potential is not known at present) [94]. The periodic potential represents the Rayleigh model applied to ferroelectricity (initially introduced in ferromagnetics

[95]) to consider the interaction with lattice, defects, dislocations, and neighboring domain walls [22, 96]. The domain wall is displaced reversibly around the equilibrium position within the potential well upon external perturbation, i.e., it returns back to the initial position after unloading. On the other hand, the domain wall is displaced irreversibly to another well and does not return to the initial position if sufficient activation energy is provided, which is determined by the well depth. The Rayleigh model presumes a statistical distribution of the activation energies, giving rise to a gradual increase of irreversible motion upon load magnitude increase. However, the potential is heavily affected by the above-introduced internal and external conditions , i.e., the domain wall motion magnitude and the reversible and irreversible contributions increase through, for example, donor doping or temperature increase (softening), which flatten the landscape and provide additional thermal activation [97]. Vice versa, acceptor doping or bias fields/stress hamper domain wall motion (hardening) by steepening the landscape. In case of exceptionally-hard ferroelectrics, for example, due to extensive acceptor doping and periodic defect arrangement, the Rayleigh potential is denoted as V-potential [66]; however, the cross-over is fluent.

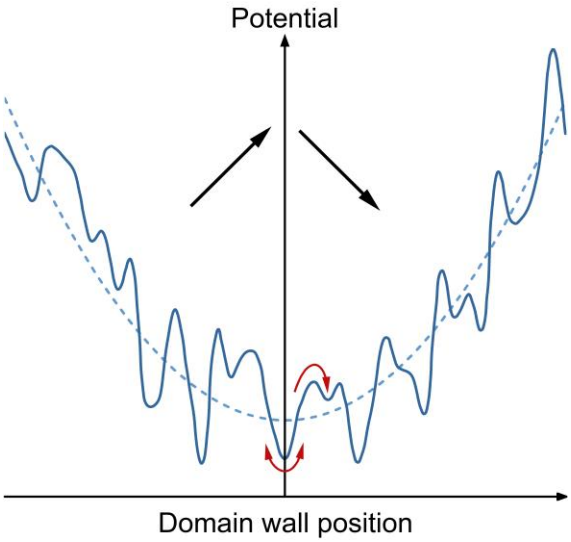

Figure 2.9. Schematic representation of the energy profile or potential landscape surrounding the equilibrium domain wall position. The profile evolves from the long-range elastic restoring force superimposed with the short-range interactions of the domain walls with, among others, lattice, defects, and other domain walls.

According to the Rayleigh model, the lattice distortion and reversible domain wall motion correlate linearly with the applied electric field or mechanical stress. The irreversible domain wall motion is non-linear and increases upon increasing excitation magnitude. Therefore, the electromechanical coefficients, such as the piezoelectric coefficient as a function of the applied electric field amplitude (E_0), are represented by the first Rayleigh equation in terms of (direction dependency is neglected for simplicity) [22]

$$d(E_0) = d_{init} + \alpha_R E_0. \tag{2.53}$$

The equation equivalently applies for the elastic compliance or dielectric permittivity [94], as well as under mechanical stress [98]. d_{init} is thereby the reversible field-independent component, while αE_0 represents the irreversible contribution with α denoted as the Rayleigh coefficient. It follows that the generated strain is expressed as [22]

$$S(E) = (d_{init} + \alpha_R E_0)E \pm \frac{\alpha_R}{2}(E_0^2 - E^2). \tag{2.54}$$

The expression is referred to as the second Rayleigh equation. It describes the parabolic field dependence of the variable (here exemplarily strain) and accounts for the evolving difference between ascending and descending load (here electric field), opening up a hysteresis due to the irreversible domain wall motion (inserts in **Figure 2.5a,b**). Note that the increasing hysteresis depicts an increasingly lossy process related to the irreversible domain wall motion. Nevertheless, also the reversible processes can be lossy, which is accounted for by implementing complex electromechanical coefficients instead of scalars in the Rayleigh **Equations (2.33)-(2.35)** [99].

The Rayleigh equations in their original form given above do not account for an initiation threshold of the irreversible domain wall motion, since a purely statistical distribution of activation energies is assumed. A more realistic scenario is a finite field value, below which the piezoelectric coefficient is approximately constant and field-independent, i.e., equal to d_{init} [99]. The threshold is expected to be more prominent in hard-type than in soft-type ferroelectrics. However, it is experimentally challenging to determine the threshold field precisely. To avoid the necessity of determining the threshold, the non-linear Rayleigh coefficient (α_R^*) is considered as a field-dependent entity in terms of [89]

$$\alpha_R^* = \alpha_{R1} + \alpha_{R2} E_0, \tag{2.55}$$

where the second term ($\alpha_{R2} E_0$) accounts for the transition from the constant to the linear regime at small fields [100]. The non-linear Rayleigh expression usually enables a very accurate representation of the measurement results.

2.3.4. Loss in ferroelectrics

Several above-described microscale processes occur simultaneously during the electro-mechanical response to external loading. All processes are considered to contribute also to the generated loss. The loss processes are commonly distinguished into four categories [40, 101, 102]: (1) Lattice loss is correlated with the lattice distortions, e.g., elongation or rotation of the polarization, occurring in all piezoelectrically active materials [103]. (2) Domain wall loss is associated with the reversible as well as irreversible motion of domain walls, occurring in all poly-domain ferroelectric crystals [104-106]. In some cases, the related interphase boundary motion or phase transitions are also considered [47]. (3) Microstructure loss is connected with poly-crystalline constraints, e.g., intergranular stress [76, 77]. (4) Dielectric loss (ohmic loss) accounts for lossy long- or short-range charge transfer. Although domain wall loss is usually the dominant contribution, the other sources should not be neglected. Note that it is sometimes attempted to correlate the mechanistic loss with the phenomenological loss description of the electromechanical coefficients (**Equations (2.36)-(2.38)**), which is not a trivial task and should be treated with care. For example, elastic loss ($tan\ \phi$), i.e., the phase angle between applied stress and generated strain, can be associated with all four loss mechanisms (except for 180° domain wall motion) and requires further analysis to distinguish the dominant contributions.

2.3.5. Relaxor-ferroelectrics

A specific ferroelectric class are relaxors, which are commonly rationalized considering the model of polar nanoregions (PNRs) [107, 108]. Those are local inhomogeneities with a dipolar moment embedded in a polarizable but non-polar matrix with an average pseudocubic crystal symmetry. Relaxors are named after their characteristic feature of possessing a pronounced

frequency dispersion or relaxation of the dielectric permittivity associated with a size distribution of the PNRs [108]. Above a ferroelectric-to-relaxor transition temperature (τ_{F-R}), relaxors are in an ergodic state, i.e., the PNRs' polarization vectors reorient between energetically equivalent crystallographic orientation and sum up to zero macroscopic polarization. The conversion into non-ergodic relaxors below the τ_{F-R} indicates that the polarization fluctuation is thermally inhibited (**Figure 2.10** (I)). In the latter state, relaxors can transform irreversibly into long-range polarized ferroelectrics (**Figure 2.10** (II)) upon application of high electric fields (poling). Relaxor-ferroelectrics in the polarized state, such as $Na_{1/2}Bi_{1/2}TiO_2$-$BaTiO_3$-based systems, reveal substantial electromechanical coupling and are considered pertinent piezoelectric materials (Section 2.4.3).

The relaxor state recovers from the induced ferroelectric state only upon heating above τ_{F-R}, i.e., the transition temperature sets basically the natural upper depolarization boundary. Thermal depolarization denotes thereby the thermally-induced disappearance of macroscopic polarization that ultimately results in electromechanical coefficients being reduced to zero. Hence, the depolarization temperature (τ_d) determines the operational temperature range of the polarized ferroelectric state and manifests a decisive limitation factor. Due to the complex electric field-temperature (E-T) phase diagrams of relaxors, τ_d and τ_{F-R} are not necessarily equal. Several other processes besides the ferroelectric-to-relaxor transition can lead to depolarization as well, such as detexturing of the domain polarization-directions in a poly-domain material or a ferroelectric-to-ferroelectric phase transition [43]. Those are common depolarization processes in classical ferroelectrics.

A specific relaxor-ferroelectric, important for the present study, is the (1-x)$Na_{1/2}Bi_{1/2}TiO_2$-x$BaTiO_3$-based solid-solution (details in Section 2.4.3), where a two-stage depolarization process has been proposed [109-111] (**Figure 2.10** (III and IV)). Temperature-dependent measurements of (0.94)$Na_{1/2}Bi_{1/2}TiO_2$-0.06$BaTiO_3$ revealed about 8 °C lower τ_d values than τ_{F-R} values [111, 112]. It has been suggested that the depolarization sequence starts with a detexturing of the domain polarization (equivalent to a classical ferroelectric) and that the macroscopic polarization vanishes prior to the ferroelectric-to-relaxor transition and the recovery onset of the ergodic relaxor state. This finding was supported by x-ray diffraction (XRD) [109], which did not give unambiguous evidence for a phase transition around τ_d. On the other hand, competing studies did not observe a clear shift between τ_d and τ_{F-R} [72, 113], although utilizing the same measurement methods and materials. Moreover, a temperature-induced increase of the non-polar pseudocubic phase at the expense of the ferroelectric phase around τ_d ($=\tau_{F-R}$) was noted [114-116]. Both indicate a second-order phase transition (**Figure 2.10** (V)) rather than a sharp displacive first-order transition like in classical ferroelectrics or Pb-based relaxors [117].

Attempts to resolve this discrepancy have utilized orientation-dependent single-crystal measurements of different (1-x)$Na_{1/2}Bi_{1/2}TiO_2$-x$BaTiO_3$ compositions, demonstrating that both scenarios are possible, since τ_d and τ_{F-R} are not necessarily linked [118]. τ_{F-R} associates with the thermal stability of the local coherence of neighboring dipole moments, which breaks up upon heating above τ_{F-R}. τ_d associates with the thermal stability of the long-range coherence of polarization directions in neighboring domains, i.e., on the domain configuration. Crystals with a rhombohedral/tetragonal phase mixture, exhibited orientation and domain configuration dependent τ_d and τ_{F-R} values, with τ_d being lower, larger, or equal to τ_{F-R}. This

indicates that both, a direct transition into the ergodic relaxor state, as well as a prior detexturing of domain polarization, can induce depolarization. Moreover, it was demonstrated that also a ferroelectric to non-ergodic relaxor transition is possible upon heating, which means that the ferroelectric domains break-up into PNRs, while the polarization directions of the PNRs remain aligned in the original poling direction. Additionally, it was pointed out that the ferroelectric rhombohedral and tetragonal phases do not necessarily exhibit equal τ_{F-R} values ($\tau_{F-R}^{tetr.} \neq \tau_{F-R}^{rhom.}$) [112, 118, 119].

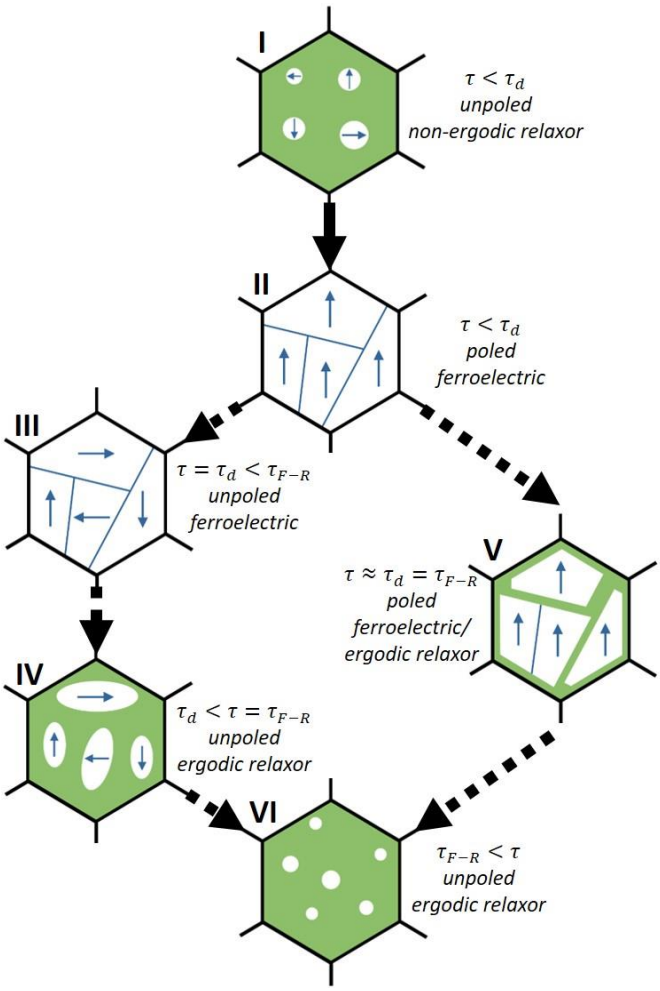

Figure 2.10. Illustration of the main stages in the depolarization process of (0.94)$Na_{1/2}Bi_{1/2}TiO_2$-0.06$BaTiO_3$, emphasizing two possible routes. White areas represent the polar (rhombohedral/tetragonal) ferroelectric phase, green areas the non-polar (pseudocubic) relaxor phase, and blue arrows the polarization direction and magnitude.

2.4. Ferroelectric material systems

A review of the material systems investigated in the study and especially their high-power properties is provided in the following. Highlighted the are lead-containing $Pb(Zr,Ti)O_3$-based ferroelectrics and the lead-free $Na_{1/2}Bi_{1/2}TiO_2$-$BaTiO_3$-based relaxor-ferroelectrics.

2.4.1. Lead-based ferroelectrics - $Pb(Zr,Ti)O_3$

$Pb(Zr_XTi_{1-x})O_3$ (PZT) is a solid solution of $PbZrO_3$ and $PbTiO_3$, forming one of the most investigated ferroelectric systems with perovskite structure [120]. The phase diagram is displayed in (**Figure 2.11**). The solid solution features an almost temperature-independent morphotropic phase boundary (MPB), separating the rhombohedral and tetragonal crystal

structures [43]. PZT-based compositions reveal strong electromechanical coupling, especially in the MPB-area (0.4 ≤ x ≤ 0.6) due to the vicinity to the structural phase transition [121, 122]. The superior electromechanical coupling in combination with a large depolarization temperature and ferroelectric-to-paraelectric transition temperature, i.e., Curie temperature (τ_c), supplanted most other ferroelectrics from piezoelectric devices. The major tools to tune the properties are acceptor- and donor-doping, which revealed an extensive variability of the material, covering an immense range of hard and soft ferroelectric properties [123]. Drawback is the toxicity of lead that triggered legislative directives to cast PZT out of broad application [124].

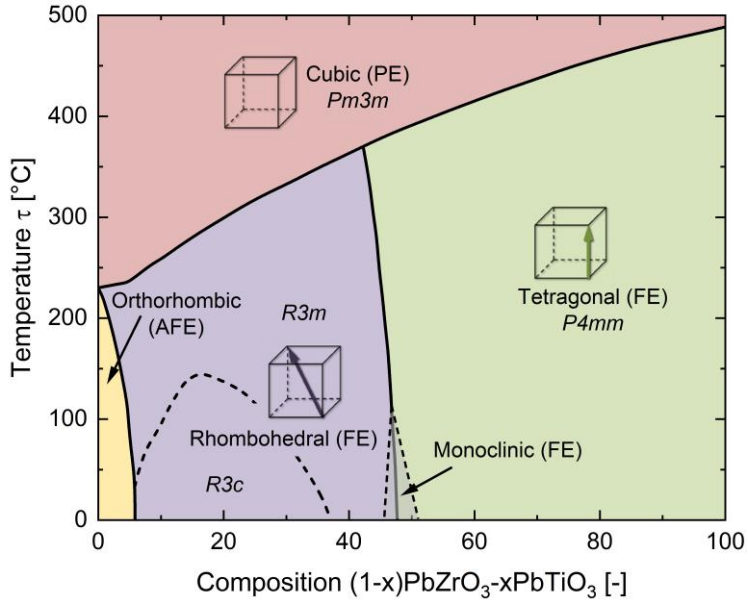

Figure 2.11. Phase diagram of the $Pb(Zr_xTi_{1-x})O_3$ solid solution highlighting the temperature (τ) and composition ranges (Zr-Ti ratio) of paraelectric (PE), ferroelectric (FE), and antiferroelectric (AFE) phases, the corresponding crystal structures, and point groups (modified after [43]). The rhombohedral phase is divided into high-temperature (R3m) and low-temperature (R3c) ranges denoted by the dashed line. A monoclinic phase evolves around the rhombohedral-tetragonal MPB [125].

2.4.2. High-power properties of $Pb(Zr,Ti)O_3$-based ferroelectrics

High-power properties are an established term in literature to denote the electromechanical coefficients under piezoelectric resonance as a function of induced vibration velocity (**Equation (2.48)**). A sharp boundary above which the resonance displacement is depicted as high-power vibration is not established. Therefore, following differentiation will be utilized to avoid ambiguity: Small-field vibration indicates the lowest experimentally achievable vibration velocity ($v \to 0$), which was in all cases well below 0.1 m/s. Low vibration velocity determines the range below 1 m/s; large vibration velocity is the range above 1 m/s. The 1 m/s border corresponds approximately to the practical power density limit of current piezoelectric resonator materials (Section 2.2.4). Note that the driving electric fields to induce the corresponding vibration velocity are always substantially below the coercive fields of the compositions ($\leq 0.5E_c$).

The two most decisive coefficients to generate large vibrations are the piezoelectric coefficient (d_{ij}) and the quality factor (Q_{ij}), determining the strain coupling to the applied electric field and the resonance strain amplification (**Equation (1.1)**). Their small-field values (note the

different scales) in several PZT compositions are summarized in **Figure 2.12** in comparison to other common ferroelectric systems. The largest combination ($d_{ij} \cdot Q_{ij}$) evolves in hard PZT compositions (and $Pb(Mn,Nb)O_3$ single-crystals) which are preferably utilized under high-power conditions.

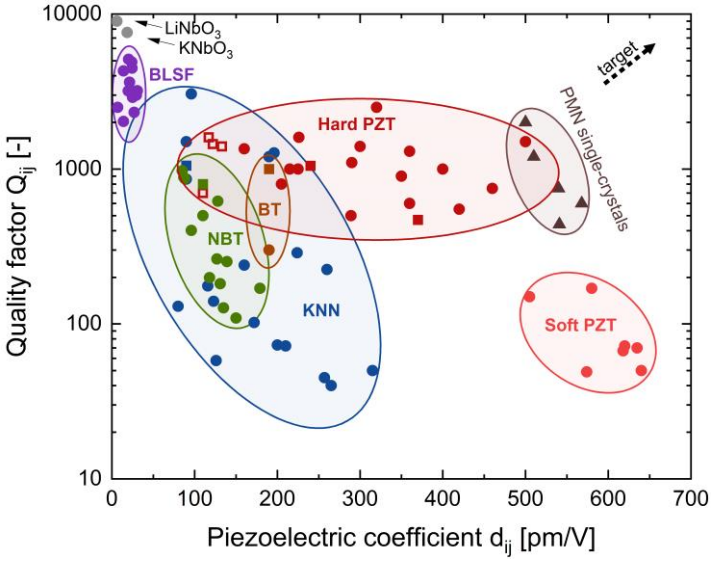

Figure 2.12. Correlation between the piezoelectric coefficient (d_{ij}) and the (resonance or not specified) quality factor (Q_{ij}) in various piezoelectrics and ferroelectrics covering the most significant material groups: lead-containing hard and soft $Pb(Zr,Ti)O_3$ ceramics (PZT) [27, 43, 102, 126-130] and $Pb(Mn,Nb)O_3$ single-crystals (PMN) [131-133], lead-free $BaTiO_3$-based (BT) [43, 134], $(K,Na)NbO_3$-based (KNN) [135-141], and $(Na_{1/2}Bi_{1/2})TiO_3$-based (NBT) [75, 127, 142-149] poly-crystalline compositions, bismuth layer structured ferroelectrics (BLSF) [150-153], and piezoelectric single-crystals $LiNbO_3$ and $KNbO_3$ [10, 128]. Circles, squares, and triangles represent quality factors in the (p), (31), and (33) vibration mode; filled and empty symbols denote the d_{33} and d_{31} coefficients, respectively.

The initialized resonance vibration velocity as a function of driving field amplitude is consequently largest in ferroelectrically hard compositions (e.g., Fe-acceptor-doped, exemplary studies are summarized in **Figure 2.13a**). However, the vibration deviates already in the low vibration velocity range from the linear correlation to the driving electric field amplitude and approaches a maximum velocity limit [41, 126, 154]. The inclination is thereby associated with a pronounced self-heating (**Figure 2.13b**) [41, 155]. The convergence of the vibration velocity towards a composition-determined limit appears qualitatively similar in rhombohedral, tetragonal, and MPB compositions, as well as in acceptor-and donor-doped compositions of PZT, although quantitatively, acceptor-doped PZTs exhibit larger velocity limits and reduced heating [41, 156].

The deviation coincides with a severe decrease of the resonance quality factor upon increasing vibration velocity (**Figure 2.13c**). Resonance impedance spectroscopy [32, 41] and pulse drive measurements (details in Section 3.1) [14, 27] evidenced the decrease utilizing different measurement approaches. The behavior is an inherent property and the detrimental drawback of PZT-based compositions under high-power conditions. In addition, further features have been reported: (1) The quality factor decrease accelerates under continuous excitation due to the coupling of vibrational and thermal effects [12], i.e., measurements under continuous vibration reveal more rapid degradation of Q_{ij} at large velocities (red circles in **Figure 2.13d**) than fast measurements without heat generation. (2) A comparative study reported different decrease rates between the transverse (31) and radial (p) modes, as well as a dependence of

the resonance quality factors on the resonator length and radius, respectively, i.e., on the resonance frequency value (**Figure 2.13f**) [157]. This finding can be considered an indication for anisotropy and frequency dependence. (3) Moreover, antiresonance quality factors are most often equal to or larger than the resonance quality factors (**Figure 2.13e**), which lead to the suggestion that antiresonance driving might be more efficient [158].

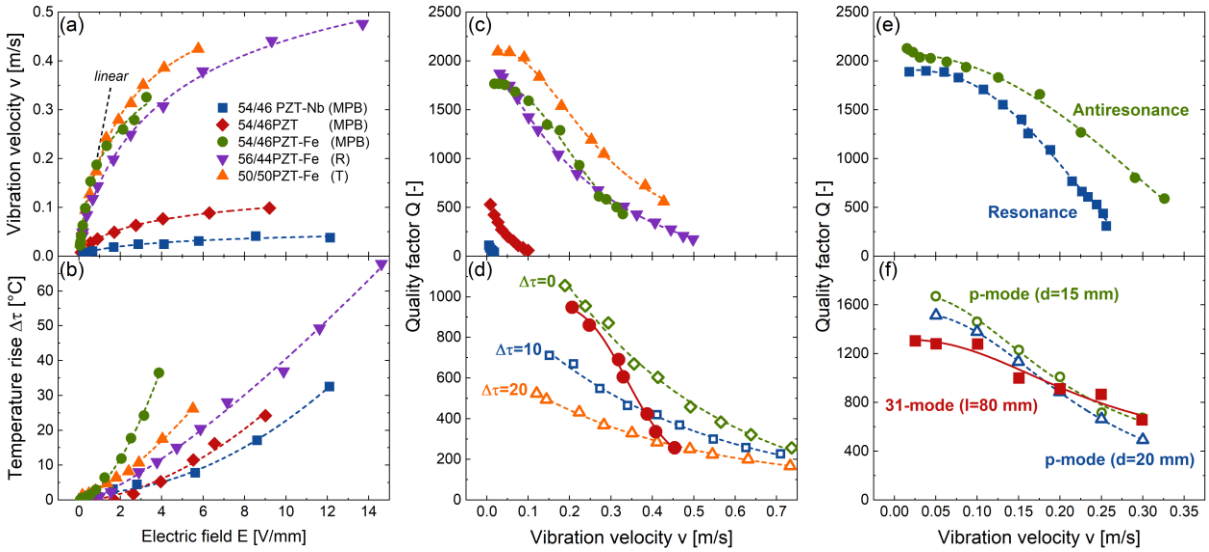

Figure 2.13. (a) Generated vibration velocity (v) as a function of driving electric field amplitude (E; small-field linear regime is denoted by black dashed line), (b) the accompanying temperature rise ($\Delta\tau$), and (c) the associated decrease of the quality factor (Q) with increasing vibration velocity in various PZTs. Figures (a)-(c) display the same representative compositions, including pure ($Pb(Zr_{0.54}Ti_{0.46})O_3$), donor-added ($Pb(Zr_{0.54}Ti_{0.46})O_3$+0.5wt.%$Nb_2O_5$), and acceptor-added ($Pb(Zr_{0.54}Ti_{0.46})O_3$+0.5wt.%$Fe_2O_3$) MPB compositions [155], as well as acceptor-added compositions on the rhombohedral ($Pb(Zr_{0.56}Ti_{0.44})O_3$+0.5wt.%$Fe_2O_3$) and tetragonal ($Pb(Zr_{0.50}Ti_{0.50})O_3$+0.5wt.%$Fe_2O_3$) site of the MPB [41]. (d) PZT quality factor as a function of vibration velocity measured under continuous excitation and the corresponding self-heating (red circles) in comparison to isothermal pulse drive measurements at different temperatures above room temperature ($\Delta\tau$) [14]. (e) Resonance versus antiresonance quality factors of the same hard PZT resonator as a function of vibration velocity [32]. (f) Quality factors in transverse (31) vibration mode compared to the radial (p) mode of resonators with the same PZT composition but different size (length (l) and disc diameters (d)) [157].

Phenomenologically, the large quality factors of hard PZT correlate with reduced dielectric, piezoelectric, and especially elastic loss (**Equations (2.45)-(2.46)**). The severe quality factor decrease is consequently associated with increasing elastic loss [106, 159]. Mechanistically it is rationalized that the small-field quality factor values in hard PZT correlate with the reduced mobility of domain walls due to acceptor-based stabilization of the domain configuration [160]. In turn, the decrease of the values upon increasing vibration velocity associates with increasing domain wall motion, induced by the increasing excitation electric field and weakened domain stabilization. Furthermore, the decrease of the quality factors, i.e., the loss increase, is correlated explicitly with emerging irreversible domain wall motion [128]. The relation is supported by the simultaneous increase of the piezoelectric, mechanical, and dielectric coefficients [27, 161]. However, direct experimental evidence of domain wall motion or a detailed consideration on the impact of other ferroelectric loss sources has not been reported yet. Also, a mechanistic explanation for the temperature, frequency, and anisotropy dependence is still missing. Clear is that state-of-the-art PZT compositions are inherently limited to the low vibration velocity range due to severe decrease of the quality factors, which diminishes the resonance amplification and terminates in detrimental self-heating. The limitation appears in hard and soft PZT regardless of the initial small-field values.

The piezoelectric, mechanical, and dielectric coefficients increase upon increasing vibration velocity, but exhibit a significantly minor dependence. It was suggested to express the elastic compliance (or Young's modulus) and the dielectric permittivity in the transverse (31) mode and low vibration velocity range by the empirical formulation (modified after [161])

$$\frac{\Delta X}{X_0} = \vartheta v^{\Gamma}, \tag{2.56}$$

where X_0 represents the small-field coefficients, ΔX the value change, v the vibration velocity, ϑ the non-linear proportionality constant, and Γ a non-linear power constant. Γ was found to be in the range of 2 [161, 162], independent of the PZT composition, and was therefore attributed to the average stored elastic energy density (**Equation (2.51)**). This means that the induced changes of the coefficients correlate with stored elastic energy (velocity square) rather than the generated vibration velocity alone. On the other hand, ϑ indicates the coefficient's stability upon increasing vibration velocity. The ϑ values possess a composition dependent variation, i.e., ϑ increases with increasing donor-doping (softening) and reduces with increasing acceptor-doping concentration (hardening), respectively [161]. It could be argued that the empirical expression is actually equivalent to the non-linear Rayleigh **Equations (2.53)-(2.55)**) with neglected linear term ($\alpha_1 E$), i.e., it represents the low field (or vibration velocity) range around the threshold transition (Section 2.3.3). The increases of the piezoelectric, mechanical, and dielectric coefficients contrast but usually do not compensate the quality factor decrease.

Further shortcuts of PZT-based compositions are an inferior heat conduction and fracture toughness, which is about two-fold lower as compared, for example, to $Na_{1/2}Bi_{1/2}TiO_2$-$BaTiO_3$ compositions. Self-heating appears inhomogeneously throughout the resonator body, but concentrates at the nodal points of the corresponding vibration mode [106]. The low heat conduction [163] leads eventually to a local overheating and terminates in thermal depolarization. Moreover, the resonators are exposed to mechanical fracture at the nodal points due to strain and stress concentration. PZT resonators are prone to fracture at low vibration velocity and are sensitive to fabrication flaws due to poor fracture toughness [164].

2.4.3. $Na_{1/2}Bi_{1/2}TiO_3$-$BaTiO_3$

The environmental and health concerns related to the toxicity of lead and governmental regulations [124] intensified the development of lead-free alternatives, including ferroelectric systems based on $Na_{1/2}Bi_{1/2}TiO_2$. One of the most promising candidates of this group is the relaxor-ferroelectric solid solution (1-x)$Na_{1/2}Bi_{1/2}TiO_3$-x$BaTiO_3$ (NBT-BT). Above the ferroelectric-to-relaxor transition temperature, the material is in an ergodic relaxor state, while below it converts into a non-ergodic relaxor with an average pseudocubic crystal symmetry. In the latter state, it transforms irreversibly into a long-range polarized ferroelectric upon application of high electric fields (poling), with a rhombohedral phase (<6 mol% $BaTiO_3$), tetragonal phase (>7 mol% $BaTiO_3$), or a phase mixture thereof in the MPB region (~6-7 mol% $BaTiO_3$) [165, 166]. The electric field-dependent phase diagram is displayed in **Figure 2.14**.

The solid solution and especially the MPB compositions are associated with a reasonably large small-field electromechanical response, including piezoelectric and coupling coefficients up to d_{33}=170 pm/V and k_{33}=0.55 [165, 167, 168]. However, the overall low electromechanical quality factors of about Q_p=150 [75], depolarization temperatures below τ_d=100 °C [72, 165,

169], and the complicated depolarization mechanisms (Section 2.3.5), are among the major deficits and concerns for the operation of the compositions under high-power conditions.

Different strategies were implemented to increase Q_{ij} and τ_d, including chemical modification by doping [113, 114, 149] and off-stoichiometry [170], grain size engineering [171], quenching [113, 172], and the formation of composites [72, 75, 83] (Section 2.3.2). The most significant enhancements of both were obtained by Zn^{2+} doping [113, 114] and composite formation with ZnO secondary phase [72, 75]. The Zn^{2+} doping follows the acceptor-doping model previously explained for PZT (**Figure 2.7a**), i.e., Zn^{2+} substitution on the perovskite B-site and the attendant formation of oxygen vacancies create point defects/complexes that hinder domain wall motion and promote a tetragonal distortion, while the large polarizability of Zn^{2+} stabilizes the ferroelectric long-range order, increases the thermal stability, and shifts the MPB [113, 114, 144]. The second-phase hardening mechanism (**Figure 2.7b**) is less well understood [75]. The observed ferroelectric hardening is most likely related to strain incompatibility and mechanical mismatch stresses induced between the ferroelectrically-switching NBT-BT and the non-ferroelectric ZnO phases, although at least an additional doping contribution cannot be excluded [84] (details in Section 2.3.2).

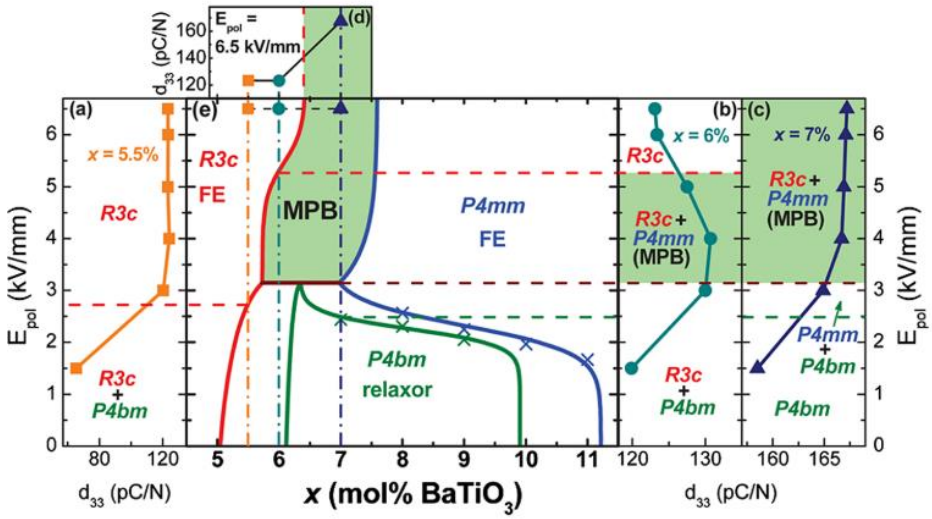

Figure 2.14. Phase diagram of (1-x)$Na_{1/2}Bi_{1/2}TiO_3$-x$BaTiO_3$ depending on the applied electric poling-field (E_{pol}), distinguishing the relaxor state, ferroelectric state (FE) with rhombohedral and tetragonal crystal structures, and the MPB region (green shaded). (a-d) indicate the piezoelectric coefficients (d_{33}) of selected compositions as a function of the poling-field. (With permission of APS Publishing, originally reported in [167].)

2.4.4. High-power properties of $Na_{1/2}Bi_{1/2}TiO_3$-based ferroelectrics

The high-power properties of NBT-based compositions are poorly investigated. However, ternary solid-solutions with $Li_{1/2}Bi_{1/2}TiO_3$ (LBT) and $K_{1/2}Bi_{1/2}TiO_3$ (KBT) with additional acceptor-doping (Mn^{2+}) received attention after demonstrating excellent stability of the resonance quality factors in a broad vibration velocity range [142, 173]. Compositions with almost no change of the quality factor values up to 1 m/s were reported. Despite the inferior piezoelectric coefficients and a constrained variability of the small-field quality factor values (**Figure 2.12**), comparative studies identified crossing points to state-of-the-art PZTs, i.e., the initially significantly larger PZT quality factors drop below the NBT values already in the low vibration velocity range (**Figure 2.15a**). Moreover, the stability is associated with rigid linearity between increasing electric field amplitude and generated vibration velocity [173]. Also in this

case, crossing points were observed, indicating a vibration velocity boundary above which NBT-based compositions outperform representative PZTs, reaching significantly larger velocities with simultaneously reduced heat generation at same driving fields. The superior thermal conduction [163] to dissipate the heat and significantly larger fracture toughness [174] to withstand the dynamic stresses additionally contribute to the intriguing high-power properties. Note that the quality factor stability is not an inherent property of lead-free perovskite ferroelectrics, e.g., acceptor doped (Cu^{2+}) $(K_{1/2}Na_{1/2})NbO_3$ exhibits comparatively large small-field quality factor values [136], but also a rapid degradation upon increasing vibration velocity [135], similar to PZT (**Figure 2.15a**). The mechanistic origin of the stability in NBT has not been explained yet.

Note that for comparing the stability of electromechanical coefficients under high-power conditions between different ferroelectric systems, it is necessary to consider further variables than only the vibration velocity, to account for the significantly different densities and Young's moduli. It has been proposed to reference the high-power properties to the maximum mechanical stress in the nodal points (T^m) [14] or the stored elastic energy density instead (Υ^m, **Equation (2.51)**) [175]. The consideration of the energy density provides a more realistic comparison of the material properties, especially with the prospection on the effective output power of the resonators in devices. The lower densities of lead-free compositions lead to a shift of the above-mentioned crossing points in favor of PZT; however, it does not compensate for the inferior stability of PZT's high-power properties compared to lead-free NBT-based compositions (**Figure 2.15b**).

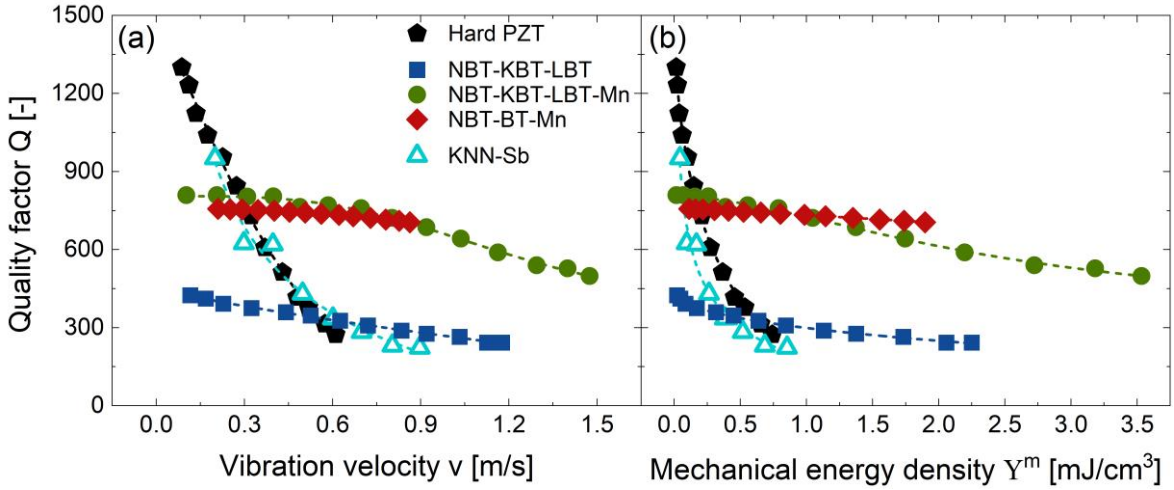

Figure 2.15: Dependence of the resonance quality factor (Q) in transverse (31) vibration mode on the (a) vibration velocity (v) and (b) the mechanical energy density (Υ^m). Depicted are several $(Na_{1/2}Bi_{1/2})TiO_3$-based solid-solutions [142, 173, 176] in comparison to acceptor-hardened $(K,Na)NbO_3$[135] and state-of-the-art hard $Pb(Zr,Ti)O_3$ [27].

3. Experimental methodology and investigated materials

An essential part of this work is the development of experimental methodologies to characterize the electromechanical properties of ferroelectrics under piezoelectric resonance and high-power conditions. This section provides an explanation of the experimental needs, a detailed description of the constructed setups, and guidance through the implemented measurement procedures. It includes (1) the resonance impedance spectroscopy and pulse drive method with burst excitation (Section 3.1.2), which are capable of determining the electromechanical coefficients as a function of vibration velocity under resonance drive; (2) the combined pulse drive method with in-situ time-resolved synchrotron diffraction (Section 3.2), to track the microstructural evolution under resonance drive; and (3) the resonance impedance spectroscopy under large DC bias electric fields (Section 3.3), which enables to deconvolute mechanistic processes in the materials using an external perturbation. Subsequently, the supportive (off-resonance) electric and structural analysis methods are introduced, detailing the applied experimental conditions (Sections 3.4 and 3.5). Finally, the investigated ferroelectric compositions are summarized (Section 3.6).

3.1. Electromechanical characterization under resonance

Ferroelectrics reveal a significant change of their electromechanical properties at large vibration velocities (Section 2.4). Determination of the electromechanical coefficients at low velocities (e.g., small-field resonance impedance spectroscopy) and their extrapolation to high velocities, which is common practice, is thus not suitable and leads to significant deviations from reality. Therefore, it is crucial that the coefficients are determined as a function of vibration velocity, which is non-trivial and to date no commercial setup exists for this purpose.

The methods can be divided into two groups [12, 177, 178] and labeled as *large-field resonance impedance spectroscopy* [179-181] and *pulse drive methods* [12, 29, 182]. Resonance impedance spectroscopy denotes an impedance sweep around the resonance (f_R) and antiresonance (f_{AR}) frequencies with a constant AC voltage excitation amplitude (**Equations (2.28)-(2.30)**). This is the most-applied technique for small-field characterization (Section 3.1.1), typically integrated in commercial impedance analyzers and described by the Piezoelectric Standardization [28, 183]. However, the appearance of a hysteretic peak distortion with increasing voltage amplitudes prohibits a direct calculation of the electromechanical coefficients [21, 177]. Moreover, the considerable energy input induces resonator heating, convoluting vibrational and thermal effects (**Figure 2.13d**). Both arise from the non-linearity of the electromechanical coefficients [24]. Models assuming equivalent circuits with non-linear elements can be used to fit the distorted impedance spectra and to calculate the coefficients, but accurate and reliable results are difficult to achieve [25, 178]. Also variations of resonance impedance spectroscopy under constant current [180], vibration velocity [37], or input power driving conditions [37] reveal certain drawbacks, which have been summarized in the supplemental material (Section 7.2).

Pulse drive methods investigate the characteristic transient response of the resonator during or after a single-frequency excitation to a high vibration level by a short voltage pulse (instead of measuring the response during a continuous drive at high velocities) [12, 29, 184]. In contrast to off-resonance, the current and displacement responses are not steady, but accelerate until reaching a steady vibration (**Figure 3.4**). Vice versa, after excitation ends, the responses do not

drop to zero immediately, but decay exponentially as a function of time. Both processes are continuous if the excitation frequency is equal to the resonance or antiresonance frequency, otherwise beating and jumping effects arise [185]. The decay frequency corresponds always exactly to the resonator's first-order resonance [29] or antiresonance frequency [182] (depending on the boundary condition), independent of the excitation frequency. The transient responses carry all information on the resonator's electromechanical properties as a function of vibration velocity and can be extracted. Most noticeable advantages of the pulse drive methods are the short duration and the decoupling of the temperature and vibration effect (heat conduction is a comparably slower process). However, reaching high measurement accuracy is challenging, and commercial setups do not exist to date. Besides providing important information for device design, these measurements are also crucial for studying basic physical mechanisms that govern the high-power behavior of piezoelectrics.

3.1.1. Small-field resonance impedance spectroscopy

Impedance sweeps in the frequency range of electromechanical resonance and antiresonance were performed using a high-precision impedance analyzer (Alpha-Analyzer, Novocotrol Technologies GmbH, Germany). The measurement was conducted in three steps. An initial rough frequency scan with step size between 50-200 Hz was carried out to determine the peak position. Subsequent fine scans with step sizes between 1-10 Hz were used to determine the resonance and antiresonance frequencies. Small measurement fields of 10 mV/mm were applied to generate minimum vibration (quasi-static condition $v \to 0$). Resonance and antiresonance quality factors (Q_{ij}^{R} and Q_{ij}^{AR}) were derived from the peak width utilizing the 3dB calculation method (**Figure 3.1**) [28, 179]

$$Q_{ij}^{R} = \frac{f_R}{\Delta f_R} \text{ and } Q_{ij}^{AR} = \frac{f_{AR}}{\Delta f_{AR}}. \tag{3.1}$$

Piezoelectric coefficients (d_{33} and d_{31}), coupling coefficients (k_{33}, k_{31}, and k_p), and elastic compliances (s_{11}^{E} and s_{33}^{E}) were determined according to the equations summarized in **Table 2.1** utilizing the resonance and antiresonance frequency values.

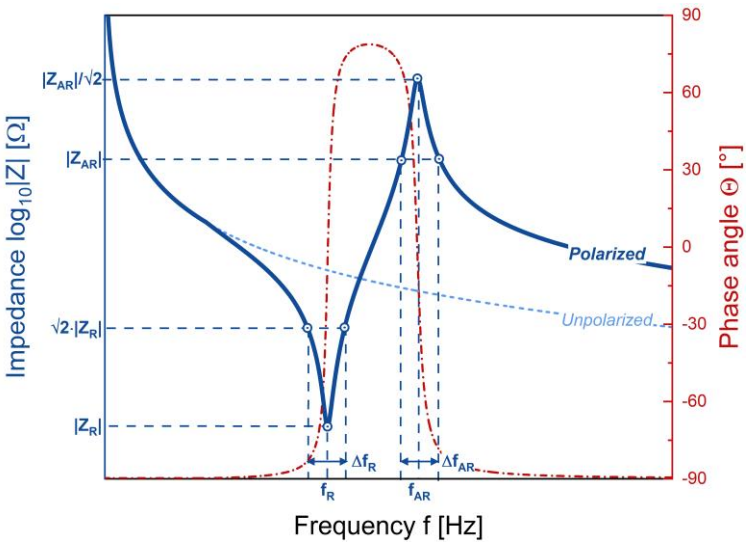

Figure 3.1. Schematic of a resonance impedance spectrum (impedance $|Z|$ as a function of frequency f) of a polarized (and unpolarized for comparison) piezoelectric resonator with the corresponding phase angle (Θ). Resonance (f_R) and antiresonance (f_{AR}) frequencies denote the peak positions; peak widths (Δf_R and Δf_{AR}) are determined at the $\sqrt{2}$-attenuation of the corresponding peak impedances ($|Z_R|$ and $|Z_{AR}|$; 3dB calculation method).

The measurements were conducted under quasi-free mechanical conditions to avoid clamping effects using a customized resonator holder mounted in a temperature chamber (T-40/25, CTS GmbH, Germany; **Figure 3.3**; details in section 3.1.2). Temperature-dependent measurements were carried out in the range of -40 – 200 °C. The resonator was heated and cooled at a 2 K/min rate and stabilized at the desired temperature for 30 min before initializing the impedance sweep. The measurement sequence was automized by implementation in LabVIEW (National Instruments, USA). The sequence included the setting and stabilization of the temperature, initialization of the rough scan in the preset frequency range, and performance of the fine scans according to the determined peak positions.

3.1.2. Pulse drive measurement with burst excitation

Experimental setup (hardware)

The experimental setup was designed based on a previous report [29]; a block schematic is presented in **Figure 3.2a**. The driving AC voltage signal (V_{ex}) was generated by a function generator (Agilent 33220A, Agilent Technologies Inc., USA), with an amplitude and frequency accuracy of ±1 % + 1 mV_{pp} and ±20 ppm. The voltage was amplified (gain 20x) in a high-frequency voltage amplifier (HAS-4052, NF Corp., Japan) with a small output impedance of 0.5 Ω and applied to the resonator placed in a customized holder. Voltage drop on the resonator (V_{SAC}) and generated current (I_{SAC}) were measured by a customized passive voltage probe and an inductive current probe (CT2, Tektronix Inc., USA). Both signals were recorded by a high-speed oscilloscope (60 Msamp/s sampling frequency; PCI-5105, National Instruments, USA). Voltage and current signals were accurate to ±0.1-2 % and ±3 %, respectively. The voltage probe was tailored to the 1 MΩ input resistance and 200 pF input capacitance of the oscilloscope, establishing a 10:1 measurement ratio to prevent overload. An electromechanical relay was implemented in series with the resonator to apply open-circuit conditions. The vibrational displacement was monitored by a laser vibrometer (OFV-5000 or OFV-505, Polytec GmbH, Germany) based on the heterodyne interferometer principle and the Doppler effect. Vibrometer settings were controlled by the VibSoft 5.4 software (Polytec GmbH, Germany); the measurement signal was recorded with the high-speed oscilloscope after a digital-to-analog conversion. The laser beam was aligned perpendicular to the center of the resonator face in the displacement direction of the corresponding vibration mode (**Figure 3.2b**). Resonator temperature was tracked by an IR thermal camera (IR8300, InfraTec GmbH, Germany) with a framerate of 80 frames/s, controlled by the IRBIS 3 software (InfraTec GmbH, Germany). A detection area of 3x3 mm in the center of the non-electroded side-face was recorded. Heat generation due to self-heating effect is pronounced at the nodal points of the vibration, which is in the resonator center in case of first-order harmonic vibration (**Figure 2.4a**) [14]. Vibrometer and thermal camera were accurately positioned perpendicular to the resonator faces and focused on the surface, reaching accuracies of ±1 nm and ±0.1 K. The measurement depends notably on the focus quality and surface finish, i.e., surface roughness diminishes displacement and temperature accuracy due to diffuse laser reflection, reduced reflection intensity, and altered surface emissivity. Please note that the vibrometer model OFV-505 was limited to a maximal capable vibration velocity of 0.8 m/s. The vibrometer model OFV-5000 provided a measurement range up to 10 m/s, however, the accessibility was limited throughout the study.

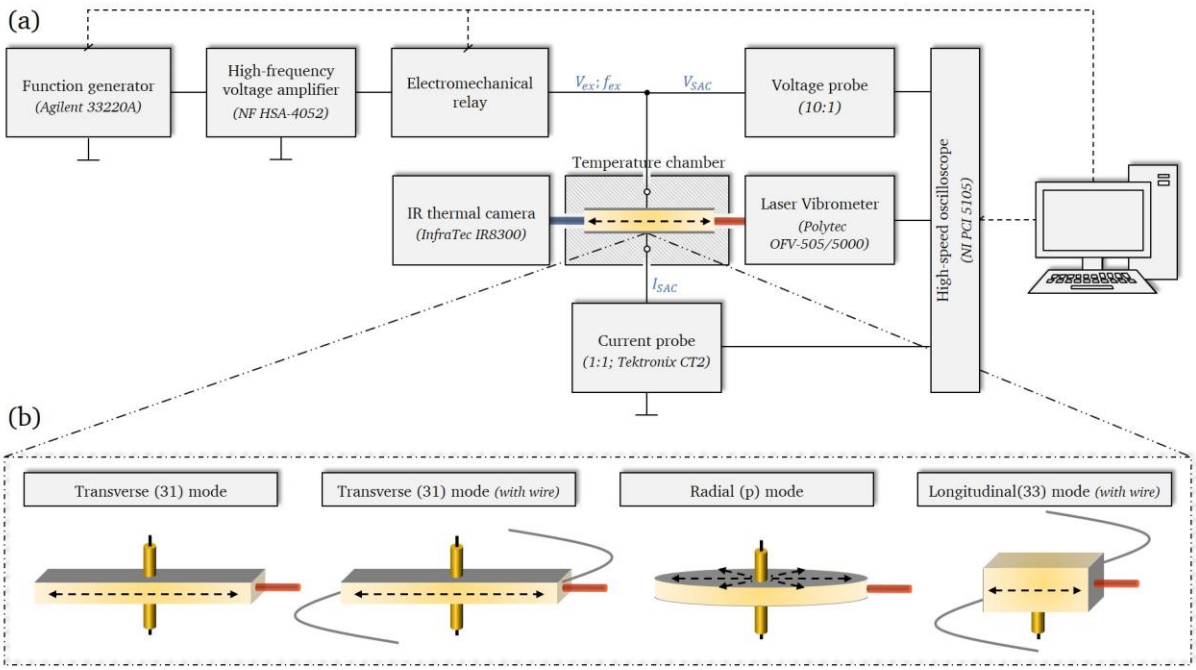

Figure 3.2: (a) Block diagram of the experimental setup for high-power pulse drive measurement with burst excitation. Blocks represent utilized equipment, full and dashed lines denote the electric and communication interconnection to the control PC (LabVIEW), and blue labels mark the measured signals. (b) Schematics of the three vibration mode resonators connected to the circuit through pin electrodes or wires and aligned to the vibrometer laser parallel to the vibration direction (wires are disconnected in transverse (31) mode; Section 4.6).

The measurements were conducted under quasi-free vibration, i.e., minimal mechanical restrictions are applied to the resonator, in order to avoid clamping effects that significantly influence the electromechanical coefficients [186]. To this end, the resonator was placed in a designed holder (**Figure 3.3**) between two spring-loaded gold-plated electrodes (1015/G, PTR Messtechnik GmbH, Germany) with 0.4 N spring preload and a 0.64 mm diameter flat contact area, both connected to the electric circuit. The upper pin-electrode moves vertically by a µm-screw to establish electric contact at minimum contact force. An additional positioning system was installed to align the resonator center accurately with the pin-electrodes and the surfaces perpendicular to the laser vibrometer and the thermal camera. Note that the geometric center coincides with the mass center and the nodal point of the first-order vibration in a homogeneous resonator. The resonator displacement is zero at the nodal point (**Figure 2.4a**); hence, clamping and friction forces should not impact the vibration. Nevertheless, at least two samples per composition were measured to ensure reproducibility. Each sample was measured three times and reloaded before each measurement to exclude the influence of positioning and clamping. The presented results are thus averaged over at least six measurements. Uncertainties of the measured values were taken into account by the standard deviation using the Gaussian uncertainty propagation theory. For reference at the low-velocity end, the above-introduced small-field resonance impedance spectroscopy was carried out in the same configuration prior to every pulse drive measurement.

The longitudinal length (33) vibration mode is distinguished from the transverse and radial modes by the polarization, applied electric field, and generated strain being parallel. To align with the laser vibrometer, the resonator was rotated by 90° and required an electric connection via Ag-wires (50 μm diameter) attached to the edges of the electroded faces with a conductive Ag-glue (G3692 Acheson Silver DAG 1415, Plano GmbH, Germany). The pin-electrodes were

disconnected and used only to hold the resonator in position (**Figure 3.2b**). Reference (31) mode measurements with wires attached to the non-electroded faces without electrical connection (**Figure 3.2b**; details in Section 4.6) were conducted to consider the wire influence on the vibration.

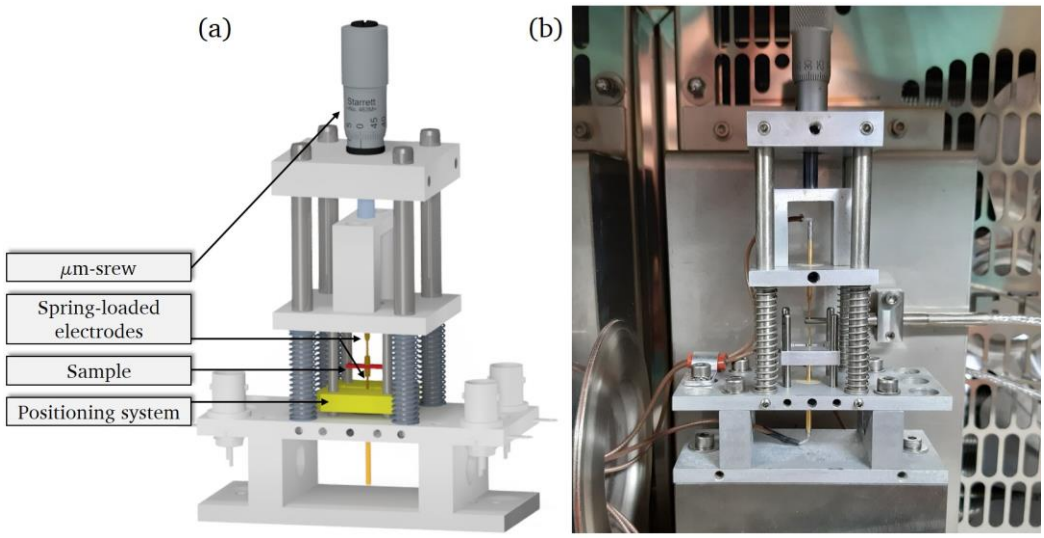

Figure 3.3: CAD model and image of the sample holder utilized for piezoelectric resonance measurements under quasi-free vibration.

The resonator holder was mounted inside a temperature chamber (T-40/25, CTS GmbH, Germany) with a range of -40 – 200 °C and temperature stability of 0.1 °C. Electric connection via shielded coaxial cables was fed through the chamber case. The laser vibrometer was positioned outside the chamber on an xyz precision stage, enabling the adjustment of the laser spot and the 484 mm optimum focus distance to the surface to account, for example, for different resonator heights and lengths. Holder and laser vibrometer were mechanically decoupled from the temperature chamber by a damping system, avoiding the transfer of vibration noise.

Measurement procedure

The setup was operated using a customized procedure implemented in LabVIEW, including the control of the frequency generator and oscilloscope setting, triggering of the function generator, laser vibrometer, relay, and thermal camera, as well as the processing of data. The high-power measurement was performed by a *combined three-stage method* (**Figure 3.4**), merging the benefits of constant voltage impedance spectroscopy and transient response measurement.

Stage I identified the large-field resonance frequency region, the time needed to reach a steady-state (denoted by number of cycles N_1), and the time needed to reach a complete decay of the transient response (denoted by number of cycles N_2). The resonator was excited by the amplified AC voltage signal (V_{ex}) for N_{1^*} number of cycles, simultaneously tracking voltage (V_{SAC}), current (I_{SAC}), and displacement (u_{SAC}). Subsequently, the resonator was short-circuited, recording the transient responses for N_{2^*} cycles (V_{ex}, N_{1^*}, and N_{2^*} are material and geometry dependent). The short-circuit condition was applied by setting the function generator to 0 V. The procedure was repeated over a frequency range in discrete frequency steps ($f_{ex}[n]$ with $n = 1, 2, \dots, n_{last}$). Amplitudes of voltage, current, and displacement in the steady-state region (green cycles in **Figure 3.4**) were determined utilizing the lock-in method and used for

the admittance calculation. The vibration velocity was calculated from the displacement amplitude and the excitation frequency (f_{ex}; **Equation (2.47)**). The maxima in the resulting admittance and vibration velocity spectra determined the resonance frequency region; the spectra overlay due to electromechanical coupling if vibration loss is not extensive [10]. Note that the large-field admittance/impedance or vibration velocity spectrum cannot be used directly for the coefficient calculations due to the above-described peak distortion [21] (details in Section 7.2). Sample temperature was monitored during the entire procedure to avoid heat generation.

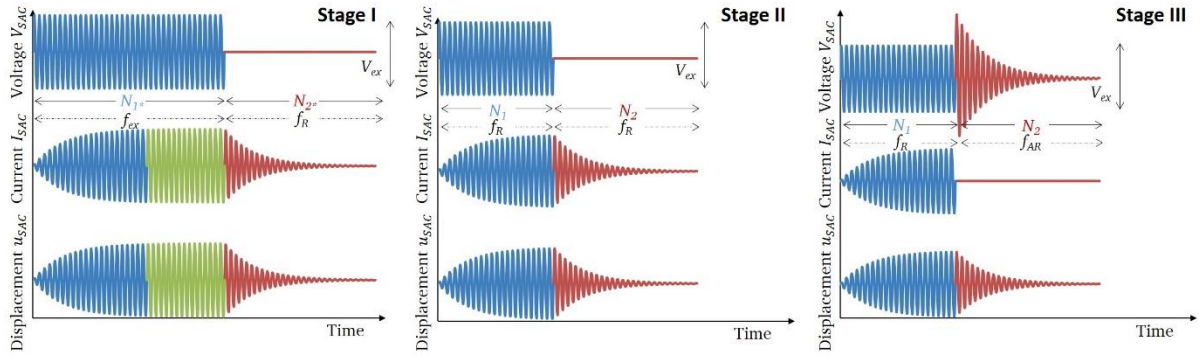

Figure 3.4: Three stages of the high-power pulse drive measurement: (I) Burst excitation (V_{ex}) at different frequencies (f_{ex}; frequency sweep) to determine the resonance region and the number of cycles (N_1) required to reach steady-state (in green) and complete decay (N_2). Burst measurement in (II) resonance and (III) antiresonance. The resonator is excited at the determined frequency of maximum vibration velocity and decays exactly at its resonance (f_R) or antiresonance (f_{AR}) frequency after short- or open-circuiting, respectively. Measurement parameters depend on the measured vibration mode, typical value ranges are N_1=500-2000 cycles, N_2=1000-3000 cycles, f_R=f_{AR}=50-450 kHz, and V_{ex}/h=3-150 V/mm (h is the resonator height in field direction). The entire measurement time per burst is <100 ms, prohibiting considerable heat generation.

In *Stage II*, the pulse drive measurement was performed in resonance [29]. Using burst excitation, the resonator was driven at the frequency of maximum vibration velocity determined in Stage I with the voltage V_{ex} for N_1 cycles. Subsequently, the resonator was short-circuited, recording the transient responses of current and displacement for N_2 cycles. In *Stage III*, the pulse drive measurement was performed in antiresonance [182]. The excited resonator was open-circuited by triggering the electromechanical relay, recording the transient responses of voltage and displacement. Note that the vibration frequency immediately changes to the fundamental resonance or antiresonance frequency after applying the short- or open-circuit conditions, respectively, independent of f_{ex} [182, 185]. However, important benefits of the excitation at the vibration maximum are the reduced V_{ex} to reach high vibration velocities, which would otherwise not be accessible due to limited amplifier output voltage, and the reduction of beating and jumping effects [185].

The maximum/minimum values of the cycles during the transient response describe decaying envelope functions (**Figure 3.5**). The decay was divided into sections determined by a 5 % displacement attenuation. The frequency in each section, which is exactly the above-mentioned first-order vibration velocity-dependent resonance or antiresonance frequency [10, 11], was determined from the maxima/minima periodicity. The envelope functions of every section were fitted by the exponential expression (X=V_{SAC}, I_{SAC}, or u_{SAC})

$$X = X_0 \cdot exp(-\frac{e}{f_{R/AR}}), \tag{3.2}$$

deriving the decay coefficient e. Assuming that the material properties are constant within every section due to the small change, the determined average voltage, current, displacement amplitudes, and frequencies were used to calculate the vibration velocity (**Equation (2.47)**), the quality factors Q_{ij}^{R} and Q_{ij}^{AR}

$$Q_{ij} = 2\pi f_{R/AR}/e \ , \tag{3.3}$$

as well as the force factors A_{ij} and B_{ij} (**Equations (2.31)-(2.32)**) [11, 27, 29, 182]. The piezoelectric, mechanical, and dielectric coefficients were calculated using the equations derived for individual vibration modes in Section 2.2.2 and summarized in **Table 2.1**.

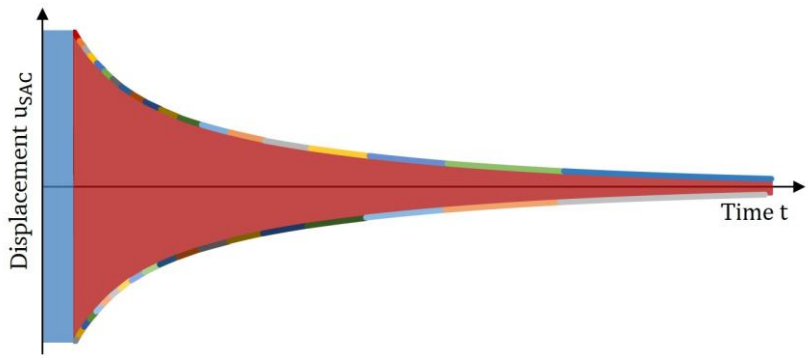

Figure 3.5: Examples of exponential functions (**Equation (3.2)**) fitted to the sectioned transient displacement.

3.1.3. Heat generation

Complementary to the pulse drive, *heat generation* measurements were carried out with the designed setup to simulate continuous drive conditions and determine the vibration-heat coupling. The resonator was excited at the resonance frequency (vibration maximum) under different voltage amplitudes, tracking the correlation between generated vibration velocity and induced temperature rise. The voltage was applied continuously for several seconds until the temperature stabilized in the entire sample volume. The excitation frequency was adjusted manually during the self-heating to keep the vibration in resonance.

3.1.4. Finite element method

Finite element method (FEM) modeling of the resonator vibrating was carried out utilizing ANSYS (ANSYS Inc., USA) and COMSOL (COMSOL Multiphysics Inc., USA) software. A 0.01 mm mesh size was implemented to determine the strain and stress distributions during resonance vibration.

3.2. Pulse drive measurement in combination with synchrotron diffraction

In recent years, x-ray diffraction methods have been extensively applied to study the dynamics of ferroelectric systems complementary to the macroscopic electrical measurements [78]. These allow direct observations of the intrinsic *hkl*-dependent lattice strain and the extrinsic domain switching strain (or other extrinsic strain mechanisms) in-situ under the applied electric field, without constraining the material´s natural boundary conditions. Strain contributions under quasi-static electric fields [187-189] or dynamic low-frequency (Hz-range) sub-coercive loading [190-193] have been deconvoluted. However, the motion of ferroelectric domain walls in kHz-range under resonance excitation has not been investigated yet.

To this end, the above-introduced pulse drive measurements were combined with time-resolved high-energy in-situ x-ray diffraction and stroboscopic data acquisition (**Figure 3.6**). The diffraction patterns were collected at the ID15 beamline [194] of the European Synchrotron Radiation Facility (ESRF) and the PETRA III P02.1 beamline of the Deutsches Elektronen-Synchrotron (DESY). The transverse length (31) vibration mode was probed with sample geometries of 24x1x1 mm³. The experiments were carried out (1) at different electric field amplitudes and the corresponding resonance frequencies to achieve targeted vibration velocities or (2) as sweeps across different frequencies using a constant electric field amplitude (Sections 4.2.1 and 0). The samples were excited consecutively by multiple burst pulses with 5000-10000 cycles per burst, short-circuited, and decayed to zero state after every pulse. The cycle number was low enough to prevent self-heating effects. The electromechanical coefficients were derived from the transient response and tracked during the entire measurement procedure to exclude sample fatigue.

X-ray beams of 0.3x0.3 mm² with energies of 75 keV (0.16534 Å wavelength; ESRF) and 60 keV (0.20673 Å wavelength; DESY) were aligned with the center of the vibrating resonator (**Figure 3.6b**). Diffraction patterns were collected in transmission geometry using an area detector (Pilatus CdTe 2M, Dectris Ltd., Switzerland). Time-resolved data collection with stroboscopic acquisition was applied [193, 195], which means that each high-frequency sinusoidal displacement cycle was divided into 16 segments (**Figure 3.6a**). The resonator excitation was synchronized with the x-ray detector, recording the diffraction intensity only during one individual segment. Assuming a resonance driving frequency in the range of 60 kHz, the recording time period was about 1 μs per cycle. The diffracted intensities of each segment were summed over multiple vibration cycles to ensure sufficient total intensities of the diffracted rings. Subsequently, the next segment was recorded by implementing a phase shift between the excitation signal and detector triggering. The process was automated by a customized LabVIEW script.

The Debye-Scherer rings of the recorded 2D diffractograms, each representing one of the 16 cycle segments, were divided into 10° cake pieces over the azimuthal angle (α; **Figure 3.6b**). $\alpha = 0°$ represents the x_3-direction with parallel scattering and electric field vectors; $\alpha = 90°$ represents the x_1-direction with parallel scattering and vibration velocity vectors. The patterns within each cake piece were radially integrated from 2° to 9° to obtain one-dimensional diffractograms with the diffracted intensities (I) as a function of the diffraction angle (2θ) [196]. Parts of these one-dimensional diffractograms covering the $\{111_{pc}\}$ singlet and the $\{002_{pc}\}/\{200_{pc}\}$ doublet and compiled for the 16 time-segments are shown as surface plots in **Figure 3.6c,d**. Depicted are exemplarily the $\alpha = 90°$ cake piece reflections of soft PZT with tetragonal crystal structure vibrating at 1.5 m/s. The pseudocubic *hkl*-reflection singlets and doublets $\{111_{pc}\}$, $\{11\bar{1}_{pc}\}$, $\{002_{pc}\}$, $\{200_{pc}\}$, $\{022_{pc}\}$, $\{220_{pc}\}$, $\{211_{pc}\}$, and $\{112_{pc}\}$ were fitted by single and double Gauss functions, respectively, to determine peak position (θ_{hkl}) and integrated peak intensity (I_{hkl}) as

$$I = I_0 + \frac{I_{hkl}}{\sqrt{\frac{\pi}{2}}p} \cdot \exp\left(-\frac{2(\theta-\theta_{hkl})^2}{p^2}\right) \text{ and} \tag{3.4}$$

$$I = I_0 + \frac{I_{hkl,1}}{\sqrt{\frac{\pi}{2}}p_1} \cdot exp\left(-\frac{2(\theta_1-\theta_{hkl,1})^2}{p_1^2}\right) + \frac{I_{hkl,2}}{\sqrt{\frac{\pi}{2}}p_2} \cdot exp\left(-\frac{2(\theta_2-\theta_{hkl,2})^2}{p_2^2}\right), \tag{3.5}$$

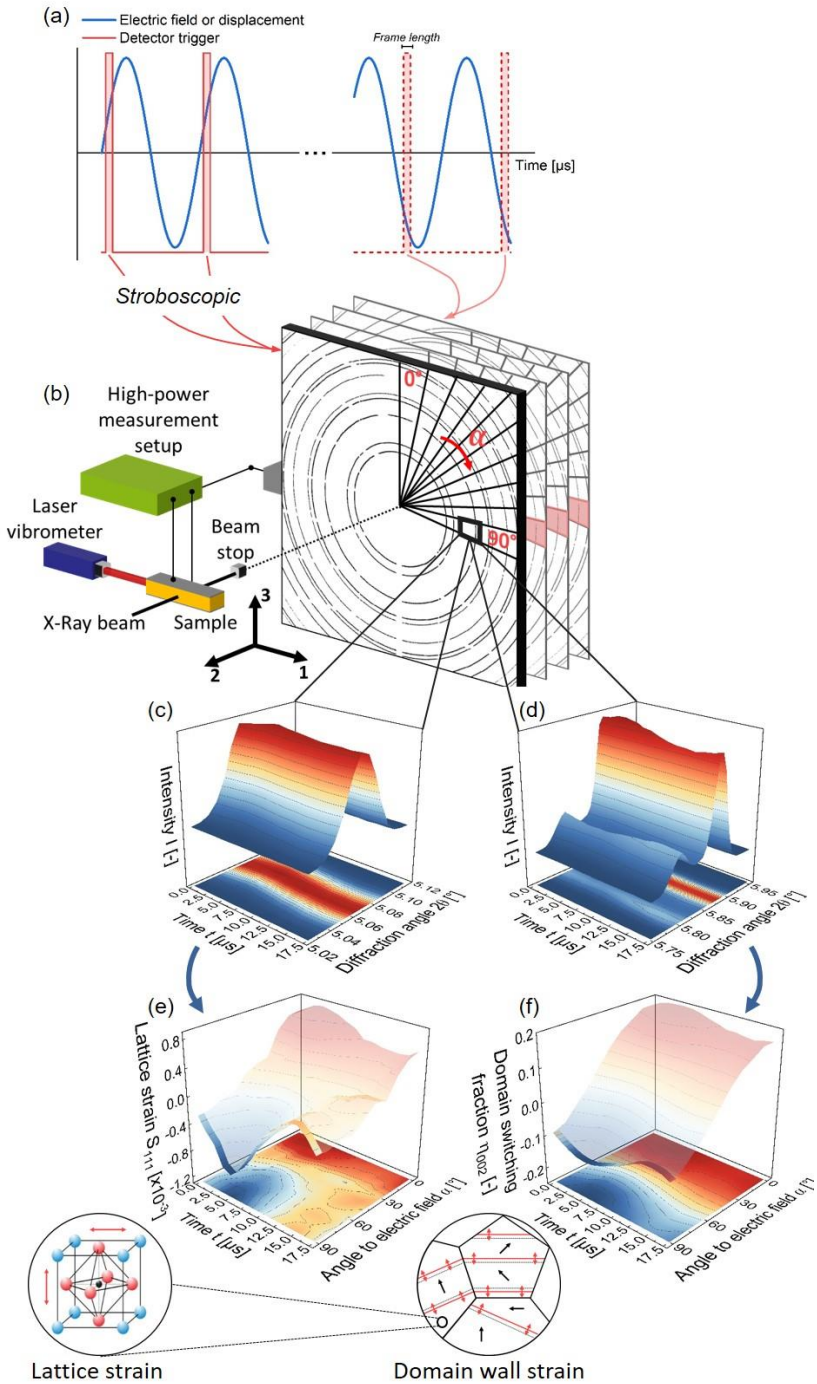

Figure 3.6. Experimental setup combining high-frequency time-resolved in-situ synchrotron diffraction with high-power piezoelectric resonance measurements. (a) Schematic of the stroboscopic data acquisition. The periodic displacement response is divided into 16 equivalent time segments; diffraction intensities are recorded only during one time-segment per cycle (frame period ~1 µs) and summed over multiple cycles. (b) Experimental configuration includes the laser vibrometer determining the edge displacement and an area detector recording the orientation-dependent 2D-diffractograms for each time-segment. The electric field is applied in the x_3-direction; the largest strain is generated in the x_1-direction due to the transverse vibration mode. (c,d) Reconstructed diffractogram section in x_1-direction perpendicular to the field (90° cake piece) exhibiting the time-evolution (t) of the $\{111\}_{pc}$ singlet and $\{002\}_{pc}/\{200\}_{pc}$ doublet reflection intensities (I), respectively, covering the 16 time-segments (complete cycle). The peak position shift of $\{111\}_{pc}$ and the intensity interchange of the $\{002\}_{pc}/\{200\}_{pc}$ reflections during the positive and negative field states evidence the lattice strain and the motion of non-180° domain walls during the resonance vibration of a soft PZT resonator at 1.5 m/s. (e,f) The reconstructed strain of the $\{111\}_{pc}$lattice plane (S_{111}) and the domain switching fraction (η_{002}) as a function of time for various azimuthal angles between 0° and 90° (angle between field and scattering vector; α), highlighted is the $\alpha = 90°$ direction determined from (c,d).

with I_0 being the base and p the peak width. The hkl lattice strain ($S_{i,hkl}$) and the domain switching fraction ($\eta_{i,002}$) were determined from the change in lattice spacing ($\Delta\theta_{hkl}$; peak position; **Equation (4.7)**) and the intensity interchange (ΔI_{hkl}; **Equations (4.8)-(4.9)**) [198]. Their time and orientation dependence is demonstrated exemplarily for the soft tetragonal PZT at 1.5 m/s in **Figure 3.6e,f**. The total lattice strain was subsequently determined from the weighted sum of the crystallographic plane strains using the Voigt approximation [199], considering the texture and multiplicity factors of individual planes (**Equation (4.10)**). The strain contribution from non-180° domain wall motion was calculated using a volume-weighted average of the lattice distortion of the domains (e.g., tetragonal c/a lattice constants ratio) over the entire orientation space (**Equation (4.11)-(4.12)**) [198, 200]. A detailed derivation of all relevant equations and a step-by-step description of the analysis procedure with the corresponding results are provided in Section 4.2.1.

3.3. Resonance impedance spectroscopy with superimposed DC bias fields

Non-linear polarization and strain response to external electric loads are among the most prominent characteristics of ferroelectric materials (Section 2.3.1). Hence, it is evident that the ferroelectric properties can be modified by superimposing a driving AC voltage signal with a static DC bias voltage. Nevertheless, the impact of DC bias fields on the electromechanical coefficients and the resonance vibration is poorly explored yet. One of the main reasons is the experimental difficulty of conducting resonance impedance spectroscopy under AC voltages combined with large DC voltages. Reported customized impedance measurement equipment [201], as well as commercial impedance analyzers, usually use the same output amplifier stage for both voltage signals (DC and AC). This means that the voltages are superimposed before amplification. The output amplifier, and thus the instruments, are either capable of sufficiently wide frequency ranges and large AC current supply but limited by low DC voltage capability, or cover a wide DC voltage range but are restricted to a narrow low-frequency range and a low AC current capability, failing to provide the required combination of both.

Moreover, the voltage signal is usually fed through a comparably large output impedance (typically ≥50 Ω, depending on the DC voltage capability). This leads to a significant reduction of the AC voltage applied to the resonator or generally "Device Under Test" (DUT) compared to the set source voltage, since the voltage is distributed proportionally between the resonator/DUT and the output impedance [202]. The voltage drop appears especially around the resonance frequency, where the resonator impedance can decrease to few Ω. In this case, the measurement cannot be performed under constant AC voltage condition throughout the entire resonance/antiresonance frequency range, as required for resonance impedance spectroscopy by the Piezoelectric Standardization (e.g., European (EN 50324) [28] or IEEE (ANSI/IEEE Std 176–1987) [183]). The issue can be illustrated already for a simple (zero DC) measurement of a hard PZT in the transverse (31) mode depicted in **Figure 3.7a**. The measurement was conducted with a state-of-the-art impedance analyzer (HVB300, Novocotrol Technologies GmbH, Germany) with 200 Ω output impedance (capable of ±150 V DC bias). It can be observed that the applied voltage drops by about two orders of magnitude around the resonance frequency. This issue is unfortunately often overlooked and can lead to significant errors in the determined material parameters even at small-field measurements. Besides, the setups are usually not equipped with simultaneous tracking of the resonator vibration, which is necessary to determine the electromechanical parameters accurately.

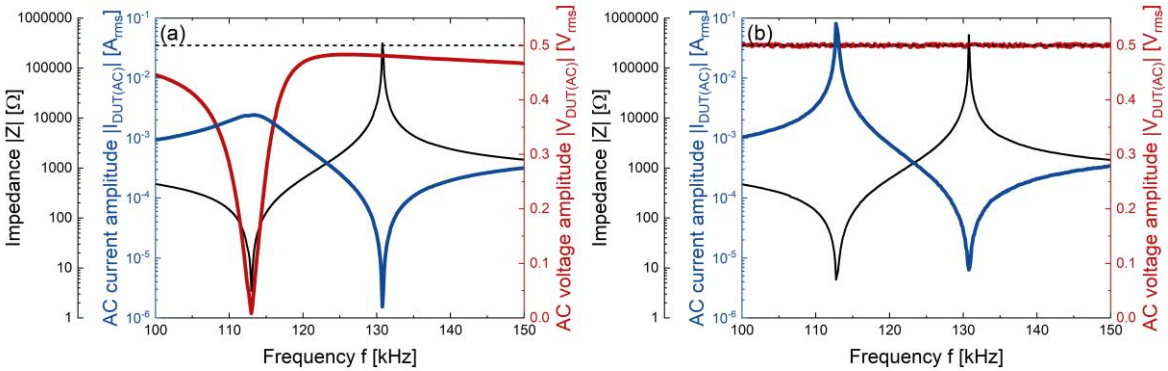

Figure 3.7. Resonance impedance sweep ($|Z|$; black curve) of a hard PZT resonator (PIC181, PI Ceramic GmbH, Germany) in transverse (31) mode measured with (a) a state-of-the-art commercial impedance analyzer (HVB300, Novocotrol Technologies GmbH, Germany) and (b) the designed setup. The voltage was set to a constant amplitude of 0.5 V_{rms} (dashed lines). Blue and red lines represent the measured current ($I_{DUT(DC+AC)}$) and true voltage applied to the resonator ($V_{DUT(AC)}$).

To overcome the shortcomings mentioned above and investigate the evolution of electromechanical coefficients in piezoelectric resonators over a wide DC bias voltage range, an experimental system was designed and realized to perform resonance impedance spectroscopy under combined AC and high-voltage DC loading. The measurement results will be discussed in Sections 4.5 and 5.3, the system characteristics are summarized in **Table 3.1**, and the setup's structure and measurement procedure are described below.

Table 3.1. Capabilities and limitations of the designed measurement system for piezoelectric resonance impedance spectroscopy under combined AC and high-voltage DC loading.

Parameter	Min	Max	Unit
Frequency range	50	500	kHz
DC bias voltage ($V_{DUT(DC)}$)	-10	10	kV
DC bias current ($I_{DUT(DC)}$)	-2	2	mA
AC source voltage (V_{SAC})	10^{-2}	10	V
AC signal current ($I_{DUT(AC)}$)	0	300	mA
Impedance measurement range	10^{-1}	10^{6}	Ω
Current measurement range	10^{-6}	$3{\cdot}10^{-1}$	A
Gas chamber pressure range	10^{-3}	2	bar
DUT vibration velocity		10	m/s

Experimental setup (hardware)[vi]

A block schematic of the measurement setup is depicted in **Figure 3.8**. The AC voltage (V_{SAC}) was generated by the second channel of the function generator. An analog buffer (high-current, wide-band amplifier with a gain of 1) was used to increase the current capability, lower the output impedance, and protect the AC source in case of dielectric breakdown of the resonator. An additional HV capacitor (DC blocking capacitor) protected the analog buffer from the generated $V_{DUT(DC)}$. The capacitor also acted as a high-pass (HP) filter for the AC voltage. The output impedance of the voltage generating site is equal to the combined impedance of the analog buffer and the blocking capacitor [202]. To keep the output impedance as low as

[vi] The hardware was designed and constructed in close collaboration with Tomaž Kos (Jožef Stefan Institute, Slovenia).

possible, a blocking capacitor with high capacitance of 120 nF was used. The low output impedance (compared to commercial impedance analyzers) enabled the impedance spectroscopy measurement under constant $V_{DUT(AC)}$ amplitude over a wide impedance range (**Figure 3.7b**). However, for the case of extremely low resonator impedance, a dedicated amplitude optimization algorithm was implemented in the control software (Block B in **Figure 3.9**) to keep $V_{DUT(AC)}$ constant by adjusting V_{SAC}.

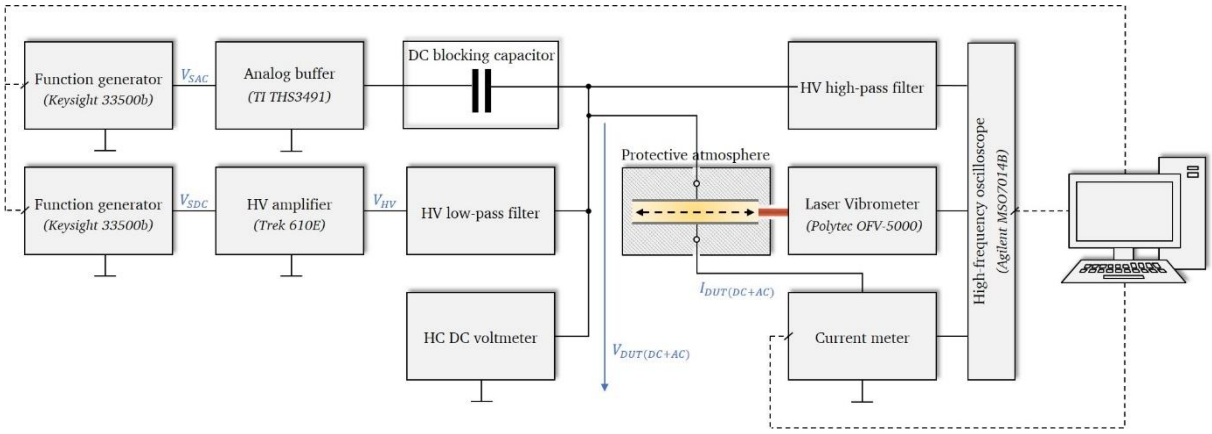

Figure 3.8. Block diagram of the experimental system for resonance impedance spectroscopy under combined AC and high-voltage DC loading. Solid lines indicate electric connection, dashed lines denote the communication interconnection to the control PC (LabVIEW), and blue labels mark the different voltage and current signals.

The system included a resonator holder (equivalent to the model introduced in **Figure 3.3**), which enabled resonator vibration without rigid boundary conditions. The resonator holder was integrated into a protective atmosphere chamber. The chamber allowed to conduct the measurements below and above atmosphere pressure (**Table 3.1**), and to use insulating gas such as SF_6 [203] (others possible) to prevent dielectric breakdown in air.

The resonator impedance is calculated as the ratio of the measured AC voltage $V_{DUT(AC)}$ and the current amplitude ($I_{DUT(AC)}$; $I_{DUT(DC)}$ is negligibly small). The $V_{DUT(AC)}$ measurement was AC coupled, i.e., an active HV HP filter removed the DC component from the applied voltage $V_{DUT(DC+AC)}$. $I_{DUT(AC)}$ was measured with a current meter in 4 selectable current ranges, covering several orders of magnitude (**Table 3.1**). The current meter incorporated 3 shunt resistors and a current probe (CT2, Tektronix Inc., USA) selectable according to the required range. In addition, a laser vibrometer (OFV-5000, Polytec GmbH, Germany) measured the generated resonator displacement. The vibration was tracked to ensure same velocities and strain states between the measurements and to adjust V_{SAC} if necessary. The signals were recorded with a high-frequency oscilloscope (MSO7014B, Agilent Technologies, USA).

In case of a dielectric breakdown of the resonator during DC voltage ramp up or down, the voltage of the DC blocking capacitor $V_{DUT(DC)}$ was applied to the output of the analog buffer, which was detrimental. Furthermore, if the breakdown occurred during the frequency sweep, high-current surges flowed into the current meter, eventually destroying parts of the current measurement circuits. Therefore, both components (analog buffer and current measurement) were equipped with overvoltage protection elements (diodes, gas arrestors, and ferrite beads) and sacrificial hardware components (simple, low-cost printed circuit boards (PCB)) that did not influence the behavior of the resonator during regular operation. Sacrificial hardware components were replaced in case of destruction.

Measurement procedure (software)[vii]

The setup was operated by an automated measurement procedure implemented in LabVIEW, including the control of system components (function generator and current measurement), data acquisition and processing, an optimization algorithm keeping $V_{DUT(AC)}$ constant, techniques to reduce the dielectric breakdown risk, and a self-calibration and self-test procedure. The flow chart of an automated resonance impedance spectroscopy measurement is depicted in **Figure 3.9**. Note that the measurement procedure invoked after $V_{DUT(DC)}$ has been automatically ramped up to the set value with a rate of 1.2 kV/min.

Block A set the frequency of the AC source (f_{AC}). Block B applied the pre-determined V_{SAC} and measures $V_{DUT(AC)}$. If the ratio of the two voltage values exceeded the upper or lower threshold, the optimization algorithm was activated. The algorithm recalculated the applied V_{SAC} in order to converge $V_{DUT(AC)}$ to the pre-determined V_{SAC} value. The process was looped until reaching a voltage ratio within the threshold limits. Due to the non-linear response of the resonator, the Newton–Raphson method [204] was utilized as the optimization algorithm. The scenario usually appeared only in the resonance vicinity in case of an extremely low resonator impedance (due to the low output impedance of the system). Subsequently, the current measurement range was selected (block C) and the data acquisition was initiated (block D). Voltage ($V_{DUT(AC)}$), current ($I_{DUT(AC)}$), and the resonator displacement ($u_{DUT(AC)}$) were recorded as a function of time. The acquisition rate was 2 GSamp/s; the acquisition time was defined by the number of excitation cycles beginning after the non-recorded transient increase of current and displacement (steady state; **Figure 3.4**) and was usually in the range of 1000-5000 cycles. After the measurement, V_{SAC} was set to zero for a period equal to the acquisition time in order to relax the resonator and prevent self-heating. The procedure was looped by recalling blocks A-D for all frequencies ($f_{AC}[n]$ with $n = 1, 2, \ldots, n_{last}$) in the specified measurement range. Condition E determined whether all frequencies have been executed and terminated the loop.

The data were processed, plotted, and stored by blocks F–G in a parallel loop. The signals recorded in the time-domain were processed using the lock-in technique [205]. Signal amplitudes and phase angles were determined with a high signal-to-noise ratio and represented the frequency-domain. The control program also incorporated a self-calibration and self-test procedure. Low tolerance resistors were used as references. All measurement data were corrected according to the values determined during the calibration procedure. The calibration was repeated after a breakdown and/or PCB replacement.

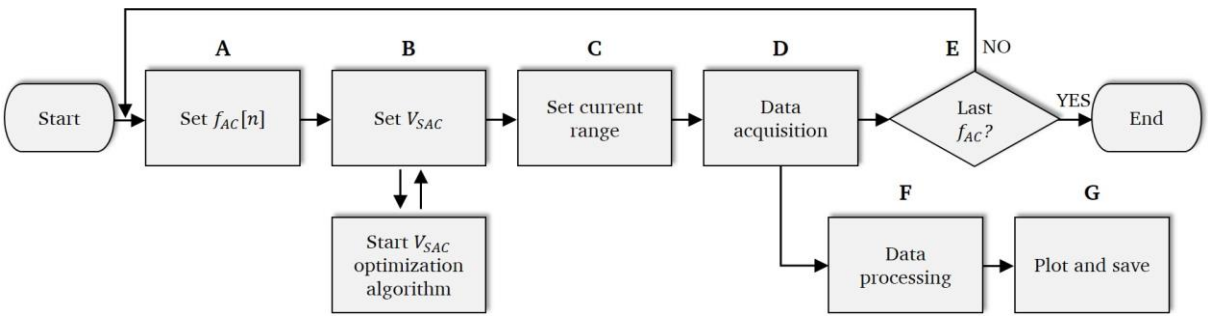

Figure 3.9. Flow chart of the automated resonance impedance spectroscopy measurement procedure implemented in LabVIEW.

[vii] The software was designed and developed in close collaboration with Tomaž Kos (Jožef Stefan Institute, Slovenia).

Verification of the setup accuracy

The functionality of the designed measurement setup was first verified by performing an impedance sweep on the same hard-type PZT resonator, as reported in **Figure 3.7a**. The result shown in **Figure 3.7b** confirms that the setup provides a constant AC voltage amplitude over the entire frequency range under investigation, despite the significant impedance change of the resonator from 5.6 Ω to 460.3 kΩ.

To test the measurement accuracy, the impedance spectrum of a reference equivalent circuit (inset of **Figure 3.10b**) was recorded and compared with measurements using commercially available impedance analyzers (**Figure 3.10**). The equivalent circuit contained a dynamic LCR branch in parallel with a static capacitance (tolerance ± 5% for capacitance and ± 10% for others), resembling a piezoelectric resonator (**Figure 2.3**) [10]. The measurement result of the designed setups is in excellent agreement with the commercial analyzers, confirming the accuracy of the system. Note that for this comparative study, equivalent circuits were chosen instead of piezoelectric materials to ensure reproducibility regardless of measurement history, aging time, or drive voltage. Furthermore, the superposition of a (moderate) DC voltage had no effect on the impedance characteristics of the equivalent circuit; thus, the measurement accuracy was confirmed even with combined AC and DC excitation.

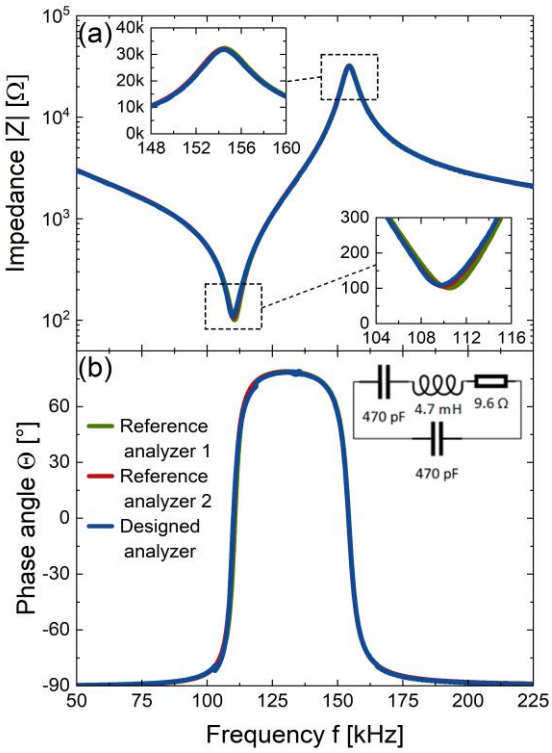

Figure 3.10. (a) Impedance magnitude ($|Z|$) and (b) phase angle (Θ) of an equivalent circuit as a function of frequency (f) measured by two different commercial reference impedance analyzers (4192A, Hewlett Packard and Alpha-A, Novocontrol Technologies) and the designed analyzer. Insets in (a) show the extended regions around the resonance and antiresonance peaks, the inset in (b) display the measured equivalent circuit.

3.4. Off-resonance electromechanical and ferroelectric characterization

Dielectric spectroscopy

Temperature-dependent dielectric permittivity measurements were carried out using a high-precision impedance analyzer (Alpha-A, Novocotrol Technologies GmbH, Germany) equipped with a temperature control system (Quatro Cryosystem, Novocotrol Technologies GmbH, Germany). Transverse (31) mode geometry samples (**Table 2.1**) were measured in the polarized and unpolarized states. The investigated temperature range was between -50 – 400 °C, measured continuously with 2 K/min heating/cooling rate at 0.1, 1, 10, and 100 kHz frequencies with 10 mV/mm AC electric field amplitude. The real part (ε'), imaginary part (ε''), and magnitude ($|\varepsilon|$) of relative permittivity were calculated from the measured impedance magnitude ($|Z|$) and phase angle (Θ) as

$$\varepsilon' = \frac{1}{\omega|Z|}\frac{h}{\varepsilon_0 lw} sin\Theta, \tag{3.6}$$

$$\varepsilon'' = \frac{1}{\omega|Z|}\frac{h}{\varepsilon_0 lw} cos\Theta, \text{ and} \tag{3.7}$$

$$|\varepsilon| = \sqrt{(\varepsilon')^2 + (\varepsilon'')^2}. \tag{3.8}$$

Piezoelectric characterization

The off-resonance inverse piezoelectric coefficients d_{33} and d_{31} were determined using a laser vibrometer (OFV-505, Polytec GmbH, Germany) and a function generator (33220A, Agilent Technologies Inc., USA). Transverse (31) mode geometry samples in polarized state were measured (**Table 2.1**). Excitation AC electric fields (E_3) of 10 V/mm amplitude and 1 kHz frequency were applied, recording the generated displacement. The measurements were conducted in a temperature range between 20 – 170 °C in-situ during continuous heating with 2 K/min using the customized sample holder (**Figure 3.3**). The coefficients were calculated from the applied field and generated edge displacement amplitude (u_3 and u_1) according to **Equation (2.8)** as (tensor abbreviation is used)

$$d_{33} = \frac{2u_3}{hE_3} \text{ and } d_{31} = \frac{2u_1}{lE_3} \tag{3.9}$$

Ferroelectric characterization

Polarization (P-E) and strain (S-E) hysteresis loops were recorded with the commercial system TF Analyzer 2000 (aixACCT Systems GmbH, Germany). Polarization was measured by applying the virtual ground method; a laser interferometer determined the longitudinal displacement. Triangular electric fields with 1 Hz frequency and a maximum amplitude of 6 kV/mm were utilized. Transverse (31) mode geometry samples in polarized and unpolarized states were immersed in silicone oil to prevent electric discharge (arching) through air. The temperature-dependent measurements in the range of 20 – 150 °C were carried out using the temperature control unit integrated in the sample holder. The silicone oil was heated at a 2 K/min rate and stabilized for 30 min at the desired temperature before initiating the measurement.

Polarization harmonics[viii]

Polarization harmonics measurements were carried out using a customized shunt-resistor circuit [206, 207]. Sinusoidal electric fields with a frequency of 1 kHz and (sub-coercive) amplitudes between 10 mV/mm and 400 V/mm were applied. The excitation voltage was generated by a lock-in amplifier (SR830 DSP, Stanford Research, USA) and amplified with a wide band amplifier (PZD700 M/S, Trek Inc., USA). The voltage drop on the shunt-resistor was measured with a high-voltage probe (P6015A, Textronix Inc., USA); the shunt-resistor (R) was chosen according to $R \ll 1/\omega C$ (C is the small-field sample capacity) to ensure main voltage drop on the sample. Amplitude and phase angle of the first- and third-order harmonics of the shunt-resistor voltage were extracted by two lock-in amplifiers (SR830 DSP, Stanford Research, USA). Polarized disk-shaped samples (6x0.5 mm^2) were pre-conditioned at the maximum voltage and measured with descending voltage amplitude. The samples were heated at 2 K/min rate and thermally stabilized for 30 min at each set temperature before initiating the measurement.

Error calculation

Instrumental uncertainties of the voltage, current, displacement, temperature, and sample geometry measurements, as well as their error propagation into the calculated polarization, permittivity, and strain were considered. However, the instrumental error was found to be negligible as compared to property disparities due to sample-to-sample variation. Therefore, all measurements were carried out on two samples of each composition. Uncertainties were calculated by the standard deviation according to the Gaussian uncertainty propagation considering only sample variation; instrumental error contributions will be pointed out explicitly if necessary.

3.5. Crystal structure and microstructure analysis

The x-ray diffraction patterns were collected at the ID15 beamline of the European Synchrotron Radiation Facility (ESRF) and the PETRA III P02.1 beamline of the Deutsches Electronen-Synchrotron (DESY). X-ray beams (0.3x0.3 mm^2) of 75 keV and 60 keV energies (0.16534 Å and 0.20673 Å wavelength), respectively, were utilized. Diffraction intensities were recorded in transmission geometry for 30 s with an area detector (Pilatus CdTe 2M, Dectris Ltd., Switzerland) in the 2θ-range from 2° to 9°.

Temperature-dependent diffraction patterns in the range of 20 – 400 °C were collected using a laboratory diffractometer (D8 Advanced, Bruker Corp., USA) in Bragg–Brentano geometry, equipped with a Cu $K_{\alpha1/\alpha2}$ radiation source (1.54060 Å and 1.54439 Å wavelength) and a linear detector (VANTEC1, Bruker Corp., USA). A 2θ-range from 15° to 80° was covered in steps of 0.02° and 0.3 s/step recording time. Lattice parameters were derived from the 2θ positions of the respective lattice plane reflections, determined by Gauss peak fitting (**Equations (3.4)-(3.5)**).

The microstructure was imaged by scanning electron microscopy (SEM; XL30 FEG, Philips Corp., Netherlands) using a backscattered electron (BSE) detector. The samples were polished to a 0.25 μm finish with a diamond paste and thermally etched at 1000 °C for 10 min. An

[viii] The measurements were performed in collaboration with Prof. Dr. Tadej Rojac (Jožef Stefan Institute, Slovenia).

automated graphical analysis implemented in LabVIEW determined the grain size distribution. The analysis identified the grain boundaries, determined the pixel area per grain, multiplied with the pixel-to-length ratio set by the SEM magnification, and calculated a diameter equivalent to the grain size assuming spherical grain shape. At least 200 grains were analyzed per composition and evaluated statistically by the standard deviation procedure.

3.6. Materials and sample preparation

The chemical nomenclatures and utilized abbreviations of the $Pb(Zr,Ti)O_3$-based and $(Na_{1/2}Bi_{1/2})TiO_3$-$BaTiO_3$-based poly-crystalline ferroelectrics prepared for the study are summarized in **Table 3.2**. PZT compositions with a tetragonal crystal structure (PZT_T) were commercial materials. Ferroelectric hardening and softening were introduced by coupled multi-element B-site substitution (Mn^{3+}, Ni^{3+}, Sb^{5+}, Nb^{5+}) [1].

PZT compositions with a rhombohedral crystal structure (PZT_R)[ix] and the NBT-BT[x] compositions were customized materials, prepared by the solid-state reaction route. Detailed processing conditions were reported before, corresponding references are summarized in **Table 3.2**. A $0.6PbZrO_3$-$0.4PbTiO_3$ ratio was chosen for PZT_R according to the phase diagram in **Figure 2.11**. Ferroelectric hardening and softening were introduced by single-element B-site substitution, utilizing y mole % Fe^{3+} acceptor-doping (PZT_R-100yFe) and y mole % Nb^{5+} donor-doping (PZT_R-100yNb), respectively.

Table 3.2. Chemical nomenclatures (composition) and utilized abbreviations of the ferroelectric resonator ceramics investigated in the study. PZT_T compositions were commercial materials; PZT_R and NBT-BT were prepared by the solid-state reaction route, detailed process parameters can be found in the provided references.

$Pb(Zr_{0.47}Ti_{0.48}[Mn_{0.33}Sb_{0.32}Nb_{0.33}]_{0.05})O_3$	Hard PZT_T	PIC181, PI Ceramic GmbH, Germany
Unknown composition	Medium-hard PZT_T	P4, CeramTec GmbH, Germany
$Pb(Zr_{0.45}Ti_{0.47}[Ni_{0.33}Sb_{0.67}]_{0.08})O_3$	Soft PZT_T	PIC151, PI Ceramic GmbH, Germany
$Pb(Zr_{0.60}Ti_{0.40})O_3$	PZT_R	[208]
$Pb(Zr_{0.60}Ti_{0.40})_{0.999}Fe_{0.001}O_3$	PZT_R-0.1Fe	[208]
$Pb(Zr_{0.60}Ti_{0.40})_{0.995}Fe_{0.005}O_3$	PZT_R-0.5Fe	[208]
$Pb(Zr_{0.60}Ti_{0.40})_{0.99}Nb_{0.01}O_3$	PZT_R-1Nb	[208]
$(Na_{0.5}Bi_{0.5})_{0.94}Ba_{0.06}TiO_3$	NBT-6BT	[72]
$(Na_{0.5}Bi_{0.5})_{0.94}Ba_{0.06}(Ti_{0.995}Zn_{0.005})O_3$	NBT-6BT-0.5Zn	[72]
$(Na_{0.5}Bi_{0.5})_{0.94}Ba_{0.06}(Ti_{0.99}Zn_{0.01})O_3$	NBT-6BT-1Zn	[72]
$(Na_{0.5}Bi_{0.5})_{0.94}Ba_{0.06}TiO_3$:0.1ZnO	NBT-6BT:10ZnO	[72]
$(Na_{0.5}Bi_{0.5})_{0.94}Ba_{0.06}TiO_3$:0.4ZnO	NBT-6BT:40ZnO	[72]
$(Na_{0.5}Bi_{0.5})_{0.91}Ba_{0.09}TiO_3$	NBT-9BT	[85]
$(Na_{0.5}Bi_{0.5})_{0.91}Ba_{0.09}TiO_3$:0.2ZnO	NBT-9BT:20ZnO	[85]

[ix] The materials were synthesized by Silvo Drnovšek (Jožef Stefan Institute, Slovenia).

[x] The materials were synthesized by Lalitha Kodumudi Venkataraman (Technische Universität Darmstadt, Germany).

NBT-BT compositions in the MPB region (rhombohedral/tetragonal phase mixture) and of tetragonal crystal structure with 6 or respectively 9 mole % $BaTiO_3$ were chosen according to the phase diagram in **Figure 2.14**. Ferroelectric hardening was achieved by y mole % Zn^{2+} acceptor-doping (NBT-6BT-100yZn). 3-0 composites with ZnO second phase were prepared by mixing and homogenizing the calcined NBT-BT powder with commercial ZnO powder before sintering according to a z % mole-ratio (NBT-6BT:100zZnO and NBT-9BT:100zZnO; 10 – 40 % mole-ratio correspond to 4 – 14 % volume ratio of ZnO inclusions).

The resonator samples were cut from sintered blocks by a diamond-wire saw, ground to the final geometry, and annealed at 400 °C for 30 min with heating and cooling rates of 5 K/min and 1 K/min, respectively, to relax the introduced surface stress. The geometries complied with the required standard site ratios [209] for the transverse length (31), longitudinal length (33), and radial (p) vibration modes (**Table 2.1**) and are depicted in **Supplemental Table 1**.

Electrodes were fabricated by Au-sputtering on the two opposite faces (**Table 2.1**). The samples were electrically polarized, field-cooled, and aged for 24 h before further measurements. The poling conditions (electric field, holding time, temperature) are summarized in **Table 3.3**. The poling was evaluated by the small-field piezoelectric coefficient (d_{33}) measured with a Berlincourt meter (PiezoMeter System PM 300, Piezotest Pte Ltd., Singapore) at 110 Hz, 2 N static force, and 0.25 N dynamic force.

Table 3.3. Polarization conditions (electric poling) of the investigated compositions (field, time, and temperature).

Composition	**Electric field** *[kV/mm]*	**Time** *[min]*	**Temperature** *[°C]*
Hard PZT_T	3	5	120
Medium-hard PZT_T	3	10	100
Soft PZT_T	2	5	120
All PZT_R	5	20	50
All NBT-BT	6	30	30

4. High-power properties of ferroelectric ceramics – A case study on $Pb(Zr,Ti)O_3$

This first result chapter aims to introduce a systematic understanding of the high-power properties of ferroelectrics. Since $Pb(Zr,Ti)O_3$-based materials are the absolutely dominantly applied ferroelectrics, the investigations in this chapter were carried out exemplarily on prototype commercial and lab-made $Pb(Zr,Ti)O_3$ compositions. First, it is rationalized how internal material properties, especially crystal structure and chemical modification by doping (ferroelectric hardening and softening), affect the piezoelectric, mechanical, dielectric, coefficients and quality factors (**Equation (2.48)**) that are essential to generate large vibration velocities in piezoelectric resonance (Section 4.1). The coefficients are considered individually as well as accumulated in a high-power figure of merit. The macroscopic measurement results are subsequently combined with in situ XRD studies to reveal the microscopic origin and the physical mechanisms of the observed behavior (Section 4.2). Afterward, the influences of external conditions on the coefficients are studied. Parameters that are considered to have the most considerable impact are examined, including frequency dispersion (Section 4.3), temperature dependence (Section 4.4), DC bias (Section 4.5), as well as different vibration modes and anisotropy (Section 4.6). The findings are elucidated phenomenologically as well as mechanistically and are complemented by previous reports. This allows to transfer the findings to Pb-free compositions and draw a general conclusion on the requirements for next-generation high-power ferroelectrics.

Parts of Sections 4.1 and 4.2 were published in the journal article *"Direct observation of domain wall motion and lattice strain dynamics in ferroelectrics under high-power resonance"*, Slabki, M., Venkataraman, L. K., Checchia, S., Fulanovic, L., Daniels, J., and Koruza, J., Phys Rev B 103 (2021).

Parts of Section 4.4 were published in the journal article *"Thermal stability of the electromechanical properties in acceptor-doped and composite-hardened $(Na_{1/2}Bi_{1/2})TiO_3$-$BaTiO_3$ ferroelectrics"*, Slabki, M., Venkataraman, L. K., Rojac, T., Rödel, J., and Koruza, J., J Appl Phys 130 (2021).

Parts of Sections 4.6 were published in the journal article *"Anisotropy of the high-power piezoelectric properties of $Pb(Zr,Ti)O_3$"*, Slabki, M., Wu, J., Weber, M., Breckner, P., Isaia, D., Nakamura, K., and Koruza, J., J Am Ceram Soc 102 (2019).

4.1. Internal influence – microstructure, crystal structure, and chemical modification

Numerous experimental studies established that ferroelectric softening by donor-doping causes a vacancy formation on the cation A-site in the perovskite crystal lattice of $Pb(Zr,Ti)O_3$ (PZT), transforming the material towards a rectangular polarization loop with low coercive field and high polarization as well as enhanced electromechanical properties and strain response upon application of electric field or mechanical stress. Contrary, ferroelectric hardening by acceptor-doping induces the creation of oxygen vacancies in the lattice, leading to a pinched polarization loop with a large coercive field and low polarization, as well as reduced electromechanical properties and strain response. Similar effects also appear in correlation with the crystal structure and the Zr/Ti ratio. Generally, the polarization as well as the electromechanical properties are lower and the loop stronger constrained in the case of a tetragonal crystal structure compared to the rhombohedral structure, with or without additional doping. The

mechanisms of this ferroelectric softening and hardening, which are still under dispute, are usually discussed in light of crystal lattice distortion and polarization switching of ferroelectric domains, which are also referred to as intrinsic and extrinsic contributions. The latter is typically quantified by the motion of the domain walls. These properties and their measurement methods have been reviewed in detail in Sections 2.3 and 3.4. However, they are insufficient or even fail to describe and predict materials' behavior under piezoelectric resonance at large vibration velocities, i.e., under high-power conditions.

Here, this classical characterization is carried out first to classify the utilized materials (Sections 4.1.1 and 4.1.2). This is followed by the important but rarely applied high-power resonance characterization (Sections 4.1.3 and 4.1.4). Two sets of tetragonal and rhombohedral PZTs are compared, including hard-type and soft-type compositions. Generating considerable strain by comparatively small electric fields using the resonance excitation represents a fundamentally different dynamic driving condition and material state. The properties will be evaluated with respect to the vibration velocity instead of the applied electric field.

4.1.1. Crystallographic, microstructural, and ferroelectric characterization of tetragonal $Pb(Zr,Ti)O_3$

Crystal structure

Three commercial tetragonal $Pb(Zr,Ti)O_3$ (PZT_T) compositions were used in this study as model state-of-the-art PZT_T materials (**Table 3.2**). The compositions were particularly selected to cover a wide range from soft to hard ferroelectrics. The diffractograms in the unpoled state are given in **Figure 4.1a**, evidencing the perovskite tetragonal crystal structure. For comparison, peaks will be denoted with pseudo-cubic notation. The $\{111\}_{pc}$ singlet (**Figure 4.1b**) and the $\{002\}_{pc}/\{200\}_{pc}$ doublet (**Figure 4.1c**) demonstrate the ferroelectric tetragonal distortion with the c/a cell ratio being the largest in the hard PZT_T (PIC181) and the smallest in the medium-hard PZT_T (P4) and soft PZT_T (PIC151) (**Table 4.1**). Impurities or secondary phases were not observed in the samples.

Table 4.1. Crystallographic, microstructural, and ferroelectric characteristics of the three investigated PZT_T compositions, determined from x-ray diffraction, SEM analysis, and bipolar P-E and S-E loop measurements.

	Hard PZT_T (PIC181)	**Medium-hard PZT_T** (P4)	**Soft PZT_T** (PIC151)
Tetragonal distortion (c/a-1) [%]	2.3	1.4	1.5
Average grain size $y_{average}$ [μm]	1.2	2.8	4.1
Poling electric field E_p [kV/mm]	3.36	3.20	1.26
Maximum polarization P_{max} [μC/cm²]	23.0	23.9	45.9
Remanent polarization P_{rem} [μC/cm²]	6.2	8.7	36.0
Maximum strain S_{max} [%]	0.17	0.16	0.55
Remanent strain S_{rem} [%]	0.00	-0.02	0.27
Coercive field E_C [kV/mm]	1.71	1.24	1.14
Internal bias field E_{ib} [kV/mm]	0.89	0.49	0.03

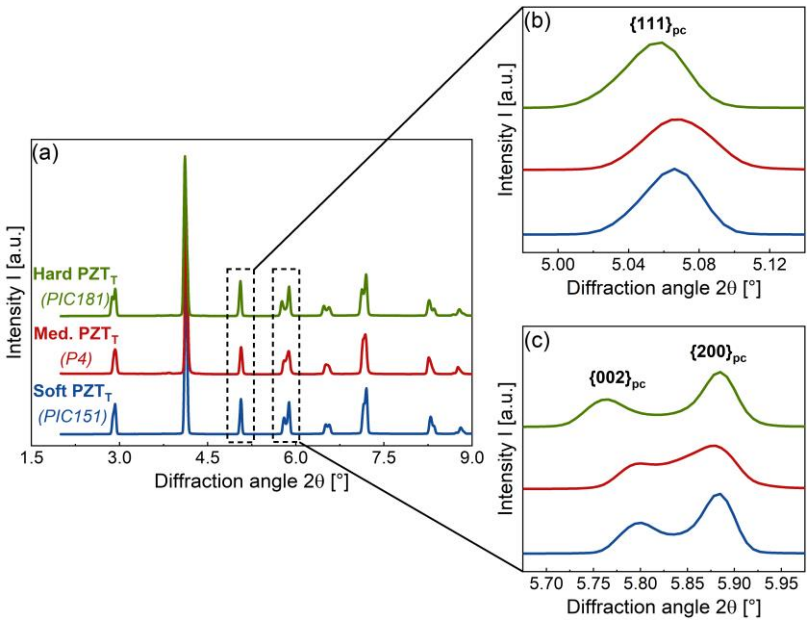

Figure 4.1. (a) Synchrotron diffractograms (λ=0.20673 Å) in the unpoled state of hard PZT$_T$ (PIC181), medium-hard PZT$_T$ (P4), and soft PZT$_T$ (PIC151) exhibit phase purity of the materials. (b,c) Enlarged diffractogram ranges exhibit $\{111\}_{pc}$ singlets and $\{002\}_{pc}/\{200\}_{pc}$ doublets, demonstrating the ferroelectric tetragonal distortion of the compositions.

Microstructure and grain size

The microstructures and the grain size distributions are displayed in **Figure 4.2**. The compositions exhibit a dense microstructure with a narrow grain size distribution. The average grain sizes are below 5 μm, which is comparably small and likely related to the acceptor/donor doping [43]. It has been reported that grain size variations in PZT-based materials substantially influence their ferroelectric and electromechanical properties associated with different domain configurations [210]. However, a noticeable grain size effect appears only in the sub-μm range. Therefore, it is unlikely that the observed small grain size variation seriously contributes to the ferroelectric property difference and will therefore be neglected in the subsequent analysis[xi].

Polarization and strain loops

The ferroelectric properties were evaluated based on the large-field bipolar P-E and S-E hysteresis loops in the unpoled (**Figure 4.3a-f**) and the poled and aged states (**Figure 4.3g-l**). The poling cycles (first cycles in the unpoled state, **Figure 4.3a-c**) reveal a square-shaped polarization loop of the soft PZT$_T$ and pinched polarization loops of the hard PZT$_T$ and medium-hard PZT$_T$. The different polarization loop-shapes originate from the chemical doping (**Table 3.2**). Hard PZT$_T$ was B-site acceptor-doped by Mn^{3+}, leading to the subsequent formation of charge compensating O^{2-} vacancies (Kröger-Vink notation [211]):

$$Mn_2O_3 + 2Ti_{Ti}^{x} + O_O^{x} \rightarrow 2Mn_{Ti}' + V_O^{\cdot\cdot} + 2TiO_2. \tag{4.1}$$

The defects remain isolated (Mn_{Ti}' and $V_O^{\cdot\cdot}$) or associate to defect complexes ($Mn_{Ti}' - V_O^{\cdot\cdot}$) [64]. Both stabilize the domain configuration and reduce the ferroelectric domain wall mobility by pinning the domain walls.

[xi] A supportive study on a fixed $Pb_{0.99}La_{0.01}(Zr_{0.52}Ti_{0.48})O_3$ composition with average grain size ranging from 0.8 to 5.5 μm revealed no remarkable influence on the high-power properties (not shown here). Samples described in [210] were used for the study.

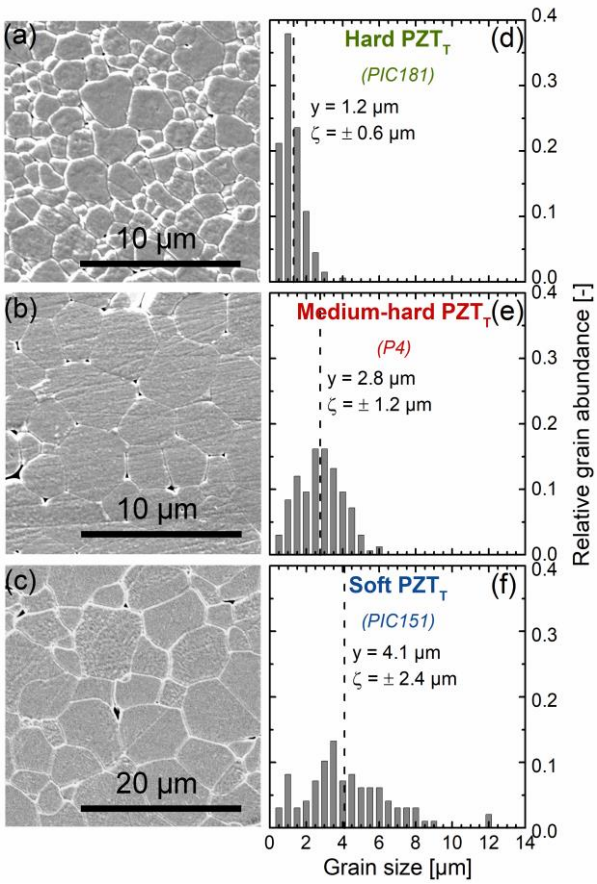

Figure 4.2. (a-c) Microstructures of the PZT$_T$ samples determined by SEM. (d-f) Corresponding average grain size (y), size variance (ζ), and distribution.

The soft PZT$_T$ was B-site donor-doped by Sb^{5+}, leading to the formation of Pb^{2+} vacancies.

$$Sb_2O_5 + 2Ti_{Ti}^{x} + Pb_{Pb}^{x} \rightarrow 2Sb_{Ti}^{\cdot} + V_{Pb}'' + 2TiO_2 + PbO. \quad (4.2)$$

The isolated defects (V_{Pb}'') enhance the domain wall mobility by flattening the potential landscape of domain wall motion [22, 94, 97].

The ferroelectric hardening results in a larger poling electric field (E_p, determined from the inflection point of the first polarization half-cycle), but a reduced maximum strain (S_{max}) as compared to the soft PZT$_T$ (**Table 4.1**), since a portion of domain walls is entirely excluded from the field response due to the strong pinning of the walls. Moreover, the remanent polarization (P_{rem}) and strain (S_{rem}) are reduced, owing to the predominantly reversible field-induced domain wall displacement, in contrast to the mainly irreversible domain polarization switching process in soft PZT$_T$.

The hard PZT$_T$ and medium-hard PZT$_T$ loops in the poled state (**Figure 4.3g-i**) reveal a distinct asymmetry and a shift along the abscissa. The shift evolves from the alignment of the defect-dipoles along the polarization vector, which counteracts the applied electric field. The shift is quantified by the internal bias field (E_{ib}) which is defined as the half-difference between the negative and positive coercive fields (E_c) determined from the strain minima. Particularly the hard PZT$_T$ reveals comparatively large coercive and internal bias fields, indicating a solid domain wall clamping, which results in later-discussed exceptionally large quality factor values.

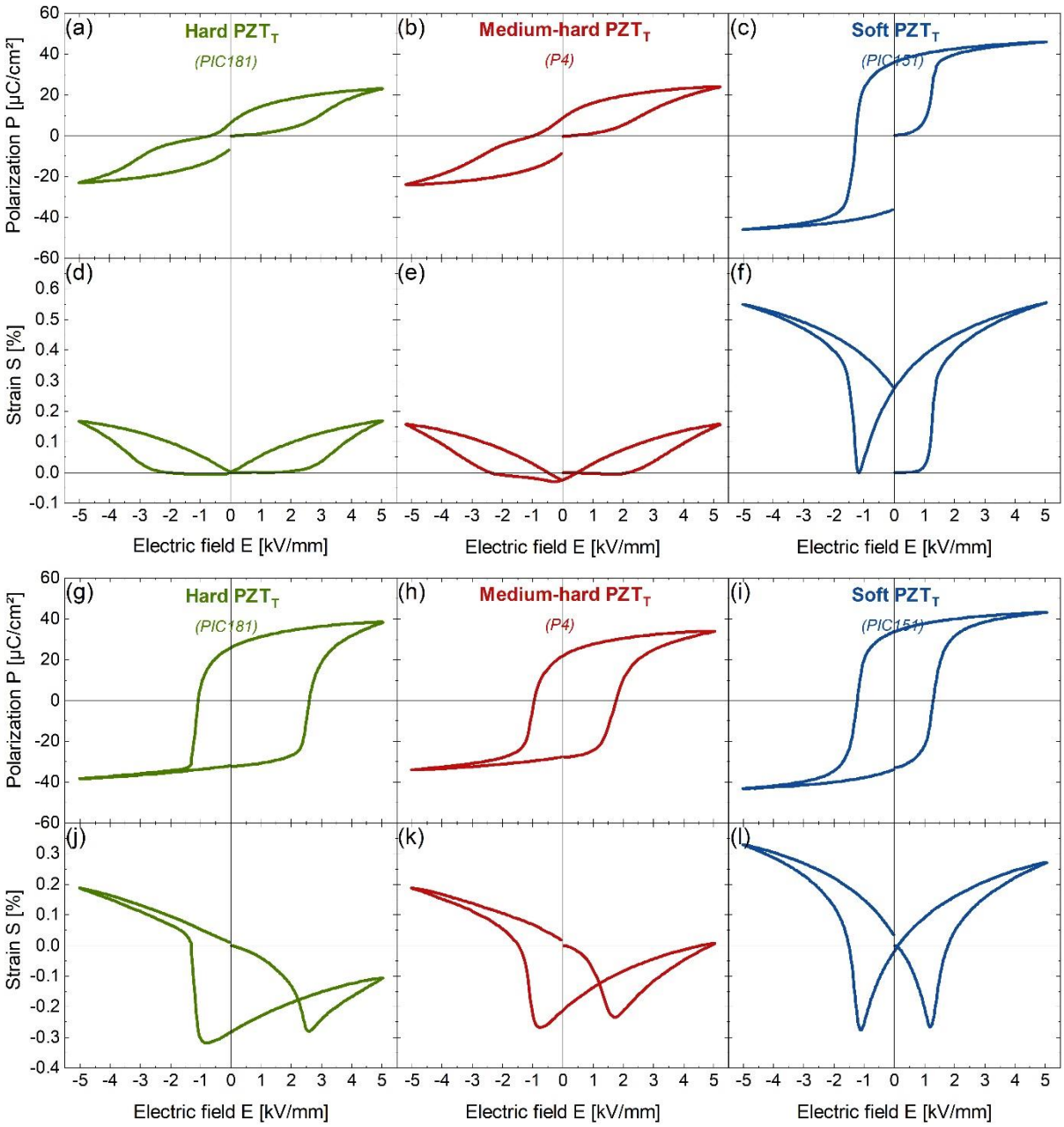

Figure 4.3. Polarization (P) and strain (S) loops of the three investigated PZT_T compositions in the (a-f) unpoled and (g-l) poled states as a function of applied bipolar electric field (E) at 1 Hz measurement frequency.

4.1.2. Crystallographic, microstructural, and ferroelectric characterization of rhombohedral $Pb(Zr,Ti)O_3$

$Pb(Zr,Ti)O_3$ based ferroelectrics appear among others in the rhombohedral or tetragonal crystal structure (or a mixture of both at the MPB) depending on the Zr/Ti ratio (**Figure 2.11**). A set of rhombohedral PZTs (PZT_R; **Table 3.2**) was prepared for comparison with the tetragonal PZT (PZT_T) introduced in the previous section, to evaluate the influence of the crystal structure on the high-power properties. A Zr/Ti ratio of 60:40 was chosen and modified by Fe^{3+} acceptor-doping and Nb^{5+} donor-doping, respectively.

Crystal structure

The diffractograms of the four compositions in the unpoled state are given in **Figure 4.4a**. The $\{111\}_{pc}/\{11\overline{1}\}_{pc}$ doublet (**Figure 4.4b**) and the $\{200\}_{pc}$ singlet (**Figure 4.4c**) demonstrate the ferroelectric rhombohedral distortion. The rhombohedral tilt angle β was found to be the largest in undoped PZT_R and smallest in hard PZT_R-0.5Fe (**Table 4.2**). Impurities or secondary phases were not observed in the samples.

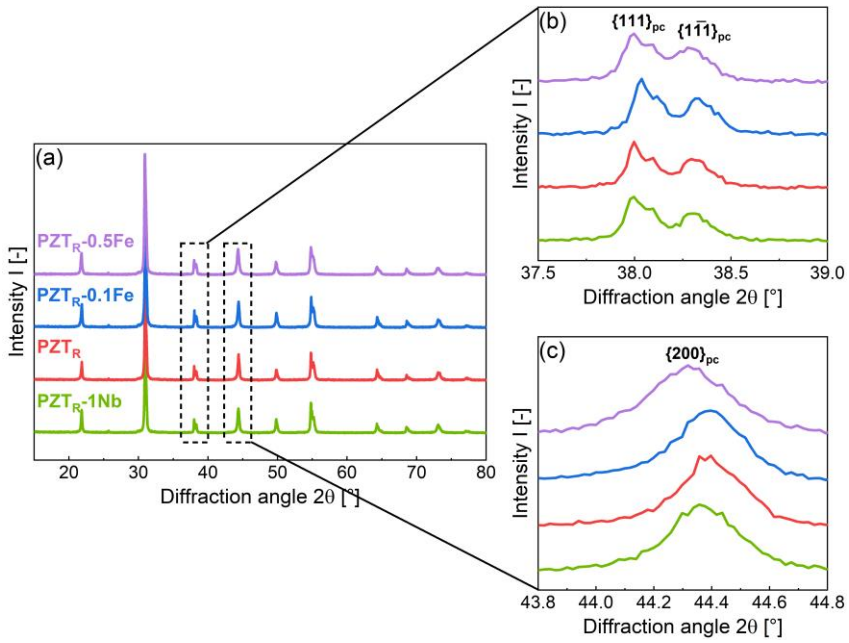

Figure 4.4. (a) Diffractograms in the unpoled state of hard PZT_R (PZT_R-0.5Fe), medium-hard PZT_R (PZT_R-0.1Fe), undoped PZT_R, and soft PZT_R (PZT_R-1Nb) exhibit phase purity of the materials. (b,c) Enlarged diffractogram ranges depict the $\{111\}_{pc}/\{11\bar{1}\}_{pc}$ doublets and $\{200\}_{pc}$ singlets, demonstrating the ferroelectric rhombohedral distortion of the compositions.

Table 4.2. Crystallographic, microstructural, and ferroelectric characteristics of the four investigated PZT_R compositions, determined from x-ray diffraction, SEM analysis, and bipolar P-E and S-E loop measurements.

	PZT_R-0.5Fe	**PZT_R-0.1Fe**	**PZT_R**	**PZT_R-1Nb**
Rhombohedral tilt angle $90° - \beta$ [°]	0.17	0.22	0.27	0.22
Average grain size $y_{average}$ [μm]	2.7	7.4	13.0	4.2
Poling electric field E_p [kV/mm]	2.78	1.98	1.45	0.95
Maximum polarization P_{max} [μC/cm²]	22.8	28.0	29.0	47.5
Remanent polarization P_{rem} [μC/cm²]	1.5	5.2	17.2	41.0
Maximum strain S_{max} [%]	0.13	0.16	0.19	0.50
Remanent strain S_{rem} [%]	0.00	0.00	0.04	0.31
Coercive field E_C [kV/mm]	1.96	0.99	1.26	0.96
Internal bias field E_{ib} [kV/mm]	1.16	0.31	0.16	0.05

Microstructure and grain size

The microstructure and the grain size distribution are displayed in **Figure 4.5**. All compositions exhibit a dense microstructure with 96-97 % relative density. The undoped PZT_R reveals a large average grain size of about 13 μm and a broad grain size distribution. Both are significantly reduced in the doped compositions, where Fe^{3+} acceptor-doping appears to have a stronger effect than the Nb^{5+} donor-doping [43]. However, the grain size of all PZT_R compositions is above the 1 μm threshold [210]; hence, impact of the grain size on the ferroelectric properties can be neglected here as well.

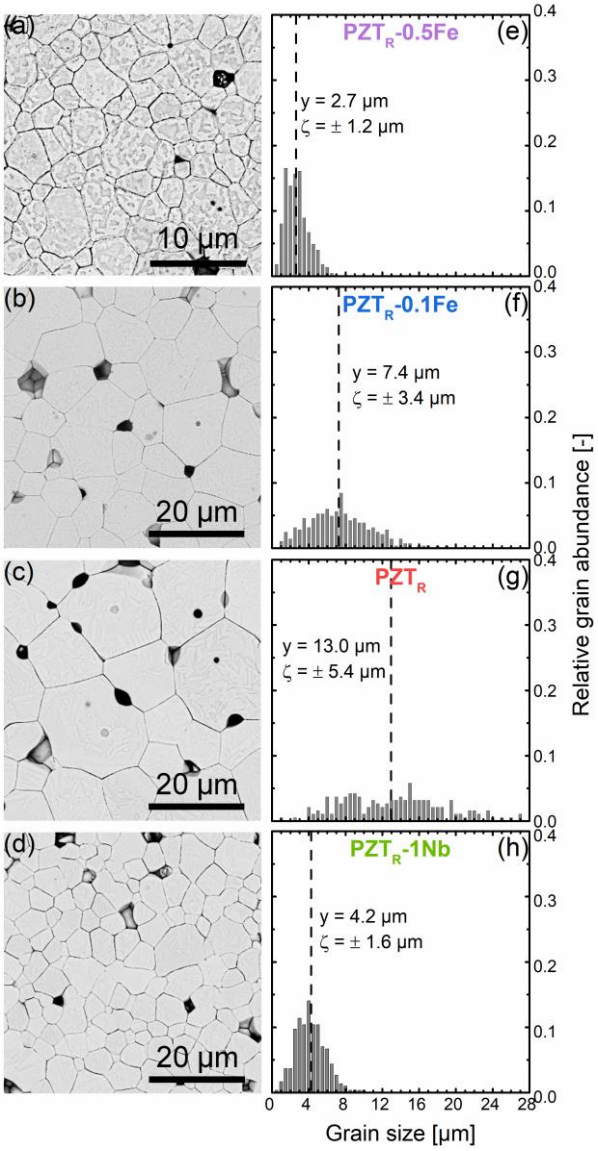

Figure 4.5. Microstructure of the PZT_R samples determined by SEM. (d-f) Corresponding average grain size (y), size variance (ζ), and distribution.

Polarization and strain loops

The large-field bipolar P-E and S-E hysteresis loops were recorded in the unpoled (**Figure 4.6a h**) and the poled and aged state (**Figure 4.6i-p**). The poling cycles (**Figure 4.6a-d**) expose a square-shaped polarization loop of PZT_R-1Nb and pinched polarization loops of PZT_R, PZT_R-0.1Fe, and PZT_R-0.5Fe. The different polarization loop shapes originate from the chemical modification, i.e., Fe^{3+} and Nb^{5+} doping, respectively, according to

$$Fe_2O_3 + 2Ti_{Ti}^{x} + O_O^{x} \rightarrow 2Fe_{Ti}' + V_O^{\cdot\cdot} + 2Ti \text{ and} \tag{4.3}$$

$$Nb_2O_5 + 2Ti_{Ti}^{x} + Pb_{Pb}^{x} \rightarrow 2Nb_{Ti}^{\cdot} + V_{Pb}'' + 2TiO_2 + PbO. \tag{4.4}$$

The ferroelectric hardening results in PZT_R-0.5Fe having the largest poling electric field, but the lowest maximum strain (**Table 4.2**). Moreover, the remanent polarization and strain are almost zero, featuring a fully reversible field-induced domain wall movement, in contrast to the mainly irreversible domain switching process in soft PZT_R-1Nb. The poled and aged loops display a distinct asymmetry and large internal bias field in PZT_R-0.5Fe (**Figure 4.6i-l**).

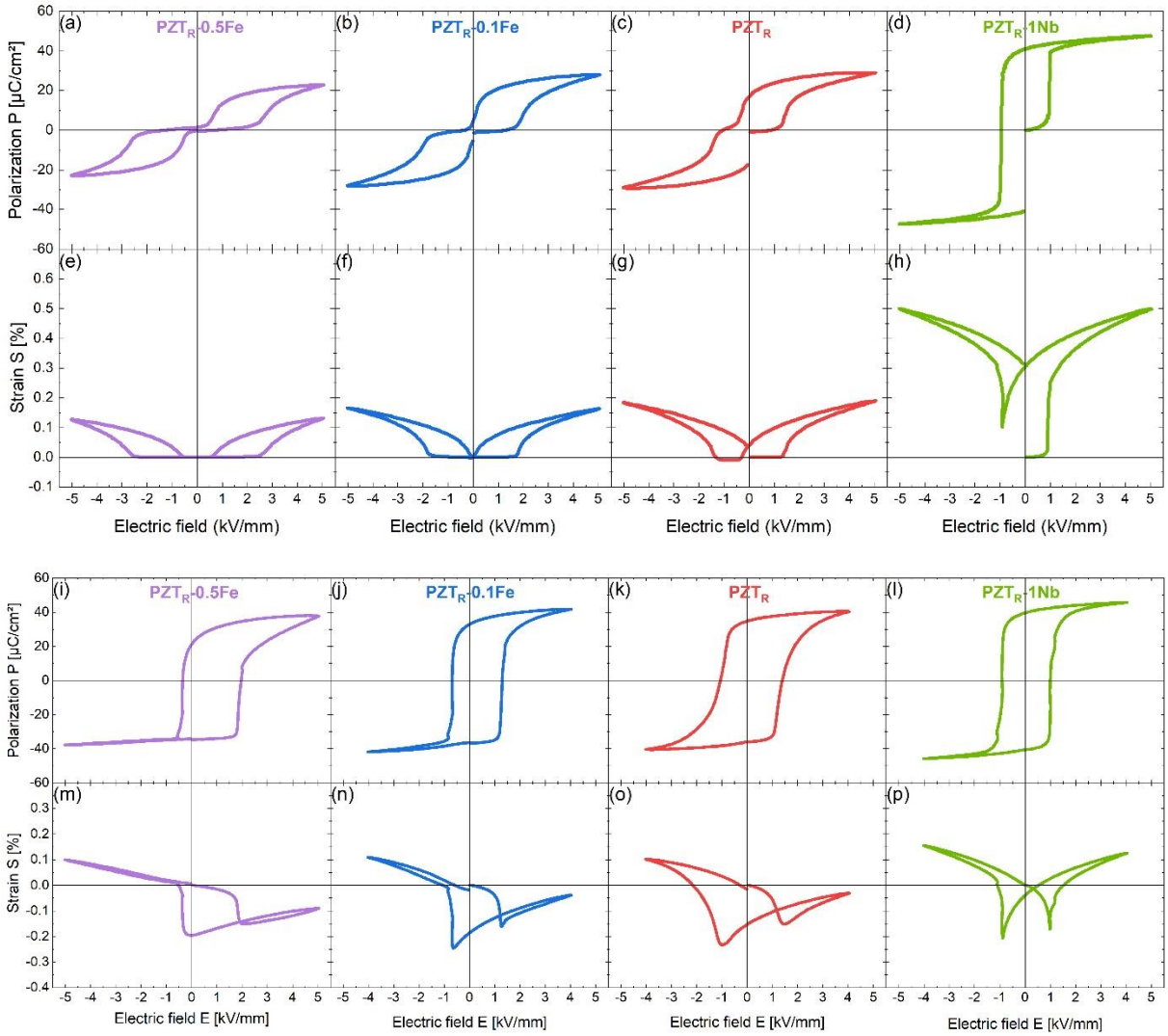

Figure 4.6. Polarization (P) and strain (S) loops of the four investigated PZT_R compositions in the (a-h) unpoled and (i-p) poled states as a function of applied bipolar electric field (E) at 1 Hz measurement frequency.

4.1.3. Electromechanical high-power properties of tetragonal Pb(Zr,Ti)O_3

The vibration velocity dependence of the electromechanical coefficients Q_{31}^{R}, Q_{31}^{AR}, d_{31}, k_{31}, s_{11}^{E}, and ε_{33}^{T} at 20 °C in the transverse (31) vibration mode was determined by the pulse drive method with burst excitation and is given in **Figure 4.7** for the three above-introduced tetragonal PZT_T compositions. It is essential to point out that the discussion on the material's high-power properties must equivalently account for two main aspects: (1) the (small-field) values of the electromechanical coefficients as well as (2) their change or stability with increasing vibration velocity. Moreover, all coefficients contributing to the vibration generation (**Equation (2.48)**) need to be considered. The majority of studies and reports published so far related to the high-power properties of ferroelectrics, focus either only on the small-field values of the electromechanical coefficients or only on the vibration velocity stability of Q_{ij}.

The hard PZT_T (PIC181) is an exceptionally hard ferroelectric, particularly in the group of Pb-based ferroelectrics, which was already demonstrated by the large coercive and bias electric fields and a slim strain hysteresis (**Figure 4.3**). Accordingly, it exhibits outstanding large small-field Q_{31}^{R} and Q_{31}^{AR} values in the range of 2300 to 2700 (**Table 4.3**). However, despite the large small-field values, Q_{31}^{R} and Q_{31}^{AR} exhibit a severe decrease with increasing vibration velocity (**Figure 4.7a**). At 1 m/s Q_{31}^{R} has already dropped to only 20 % of the initial value; at higher vibration velocity it stabilizes around 110. This behavior was previously observed in several PZT compositions [12, 27, 41] and was described as the main detriment for high-power applications. Interestingly, the largest slope of decrease of Q_{31}^{R} and Q_{31}^{AR} appears in the range between 0.4 m/s and 1 m/s, below that range the decrease is moderate, indicating a threshold vibration velocity. As expected for ferroelectrically-hardened piezoceramics, the d_{31}, k_{31}, s_{11}^{E}, and ε_{33}^{T} values are comparatively small (**Table 4.3**) and marginally increase with increasing vibration velocity. Their evolution is accurately resembled by a second-order polynomial fit ($R^2 \geq 0.991$ in all cases)

$$\frac{\Delta X}{X_0} = \frac{X - X_0}{X_0} = \xi v + \vartheta v^2, \tag{4.5}$$

with X_0 being the intercept, ξ the linear, and ϑ the quadratic coefficient (X: d_{31}, k_{31}, s_{11}^{E}, or ε_{33}^{T}). The relation is a modified expression of the empirical [161] and non-linearity models [162, 178] for PZT-based ferroelectrics in the low vibration velocity range (**Equation (2.56)**). The additional linear term accounts for the pronounced linearity of the coefficients in the large vibration velocity range and corresponds to the non-linear Rayleigh law (**Equations (2.53)-(2.55)**).

The medium-hard PZT_T reveals a qualitatively similar behavior. The small-field Q_{31}^{R} and Q_{31}^{AR} values are smaller compared to hard PZT_T (note the different scales between **Figure 4.7a-c**), but demonstrate a similar decrease in magnitude, dropping by 80 % already at 1 m/s and stabilizing at 40 above 1 m/s. A threshold vibration velocity is not observed. The small-field d_{31}, k_{31}, s_{11}^{E}, and ε_{33}^{T} values are very similar to those of hard PZT_T; however, k_{31} and ε_{33}^{T} exhibit a slope with larger increase.

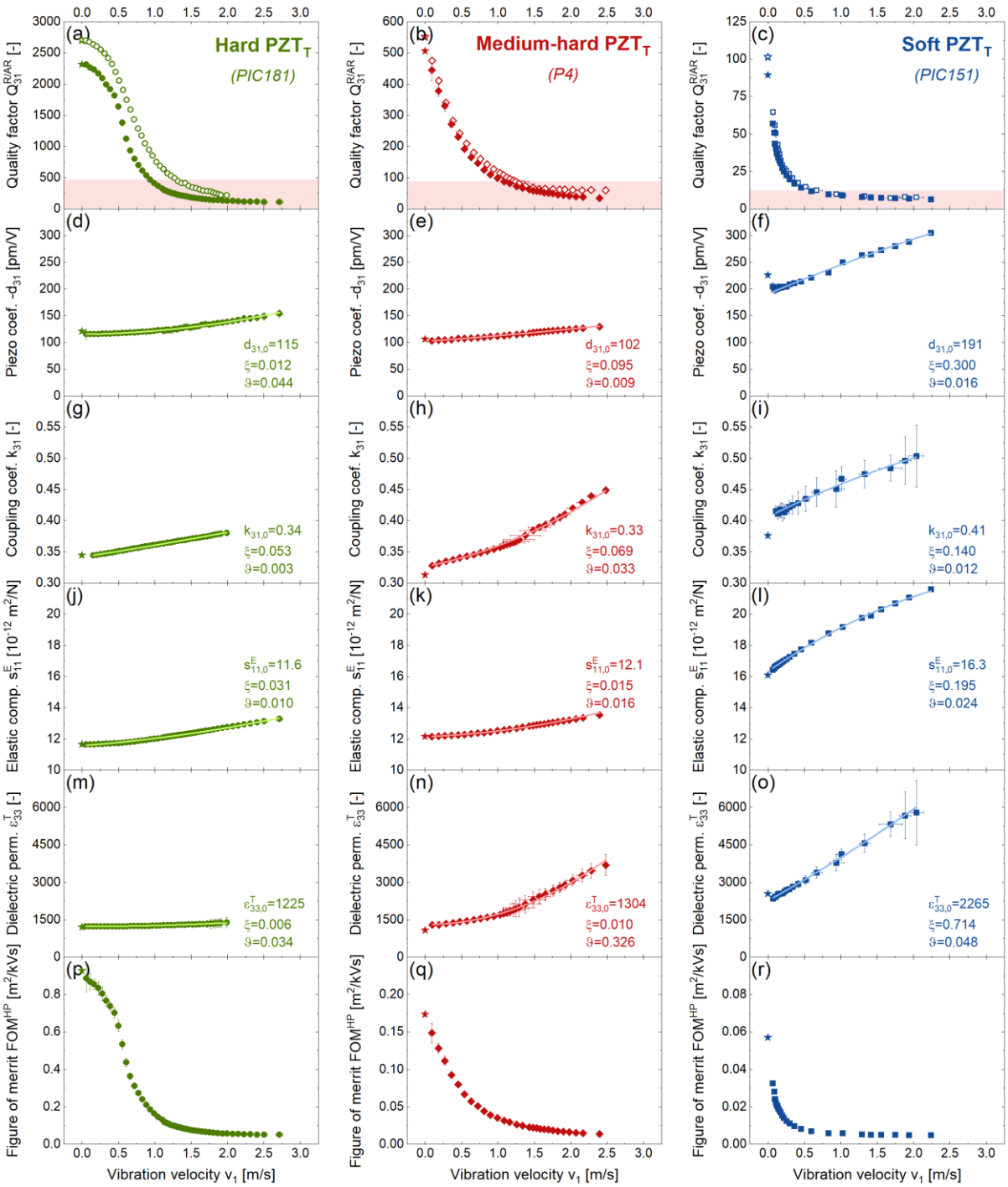

Figure 4.7. Electromechanical coefficients (a-c) Q_{31}^{R} (solid symbols) and Q_{31}^{AR} (open symbols), (d-f) d_{31}, (g-i) k_{31}, (j-l) s_{11}^{E}, (m-o) ε_{33}^{T} and (p-r) high-power figure of merit (FOM^{HP}, **Equation (4.6)**) of the three investigated PZT$_T$ compositions in the transverse (31) vibration mode as a function of vibration velocity (v_1) at 20 °C. The data points denoted as stars at 0 m/s depict the small-field values determined from resonance impedance spectroscopy (**Table 4.3**). The red-shaded area in (a-c) marks the region where the $Q_{31}^{R/AR}$ values fall below 20 % of the initial value. The electromechanical coefficients in (d-o) were fitted by a second-order polynomial (**Equation (4.5)**), intercept, linear (ξ), and quadratic (ϑ) coefficients are depicted in the figures. Please note that the samples were measured until mechanical fracture, limiting the vibration velocity range to 2.6 m/s. Q_{31}^{R} exhibits a significant stronger change than d_{31}, k_{31}, s_{11}^{E}, ε_{33}^{T} and determines the vibration velocity dependence of FOM^{HP}.

Table 4.3. Small-field electromechanical coefficients (Q_{31}^{R}, Q_{31}^{AR}, d_{31}, k_{31}, s_{11}^{E}, ε_{33}^{T}) and high-power figure of merit (FOM^{HP}, **Equation (4.6)**) of the transverse (31) vibration mode at 20 °C, determined by resonance impedance spectroscopy. Piezoelectric coefficient (d_{33}) measured by Berlincourt meter.

	Hard PZT$_T$ (PIC181)	**Medium-hard PZT$_T$** (P4)	**Soft PZT$_T$** (PIC151)
Resonance quality factor Q_{31}^{R} [-]	2313	505	89
Antiresonance quality factor Q_{31}^{AR} [-]	2702	551	101
Piezoelectric coefficient $-d_{31}$ [pm/V]	121	106	226
Coupling coefficient k_{31} [-]	0.34	0.31	0.38
Elastic compliance s_{11}^{E} [10^{-12} m²/N]	11.6	12.2	16.1
Dielectric permittivity ε_{33}^{T} [-]	1195	1066	2542
Figure of merit FOM^{HP} [m²/kVs]	0.93	0.17	0.06
Piezoelectric coefficient d_{33} [pm/V]	283	273	552

The soft PZT$_T$ exhibits the expected lowest small-field Q_{31}^{R} and Q_{31}^{AR} values, but substantially larger d_{31}, k_{31}, s_{11}^{E}, and ε_{33}^{T} values. Both trends are related to the ferroelectric-softening, which was exposed before by the small coercive electric field and a broad strain hysteresis (**Figure 4.3**). The material demonstrates also a severe decrease of Q_{31}^{R} and Q_{31}^{AR} and a pronounced increase of k_{31}, d_{31}, s_{11}^{E}, and ε_{33}^{T} at large vibration velocity, with noticeably larger decreasing and increasing slopes than the other two compositions.

To consider all coefficients simultaneously, a high-power figure of merit (FOM^{HP}) was derived based on **Equation (2.48)**:

$$FOM^{HP} = \frac{-d_{31}}{\sqrt{s_{11}^{E} \cdot \rho}} \cdot Q_{31}^{R}. \tag{4.6}$$

The FOM^{HP} determines the vibration velocity generation at a given electric field amplitude in resonance and is displayed in **Figure 4.7p-r** as a function of vibration velocity (small-field values are listed in **Table 4.3**). The initially large small-field FOM^{HP} values rapidly decrease at large vibration velocity. The rapid decrease of the FOM^{HP}s obviously resembles the decrease of the Q_{31}^{R} at large vibration velocity, which is not equivalently compensated by an increase of d_{31}.

4.1.4. Electromechanical high-power properties of rhombohedral Pb(Zr,Ti)O$_3$

The high-power properties of the four characteristic rhombohedral PZT$_R$ compositions are shown in **Figure 4.8**. The electromechanical coefficients Q_{31}^{R}, Q_{31}^{AR}, d_{31}, k_{31}, s_{11}^{E}, and ε_{33}^{T} as well as the FOM^{HP} are given as a function of vibration velocity at room temperature. The small-field Q_{31}^{R} and Q_{31}^{AR} values increase with increasing Fe^{3+}-doping concentration and decrease with Nb^{5+}-doping, which is the expected effect of hard- and soft-doping (**Table 4.4** and **Figure 4.8a-d**, please note the different scales). The values of PZT$_R$-0.5Fe increase by a factor of around 3 and decrease by a factor of 2 in PZT$_R$-1Nb, as compared to undoped PZT$_R$. The influence of the chemical modification on Q_{31}^{R} and Q_{31}^{AR} is enourmous and significantly larger than on the other electromechanical coefficients.

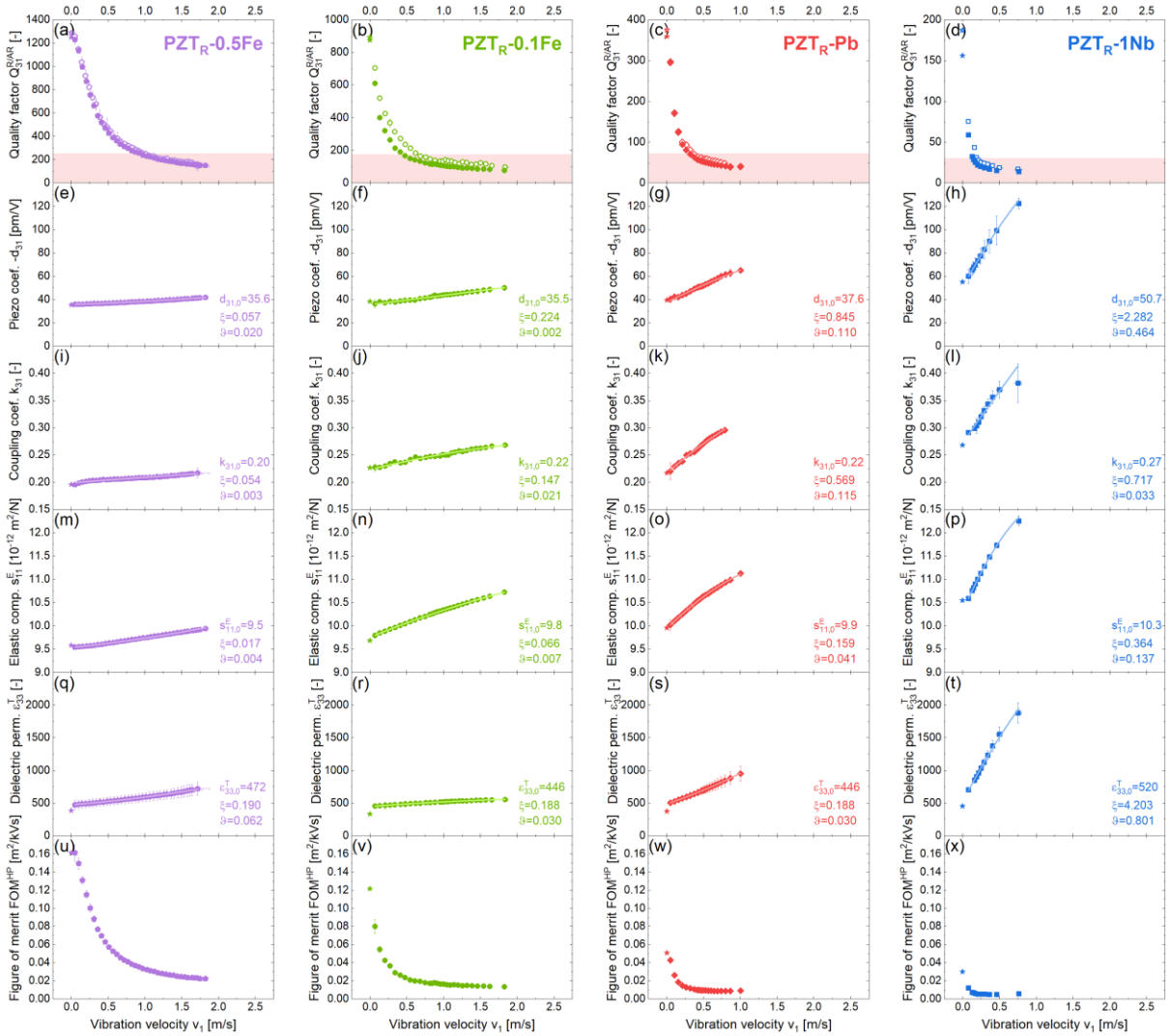

Figure 4.8. Electromechanical coefficients (a-d) Q_{31}^{R} (solid symbols) and Q_{31}^{AR} (open symbols), (e-h) d_{31}, (i-l) k_{31}, (m-p) s_{11}^{E}, (q-t) ε_{33}^{T} and (u-x) high-power figure of merit (FOM^{HP}, **Equation (4.6)**) of the four investigated PZT$_R$ compositions in the transverse (31) vibration mode as a function of vibration velocity (v_1) at 20 °C. The data points denoted as stars at 0 m/s depict the small-field values determined from resonance impedance spectroscopy (**Table 4.4**). The red-shaded area in (a-d) marks the region where the $Q_{31}^{R/AR}$ values fall below 20 % of the initial value. The electromechanical coefficients in (d-o) were fitted by a second-order polynomial (**Equation (4.5)**), intercept, linear (ξ), and quadratic (ϑ) coefficients are depicted in the figures. Q_{31}^{R} exhibits a significant stronger change than d_{31}, k_{31}, s_{11}^{E}, ε_{33}^{T} and determines the vibration velocity dependence of FOM^{HP}.

Despite the significant variation of the small-field values, all compositions exhibit a qualitatively similar vibration velocity dependence. Q_{31}^{R} and Q_{31}^{AR} rapidly decrease and stabilize with increasing vibration velocity, which was similarly observed in the PTZ$_T$ compositions (**Figure 4.7**). The largest decrease slope appears already at small vibration velocities below 1 m/s, without an apparent threshold. Quantitatively, the slope and the residual Q_{31}^{R} and Q_{31}^{AR} values increase with Fe^{3+}-doping concentration and decrease with Nb^{5+}-doping. The different slopes can be quantified by the vibration velocity at which the Q_{31}^{R} drops to 20 % of the initial value, which was determined to be 0.95 m/s, 0.45 m/s, 0.31 m/s, and 0.14 m/s from PZT$_R$-0.5Fe to PZT$_R$-1Nb (**Figure 4.8**). Same applies to Q_{31}^{AR}, since Q_{31}^{R} and Q_{31}^{AR} did not exhibit a noteworthy dispersion in none of the composition.

Table 4.4. Small-field electromechanical coefficients (Q_{31}^{R}, Q_{31}^{AR}, d_{31}, k_{31}, s_{11}^{E}, ε_{33}^{T}) and high-power figure of merit (FOM^{HP}, **Equation (4.6)**) of the transverse (31) vibration mode at 20 °C, determined by resonance impedance spectroscopy. Piezoelectric coefficient (d_{33}) measured by Berlincourt meter.

	PZT_R-0.5Fe	**PZT_R-0.1Fe**	**PZT_R**	**PZT_R-1Nb**
Resonance quality factor Q_{31}^{R} [-]	1248	874	359	156
Antiresonance quality factor Q_{31}^{AR} [-]	1287	890	374	187
Piezoelectric coefficient $-d_{31}$ [pm/V]	35	38	39	55
Coupling coefficient k_{31} [-]	0.20	0.23	0.22	0.27
Elastic compliance s_{11}^{E} [10^{-12} m²/N]	9.6	9.7	10.0	10.5
Dielectric permittivity ε_{33}^{T} [-]	385	332	372	449
Figure of merit FOM^{HP} [m²/kVs]	0.16	0.12	0.05	0.03
Piezoelectric coefficient d_{33} [pm/V]	103	116	119	170

The small-field values of the coefficients d_{31}, k_{31}, s_{11}^{E}, and ε_{33}^{T} decrease with Fe^{3+}-doping and increase with Nb^{5+}-doping (**Table 4.4**). However, the variation between the compositions is comparatively small. All coefficients increase fairly linearly as a function of vibration velocity. Here, they reveal a significant difference in the slope, which increases substantially from PZT_R-0.5Fe to PZT_R-1Nb (**Figure 4.8e-t**).

The resulting FOM^{HP}s (**Equation (4.6)**) of the PZT_R compositions are shown in **Figure 4.8u-x**. The values are largest in PZT_R-0.5Fe and smallest in PZT_R-1Nb (**Table 4.4**) in the entire vibration velocity range, demonstrating that the increase of d_{31}, k_{31}, s_{11}^{E}, and ε_{33}^{T} by soft-doping cannot compensate for the small Q_{31}^{R} values. In all compositions FOM^{HP} rapidly decreases with increasing vibration velocity, which resembles the course of Q_{31}^{R} and is not compensated by increase of d_{31}.

4.1.5. Discussion and conclusions

These general observations demonstrate that the high-power properties and stability are predominantly dictated by the behavior of Q_{ij}, which is subjected to substantially greater changes than any other coefficient. It highlights the dominant and decisive role of Q_{ij} for the high-power sustainability of materials and underlines the fundamental detriment of the state-of-the-art PZT compositions, independent of the crystal structure or chemical modification. It is crucial to differentiate between the absolute values and the relative change at large vibration velocity to uncover the mechanisms.

(1) Small-field $Q_{31}^{R/AR}$ values exhibit a significantly more pronounced variation through compositional changes, i.e., softening and hardening, than any other coefficient (d_{31}, k_{31}, s_{11}^{E}, or ε_{33}^{T}). It will be emphasized later that also other parameters, such as temperature, have an explicitly larger influence on Q_{ij} than on the other electromechanical coefficients. This opens up the opportunity to tune and maximize the high-power performance easier and in a much broader range by considering the material's quality factor with equal importance as, for example, the piezoelectric coefficient (**Figure 2.12**).

(2) However, the extreme sensitivity leads also to the severe decrease of $Q_{31}^{R/AR}$ already at comparatively low vibration velocities in all PZT compositions. It turns out that the ferroelectric hardening strongly increases the small-field $Q_{31}^{R/AR}$ values but has little impact on the stability of $Q_{31}^{R/AR}$ at large vibration velocity, i.e., on the slope of $Q_{31}^{R/AR}$ decrease. Vice versa, the increasing slope of the piezoelectric, mechanical, and dielectric coefficients is effectively suppressed. Moreover, the decrease is similar in PZT_T and PZT_R, a considerable dependence on the crystal structure is not evident. To emphasize this finding, the relative change of Q_{31}^{R} with increasing vibration velocity, given as $Q_{31}^{R}/Q_{31}^{R,0}$, is mapped in **Figure 4.9a**. The clustering of all compositions underlines the very similar vibration velocity dependence, despite the significant variation of the absolute $Q_{31}^{R/AR}$ values of the hard and soft ferroelectrics. The clustering holds true also under consideration of previously reported PZT compositions [27, 155]. To quantify the similarity of the Q_{31}^{R} decrease, the relative change of Q_{31}^{R} was fitted by an exponential expression (**Equation (4.13)**), origin of the expression will be derived in detail in Section 4.2.1), shown for hard and soft PZT_T in **Figure 4.9b**. Under consideration of the threshold range of hard PTZ_T (Section 4.1.3), the two materials reveal notably similar attenuation coefficients χ, independent of the large Q_{31}^{R} difference. It appears that the vibration velocity dependence of $Q_{31}^{R/AR}$ is determined by intrinsic material properties, with no essential improvement through hardening. This general observation is directly extendable to other ferroelectric systems and will be accentuated in Section 5.1 on $(Na_{0.5}Bi_{0.5})TiO_3$-based compositions that exhibit a very similar clustering but a significantly different vibration velocity dependence. It will be demonstrated that the rapid decrease of $Q_{31}^{R/AR}$ is not a general behavior of all ferroelectrics and that high-power properties differ between materials much stronger than within a material system.

(3) The high-power properties of piezoceramics are best expressed by the high-power figure of merit determined by several electromechanical coefficients. However, the absolute values as well as the stability at large vibration velocity are dictated by Q_{31}^{R} due to its sensitivity and extensive variation range. Subsequently, FOM^{HP} is prone to a substantial decrease at comparatively low vibration velocity (<1 m/s) that cannot be equivalently compensated by an increase of the other coefficients (**Figure 4.7** and **Figure 4.8**). The hard PZT compositions exhibit large FOM^{HP} values throughout the entire vibration velocity range. However, the weak high-power stability is apparently a fundamental characteristic and deficit of PZT-based materials, independent of the rhombohedral or tetragonal crystal structure and ferroelectric softening or hardening. The severe decrease diminishes the strain amplification in resonance, limiting the maximum vibration velocity and power output and thus the application of these materials in high-power devices. The decrease of Q_{31}^{R}, which is inversely proportional to the increase of the total loss, leads also to strong self-heating (Section 4.6.4) and eventually thermal depolarization of the material.

(4) It is evident that the material's small-field properties do not represent its high-power properties, while the strong non-linearity prohibits an extrapolation of the small-field values to large vibration velocity, which is surprisingly nevertheless still common practice. Please note that the measured vibration velocity range was limited to about 2.6 m/s. This limit determined the average vibration velocity of samples' fracture, which will be elaborated in more detail in Section 5.1.

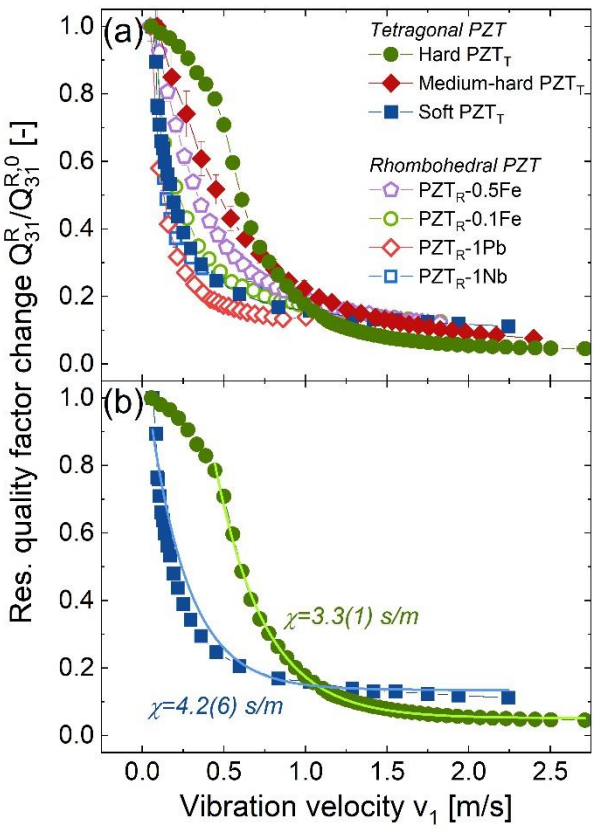

Figure 4.9. (a) Relative change of the resonance quality factor ($Q_{31}^R/Q_{31}^{R,0}$) as a function of vibration velocity (v_1). The PZT$_T$ and PZT$_R$ compositions cluster, exhibiting a very similar Q_{31}^R change, determined by the properties of the basic material and independent of the small-field Q_{31}^R values, i.e., independent of ferroelectric hardening/softening and crystal structure. (b) Q_{31}^R change of hard PZT$_T$ and soft PZT$_T$ is quantified by an exponential expression (**Equation (4.13)**), revealing similar attenuation coefficients (χ) despite a large difference of the Q_{31}^R values.

The manifold increase of the small-field Q_{31}^R and Q_{31}^{AR} values and the decrease of d_{31}, k_{31}, s_{11}^E, and ε_{33}^T through ferroelectric-hardening implies that the Q_{ij} increase is closely correlated with the reduced motion of domain walls, which is the most significant extrinsic strain contribution and largest origin of loss in PZT. Specifically, the Q_{ij} increase or the decrease of loss, respectively, must be correlated to the reduction of the out-of-phase component of domain wall motion with respect to the in-phase component, which usually deduces from the transition from (irreversible) domain wall displacement to (reversible) domain wall bending[xii]. Acceptor-doping is not expected to have a noticeable impact on the intrinsic strain contribution, i.e., the pure piezoelectric properties, nor on the intrinsic loss. Subsequently, the decrease of Q_{31}^R with increasing vibration velocity must be the consequence of rapidly increasing magnitude and strain contribution from domain wall motion. It follows that the domain pinning strength and the stabilization of the domain configuration by the introduced defects and defect complexes reduce rapidly with increasing vibration velocity. This result is consistent with the conclusions of earlier studies (e.g. [12]); however, it pends to be proven by direct experimental observations, which will be elaborated in the next Section 4.2.

[xii] A more distinct differentiation between the domain wall motion components and the reversible/irreversible domain wall displacement will be elucidated in Sections 4.4 and 4.5.

4.2. X-ray diffraction analysis

The excellent piezoelectric properties and electromechanical coupling of ferroelectrics originate from a combination of the inherent crystal lattice anisotropy (intrinsic contribution or pure piezoeffect) and the presence of ferroelectric/ferroelastic domains (extrinsic contribution). External perturbations, such as electric field or mechanical stress, affect the ferroelectric system in two ways: They distort the crystal lattice and initiate a domain wall vibration or movement, exerting a driving force on the domain walls by favoring a specific polarization/strain direction. The motion of non-180° domain walls (separate regions with a relative polarization vectors angle unequal 180°, Section 2.3) contributes thereby significantly to the induced electromechanical strain. The contribution can reach up to 50 % of the generated strain, depending on the domain wall mobility [78]. The mobility is determined by the potential landscape and altered, among others, through chemical doping. Thereby, domain wall motion (reversible and irreversible) is also the predominant source for nonlinearity, hysteresis, and loss [38, 68]. Since the quality factor designates the inverse of the total loss in the material, the values must inherently be related to the domain wall mobility. The defect-generated pinning of the domain walls in acceptor-doped (Mn^{3+} and Fe^{3+}) hard ferroelectrics revealed a significant increase of Q_{31}^{R}, demonstrating the enormous impact of the domain wall mobility on the quality factor (**Figure 4.7** and **Figure 4.8**) [66, 68, 69]. Following this mechanism, it was deliberated above that the decrease of Q_{31}^{R} at large vibration velocity must be related to increasing domain wall motion.

However, this long-standing argument [155] is not as straightforward as it might appear. It should be noted that the majority of the Q_{31}^{R} change occurs already at comparatively low vibration velocity. Driving the materials at those vibration velocities requires only low electric field amplitudes, well below the coercive field or the pinning-depinning transition [212]. For example, the majority of Q_{31}^{R} decrease (80 %) in the hard PZT_T (PIC181) occurs below 1 m/s (**Figure 4.7**). Driving the sample at this vibration velocity requires a field of 10 V/mm, which is only 0.6 % of the coercive field (**Table 4.1**). Such small driving electric fields are not expected to induce a significant motion of domain walls. Thus, a direct proof of domain wall motion under resonance drive is required, as well as a correlation to the decreasing Q_{31}^{R} values.

A XRD-based experimental approach was introduced to study the structural changes and the microscopic origins of the large electromechanical strain response and vibration velocity at the piezoelectric resonance (methodology and experimental details were introduced in Section 3.2). The high-power piezoelectric burst-excitation measurements were combined with time-resolved high-energy in-situ x-ray diffraction and stroboscopic data acquisition. The simultaneous macro-and microscopic observations in real-time provided a direct insight into the mechanisms of domain wall motion and lattice strain during resonance drive and delivered a correlation to the quality factor change at large vibration velocity. The results were supported by FEM simulations. The study was exemplarily carried out on the hard and soft PZT_T.

4.2.1. Microscale strain contribution as a function of vibration velocity

The strain contributions from the lattice and the motion of non-180° domain walls were determined at different vibration velocities. **Figure 4.10** exhibits the Q_{31}^{R} of hard and soft PZT_T as a function of vibration velocity measured during the x-ray irradiation, where the red squares mark the selected representative vibration velocities. Please note that the Q_{31}^{R} values are overall

lower as compared to the results in **Figure 4.7a,c**, which is not related to the x-ray irradiation but to the frequency dependence of Q_{31}^{R}, which will be elucidated in Section 4.3. Samples with a lower resonance frequency were used in the diffraction study to increase the x-ray exposure time and thus the recorded intensity. The Q_{31}^{R} is shifted to lower values without a noticeable change of the vibration velocity dependence; thus, the diffraction results are assumed to be generally valid, independent of the frequency.

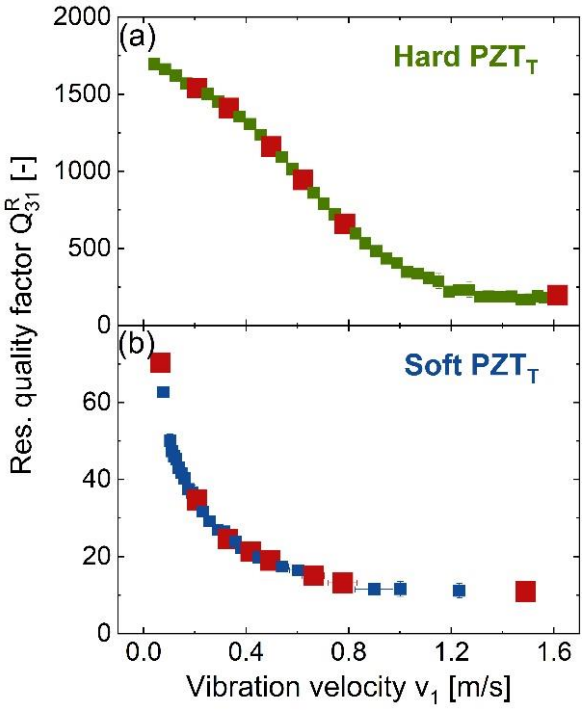

Figure 4.10. Resonance quality factor in transverse length mode (Q_{31}^{R}) as a function of macroscopic edge vibration velocity (v_1). The maximum electric field amplitudes (E_3^{max}) were 40 V/mm (hard PZT$_T$) and 120 V/mm (soft PZT$_T$). Red points mark the conditions at which the diffraction experiments were conducted.

Time-dependent evolution of XRD pattern

At every vibration velocity, the sinusoidal strain cycle was divided into time-segments to resolve the evolution of the XRD pattern (**Figure 3.6a**). An individual 2D diffractogram was recorded stroboscopically during each time-segment (**Figure 3.6b**). The Debye-Scherer rings of every diffractogram were subsequently sectioned over the azimuthal angle (α) and radially integrated over the diffraction angle (θ, Section 3.2). In **Figure 4.11** the time-dependent evolution of the XRD patter was reconstructed exemplarily for hard PZT$_T$ at 1.6 m/s and soft PZT$_T$ at 1.5 m/s. Shown are the azimuthal 90°-segments. $\alpha = 90°$ is equivalent to the x_1-direction (**Figure 3.6b**), the direction of largest strain amplitude in the transverse (31) vibration mode; poling and driving applied fields are applied in the x_3-direction, which is equivalent to $\alpha = 0°$.

hkl-lattice strain and domain switching fraction

The orientation- and time-dependent *hkl*-lattice strain ($S_{i,hkl}$) was determined from the lattice spacing, i.e., from the 2θ-peak position change with respect to the zero-field unpoled state, according to

$$S_{hkl} = \frac{\sin(\theta'_{hkl})}{\sin(\theta_{hkl})} - 1. \tag{4.7}$$

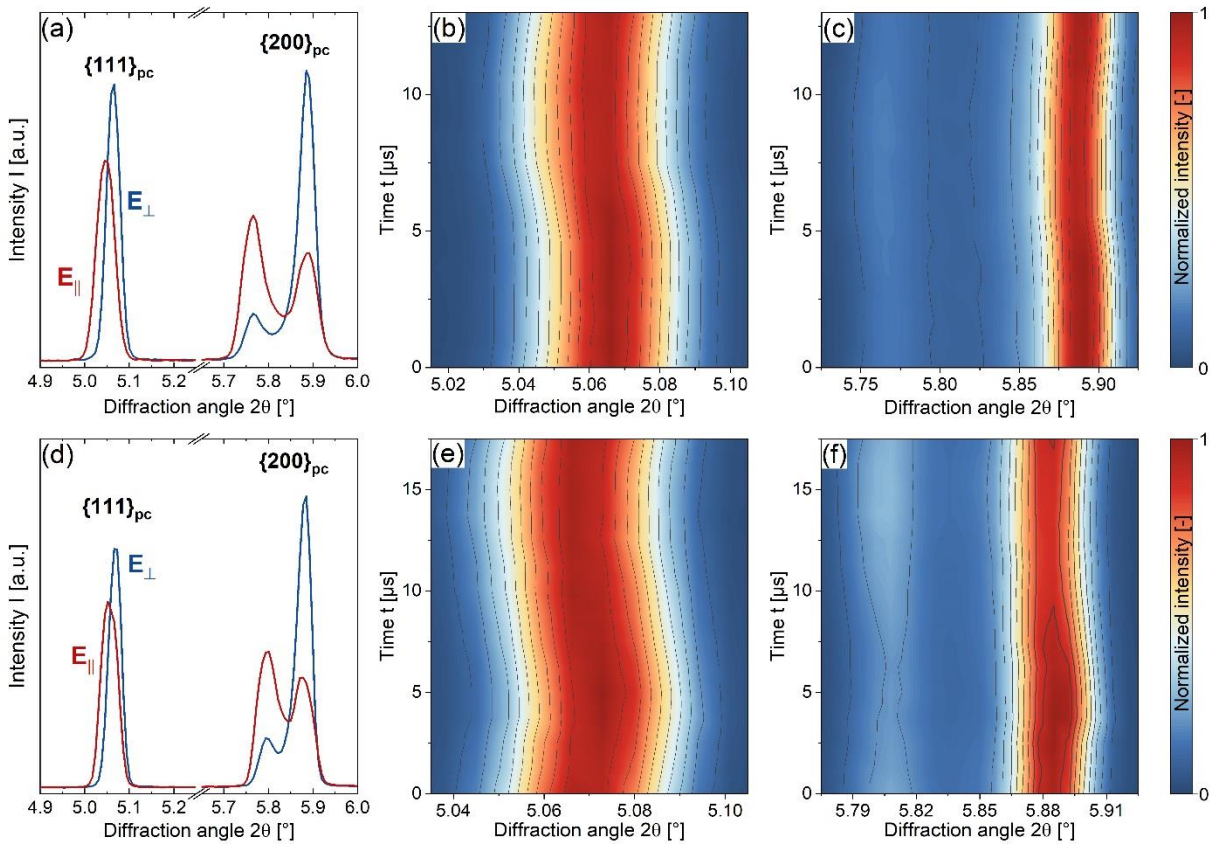

Figure 4.11. Diffractograms of polarized (a) hard PZT_T and (d) soft PZT_T feature the $\{111\}_{pc}$ and $\{200\}_{pc}$ peaks parallel to the polarization and applied electric field direction and perpendicular to the applied field in the direction of the largest strain amplitude in the transverse vibration mode (31). The $\{002\}_{pc}/\{200\}_{pc}$ splitting depicts the tetragonal distortion and polarization-induced texturing. The reconstructed diffractogram sections highlight the time-dependent evolution of the $\{111\}_{pc}$ and $\{200\}_{pc}$ peaks perpendicular to the applied electric field in (b,c) hard PZT_T and (e,f) soft PZT_T during the resonance vibration at 1.6 m/s and 1.5 m/s, respectively. The time scale depicts a single vibration cycle and represents all periodic cycles, during which the intensity was stroboscopically acquired and integrated.

The orientation- and time-dependent fraction of non-180° domains (tetragonal 90° domains) that switched their polarization was determined from the intensity interchange of the $\{002\}_{pc}/\{200\}_{pc}$ double peak with respect to the zero-field unpoled state as [198]

$$\eta_{002} = \frac{I_{002}/I'_{002}}{I_{002}/I'_{002} + 2\, I_{200}/I'_{200}} - \frac{1}{3}. \tag{4.8}$$

In case of a rhombohedral crystal structure the switching fraction ($\eta_{i,111}$) is determined from the $\{111\}_{pc}/\{11\bar{1}\}_{pc}$ double peak and expressed in terms of

$$\eta_{111} = \frac{I_{111}/I'_{111}}{I_{111}/I'_{111} + 3\, I_{11\bar{1}}/I'_{11\bar{1}}} - \frac{1}{4}. \tag{4.9}$$

In all cases, θ_{hkl} and I_{hkl} represent the hkl peak position and intensity in the poled state and under load, while θ'_{hkl} and I'_{hkl} represent the respective values of a virgin unpoled sample and zero-field.

The calculation was carried out for every time-segment of the vibration cycle (time-dependence) and every azimuthal section of the 2D diffractogram (direction-dependence). By

that, the evolution of θ_{hkl} and I_{hkl} under electric field cycling (**Figure 4.11**) was transferred into time-dependent S_{hkl} and η_{hkl}. Subsequently, the time-dependence was resembled by a sinusoidal fit to extract the amplitude of *hkl*-lattice strain (ΔS_{hkl}) and the amplitude of domain switching ($\Delta\eta_{hkl}$, **Figure 4.14**) during resonance vibration at every probed vibration velocity.

Table 4.5. Labeling of the utilized strain coefficients, grouped by the experimental methods adopted for their determination.

Strains measured by XRD	
$\boldsymbol{S_{i,hkl}}$ & $\boldsymbol{S_{i,lattice}}$	Individual *hkl* plane strain and total lattice strain
$\boldsymbol{\eta_{i,hkl}}$ & $\boldsymbol{S_{i,non-180°}}$	Domain switching fraction and total strain contribution from non-180° domain wall motion
$\boldsymbol{S_{i,XRD}}$	Total sample center strain determined from XRD
Strains measured by laser vibrometer	
$\boldsymbol{S_{i,el}}$	Electromechanically induced strain
$\boldsymbol{S_{i,mech}}$	Mechanically induced strain
$\boldsymbol{S_{i,HP}}$	Total vibration strain (sample average)
$\boldsymbol{S_{i,HPmax}}$	Total vibration strain (center maximum)
Strain calculated by FEM simulation	
$\boldsymbol{S_{i,FEM}}$	FEM simulated strain

The calculated strains of the individual *hkl*-lattice plains at different vibration velocities are given in an polar representation (**Figure 4.12**). The radius of the polar plot corresponds to the lattice strain amplitude in the x_1-direction (90° section to the applied electric field, **Figure 3.6b**), which is the direction of the largest strain in the 31-mode. The angle φ corresponds to the angle between the strain direction and the tetragonal polar axis [001] of the lattice. The lattice strains vary noticeably depending on the crystallographic orientation.

At low vibration velocities, the largest strain amplitudes appear in the {002} lattice plains. At large vibration velocities, however, particularly in soft PZT_T at 1.5 m/s, the maximum strain is generated in the {202} lattice plains instead of the {002} lattice plains, which has been similarly reported under off-resonance conditions [192]. Different mechanisms were discussed to explain the orientation-dependent distortion. Theoretical models for tetragonal perovskites based on the Landau-Ginzburg-Devonshire theory predict a maximum strain along and minimum strain across the polarization direction [001] in case of an extender ferroelectric [62, 213]; a distortion around 45° is predicted for rotator ferroelectrics. Thus, the distortion might indicate an increasing rotation instead of extension of the polarization vector during resonance vibration. Another source for distortion are inter-/intragranular interactions between lattice strain and domain wall motion [77, 192]. The increasing distortion at large vibration velocity would thus be the first indicator for increasing domain wall motion. A concluding deconvolution of the mechanisms is not possible at this point. A qualitatively equivalent lattice strain distribution is also observed in the x_3-direction (α=0° section).

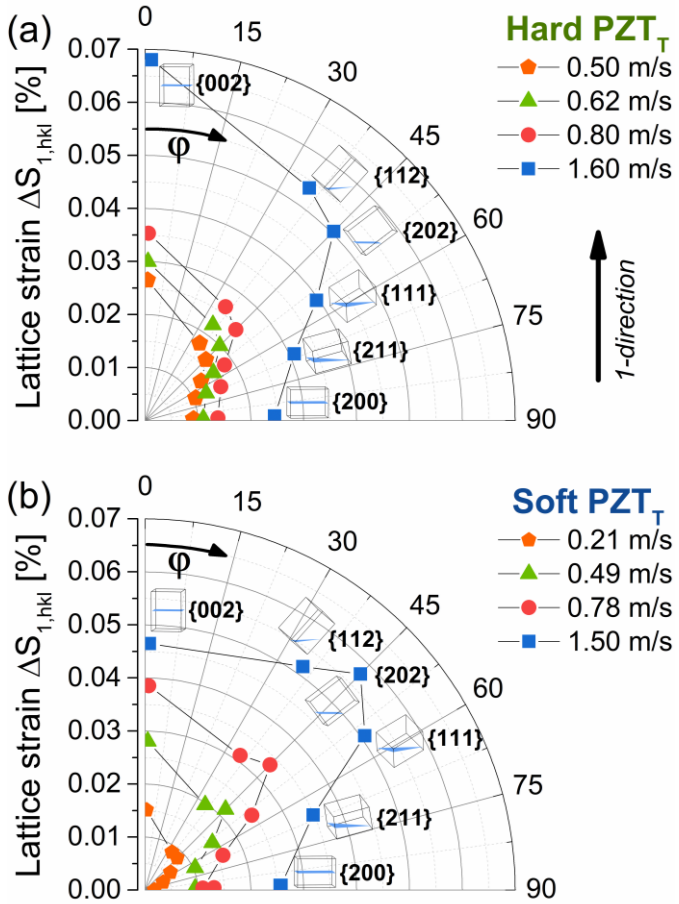

Figure 4.12. Strain of individual *hkl*-lattice planes at different vibration velocities. The radius corresponds to the strain amplitude in the x_1-direction ($\Delta S_{1,hkl}$); φ denotes the angle between the tetragonal polar axis [001] and the strain direction. The inserted tetragonal unit cells represent the crystallographic orientation of grains and domains in real space, with the *hkl*-plane perpendicular to the vibration direction.

The amplitude of domain wall motion is depicted in **Figure 4.13**, expressed by the fraction of switching domains during resonance vibration at different vibration velocities. The fraction is plotted over the azimuthal angle, demonstrating that the majority of domain switching occurs in grains with a pseudocubic [001] orientation parallel and perpendicular to the applied electric field. Less switching occurs for orientations between these two extremes, due to unfavorable orientation and is zero at angles between 35-45°. The detected $\Delta\eta_{002}$ values reach up to 0.040, or 4 %. This is small compared to domain switching fractions observed during electrical poling, which can exceed 30 % [191]. However, the range is comparable to values measured under subcoercive off-resonance loading at much larger electric fields [190, 214]. Moreover, it confirms domain wall motion during resonance vibration. $\Delta\eta_{002}$ is larger in the direction perpendicular to the electric field ($\alpha = 90°$) than parallel to the electric field ($\alpha = 0°$), which is opposite under off-resonance conditions, confirming that the driving forces are largest perpendicular to the electric field in the transverse vibration mode. Most importantly, however, is that the domain switching fraction is larger in soft PZT_T than in hard PZT_T, and that it increases with increasing vibration velocity.

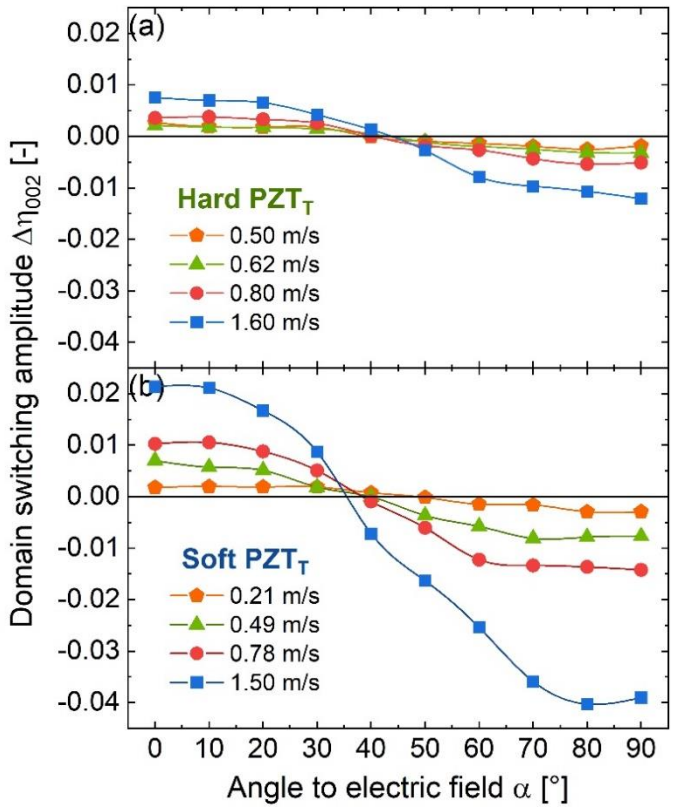

Figure 4.13. Domain switching amplitude ($\Delta\eta_{002}$) as a function of angle to the applied electric field (α) at different vibration velocities in (a) hard PZT$_T$ and (b) soft PZT$_T$. Largest $\Delta\eta_{002}$ appears perpendicular to the electric field in the main strain direction of the (31) transverse vibration mode and increases at large vibration velocity.

It is also important to note that the time-evolution of η_{002} can be accurately replicated by the above-mentioned sinusoidal fit. **Figure 4.14** depicts exemplarily η_{002} ($\alpha = 90°$) of the hard and soft PZT$_T$ vibrating at 1.6 m/s and 1.5 m/s, respectively, and the corresponding fit. η_{002} is symmetric during electric field or strain increase and decrease even in soft PZT$_T$, indicating a predominantly reversible domain wall motion. Irreversible domain wall motion would expose a distortion of η_{002} during electric field decrease as compared to the increase. However, it should be noted that irreversible domain wall motion is substantially smaller than reversible domain wall motion in the small-field regime [93, 99]. It is likely that the measurement resolution is not sufficient to separate these two contributions.

Lattice and domain wall strain contributions

The convoluted total lattice strain ($S_{i,lattice}$) was calculated by a weighted sum of seven crystallographic plane strains ($\{111_{pc}\}$, $\{002_{pc}\}$, $\{200_{pc}\}$, $\{022_{pc}\}$, $\{220_{pc}\}$, $\{211_{pc}\}$, and $\{112_{pc}\}$) using the Voigt approximation [199], where p_{hkl} is the texture factor and m_{hkl} the multiplicity factor of individual planes:

$$S_{lattice} = \frac{\sum_{hkl} p_{hkl} m_{hkl} \Delta S_{hkl}}{\sum_{hkl} p_{hkl} m_{hkl}}. \tag{4.10}$$

The total strain contribution from non-180° domain wall motion ($S_{j,non-180°}$) was calculated using a volume-weighted average of the lattice distortion of the domains and the domain switching amplitude over the entire orientation space [198, 200]

$$S_{non-180°} = \frac{(c-a)}{a} \sum_{i=1}^{n} 3\, \Delta\eta_{002}(\alpha_i)\, cos^2\alpha_i\, [\cos(\alpha_i + \Delta\alpha) - \cos(\alpha_i - \Delta\alpha)]. \tag{4.11}$$

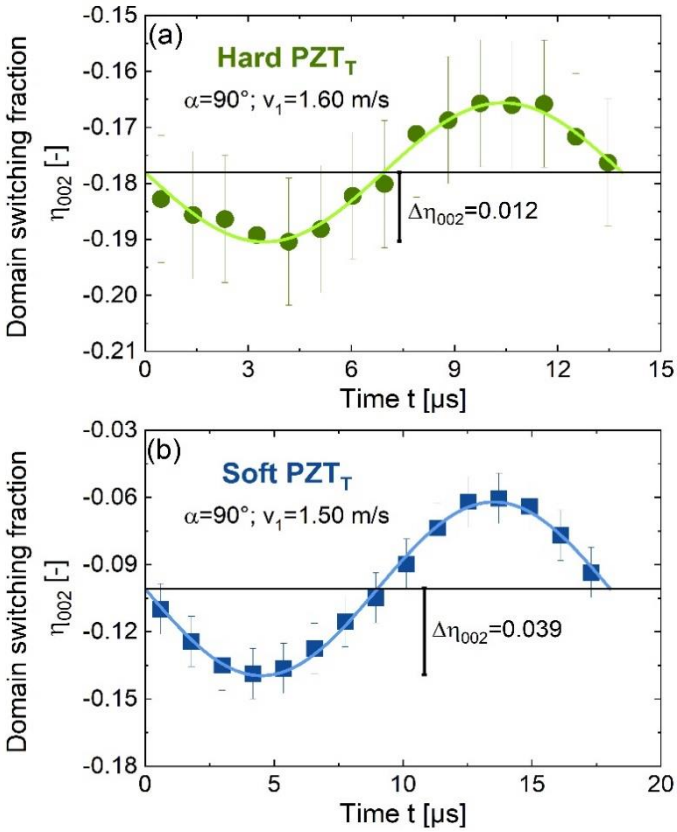

Figure 4.14. Time-dependence (t) of the domain switching fraction (η_{002}) in the x_1-direction ($\alpha = 90°$) in (a) hard PZT$_T$ and (b) soft PZT$_T$ at maximum vibration velocity of 1.60 m/s and 1.50 m/s, respectively. The solid line depicts the sinusoidal fit with the domain switching amplitude $\Delta\eta_{002}$ (compare to **Figure 4.13**). The symmetric time-evolution of η_{002} indicates a predominantly reversible domain wall motion, noticeable irreversible domain wall switching is not observed.

Here, a and c are the tetragonal lattice parameters, $cos^2\alpha_i$ accounts for the strain transformation in the orientation space, and $[\cos(\alpha_i + \Delta\alpha) - \cos(\alpha_i - \Delta\alpha)]$ accounts for the solid angle nonlinearity in a discrete data set [200]. $\Delta\alpha$ is the half-width of the azimuthal intervals and equal to 5°.

In case of a rhombohedral crystal structure, the strain is calculated utilizing the hkl-lattice spacing (d_{hkl}) according to

$$S_{non-180°} = \frac{(d_{111} - d_{11\bar{1}})}{d_{11\bar{1}}} \sum_{i=1}^{n} 4\, \Delta\eta_{111}(\alpha_i)\, cos^2\alpha_i\, [\cos(\alpha_i + \Delta\alpha) - \cos(\alpha_i - \Delta\alpha)]. \qquad (4.12)$$

The finally determined transverse strains S_1 (⊥ electric field) and longitudinal strains S_3 (∥ electric field) are shown in **Figure 4.15** as a function of vibration velocity. The decrease of Q_{31}^R with increasing vibration velocity in both materials is obviously accompanied by an increase of the lattice strain and the strain contribution from domain wall motion. Both strain contributions are largest in the x_1-direction, confirming the transverse (31) vibration as the largest-amplitude mode in the used resonator geometry. The comparison of both materials reveals lower $S_{i,non-180°}$ values in hard PZT$_T$ as well as a shallower increase of $S_{i,non-180°}$ with increasing vibration velocity, which can be associated with the introduced ferroelectric hardening and stabilization of the domain structure. The $S_{lattice}$ values are comparable in both materials.

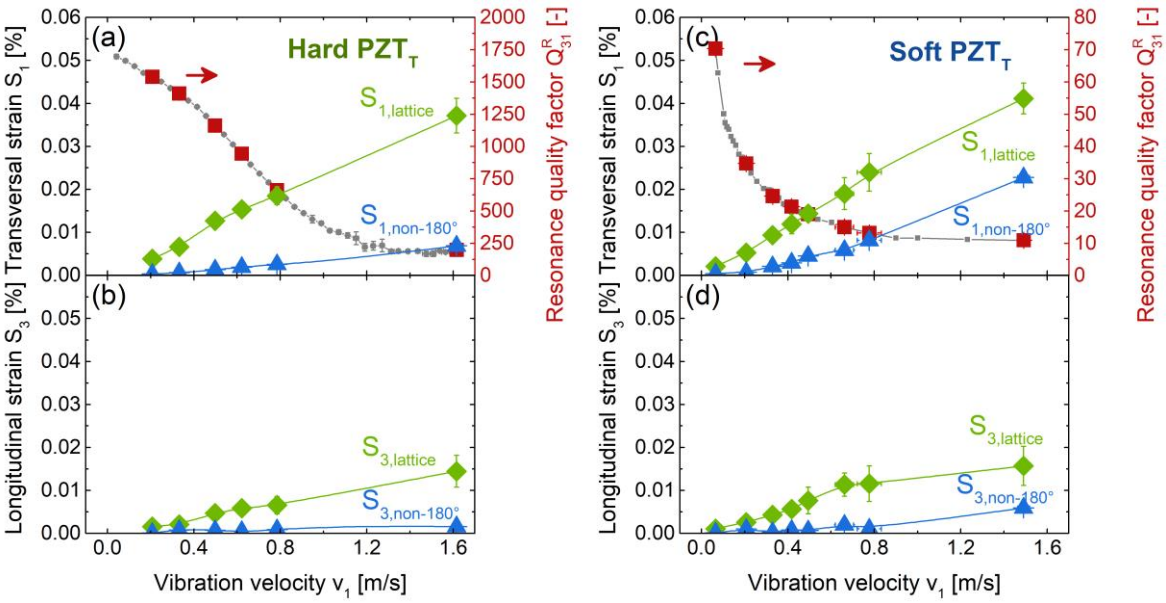

Figure 4.15. Resonance quality factor (Q^R_{31}) and the strain contributions from lattice distortion ($S_{i,lattice}$) and non-180° domain wall motion ($S_{i,non-180°}$) as a function of vibration velocity (v_1) for (a,b) hard PZT$_T$ and (c,d) soft PZT$_T$. (a,c) illustrate the transverse strains (S_1) perpendicular to the applied electric field in the main strain direction of the (31) vibration mode. (b,d) show the longitudinal strains (S_3) parallel to the applied electric field.

Macroscale vs. microscale strain

In order to verify the strain values determined by XRD, they are compared to the macroscopic strain measured with the laser vibrometer (**Figure 3.6**). The total strain determined from the XRD data ($S_{i,XRD}$) and the macroscopic transverse strain measured at the edge of the sample ($S_{i,HP}$; high-power measurement) are depicted in **Figure 4.16**. Note that $S_{i,XRD}$ is the sum of the two contributions $S_{i,lattice}$ and $S_{i,non-180°}$ [19]. Other extrinsic strain contribution, like phase transitions [215], were not detected.

Figure 4.16a,b illustrates that $S_{1,XRD}$ is larger than $S_{1,HP}$ in the entire vibration velocity range. This difference can be explained by considering the FEM model of the sample's internal mechanical strain and stress distributions (**Figure 4.16c**) and the different measurement positions on the sample. The simulation of the hard PZT$_T$ sample in resonance vibration at 0.6 m/s edge vibration velocity demonstrates that the strain and stress amplitudes in x_1-direction exhibit a sinusoidal distribution with a maximum at the center of mass of the vibrating sample. This is in accordance with the theoretical distribution of a fundamental harmonic (**Figure 2.4**), as opposed to a quasi-static electric field, which induces a homogeneous strain distribution over the entire sample length.

Thus, $S_{1,XRD}$, which was measured in the high-strain region in the sample's center (**Figure 3.6**), is naturally larger than $S_{1,HP}$, which was determined at the sample's edge, representing the average strain over the entire sample. The theoretical ratio of $\pi/2$ (~1.57) between the maximum and average values of a sinusoidal distribution is in good agreement with the $S_{1,XRD}/S_{1,HP}$ ratio denoted in **Figure 4.16a,b** by blue squares. Also the FEM simulation of the hard PZT$_T$ gives a center strain value (S_{FEM}, star symbol in **Figure 4.16a**), which is in good agreement with $S_{1,XRD}$. The good agreement of the macroscopic and microscopic scale as well as the simulation validates the correctness of the introduced strain measurement method through XRD analysis.

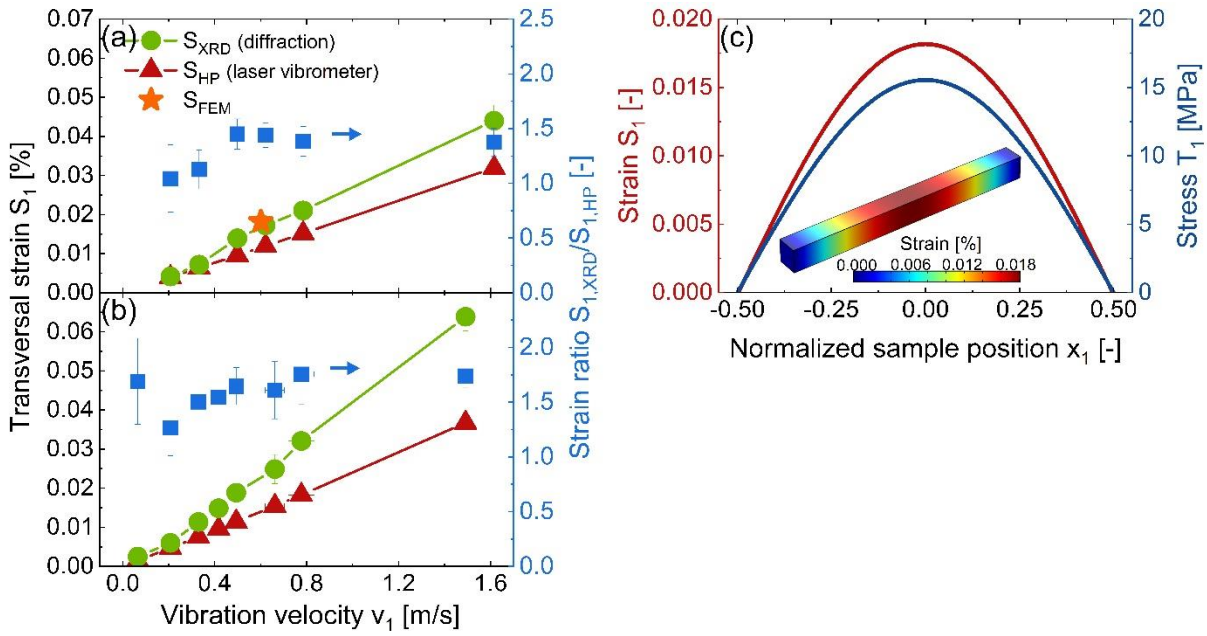

Figure 4.16. Transverse strain (S_1) versus the vibration velocity (v_1) of (a) hard PZT$_T$ and (b) soft PZT$_T$ obtained from the XRD measurement ($S_{1,XRD}$, sample center) and macroscopic high-power measurement with the laser vibrometer ($S_{1,HP}$, sample edge), and calculated from the FEM model ($S_{1,FEM}$, sample center), as well as the strain ratio ($S_{1,XRD}/S_{1,HP}$). (c) FEM sample model and traces of the transverse strain (S_1) and (von Mises) stress (T_1) amplitude distributions in x_1-direction over the hard PZT$_T$ normalized sample position at 0.6 m/s vibration velocity. The agreement between the macroscopic, microscopic, and simulated strain under consideration of the measurement position on the sample validates the XRD-based strain analysis.

Domain wall motion increase and quality factor decrease

Figure 4.15 illustrated that the domain wall motion generated strain increases at large vibration velocity. In addition, also the ratio $S_{1,non-180°}/S_{1,XRD}$ clearly increases at large vibration velocity, demonstrated in **Figure 4.17**. This means that not only the domain wall motion generated strain increases, but particularly its contribution portion to the total stain. Under the previously introduced assumption that the extrinsic strain generation is correlated with larger loss than the intrinsic strain generation, the increasing contribution of $S_{1,non-180°}$ to $S_{1,XRD}$ is the actual reason for the decrease of Q_{31}^R. Moreover, the ratio is significantly larger in soft PZT$_T$, explaining the inherently lower Q_{31}^R values. Note that the higher electric field amplitudes used for soft PZT$_T$ to achieve the same vibration velocity (soft PZT$_T$: $E_3^{max} = 120$ V/mm, hard PZT$_T$: $E_3^{max} = 40$ V/mm) cannot explain the observed difference in the strain contribution ratio, since they are still significantly lower than the coercive field (<10 %; **Table 4.1**). In general, the domain wall contribution (7 – 15% for hard PZT$_T$ and 12 – 35% for soft PZT$_T$) is slightly lower as compared to off-resonance conditions at lower frequencies [78, 190], which is likely the consequence of the frequency-dependent domain wall response [47, 62, 92] (Section 4.3).

Table 4.6. Exponential fitting parameters (**Equation (4.13)**) of the vibration velocity (v_1) dependent strain ratios ($S_{1,non-180°}/S_{1,XRD}$) depicted in **Figure 4.17**.

	B_{max} [%]	$B_{max} - B_0$ [%]	χ [s/m]
Hard PZT$_T$	18.5(2)	4.3(3)	0.98(3)
Soft PZT$_T$	42.4(7)	7.4(11)	1.08(5)

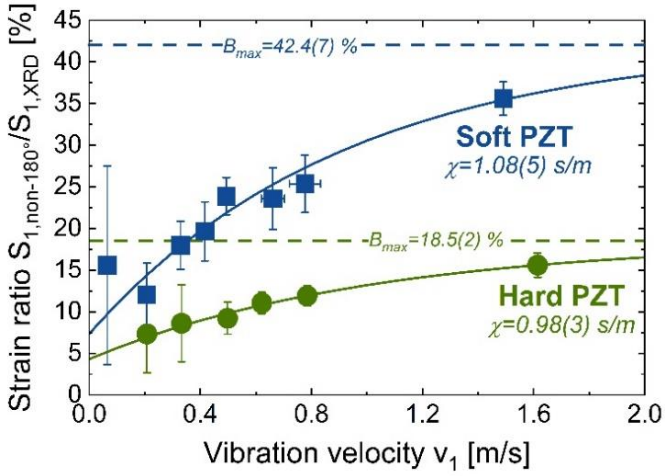

Figure 4.17. Strain ratio revealing the relative strain contribution from non-180° domain wall motion ($S_{1,non-180°}$) to the total strain determined by XRD measurement ($S_{1,XRD}$, sum of $S_{1,lattice}$ and $S_{1,non-180°}$). Continuous lines depict the exponential dependency (**Equation (4.13)**), while dashed lines indicate the determined saturation ratio.

The strain ratios of hard and soft PZT$_T$ increase nonlinearly and saturate at large vibration velocities, associating inversely with the evolution of Q_{31}^R (**Figure 4.10**). Moreover, a similar increase and saturation of the strain contribution from domain wall motion was observed under weak-field off-resonance conditions by macroscopic mechanical stress-dependent [93] and microscopic electric field-dependent [78] measurements. This behavior was described by the Rayleigh law and the motion of domain walls in an energy potential landscape [22] (Section 2.3.3). It is deliberated that the material behavior determined here is phenomenologically very similar; however, the formalism cannot be directly transferred, since the XRD analysis does not allow a clear deconvolution of reversible and irreversible non-180° domain wall motion. Therefore, it is suggested to describe the strain ratios (**Figure 4.17**) by an associated exponential relation

$$\frac{S_{non-180°}}{S_{XRD}} = B_{max} - B_0 e^{-\chi v}. \tag{4.13}$$

B_{max} determines the maximum achievable strain ratio of the material. It depicts the strain contribution from non-180° domain wall motion at very large vibration velocity, yet below the ferroelectric switching region, i.e., within the so-called Rayleigh regime [94]. The value is related to the stabilization of the domain configuration, e.g., by acceptor doping or other hardening mechanisms. $B_{max} - B_0$ determines the y-axis intercept at 0 m/s, i.e., the strain ratio at low vibration velocity. Other than in the Rayleigh formalism, the strain ratio does not decrease towards zero at zero vibration velocity, but approaches a finite value (reversible domain wall motion), since the strain contribution from all domain wall motion is considered, not only from the irreversible motion. Finally, χ is the attenuation coefficient and describes the increase in the strain ratio. $B_{max} - B_0$ is lower for hard PZT$_T$ as compared to soft PZT$_T$ (**Table 4.6**) and corresponds to the significantly larger small-field Q_{31}^R. B_{max} is significantly

lower in hard PZT_T as well, which is associated with the higher Q_{31}^R values at large vibration velocity. Note that the absolute differences should be treated carefully due to the increasing experimental uncertainty at low vibration velocity and the limited number of data points at large vibration velocity. Most interestingly, however, is the χ coefficient, which appears to be linked to the decrease of Q_{31}^R as a function of vibration velocity. Although the two PZT_T compositions reveal distinctly different Q_{31}^R values, the χ value is close to 1 s/m for both materials (**Table 4.6**). This indicates a very similar increase of the strain ratio and Q_{31}^R decrease with increasing vibration velocity, determined by the intrinsic properties of the basic tetragonal PZT_T, which has also been demonstrated in **Figure 4.9**.

4.2.2. Origin of domain wall driving force

Main feature of the piezoelectric resonance drive is the opportunity to induce large strain amplitudes with comparatively small electric fields by choosing exactly the resonance frequency as the driving frequency. It was demonstrated that the main contribution to the overall sample strain comes from the lattice (intrinsic contribution), while the smaller domain wall contribution (extrinsic contribution) increases at large vibration velocity and is presumably the decisive reason for the Q_{31}^R decrease. However, the utilized electric field amplitudes are unusually small to induce the observed lattices strain and especially the domain wall motion. Thus, to evaluate the role of the electric field, the evolution of the vibration velocity during a frequency down-sweep across the samples' resonance frequency at a constant electric field amplitude was tracked (**Figure 4.18**). The field amplitude was selected such that a peak vibration velocity of 0.8 m/s was reached at resonance.

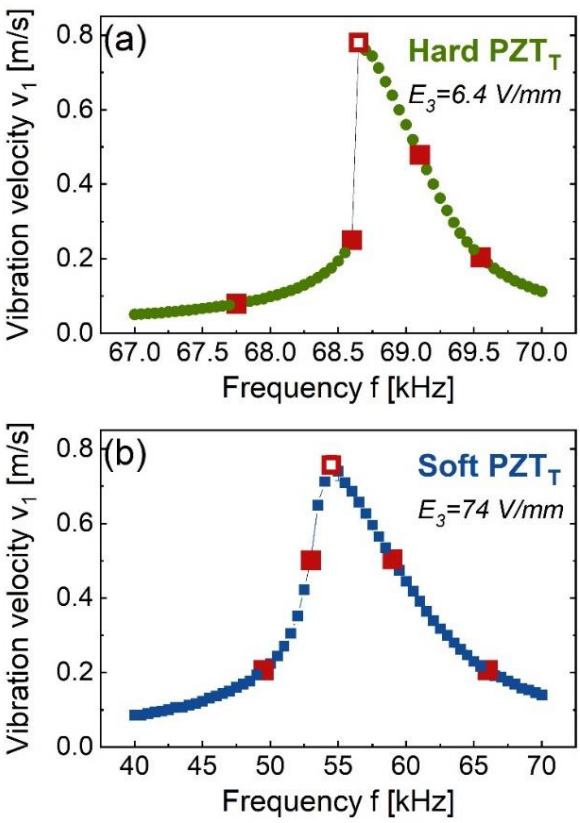

Figure 4.18. Vibration velocity (v_1) as a function of the driving frequency (f) at and around the samples' resonance frequency (f_R, indicated by open symbols) at constant electric field amplitudes (E_3) of 6.4 V/mm (hard PZT_T) and 74 V/mm (soft PZT_T). Measurements were done with decreasing frequency. Red points mark the conditions at which the XRD experiments were conducted.

Hard and soft PZT_T exhibit both an asymmetric vibration velocity peak, which directly correlates with the reported impedance asymmetry in frequency-dependent measurements (Section 3.1.1 and [12, 21, 216]). The asymmetry is especially pronounced in hard PZT_T, exhibiting characteristic peak distortion and hysteretic jump around the resonance frequency, caused by the nonlinear vibration velocity-dependence of the electromechanical coefficients.

$S_{1,lattice}$ and $S_{1,non-180°}$ were tracked at selected frequencies at and around the resonance frequency (**Figure 4.19**). Red symbols mark these frequencies in **Figure 4.18**. $S_{1,lattice}$ and also $S_{1,non-180°}$ are clearly enhanced at the resonance, although the applied electric field amplitude is the same for all measurement points. This experimentally confirms that there must be another stimulus at the resonance additional to the externally applied electric field that drives the domain wall motion and leads to the Q_{31}^{R} decrease. This is the dynamic mechanical stress that builds up in the sample around the resonance (**Figure 4.16c**).

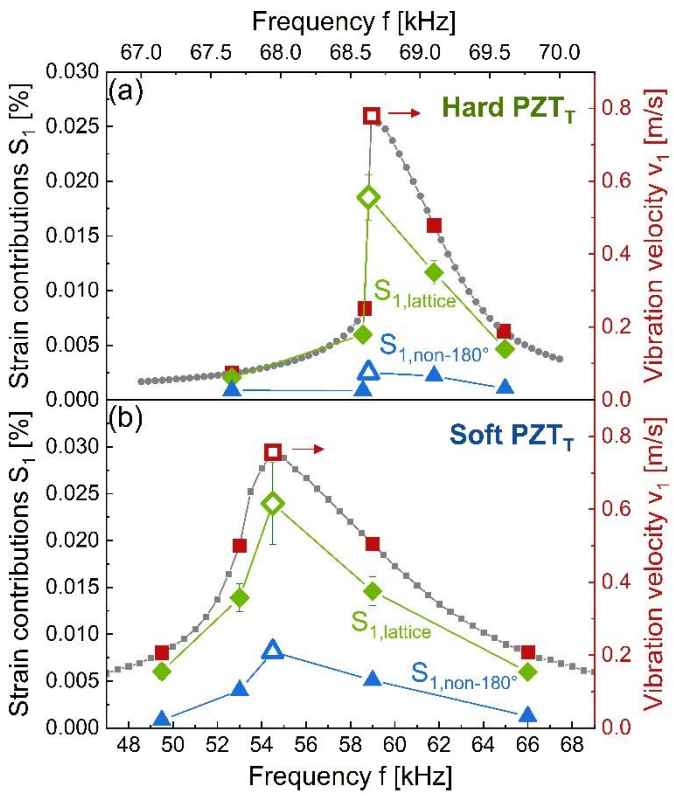

Figure 4.19. Lattice strain ($S_{1,lattice}$) and strain contribution from non-180° domain wall motion ($S_{1,non-180°}$), determined from the XRD measurement, in comparison to the vibration velocity (v_1), determined from pulse drive measurement, as a function of driving frequency (f) measured at and near the resonance frequency (f_R, marked by open symbols) for (a) hard and (b) soft PZT_T. Strain contributions exhibit a maximum at the resonance, although the electric field amplitude is constant throughout the measured frequency range.

Strain in piezoelectrics can be induced by the electromechanical coupling ($S_{1,el} = d_{31} \cdot E_3$) and mechanical stresses ($S_{1,mech} = s_{11}^{E} \cdot T_1$), as described by the constitutive **Equation (2.8)**. The contributions were evaluated by measuring the vibration velocity-dependent d_{31} and s_{11}^{E} coefficients using the high-power pulse drive measurement (**Figure 4.20b**). Both coefficients increase at large vibration velocity, indicating the previously discussed ferroelectric softening (Section 4.1.3). However, the calculated $S_{1,el}$, determined from the applied E_3 and the measured d_{31}, is about two orders of magnitude lower than the $S_{1,HP}$ (**Figure 4.20a**) and can be neglected, resulting in $S_{1,HP} \cong S_{1,mech}$. The measured $S_{1,HP}$ and s_{11}^{E} can thus be used to

calculate the average mechanical stress $T_{1,average}$ (**Figure 4.20c**). Additionally, the stress amplitude in the sample´s center, which we denote as maximum stress amplitude, $T_{1,max}$, can be calculated using the sample´s density, ρ [14]:

$$T_{1,max} = \sqrt{\frac{\rho}{s_{11}^{E}}}\, v_1. \tag{4.14}$$

Both stress amplitudes increase at large v_1, with the ratio $T_{1,max}/T_{1,average}$ being always close to $\pi/2$, which is the theoretical ratio of maximum and average values of a sinusoidal distribution. Additionally, the star in (**Figure 4.20c**) marks the $T_{1,max}$ value determined from FEM calculations at 0.6 m/s (**Figure 4.16c**), which correlates well to the experimental value. The stress amplitude values are in the range of up to 40 MPa, which is around 50 % of the coercive stress and sufficient to induce significant domain wall motion, which has been evidenced under off-resonance conditions [217].

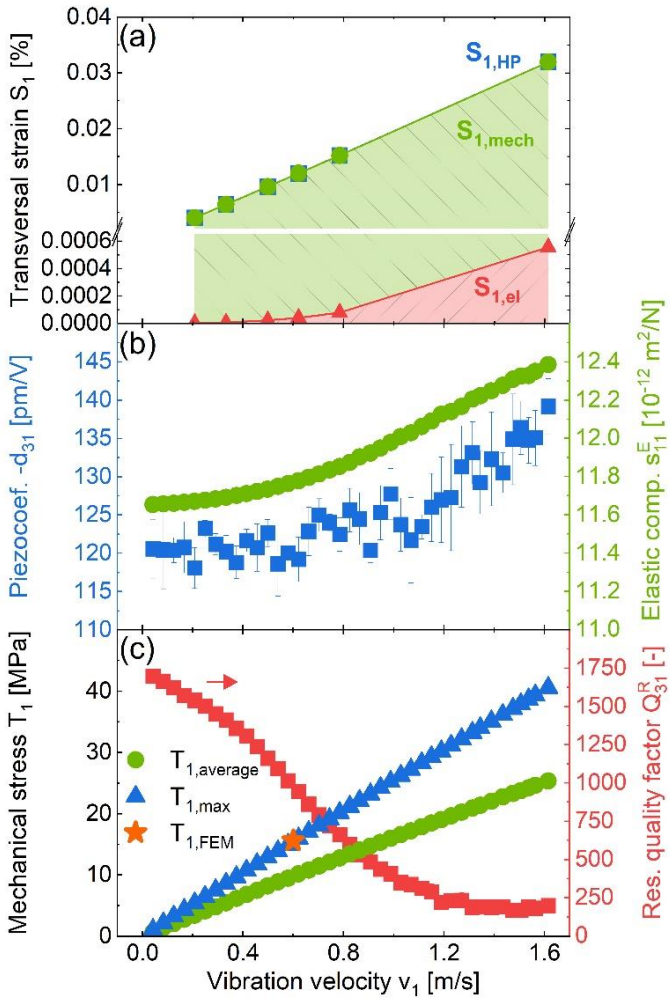

Figure 4.20. (a) Electromechanical ($S_{1,el}$) and mechanical transverse strain ($S_{1,mech}$), calculated from the piezoelectric coefficient and the elastic compliance utilizing the linear constitutive **Equation (2.8)**, as well as the total strain ($S_{1,HP}$), obtained from macroscopic pulse drive measurement with the laser vibrometer, as a function of the vibration velocity (v_1) in hard PZT$_T$. (b) Corresponding piezoelectric coefficient ($-d_{31}$) and elastic compliance (s_{11}^{E}) as a function of vibration velocity (v_1) for hard PZT$_T$. (c) Resonance quality factor (Q_{31}^{R}), determined from the pulse drive measurement, contrasted to the calculated average ($T_{1,average}$) and maximum ($T_{1.max}$) mechanical stress values in the sample and the FEM-simulated center stress value ($T_{1,FEM}$). Dynamic mechanical stress is the origin of the strain amplification in piezoelectric resonance, including the induced domain wall motion.

It can be concluded that in case of resonance drive, the electric field is used only as a stimulus to bring the sample into resonant vibration and to yield elastic energy through electromechanical coupling. However, the main contributor to the large vibration strain is the dynamic mechanical stress that builds up in a piezoceramic sample during resonance through the stored total elastic energy [218]. Besides producing a significant lattice strain, in perovskite ferroelectrics, this stress is also the main driving force for the movement of ferroelastic non-180° domain walls.

4.2.3. Conclusions

(1) A direct structure-property correlation between increasing domain wall motion and decreasing Q_{31}^{R} at high resonance vibration velocity has been revealed. The domain wall motion is accompanied by significant extrinsic loss. Consequently, the increasing share of domain wall motion contribution to the total generated strain results in a pronounced variation of the Q_{31}^{R} values, while other piezoelectric coefficients are reasonably constant over a wide range of vibration velocities. This provides direct structural evidence to confirm the long-standing hypothesis of the role of extrinsic contribution in the loss in piezoelectric resonance.

(2) By quantifying the strain contributions for the two PZT_T compositions, it was demonstrated that compositional modifications (acceptor/donor doping) change the domain wall generated strain contribution, as well as the Q_{31}^{R} values. However, the increase of the domain wall motion and the high-power stability of Q_{31}^{R} are determined by the properties of the basic material and can be characterized by the attenuation parameter χ. It is therefore proposed that the attenuation coefficient could be considered as a characteristic parameter for a general evaluation of a ferroelectric material's resistance against a Q_{31}^{R} decrease at large vibration velocity. It is expected that the high-power characteristic of material families can be generalized based on χ, which should be further experimentally confirmed.

(3) In contrast to off-resonance conditions, the applied electric field only triggers the vibration, while the emerging dynamic mechanical stress is the main driving force for the large vibration velocity and strain. The observed domain wall motion is thus the lattice's response to the stress by periodically switching the polar axis away from a direction of maximum compression and into a direction of maximum tension.

4.3. Frequency dependence of the quality factor

Experimental approaches and theoretical treatments of domain walls in several types of ferroic materials (electric or magnetic) led to two general predictions [62, 89]. One is the nonlinear dependence of the ferroelectric/ferroelastic and piezoelectric properties on the amplitude of applied electric field or mechanical stress, which follows the Rayleigh-law and describes the field-depend motion of the ferroelectric/ferroelastic domain walls through a defect generated potential landscape. The other is the logarithmic dependence of the properties on the field frequency, determined by the relaxation time of the involved mechanisms, including domain wall displacement or defect reorientation and hopping. While these dependencies are well investigated under sub-switching off-resonance conditions, comparably little is known about them under high-power piezoelectric resonance.

After demonstrating the field amplitude and vibration velocity dependency of the electromechanical properties (Section 4.1), their frequency dependence is investigated here. It is evaluated how the small-field values, as well as the vibration velocity dependence, evolve as a function of the resonance frequency. Under sub-switching off-resonance conditions, a distinct frequency-effect appears in the low-frequency Hz-range and diminishes typically above few kHz [61, 219], although domain wall contribution persists usually up to frequencies of around 10^9 Hz [220, 221]. Piezoelectric resonance frequencies are usually in the range of several kHz to several hundreds of kHz, thus a distinct frequency-effect is not necessarily expectable. However, the revealed sensitivity of Q_{ij} to even small changes of domain wall mobility might still lead to a pronounced frequency dependence.

The frequency-effect is an additional consideration in the mechanistic correlation between high-power properties and domain wall motion. Furthermore, it is a crucial boundary condition for the comparison of electromechanical properties in resonance between different materials and it is an important information for the applicability of the material in dedicated frequency ranges.

4.3.1. Resonance frequency

Under off-resonance conditions, the field-frequency can be chosen arbitrarily. However, under resonance drive, the field-frequency is restricted to the position of the resonance in the frequency spectrum. The resonance frequency of a piezoelectric element is determined by the material properties, the sample geometry, and the vibration mode. In the transverse (31) vibration mode the resonance frequency (f_R) results from the elastic compliance (s_{11}^E), density (ρ), and sample length (l) in the direction of maximum strain (x_1-direction) according to [28]

$$f_R = \frac{1}{\sqrt{4\rho s_{11}^E \cdot l}} = \frac{N_{11}^E}{l}. \tag{4.15}$$

N_{11}^E is the geometry independent frequency coefficient, but depends on the vibration velocity, due to the vibration velocity dependence of s_{11}^E (**Figure 4.7**). Thus, also f_R is a function of vibration velocity and usually decreases at large velocities. Both result from increasing ferroelectric softening at large vibration velocity, which was elaborated before (Sections 4.1 and 4.2). However, f_R can also be shifted by adjusting the sample's length, while width and thickness have no influence, as long as mode-determined site-ratios are obeyed [28].

4.3.2. Logarithmic frequency dependence

Using the high-power pulse drive method, hard PZT_T (PIC 181) samples in (31) geometry and different lengths between 8 mm and 30 mm were examined. The corresponding small-field resonance frequencies are depicted in **Table 4.7**. Q_{31}^R exhibits a severe decrease with increasing vibration velocity in all samples (**Figure 4.21a**). The decrease was discussed in detail before (Sections 4.1 and 4.2). More important here is that the sample's length increase and the subsequent f_R decrease induce a down-shift of the Q_{31}^R values over the entire vibration velocity range. The down-shift is not correlated with the sample's mass, since samples with a width variation but constant length and small-field f_R do not exhibit a distinct Q_{31}^R difference (**Figure 4.21b**). The shift appears to be correlated with the frequency.

Table 4.7. Geometry dependent small-signal resonance frequencies (f_R) of hard PZT$_T$ (PIC 181) samples.

Length x width x height [mm]	8x1x1	15x1x1	24x1x1	24x2x1	24x3x1	30x1x1
Resonance frequency f_R [kHz]	202.21	110.16	69.04	69.19	69.03	55.34

Figure 4.21c depicts the extracted Q_{31}^R values at low vibration velocity (at 0.04 m/s) and high vibration velocity (at 0.78 m/s) as a function of the resonance frequency. The Q_{31}^R values clearly increase for large f_R. Moreover, the frequency-dependence is represented by a logarithmic relation, which was originally introduced for the piezoelectric coefficient (modified after [96]):

$$Q_{31}^R(\omega_R) = Q_{31}^{R,0} - \psi \cdot ln\left(\frac{1}{\omega_R}\right), \tag{4.16}$$

where ω_R is the angular resonance frequency and ψ the logarithmic fitting parameter. ψ is larger at small vibration velocity than at large vibration velocity by a factor of about 4, which indicates a stronger frequency-dependence at small vibration velocity. This is also apparent in **Figure 4.21a,** which exhibits a larger dispersion of Q_{31}^R at small vibration velocity than at large vibration velocity. The logarithmic dependence evidences a similar type of frequency dependence as it was observed for the dielectric permittivity and piezoelectric coefficient [96, 222]. However, the logarithmic terms cannot be directly compared due to different driving conditions and frequency ranges. Nevertheless, following the same model, it can be concluded that the reversible and even more the irreversible domain wall motions are increasingly inhibited at large frequencies.

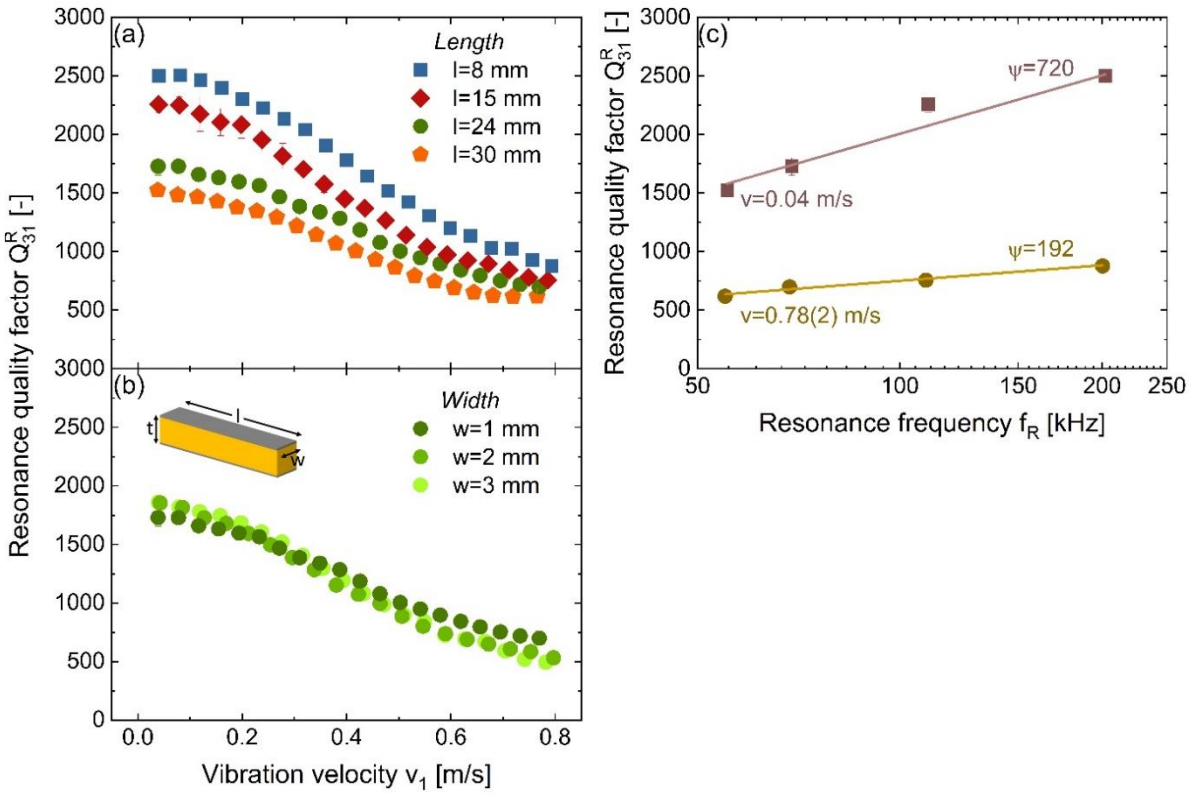

Figure 4.21. Hard PZT$_T$ resonance quality factor (Q_{31}^R) as a function of vibration velocity (v_1) measured at different resonance frequencies (f_R), which were determined by the sample (a) length and (b) width (**Table 4.7**). (c) Extracted Q_{31}^R values as a function of f_R at small (0.04 m/s) and large (0.78 m/s) v_1 and the corresponding logarithmic fit and logarithmic fitting parameter (ψ, **Equation (4.16)**). f_R decreases with increasing sample length, leading to a decrease of Q_{31}^R, which follows a logarithmic frequency dependence. Changes of the sample width have not impact.

However, the difference in the domain wall motion between the investigated resonance frequencies must be comparatively small. The piezoelectric coefficient does not exhibit a clear frequency-dependent change (**Figure 4.22a**). Also the elastic compliance reveals only a minor frequency dispersion, with a variation of less than 1 % (**Figure 4.22b**). In both cases, it can be assumed that the measurement uncertainty and variation between samples influence the values stronger than the frequency dependence itself.

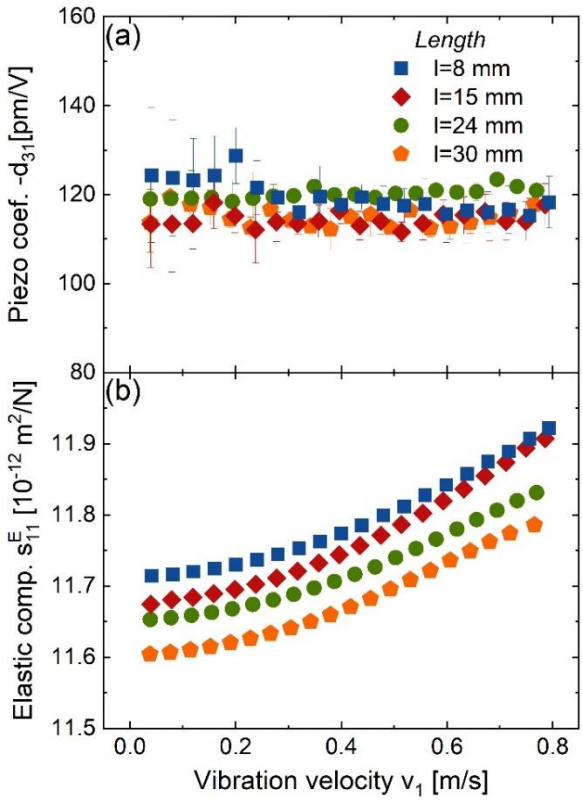

Figure 4.22. Hard PZT$_T$ (a) piezoelectric coefficient (d_{31}) and (b) elastic compliance (s_{11}^E) as a function of vibration velocity (v_1) measured at different resonance frequencies (f_R), which were determined by the sample length (**Table 4.7**). Both coefficients do not exhibit a distinct frequency dependence.

4.3.3. Frequency-dependent domain wall strain contribution

In order to confirm the correlation between the frequency-dependent change of Q_{31}^R and domain wall mobility, the contribution of the domain wall generated strain to the total strain was tracked using the in-situ high-energy XRD method (Section 4.2). **Figure 4.23** displays the Q_{31}^R values at 0.78 m/s as a function of f_R (adapted from **Figure 4.21c**) and the corresponding strain ratios $S_{1,non-180°}/S_{1,XRD}$. Please note that at all resonance frequencies the measurements were conducted at nearly equal vibration velocity, which implies equal strain states (**Equation (2.47)**) and validates the strain ratio comparison independent of the frequency. The strain ratio decreases with increasing frequency and correlates with the increasing Q_{31}^R, confirming the predicted reduced domain wall motion and contribution to the total strain. The reduced domain wall motion is compensated by an enhanced lattice strain, which experimentally required larger excitation electric field amplitudes to reach the same vibration velocity and strain amplitude. The strain ratio decrease is notable, but distinctly smaller than the experimental (instrumental) uncertainty and should thus be treated carefully. Further experimental confirmation is required, for example, at lower vibration velocities, where a more significant strain ratio variation is expected.

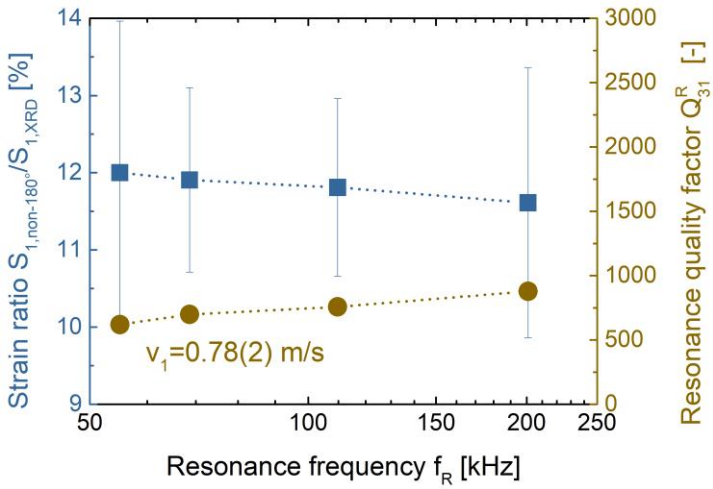

Figure 4.23. Hard PZT$_T$ resonance quality factor (Q^R_{31}) at vibration velocities of 0.78 m/s as a function of the resonance frequencies (f_R) (adopted from **Figure 4.21c**) and the corresponding strain ratio ($S_{1,non-180°}/S_{1,XRD}$) reveal the relative strain contribution from non-180° domain wall motion to the total strain determined by XRD measurement. Dashed lines are a guidance for the eye, depicting the correlation between increasing Q^R_{31} and decreasing domain wall strain contribution.

4.3.4. Conclusions

It was experimentally demonstrated that Q^R_{31} exhibits a distinct frequency dependence and increases with increasing resonance frequency following a logarithmic relation. The frequency dispersion is extensive at small vibration velocities and reduces at larger vibration velocities. It is concluded that the observed effect is related to the previously reported behavior of dielectric permittivity and piezoelectric coefficient in PZT-based poly-crystals, where, for example, the ε_{33} and d_{33} coefficients exhibit a logarithmic frequency dependence with the logarithmic term being dependent on the electric field and mechanical stress amplitude [61, 92, 96, 219, 222]. The effect obeys the general prediction for the field and frequency dependence of the domain wall pinning in ferroic systems [62, 89]. Therefore, the explanation of the effect can be based on the same mechanistic treatment. It follows that the increase of Q^R_{31} is correlated with a reduced domain wall motion and strain contribution at large frequency. Mainly, the (irreversible) out-of-phase component of the domain wall motion reduces, compared to the (reversible) in-phase component (Section 4.4). Origin of this frequency dependence is the relaxation time of the involved processes, i.e., the inertia of the domain wall displacement. The reduced domain wall motion was directly observed and confirmed by the XRD analysis. However, the observed change is small, which is likely associated with the investigated high-frequency regime. Therefore, the frequency dependency manifests mainly in the very sensitive quality factor, but has little effect on the piezoelectric coefficient or the elastic compliance.

Nevertheless, it must be noted that the quality factor convolutes all loss sources in the material. Despite the generally conclusive explanation based on domain wall mobility, other effects might also contribute to the frequency-dependence and need to be considered. While the intrinsic loss is not expected to reveal a distinct frequency dependence, conductivity and the effective dielectric loss are known to have a pronounced frequency dependence and to decrease at large frequencies [43]. To the author's knowledge, the role of the dielectric loss in piezoelectric resonance is not entirely understood yet and will be further elaborated in the subsequent section. In any case, the frequency is a crucial parameter to consider for a reliable and reproducible high-power characterization and comparison of materials and must not be neglected.

4.4. Temperature dependence of the high-power electromechanical properties

Temperature fundamentally impacts ferroelectric and electromechanical properties. Tracking the property evolution as a function of temperature allows to draw conclusions on mechanistic processes and to quantify characteristic temperatures, such as the ferroelectric-to-paraelectric transition (Curie temperature), depolarization, or structural transformation. Moreover, temperature dependence is an essential limiting factor for the material's operational range, particularly under high-power conditions. Not only the thermal loading during operation is limited (e.g., due to the vicinity to a heat source), but also a temperature increase at large vibration velocity is unavoidable due to the self-heat effect (Section 2.4.2). The maximum usable vibration velocity is thus limited by the material's temperature stability to avoid, for example, thermal depolarization or thermal run-away effects.

The temperature dependence of the electromechanical properties in resonance will be investigated in the following. The study focuses on the previously introduced tetragonal and rhombohedral PZT compositions and considers other acceptor-doped ferroelectric systems for comparison. First, the small-field electromechanical coefficients will be discussed. The values represent a cross-section through the material's temperature-vibration velocity landscape perpendicular to the vibration velocity axis. Afterwards, the vibration velocity dependence of the coefficients at selected temperatures will be analyzed, which is the cross-section perpendicular to the temperature axes. Finally, the entire temperature-vibration velocity landscape is reconstructed. The aim is to identify the parameters that determine and limit the high-power operation window of PZT-based compositions and to elucidate the responsible mechanisms.

4.4.1. Thermal stability of the electromechanical properties in tetragonal $Pb(Zr,Ti)O_3$

The evolution of the small-field electromechanical coefficients (Q_{31}^R, d_{31}, k_{31}, s_{11}^E) as a function of temperature was tracked by resonance impedance spectroscopy. Especially hard PZT_T revealed a significant temperature-dependence of Q_{31}^R (**Figure 4.24a** and **Figure 4.25a**), which is divided into three temperature ranges. Below 0 °C, Q_{31}^R exhibits a slight increase and a plateau with the largest Q_{31}^R values of the entire probed temperature regime. In the narrow range between 0 °C and 70 °C, the values drop by almost 80 % with an immense rate of -33/°C. Above 70 °C, Q_{31}^R decreases moderately and approaches 0 at around 300 °C, where the thermal depolarization process sets in. The piezoelectric coefficient increases continuously in the entire temperature range (**Figure 4.24d**), which is associated with the increase of the dielectric permittivity (**Supplemental Figure 7.9a,b**), since the coupling coefficient and the elastic compliance (slightly) decrease (**Figure 4.24g,j; Equation (2.12)**).

The medium-hard PZT_T reveals a very similar temperature behavior. Q_{31}^R strongly increases until 20 °C, followed by a broad plateau and a continuous decrease above 120 °C (**Figure 4.24b**). The difference of the Q_{31}^R values between the maximum at 120 °C and the two minima at the low and high temperature ends is significant, the values increase and decrease by a factor of 3.5. The piezoelectric coefficient and the elastic compliance increase upon heating, while the coupling coefficient decreases (**Figure 4.24e,h,k**). The three coefficients reveal distinct changes in the slopes. However, they do not exhibit a clear trend, which would mimic or correlate with the substantial increase and subsequent decrease of Q_{31}^R.

In contrast to the hard compositions, soft PZT_T displays an almost constant Q_{31}^R in a wide temperature range, with only a slight increase and subsequent drop in the vicinity of the thermal depolarization (**Figure 4.24c**). The piezoelectric coefficient increases with increasing temperature, while the coupling coefficient and the elastic compliance decrease (**Figure 4.24f,i,l**).

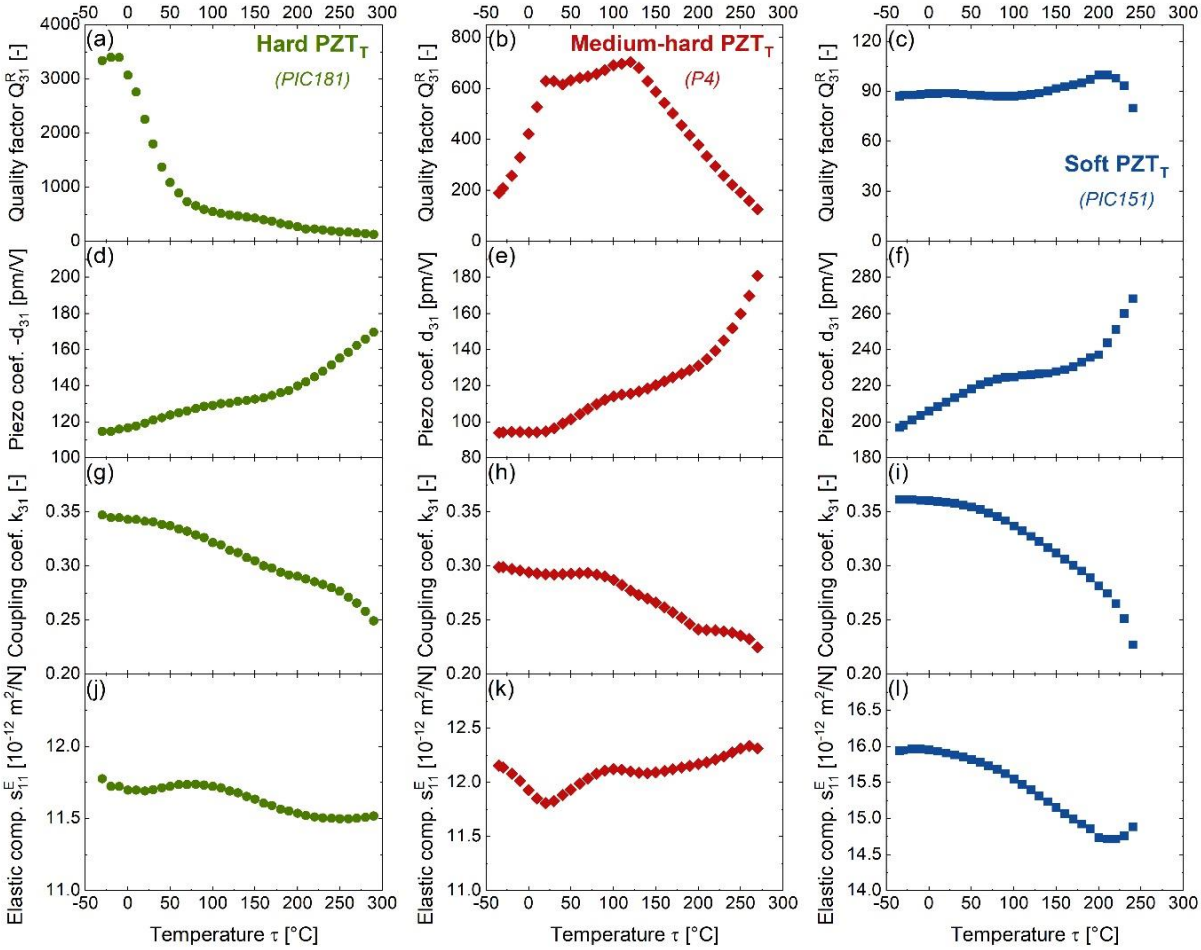

Figure 4.24. Small-field ($v_1 \rightarrow 0$ m/s) electromechanical coefficients (a-c) Q_{31}^R, (d-f) d_{31}, (g-i) k_{31}, and (j-l) s_{11}^E of the three PZT_T compositions in the transverse (31) vibration mode as a function of temperature (τ) during the first heating cycle after poling (note the different scales). Q_{31}^R reveals a distinctly different temperature-dependent behavior than the other coefficients, indicating the contribution of different processes to the thermal evolution of the coefficients.

Reversibility of thermally induced changes

The thermally induced changes of the electromechanical coefficients, particular the Q_{31}^R peak in the acceptor-doped PZT_T compositions, are in large part reversible upon heating and cooling (below depolarization temperature). **Figure 4.25** demonstrates the first three heating cycles of hard PZT_T after poling and aging. The Q_{31}^R peaks evolve in all cycles; however, the peak maximum shifts to higher temperature and decreases in magnitude. After the third cycle, further changes do not appear and the behavior becomes fully reversible upon consecutive heating and cooling. Also, the piezoelectric coefficient, the coupling coefficient, and the elastic compliance exhibit a reversible behavior and additionally "flatten" out. Distinct slope changes appear only during the first heating half-cycle and disappear already during the first cooling. Repetitive thermal cycling does not show any further changes. Since the other PZT_T compositions reveal

an equivalent behavior, it can be concluded that the temperature dependence of the electromechanical coefficients in PZT_T originates from reversible processes; irreversible changes are small and appear mainly during the first temperature increase, remaining irreversible contributions vanish latest after the third heating cycle. Thus, the Q_{31}^R peak in acceptor-doped PZT_T could potentially be engineered to the desired temperature range to maximize Q_{31}^R. To this end, the mechanistic origin of the peak is investigated in the following.

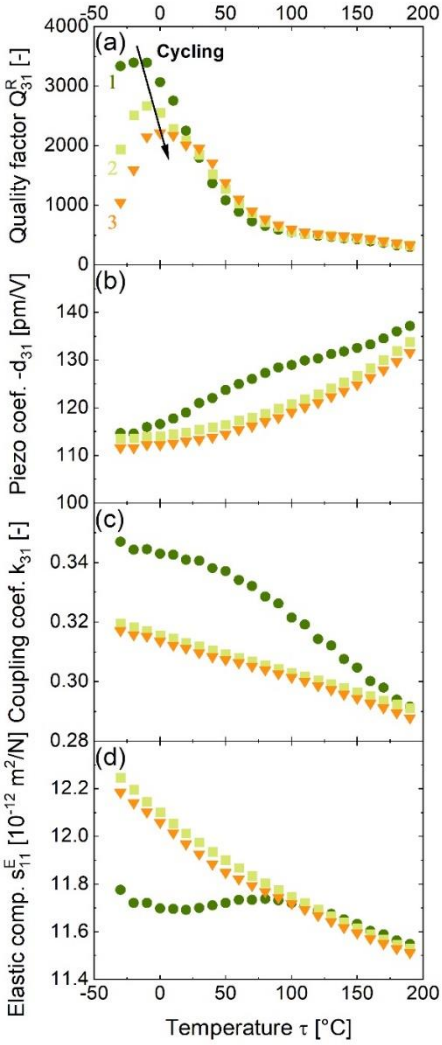

Figure 4.25. Small-field ($v_1 \rightarrow$ 0 m/s) electromechanical coefficients (a) Q_{31}^R, (b) d_{31}, (c) k_{31}, and (d) s_{11}^E of the hard PZT_T (PIC181) in the transverse (31) vibration mode as a function of temperature (τ) during the first three heating cycles after poling. The coefficients demonstrate pronounced reversibility; remaining irreversible changes terminate within the first three heating cycles.

4.4.2. Thermal stability of electromechanical properties in rhombohedral $Pb(Zr,Ti)O_3$

The electromechanical coefficients of PZT_R as a function of temperature are illustrated in **Figure 4.26**. The compositions reveal a qualitatively analogous temperature dependence to PZT_T. Hard PZT_R-0.5Fe exhibits a comparatively sharp Q_{31}^R peak with a maximum at around 110 °C. With the reduction of acceptor-doping concentration in PZT_R-0.1Fe and undoped PZT_R, the magnitude of the Q_{31}^R maximum reduces and the peak broadens over a wide temperature range. Soft PZT_R-1Nb shows an almost constant Q_{31}^R, with only a small increase at around 250 °C, which is in the vicinity of the thermal depolarization. The piezoelectric coefficient, the coupling coefficient, and the elastic compliance exhibit a similar temperature dependence throughout all

compositions. The coefficients increase nearly continuous with increasing temperature and do not display a distinct anomaly in terms of slope change, which would correlate with the profound temperature change of Q_{31}^{R}.

It is obvious that in the ferroelectrically hardened compositions of PZT_R and PZT_T, Q_{31}^{R} is subjected to a significant temperature dependence. In the softened compositions Q_{31}^{R} is almost constant throughout the entire temperature range. At the same time, the thermally induced changes of the piezoelectric coefficient[xiii], the coupling coefficient[xiv], and the elastic compliance are smaller in hard than in soft compositions. The occurrence of a distinct peak and the enormous change in Q_{31}^{R} is apparently associated with acceptor-doping, while the doping element and concentration influence the peak width and position. It must be pointed out that the emergence of a strong temperature dependence of Q_{31}^{R} is not limited to $Pb(Zr,Ti)O_3$, but also appears in other convention ferroelectrics such as Fe-doped $BaTiO_3$ (**Supplemental Figure 7.5**), as well as in relaxor-ferroelectrics like Zn-doped $(Na_{0.5}Bi_{0.5})TiO_3$-$BaTiO_3$ (**Figure 5.12**). The slope change from positive to negative indicates thereby that at least two processes with opposite temperature dependencies contribute to the observed behavior. The processes are, however, not clearly represented in d_{31}, k_{31}, and s_{11}^{E}, and will be further elucidated below.

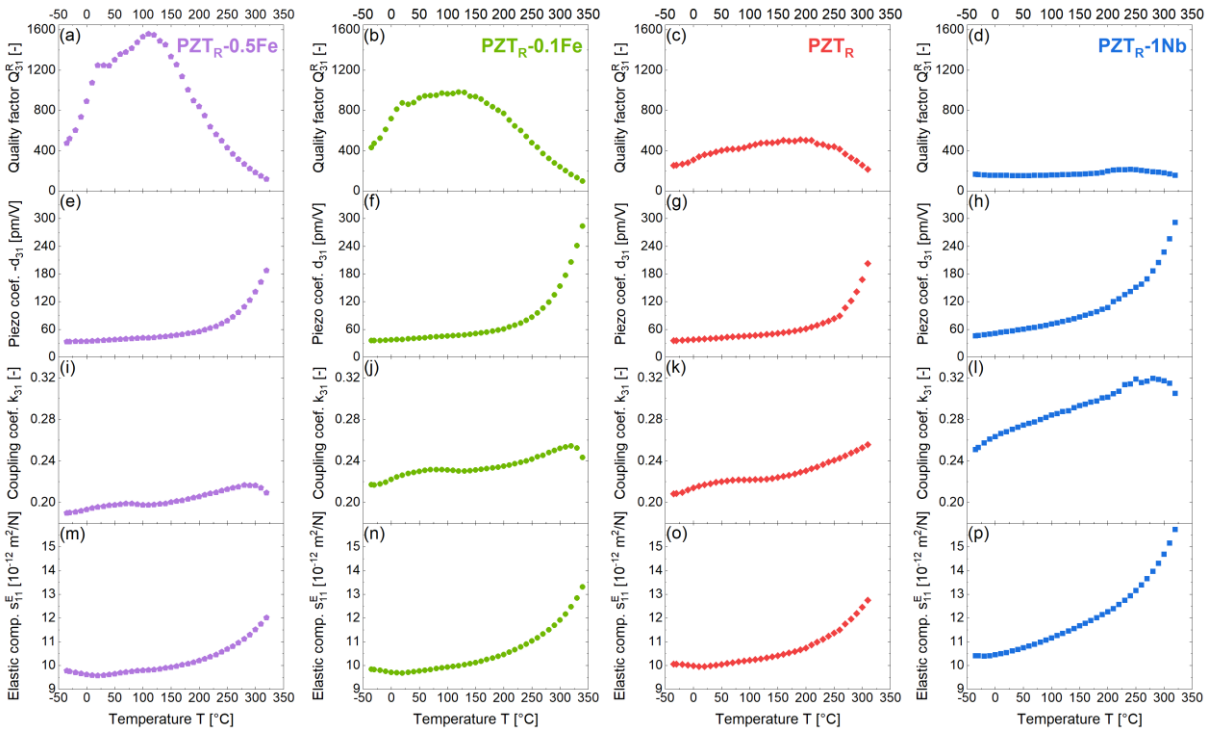

Figure 4.26. Small-field ($v_1 \rightarrow 0$ m/s) electromechanical coefficients (a-d) Q_{31}^{R}, (e-h) d_{31}, (i-l) k_{31}, and (m-p) s_{11}^{E} of the four PZT_R compositions in the transverse (31) vibration mode as a function of temperature (τ) during the first heating cycle after poling (note the different scales). The temperature-induced changes of Q_{31}^{R} are larger in the acceptor-doped compositions and increase upon doping concentration, while the temperature-induced changes of d_{31}, k_{31}, and s_{11}^{E} are vice versa larger after donor-doping.

[xiii] The d_{31} increase is correlated with the increase of ε_{33}^{T} (**Equation (2.12)**), which are both a consequence of enhanced domain wall motion due to thermal activation.

[xiv] k_{31} and s_{11}^{E} increase in PZT_R and decreases in PZT_T as a function of temperature. The reason for that is likely the inclination of the MPB in the compositional phase diagram. With increasing temperature, PZT_R approaches the MPB, while PZT_T shifts away from the MPB, which leads to a ferroelectric softening or hardening, respectively, correlated with the lattice distortion [43].

4.4.3. Origin of the quality factor temperature dependence

In order to reveal the origin of the strong temperature dependence of Q_{31}^{R}, the properties of the PZT_R compositions were further investigated by off-resonance methods. Those included polarization and strain hysteresis loops, Rayleigh-type and polarization harmonics measurements, as well as frequency and temperature-dependent dielectric permittivity tracking. These measurements should identify thermally-induced processes in the materials, which can be transferred back to rationalize the temperature dependence of the properties under resonance conditions. The study was carried out on the PZT_R compositions, since they are sufficiently far away from the morphotropic phase boundary to avoid the influence of mixed phases on the properties. It was discussed above that domain wall motion is a major loss source; therefore, the temperature dependence of the domain wall mobility is examined first.

An enlarged ferroelectric lattice distortion usually reduces the domain wall mobility [13, 59]. Therefore, x-ray patterns of the PZT_R compositions were recorded as a function of temperature to track the evolution of the rhombohedral distortion. Full range patterns at selected temperatures are shown in **Figure 4.27a** exemplarily for PZT_R-0.5Fe. The $\{111\}_{pc}$ and $\{200\}_{pc}$ peaks were extracted (**Figure 4.27b,c**) and fitted by the Gauss functions (**Equations (3.4)-(3.5)**) to calculate the lattice constant (b) and tilt angle (β) [197]. Both are given as a function of temperature in **Figure 4.27d,e** for all PZT_R compositions. The values scatter slightly due to the simple fit; however, it is evident that all compositions exhibit a continuously decreasing lattice constant[xv] and a reducing ferroelectric distortion upon heating, in terms of the tilt angle progressing towards 90° (paraelectric cubic phase). The ferroelectric-to-paraelectric phase transitions occur between 300 – 350 °C, evidenced by the extinction of the rhombohedral tilt (90°-β=0). The decreasing ferroelectric distortion suggests a continuous thermally induced ferroelectric softening of the compositions and increasing domain wall mobility, which correlates with the increase of d_{31}, k_{31}, and s_{11}^{E} and the decrease of Q_{31}^{R} at high-temperatures (above 110 °C, **Figure 4.26**). However, the result does not evidence any correlation to the pronounced increase of Q_{31}^{R} in the range between 20 – 110 °C, which was observed particularly for PZT_R-0.5Fe (**Figure 4.26a**).

In order to probe specifically the temperature dependence of the domain wall mobility and the domain wall pinning strength of the introduced defects, polarization and strain hysteresis loops were recorded at selected temperatures (**Supplemental Figure 7.6**). Mainly the measurement range between 20 – 150 °C was covered, where the increase and subsequent decrease of Q_{31}^{R} in the acceptor doped PZT_R compositions were detected (**Figure 4.26a,b**). Temperatures below 20 °C and above 150 °C were experimentally not accessible. All compositions exhibit a slimming of the polarization loops with increasing temperature and a decreasing asymmetry of the polarization and strain hysteresis. The extracted coercive and bias electric fields are displayed in **Figure 4.28a/b**. The change of the loop shape and the substantial decrease of the coercive and bias electric fields in all PZT_R compositions indicate a significantly enhanced domain wall mobility and reduced pinning strength of the introduced acceptor defects (in acceptor-doped compositions), due to the thermal activation of the domain wall displacement and the migration of oxygen vacancies. Additionally, the tip rounding of the polarization loops in PZT_R-0.5Fe and PZT_R-0.1Fe indicate an increasing conductivity and leakage at high temperature.

[xv] PZT is a negative thermal expansion coefficient material [223].

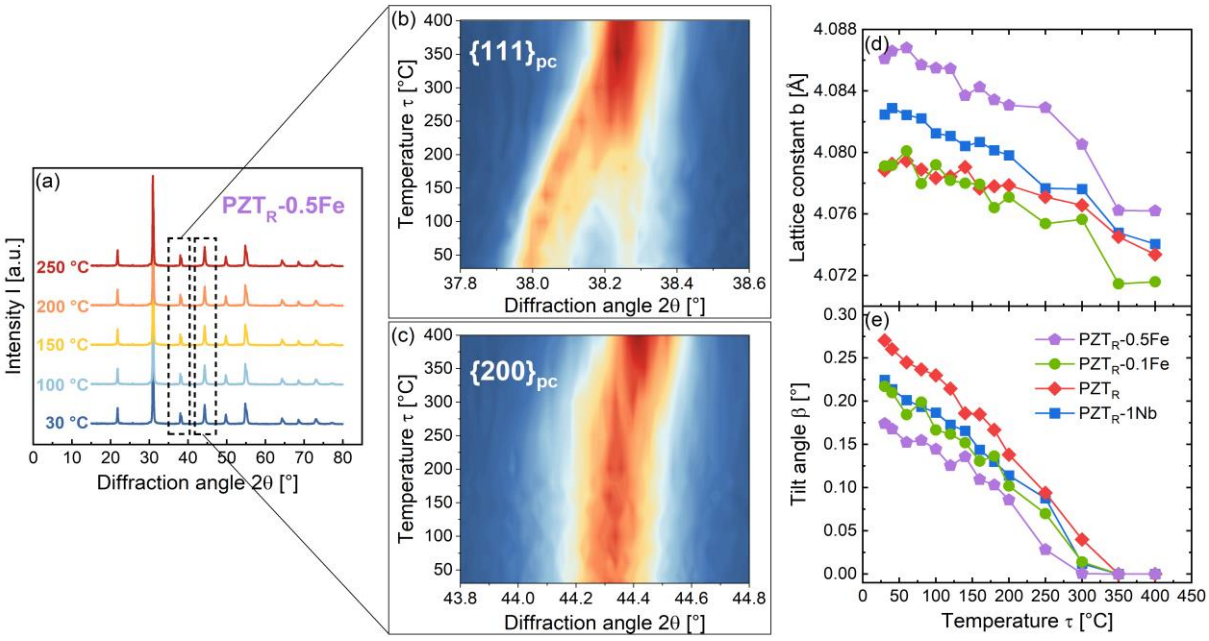

Figure 4.27. (a) Full range x-ray pattern of the hard PZT$_R$-0.5Fe composition at different temperatures and (b,c) the temperature dependence of the extracted $\{111\}_{pc}$ and $\{200\}_{pc}$ peaks. (d,e) Evolution of the lattice constant (b) and rhombohedral distortion (90°-β, β is the tilt angle) of all four PZT$_R$ compositions with increasing temperature (τ), calculated from the Gauss fit of the extracted peaks. All compositions reveal a decreasing lattice constant and ferroelectric distortion upon heating, hinting towards a facilitated domain wall motion.

To deconvolute the actual characteristics of the domain wall motion (linear/nonlinear, reversible/irreversible, hysteretic/anhysteretic), a harmonics analysis of the subcoercive polarization response was performed as a function of electric field amplitude at selected temperatures. The real (ε'_{33}) and imaginary (ε''_{33}) parts of the relative dielectric permittivity (**Supplemental Figure 7.7**) were determined from the 1st polarization harmonic ($|P_3^{1st}| = \varepsilon_0|\varepsilon_{33}|E_3$). The field amplitude dependence of ε'_{33} and ε''_{33} at each temperature was fitted using the non-linear Rayleigh **Equations (2.53)** and **(2.55),** and is represented by the Rayleigh coefficients (α_{R1} and α_{R2}) as a function of temperature in **Figure 4.28c,d**.

All compositions exhibit increasing ε'_{33} values with increasing field amplitude. This is known to be correlated with a field-induced increase of the irreversible domain wall displacement, which has a strong hysteretic response [105]. The hysteretic character is evidenced by the substantial increase of ε''_{33}, which gives rise to the dielectric loss (**Supplemental Figure 7.7i-l**), expressed by the ratio of the two complex component ($tan\ \delta = \frac{\varepsilon''_{33}}{\varepsilon'_{33}}$).

In addition to the field dependence, also a pronounced temperature dependence can be observed. The small-field ε'_{33} and ε''_{33} values as well as the slopes of their field-dependence increase at high temperatures (expressed by α_{R1} and α_{R2} in **Figure 4.28c,d**). These temperature-dependent changes indicate a thermally activated increase of the reversible domain wall displacement (small-field ε'_{33} values), as well as increasing irreversible domain wall displacement (slope of ε'_{33} field-dependence or α_{R1}), and an increasingly hysteretic character of the domain wall motion (slope of ε''_{33} field-dependence or α_{R2}) [94, 99]. Although the magnitudes of the changes are different across the compositions, the general temperature dependence is qualitatively very similar. Furthermore, it is important to highlight that the relative increase of the dielectric loss ($\Delta tan\ \delta$) exhibits the same field dependence at every

temperature (**Supplemental Figure 7.7m-p**), while the ε'_{33}-ε''_{33} relation remains reasonable linear (**Supplemental Figure 7.7q-t**). Both indicate that only the domain wall motion exhibits a field dependence in the probed range. The increasing electric field activates or enhances no other polarization mechanisms (e.g., domain switching or charge carrier transport) [224, 225].

In order to verify that the field and temperature-induced increase of the permittivity originates from domain wall motion and not from another polarization contribution, the 3rd polarization harmonic was tracked simultaneously (**Supplemental Figure 7.8**). The 3rd-harmonic is predominantly sensitive to the nonlinearity of the domain wall motion and is usually not shadowed by other effects [226]. The subcoercive polarization magnitude ($|P_3^{3rd}|$) and phase angle (δ^{3rd}) at 30 % of the coercive field and different temperatures are shown in **Figure 4.28e/f**. The increase of the polarization magnitude and phase angle with increasing field amplitude, as well as the increase of their slopes at higher temperatures, clearly indicate activation and enhancement of (nonlinear) domain wall motion and softening of the compositions [97, 227].

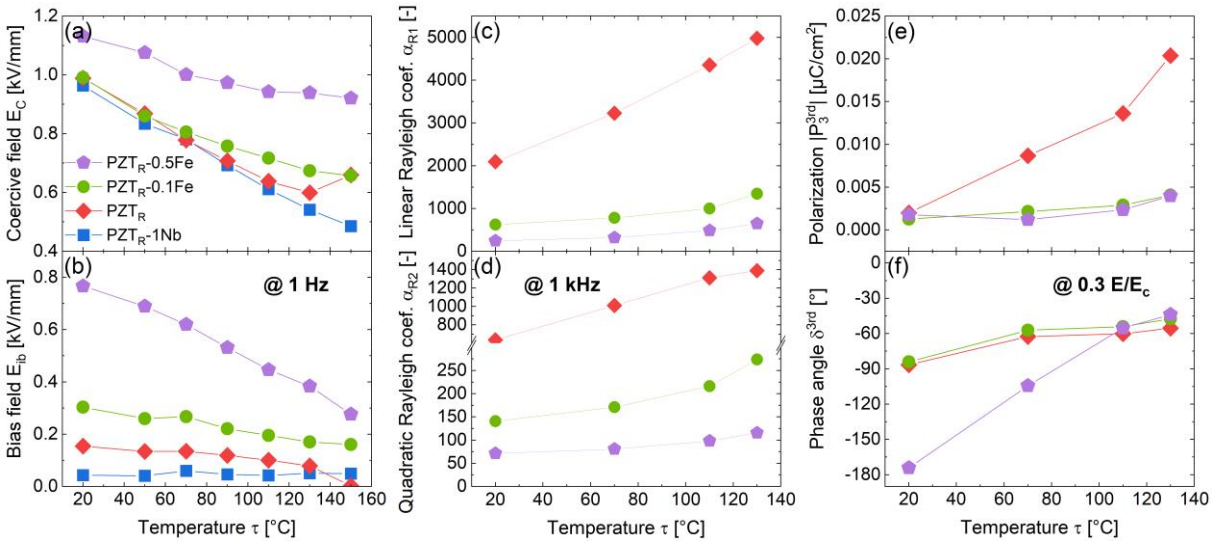

Figure 4.28. (a,b) Temperature-depended (τ) coercive (E_c) and bias (E_{ib}) electric fields of the four PZT$_R$ compositions, determined from the minima in the strain hysteresis loops at 1 Hz (**Supplemental Figure 7.6**). (c,d) Temperature-depended real (α_{R1}) and imaginary (α_{R2}) Rayleigh coefficients (**Equation (2.53)** and **(2.55)**), determined from the electric field-dependent 1st harmonic dielectric permittivity at 1 kHz (**Supplemental Figure 7.7**). (e,f) Temperature-depended 3rd harmonic polarization ($|P_3^{3rd}|$) and phase angle (δ^{3rd}) at 1 kHz and 30 % of the coercive electric field (**Supplemental Figure 7.8**). All measurements indicate a thermally activated enhancement of the domain wall motion in all compositions.

In summary, a continuous thermally activated increase of domain wall motion is identified in the range between 20 – 150 °C. The domain wall mobility or magnitude of domain wall motion alone can thus not explain the observed increase and subsequent decrease of Q_{31}^R (acceptor-doped compositions) or the almost temperature independence of Q_{31}^R (donor-doped composition) in the same temperature range.

To expose other loss contributions than domain wall motion, frequency- and temperature-dependent studies of the dielectric permittivity were conducted. The temperature range from -50 °C to 400 °C was covered, including the range of the resonance measurements (**Figure 4.26**) and the region beyond the Curie temperature (τ_c) of the PZT$_R$ compositions. **Figure 4.29** displays the temperature dependence of the small-field dielectric permittivity of

hard PZT_R-0.5Fe compared to the soft PZT_R-1Nb (other compositions are displayed in **Supplemental Figure 7.10**). In both cases, the real part of the dielectric permittivity (ε'_{33}) increases at high temperatures with a distinct peak at the τ_c at around 330 °C (**Figure 4.29a,c**). However, while in soft PZT_R-1Nb also the imaginary part of the dielectric permittivity (ε''_{33}) increases continuously, in hard PZT_R-0.5Fe it exhibits a complex temperature dependence with three stages. Upon heating, ε''_{33} significantly decreases until 0 °C (note the logarithmic scale), followed by a broad valley and a subsequent rapid increase. Moreover, above 0 °C ε''_{33} in hard PZT_R-0.5Fe reveals a strong frequency dispersion, which determines the temperature width of the valley and the set-in of the increase. As a result, both materials exhibit a continuous increase of the dielectric permittivity magnitude ($|\varepsilon_{33}|$) with a peak at the τ_c (**Figure 4.29b,d**). However, soft PZT_R-1Nb shows a rather constant dielectric loss ($tan\ \delta$) up to the Curie temperature, while the dielectric loss in hard PZT_R-0.5Fe follows the three stage temperature behavior determined by ε''_{33}. Most importantly, note that the evolution of the dielectric loss with temperature, particularly at 100 kHz, which is in the vicinity of the resonance frequency ranges of the samples in **Figure 4.26**, closely matches the temperature evolution of Q^R_{31} (or precisely the inverse of Q^R_{31}, **Figure 4.26a/d**). The correlation is a strong hint that the mechanisms influencing the dielectric loss under off-resonance conditions have also a significant impact on the loss contributions in resonance, which are represented by Q^R_{31}.

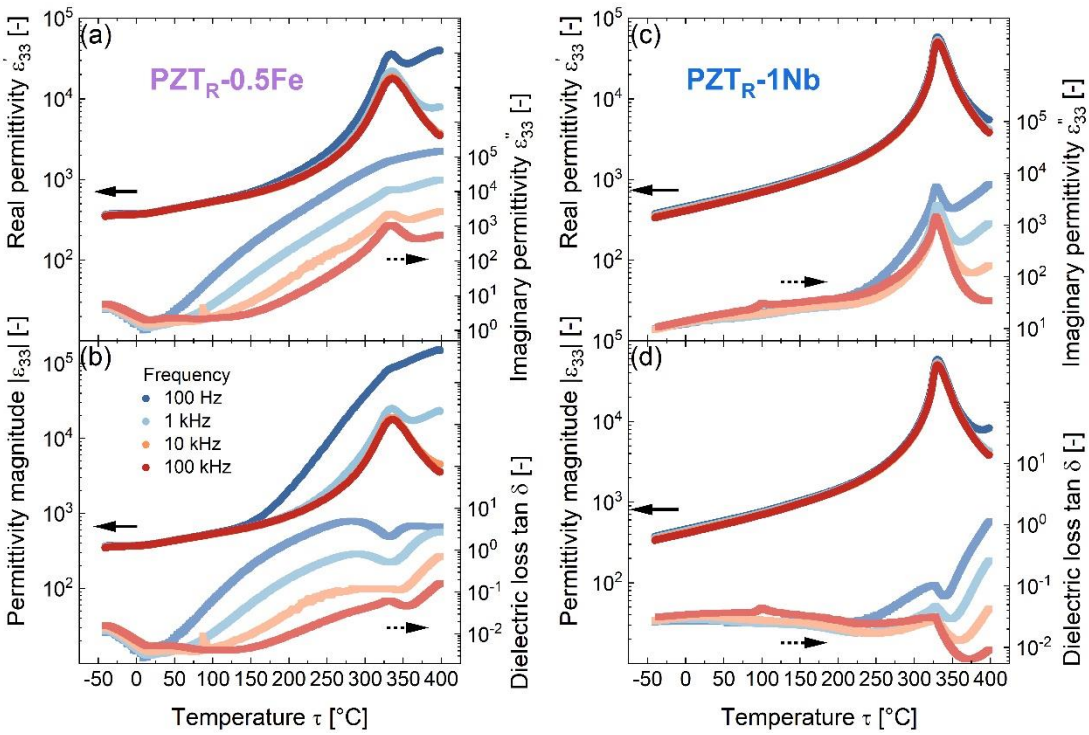

Figure 4.29. Magnitude ($|\varepsilon_{33}|$), real (ε'_{33}), and imaginary (ε''_{33}) part of the effective dielectric permittivity and the dielectric loss ($tan\ \delta$) of acceptor-doped PZT_R-0.5Fe and donor-doped PZT_R as a function of temperature (τ) measured at different off-resonance frequencies. The dielectric loss resembles inversely the temperature evolution of Q^R_{31} (**Figure 4.26**) and evidences its contribution to the small-field Q^R_{31} values.

The observed evolution difference is most likely related to the conductivity of the compositions. The measured current density ($J(\omega)$) as a function of applied electric field ($E(\omega)$) can be expressed as [228]

$$J(\omega) = j\omega\varepsilon_0\tilde{\varepsilon}(\omega)E(\omega), \tag{4.17}$$

where $E(\omega) = E_0 \exp(j\omega t)$, ω is the angular frequency, ε_0 the vacuum permittivity, and $\tilde{\varepsilon}(\omega)$ the effective relative dielectric permittivity (written as $\varepsilon(\omega)$ in the following for convenience). $\varepsilon(\omega)$ can be expressed in a complex form as

$$\varepsilon(\omega) = \varepsilon'(\omega) - j\left[\varepsilon''(\omega) + \frac{\sigma_0}{\varepsilon_0 \omega}\right], \tag{4.18}$$

with σ_0 being the DC conductivity. The real and imaginary parts of the measured permittivity contain all complex dielectric responses, i.e., their components in-phase and out-of-phase with the applied electric field, respectively. The dielectric responses are all charge displacement mechanisms that contribute to polarization and conduction, particularly dipole elongation and rotation, domain wall displacement (reversible and irreversible), and free charge carrier migration (short-range ionic or electronic hopping). The imaginary part has an additional contribution from long-range DC conductivity.

The real and especially the imaginary part of permittivity in soft PZT_R-1Nb are determined mainly by the polarization contribution from domain wall motion up to the MHz range [91, 229, 230]. Other loss sources, including conductivity, have a minor or negligible contribution [43, 231]. Ionic conductivity is minimal despite the donor-doping, since the introduced defects, i.e., lead vacancies, are strongly localized. Thus, the conductivity has a predominantly electronic nature (n-type semiconductor), which becomes relevant only at elevated temperatures due to the wide energy bandgap of PZT (~3.52 eV) [61]. It turns out that the thermally activated increase of domain wall motion (**Figure 4.28**) contributes evenly to ε'_{33} and ε''_{33} and results in approximately constant dielectric loss over a wide temperature range with only a minor frequency dispersion (**Figure 4.29d**). An increase of the dielectric loss and a distinct frequency dispersion evolve only when the temperature approaches the τ_c, which is an effect of the thermodynamic instability in terms of a ferroelectric-to-paraelectric phase transition and emerging electronic conductivity.

In hard PZT_R-0.5Fe, where the domain walls are immobilization through the acceptor-doping, conductivity induces a paramount contribution to the imaginary part of permittivity and the dielectric loss and overshadows the domain contribution, especially at large temperatures [61]. Evidence for the conductivity contribution are the distinct frequency dispersion of the imaginary part, the temperature-dependent increase of the dielectric loss, as well as the smearing of the phase transition (**Figure 4.29a,b**). The conductivity is thereby of ionic nature[xvi] based on the hopping and migration of oxygen vacancies introduced by the acceptor doping (i.e., Fe-doping) [65, 233]. The activation energy is in the range of 0.77-0.80 eV for the short-range hopping and 0.94 eV for the long-range migration [61], which is significantly lower than the activation energy for conductivity in soft PZT_R.

While the increase of dielectric loss at elevated temperatures is reasonably well understood, the reason for the decrease between -50 °C and 0 °C is not entirely clear, since domain wall motion and conductivity are expected to "freeze" at low temperatures [89, 224]. Two explanations appear most likely: The decrease could be related to a thermodynamic instability in terms of a polymorphic phase transition below -50 °C. Elastic measurements and structural investigations have observed that the tetragonal and rhombohedral PZT phases undergo a phase

[xvi] Electronic conduction via Fe^{2+} and Fe^{3+} cations was excluded by electron paramagnetic resonance (EPR) investigations [64, 232].

transformation into a monoclinic phase below -73 °C [234, 235]. A large number of degrees of freedom (polarization directions) facilitates polarization rotation and domain wall motion and lead to a peak in dielectric loss (similar to the peak at the τ_c). Upon heating above the transition temperature, the dielectric loss decrease due to increasing distance to the instability and the tail is observed in the probed temperature range. The reason why the tail does not appear in the soft PZT_R-1Nb might be the shift of the transition to lower temperature due to Nb-doping. The other explanation are inhomogeneities in the material, such as small amounts of secondary phases, grain boundaries, or near-electrode layers, which can contribute differently to the conductivity and reveal different temperature dependencies [228]. This means that, for example, the grain boundary conductivity decreases with increasing temperature, while the bulk conductivity increase. Further investigations are required to deconvolute the contributions.

In summary, the dielectric response of the hard and soft PZT_R compositions is qualitatively different, which can be traced back to the presence of hopping conduction in the hard compositions and its absence in the soft compositions in the same frequency and temperature range. The correlation of the dielectric loss with the temperature dependence of Q_{31}^R suggests a crucial role of mobile charge carriers for the electromechanical properties in resonance.

4.4.4. Thermal impact on high-power properties of tetragonal $Pb(Zr,Ti)O_3$

The electromechanical coefficients Q_{31}^R, d_{31}, and s_{11}^E were measured in the transverse (31) vibration mode as a function of vibration velocity at selected temperatures to probe the impact of thermal load on the high-power properties of the PZT_T compositions (**Figure 4.30**). The temperatures were selected according to the small-field measurements (**Figure 4.24**) to cover the range where Q_{31}^R increases and decreases upon heating. Please note that the samples were heated/cooled and homogenized externally; temperature changes through self-heating effects were excluded by the experimental procedure of the high-power measurements to decouple the heat sources. The values determined by the pulse drive method with burst excitation at low vibration velocities agree well with the small-field resonance impedance spectroscopy values, which are given as star symbols in **Figure 4.30**.

The results verify the enormous thermally induced change of Q_{31}^R. For example, in case of hard PZT_T, the low velocity Q_{31}^R values decrease by a factor of almost 5 upon heating from 20 °C to 100 °C[xvii]. However, there is no significant thermal impact on the vibration velocity stability of Q_{31}^R. This means that Q_{31}^R exhibits a rapid decrease upon increasing vibration velocity, even after a considerable increase of the low velocity Q_{31}^R values through cooling to 0 °C in hard PZT_T (**Figure 4.30a**) or heating to 100 °C in medium-hard PZT_T (**Figure 4.30b**). Similar trends were indicated in previous reports, where the temperature variation was introduced by self-heating effects in the samples [14]. A detailed comparison of the stability will be elucidated in the next section. Nevertheless, it can already be noted that the rapid decrease of Q_{31}^R, which has been revealed as a general inherent characteristic and drawback of PZT-based compositions (**Figure 4.9**), experiences no significant modification or stabilization upon temperature variation, besides some minor slope changes.

[xvii] 100 °C is a common benchmark temperature, determined by the boiling point of water under normal pressure, which is often considered as the border between ambient and high-temperature applications.

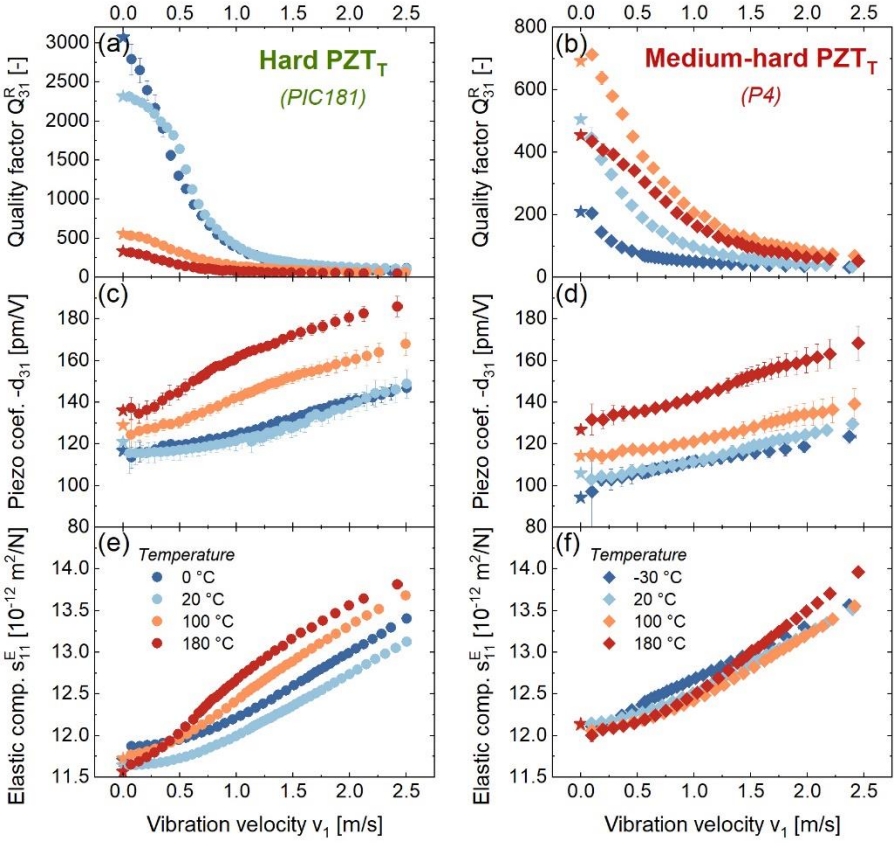

Figure 4.30. Electromechanical coefficients (a,b) Q^R_{31}, (c,d) d_{31}, and (e,f) s^E_{11} of hard PZT$_T$ (PIC181) and medium-hard PZT$_T$ (P4) in the transverse (31) vibration mode as a function of vibration velocity (v_1) at different temperatures (note the different scales). The data points denoted as stars at 0 m/s depict the small-field values determined from resonance impedance spectroscopy, which agree well with the pulse drive measurements at low vibration velocity.

A similar conclusion also applies to d_{31} and s^E_{11} of both compositions (**Figure 4.30c-f**). The coefficients increase with increasing vibration velocity and exhibit a distinct temperature dispersion, which follows the temperature dependence of the small-field values. The temperature dispersion increases at large vibration velocities, indicating a slight temperature-induced increase of the slopes. These changes in slope, as well as the temperature-dependent changes of the small-field d_{31} and s^E_{11} values, are most likely related to the thermally activated mobility of domain walls, which are driven by the dynamic mechanical stress and/or applied electric field under resonance excitation.

The temperature-dependent pulse drive measurements yield property maps, which summarize the above-determined findings and predict the high-power performance of the compositions in the entire vibration velocity-temperature space. Maps of Q^R_{31}, d_{31}, s^E_{11}, and FOM^{HP} in **Figure 4.31** (Q^{AR}_{31}, k_{31}, and ε^T_{33} are given in **Supplemental Figure 7.11**) demonstrate clearly the flat landscape of d_{31} and s^E_{11}, with an overall smooth increase towards large temperature and vibration velocity in hard PZT$_T$ and medium-hard PZT$_T$ (**Figure 4.31c-f**). On the other hand, Q^R_{31} exhibits a severe change upon both temperature and vibration velocity variation in a wide value range (**Figure 4.31a,b**). Since the high-power FOM^{HP} is dominated by Q^R_{31} (Section 4.1), both compositions exhibit a valuable high-power performance only in a limited and narrow temperature and vibration velocity window (**Figure 4.31g,h**), which is the essential detriment of PZT-based ferroelectrics for high-power use.

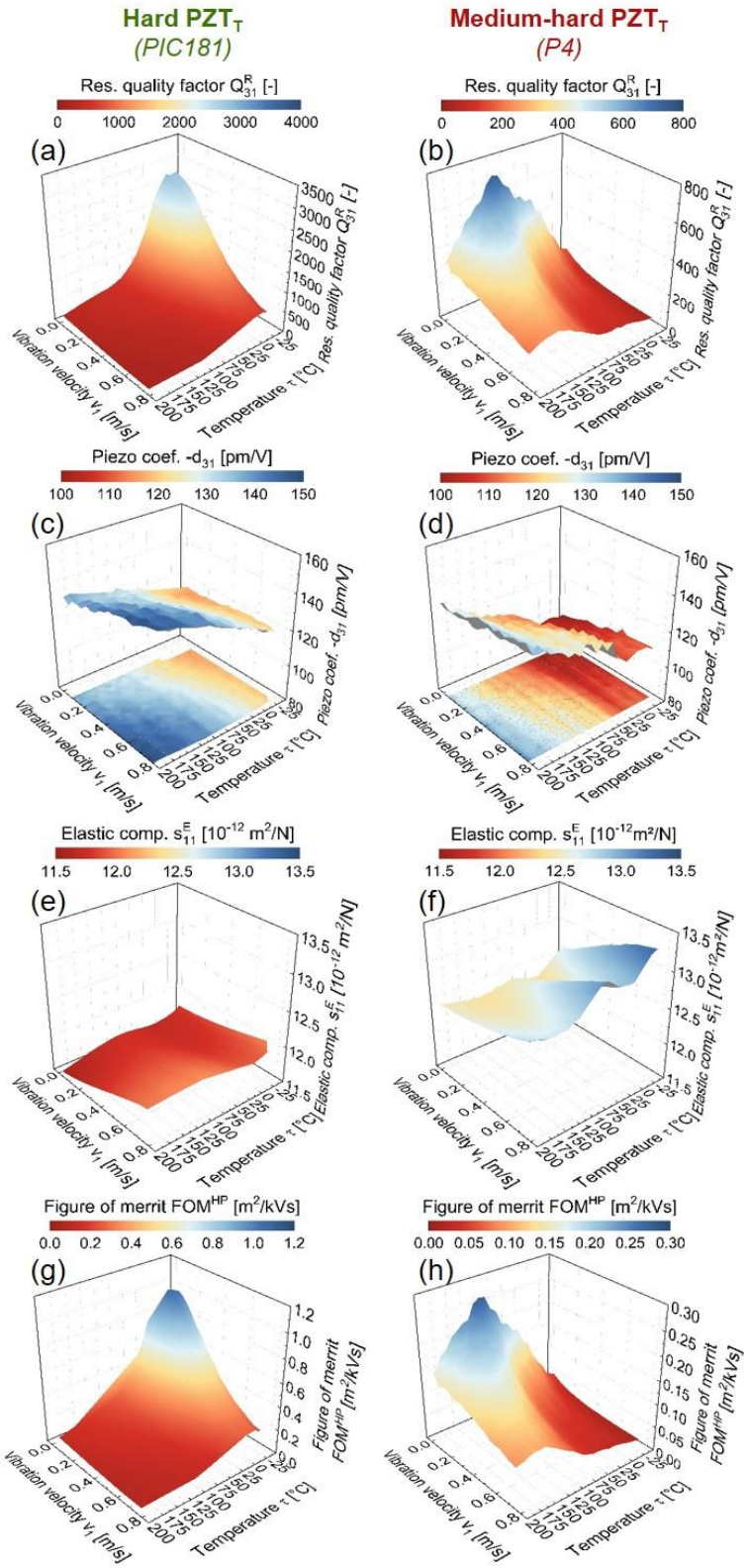

Figure 4.31. Temperature (τ) and vibration velocity (v_1) maps of the electromechanical coefficients (a,b) Q_{31}^R, (c,d) d_{31}, (e,f) s_{11}^E, and (g,h) FOM^{HP} of hard PZT$_T$ (PIC181) and medium-hard PZT$_T$ (P4) in the transverse (31) vibration mode. The severe decrease of Q_{31}^R upon increasing temperature and vibration velocity cannot be compensated by the other coefficients and significantly limits the high-power operation range of the PZT$_T$ compositions.

4.4.5. Thermal impact on high-power properties of rhombohedral Pb(Zr,Ti)O$_3$

The coefficients Q_{31}^{R}, d_{31}, s_{11}^{E}, and FOM^{HP} of the PZT$_R$ compositions in the transverse (31) vibration mode are presented in **Figure 4.32** as a function of vibration velocity at selected temperatures (Q_{31}^{AR}, k_{31}, and ε_{33}^{T} are given in **Supplemental Figure 7.12**). The values determined by the pulse drive method with burst excitation at low vibration velocities agree well with the small-field resonance impedance spectroscopy values, which are given as star symbols. In all compositions, Q_{31}^{R} rapidly decreases with increasing vibration velocity (**Figure 4.32a-d**). Moreover, the Q_{31}^{R}-v_1 evolution exhibits a distinct temperature dispersion, particularly in hard PZT$_R$-0.5Fe, while in undoped PZT$_R$ and soft PZT$_R$-1Nb the Q_{31}^{R}-v_1 evolution is mostly temperature-independent. The dispersion follows the temperature-dependence of the small-field Q_{31}^{R} (**Figure 4.26a-d**) and reveals a Q_{31}^{R}-v_1 temperature optimum for the acceptor-doped compositions at the previously determined Q_{31}^{R}-peak temperature (**Figure 4.26**). For example, Q_{31}^{R}-v_1 of hard PZT$_R$-0.5Fe is largest at 100 °C over the entire vibration velocity range, and decreases upon heating to 200 °C and even more upon cooling to -30 °C (**Figure 4.26a**). This transfers directly into substantially (by a factor of ~2) larger vibration velocity generation at 100 °C compared to -30 °C under continuous excitation with constant driving electric fields (**Supplemental Figure 7.13**). Important thereby is, however, that the Q_{31}^{R} stability, i.e., the relative change of Q_{31}^{R} (expressed by $Q_{31}^{R}/Q_{31}^{R,0}$) as a function of vibration velocity, remains mostly temperature-independent (**Figure 4.33**). The measurement results of the PZT$_R$ compositions strengthen and generalize the above findings that temperature has a significant influence on the Q_{31}^{R} values (particularly in acceptor-doped compositions), but not on their relative change upon increasing vibration velocity. It follows that the mechanisms, which lead to the thermally induced quantitative change of Q_{31}^{R}, have no important impact on its relative change with increasing vibration velocity.

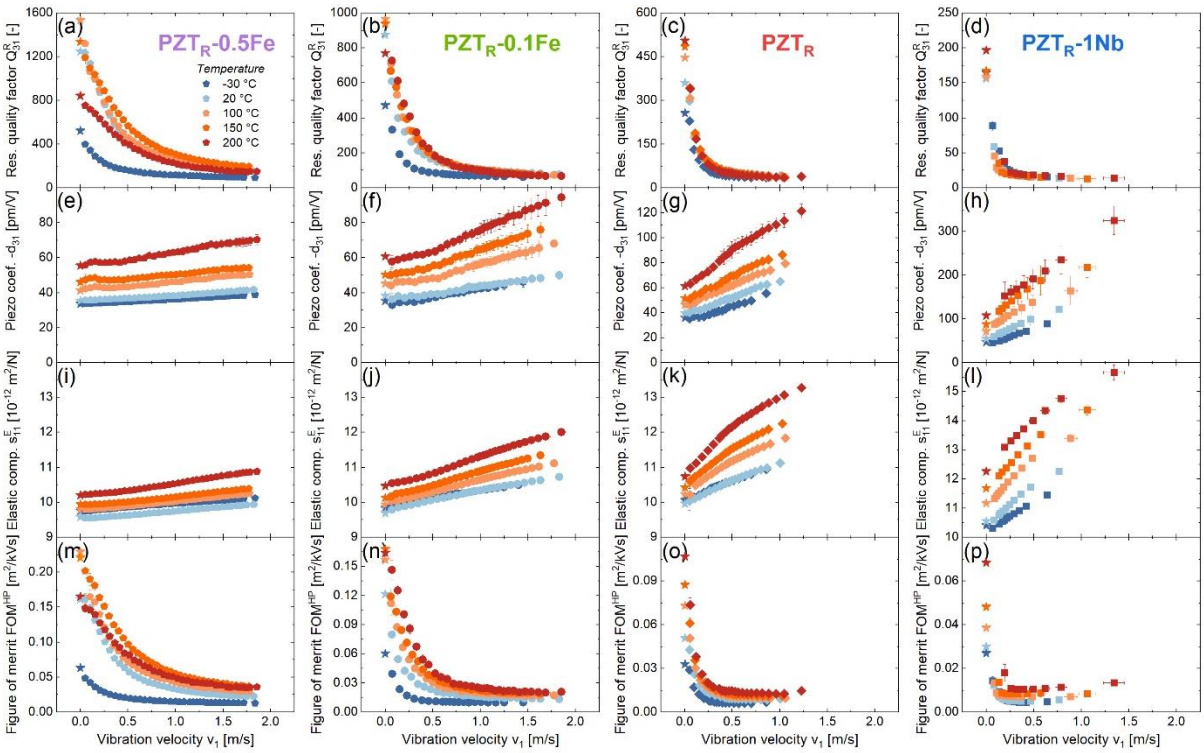

Figure 4.32. Electromechanical coefficients (a-d) Q_{31}^{R}, (e-h) d_{31}, (i-l) s_{11}^{E}, and (m-p) FOM^{HP} of the four PZT$_R$ compositions in the transverse (31) vibration mode as a function of vibration velocity (v_1) at different temperatures. The data points denoted as stars at 0 m/s depict the small-field values determined from resonance impedance spectroscopy.

The coefficients d_{31} and s_{11}^E increase with increasing vibration velocity and exhibit as well a distinct temperature dispersion, following the temperature evolution of the small-field values (**Figure 4.32e-l**). The temperature dispersion increases at large vibration velocity, indicating a temperature-induced increase of the slopes. In contrast to Q_{31}^R, the dispersion and the increase in slope are prominent in the donor-doped and undoped compositions and less pronounced in the acceptor-doped compositions (note the different scales).

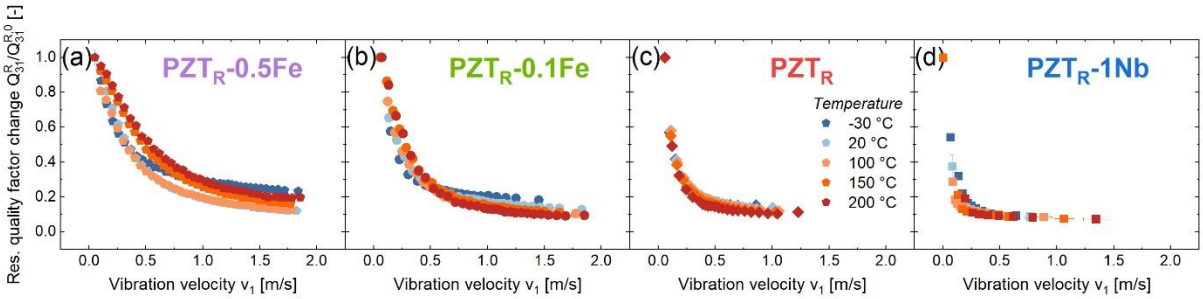

Figure 4.33. Relative change of the resonance quality factor ($Q_{31}^R/Q_{31}^{R,0}$) as a function of vibration velocity (v_1). Every PZT$_R$ composition demonstrates a very similar Q_{31}^R change, independent of the temperature and the small-field Q_{31}^R values. The clustering evidences that the inherently strong decrease of Q_{31}^R with increasing vibration velocity is determined by other processes than the thermally induced increase/decrease of the absolute Q_{31}^R values.

4.4.6. Discussion and conclusions

The resonance quality factor Q_{31}^R (equivalent arguments are valid for the antiresonance quality factor Q_{31}^{AR}) reveals a distinctly different dependence on temperature than the piezoelectric, mechanical, and dielectric coefficients (d_{31}, k_{31}, s_{11}^E, ε_{33}^T). The latter exhibit a relatively continuous increase or decrease of the small-field values throughout the entire probed temperature range (**Figure 4.24** and **Figure 4.26**) and also increase continuously upon increasing vibration velocity (**Figure 4.30** and **Figure 4.32**). This results in mostly flat and slightly tilted vibration velocity-temperature landscapes (**Figure 4.31**). The changes are thereby correlated with the decreasing lattice distortion (**Figure 4.27**), the thermal activation of domain wall motion (**Figure 4.28**), and the reduced domain wall pining potential of the introduced defects (interrelated with the enhanced mobility of oxygen vacancies in acceptor-doped compositions, **Figure 4.29**). The magnitude of these changes is more prominent in the ferroelectrically soft (donor-doped) compositions than in the hard (acceptor-doped) compositions, due to their susceptibility to large domain wall motion magnitudes and flat energy potential.

Q_{31}^R reveals an entirely different thermal behavior, with prominent ranges of increase, no change, or decrease upon heating (**Figure 4.24** and **Figure 4.26**). These changes are especially pronounced in the ferroelectrically hard compositions, while soft compositions exhibit an almost temperature-independent behavior. At the same time, however, Q_{31}^R decreases rapidly with increasing vibration velocity at all temperatures in all compositions (**Figure 4.30** and **Figure 4.32**). It turns out that the instability of Q_{31}^R is temperature independent (**Figure 4.33**), although the entire Q_{31}^R-v_1 characteristic is shifted to larger or lower values according to the small-field temperature evolution (**Figure 4.24** and **Figure 4.26**).

The mechanistic explanation for this behavior is multiplex and requires the following generalized consideration: Since all charge-displacing or strain-generating mechanisms have a lossy nature (Section 2.3.4), the formalism used to express phenomenologically lossy

electromechanical coefficients (Section 2.2.3) can be applied to describe the mechanistic processes. This means that the charge-displacing or strain-generating mechanisms must be treated as complex entities, represented by in-phase and out-of-phase components with respect to the external driving force. The sum of the components determines the total generated polarization/strain magnitude, while the ratio of the components determines the loss. Relevant processes for the studied ferroelectrics include intrinsic (lattice) processes (dipole elongation and rotation), extrinsic (non-lattice) processes (reversible and irreversible domain wall motion), and free charge carrier migration (short-range ionic or electronic hopping).

These processes can be roughly classified into two basic groups. Polarization elongation and rotation, as well as reversible domain wall motion, exhibit dominant in-phase components, resulting in an anhysteretic character and inherently small but non-zero loss magnitudes. Irreversible domain wall motion and other extrinsic processes exhibit significant out-of-phase components, resulting in a hysteretic character and large loss magnitudes. This was evidenced above, for example, by the Rayleigh-type measurements, and is well known from literature [62, 89, 91, 105, 226]. Moreover, while the former group reveals a mostly linear increase upon increasing external load, the latter usually exhibits a much more significant non-linear increase. The resonance and off-resonance properties and their evolution upon electric, mechanical, and thermal loading can be correlated and explained consistently using these considerations.

Donor-doped ferroelectrics exhibit an extensive domain wall motion in addition to the intrinsic response, which, with the implementation of the Rayleigh and V-potential models [88, 89, 107], originates from a flat energy potential. The large mobility is correlated with a notable portion of reversible as well as irreversible domain wall motion (**Figure 4.17**), leading to a comparably large loss in the material (out-of-phase to in-phase ratio). The out-of-phase component of the domain wall motion is thereby the main contribution to the large dielectric loss under off-resonance conditions and electric excitation (**Figure 4.29c,d**), as well as to the large elastic loss and small Q_{31}^{R} values under electric/mechanical drive and resonance conditions at moderate temperatures (**Figure 4.24c** and **Figure 4.26d**). The dielectric loss (**Supplemental Figure 7.7l**) and elastic loss rise (Q_{31}^{R} values decrease, **Figure 4.32d**), since it is primarily the irreversible domain wall motion that enhances upon larger external (electric and/or mechanical) perturbation. However, under thermal loading, all contributions are activated equivalently. Meaning that the out-of-phase to in-phase ratio does not significantly change, although, the overall magnitude of domain wall motion strongly increases (**Figure 4.28**). This is evidenced among others by an almost constant dielectric loss over a broad temperature range (**Figure 4.29d**), a similar increase of the dielectric loss upon electric field increase at different temperatures (**Supplemental Figure 7.7p**), and the fact that the Q_{31}^{R}-v_1 evolution is determined by the vibration velocity and is independent of the temperature (clustering; **Figure 4.33d**).

The same argumentation is consistently valid for the acceptor-doped ferroelectrics with some additional effects. Acceptor-doping reduces the domain wall mobility by steepening the potential and pinning the domain walls. It mainly reduces the out-of-phase contribution compared to the in-phase contribution, leading to a domain wall bowing rather than spatial translation, i.e., a predominantly reversible domain wall motion. This results in a reduced loss in the material and is evidenced at moderate temperatures and small external perturbation by a comparatively small dielectric loss (off-resonance condition; **Figure 4.29b**) as well as small elastic loss and large Q_{31}^{R} values (resonance condition; **Figure 4.24a,b** and **Figure 4.26a,b**).

With increasing external perturbation, it is again primarily the irreversible domain wall motion that increases, resulting in rising dielectric loss (**Supplemental Figure 7.7i,j**) and elastic loss (decreasing Q_{31}^{R}; **Figure 4.32a,b**)[xviii]. Under thermal loading, all contributions are thermally activated. This means that the out-of-phase to in-phase ratio does not significantly change, while the overall magnitude of domain wall motion strongly increases (**Figure 4.28**). This is confirmed by the quantitatively equal rise of the dielectric loss upon electric field increase at different temperatures (**Supplemental Figure 7.7m,n**) and the temperature independent Q_{31}^{R} stability upon increasing vibration velocity (clustering; **Figure 4.33a,b**). However, other than in the donor-doped compositions, an additional considerable conductivity contribution is thermally activated, which is strongly temperature- and frequency-dependent. The conductivity is a consequence of the acceptor doping and the domain wall pinning through oxygen vacancy generation, which reveal low activation energy for ionic hopping. The conductivity exceeds the domain wall contribution to the dielectric loss at low vibration velocities (**Figure 4.29**), but is not dependent on the applied electric field or mechanical stress amplitude, i.e., the above-discussed relative changes of the dielectric loss upon electric field increase (**Supplemental Figure 7.7m,n**) and changes of Q_{31}^{R} with increasing vibration velocity (**Figure 4.33a,b**) remain temperature independent. The conductivity has thus a constant contribution to the loss and Q_{31}^{R}, determined by the temperature, and is responsible for the shift of the Q_{31}^{R}-v_1 evolution (**Figure 4.32a,b**). Potentially, it also contributes to the frequency dependence of Q_{31}^{R} (discussed in Section 4.3).

This discloses in a generalized form that the piezoelectric, mechanical, and dielectric coefficients (d_{31}, k_{31}, s_{11}^{E}, ε_{33}^{T}) are determined by the summed component magnitude (absolute values) of all charge displacing or strain-generating processes. However, the loss, and thus the quality factors Q_{ij}, are determined by the ratio of the in-phase and out-of-phase components and not by the magnitude alone. This results in a different response of Q_{ij} to external loading and is likely the reason for the much larger sensitivity to any kind of change of domain wall motion. The above elucidated and evidenced correlation between increasing domain wall motion magnitude and decreasing $Q_{31}^{R/AR}$ values (Section 4.2.1) is nonetheless still valid, with the additional remark that the increasing domain wall motion is mainly correlated with the paramount increase of the (reversible/irreversible) out-of-phase contributions.

As a consequence, a material with good high-power properties (e.g., large Q_{31}^{R} and d_{31} values), which are stable in a broad temperature and vibration velocity range, requires strong pinning of the out-of-phase components of the charge-displacing and strain-generating mechanisms, like irreversible domain wall motion, that is not weakened by external perturbations. Furthermore, it requires low conductivity with considerably large activation energy. Acceptor-doping is the most established method to reduce domain wall mobility. However, it necessitates a fine-tuning in order to engineer the Q_{31}^{R} maximum (conductivity minimum) to the desired temperature regime, while the increase of the Q_{31}^{R} values narrows down the temperature width of the maximum. Other strategies to immobilize the domain walls without adding a conductivity contribution, like DC bias (Sections 4.5 and 5.3) or introducing strain incompatibilities and

[xviii] Note that the relative change of the Q_{31}^{R} values is similar between the acceptor- and donor-doped compositions (**Figure 4.32**), while the relative change of the off-resonance dielectric loss (**Supplemental Figure 7.7**) reveals qualitative differences. These are presumed to be related to the fact that under the predominantly mechanical loading in resonance, loss originates from the ferroelectric/ferroelastic (non-180°) domain walls, while under the off-resonance electric loading also purely ferroelectric (180°) domain walls contribute to the loss.

stress mismatches through second phases (Section 5.1), might be more promising. It should still be noted that although the thermal effects have a severe impact on the Q_{31}^{R} values and the ferroelectric hardening, they do not significantly influence the rapid decrease of Q_{31}^{R} with increasing vibration velocity (alike chemical doping). The relative change of Q_{31}^{R} remains an inherent property of PZT-based composition, independent of the temperature or the dopant nature and concentration, as predicted above.

4.5. Impact of DC bias field on the electromechanical properties

Non-linear polarization and strain responses to an external (sub- or above-coercive) electric or mechanical load are among the most prominent characteristics of a ferroelectric material. Hence, ferroelectric properties can be modified by superimposing the excitation signal (e.g., driving AC voltage) with static mechanical stress or DC bias voltage. For example, it has been reported that compressive stress[xix] and DC bias voltage increase the performance of ferroelectrically hard PZT ceramics in ultrasonic transducers [237].

The impacts of these static external perturbations on the electromechanical properties have been studied under off-resonance conditions [54, 57, 238] as well as under resonance conditions [201]. It was demonstrated that ferroelectrics experience a pronounced ferroelectric hardening upon applying a DC bias field along the polarization direction, and a softening if the field is applied opposite to the polarization direction. These changes were evidenced in terms of respectively decreasing and increasing piezoelectric coefficients (d_{33} and d_{31}), elastic compliance (s_{11}^{E}), coupling coefficient (k_{33} and k_p), and permittivity (ε_{33}^{T}). Since the non-linear response in ferroelectrics originates from extrinsic contributions, which are predominantly determined by the domain configuration and the mobility of domain walls, the observed ferroelectric hardening was referred to the immobilization of domain walls by the external field and the alignment of the polarization vector along the field direction.

Surprisingly, the impact of DC bias fields on the quality factor was not well studied and understood yet, although it is an interesting alternative to conventional hardening approaches. Possible reasons are the sophisticated experimental setup requirements to provide large DC bias voltages under resonance conditions (Section 3.3). Wang et al. [201] reported an increase of Q_{31} with increasing DC bias field along the polarization direction in a soft PZT composition; a decrease of Q_{31} was observed under DC bias opposite to the polarization direction. However, the measurement range was limited to a bias of only ± 0.4 kV/mm, which was well below the coercive and poling electric fields.

This section investigates the impact of large DC bias fields on the electromechanical properties of hard-type and soft-type PZT compositions. Small-field electromechanical coefficients are determined by resonance impedance spectroscopy while DC voltage is applied to the samples. A DC bias field range along and opposite to the polarization direction between the poling field and the polarization reversal coercive field is covered. In particular, the evolutions of the resonance and antiresonance quality factors are tracked and compared to the piezoelectric,

[xix] From the application point of view, DC bias voltages are arguably simpler to implement to tune material properties, since they can be superimposed e.g., on the driving AC voltages and used in positive or negative polarity. Mechanical stress is usually implemented only as compressive loading, since tensile stress in MPa range is difficult to apply and leads to earlier fracture of piezoceramics due to the low fracture toughness [236]. Compressive stress along the polarization direction destabilizes the domain configuration and leads to ferroelectric softening. Hardening with compressive stress requires the application of stress perpendicular to poling direction, which is usually not practical.

mechanical, and dielectric coefficients (d_{31}, k_{31}, s_{11}^E, ε_{33}^T). It is aimed to further enlighten the mechanisms that determine a material's quality factor and high-power properties (FOM^{HP}) using this external manipulation.

4.5.1. Small-field electromechanical coefficients under DC bias field

Figure 4.34 displays the small-field electromechanical coefficients of hard PZT_T and soft PZT_T as a function of the applied DC bias field. The coefficients were determined by resonance impedance spectroscopy utilizing the designed measurement system[xx] (Section 3.3). Positive and negative field values denote the DC bias applied along and opposite the polarization direction, respectively. The descending DC bias field measurement is shown, from maximum positive to minimum negative DC bias field. In both compositions, Q_{31}^R as well as Q_{31}^{AR} increase with increasing bias. Two characteristics are thereby most prominent: (1) Q_{31}^{AR} increases stronger than Q_{31}^R and (2) $Q_{31}^{R/AR}$ are much stronger affected by the DC bias field in hard PZT_T than in soft PZT_T. Note that the effects appear qualitatively equivalent in the PZT_R compositions (**Supplemental Figure 7.14**), which, however, exhibit a considerably weaker susceptibility to the bias than PZT_T.

Particularly in hard PZT_T, the impact on $Q_{31}^{R/AR}$ is enormous. The values increase rapidly by a factor of 4.5 (Q_{31}^R) and 6.1 (Q_{31}^{AR}) already at 2 kV/mm and saturate at higher fields (**Figure 4.35a**). In soft PZT_T and the PZT_R compositions, $Q_{31}^{R/AR}$ increase continuously and almost linearly over the entire field range. Dielectric breakdowns at high DC fields (>5 kV/mm) occur prior to a $Q_{31}^{R/AR}$ saturation. At negative DC bias fields, $Q_{31}^{R/AR}$ values decrease and eventually drop to zero in the vicinity of the coercive field (1.9 kV/mm in hard PZT_T and 1.1 kV/mm in soft PZT_T; **Figure 4.3**), featured by the disappearance of the resonance/antiresonance peaks from the impedance spectrum. Only Q_{31}^R in hard PZT_T reveals an increase at negative DC bias fields, which is different from the other compositions.

The piezoelectric, mechanical, and dielectric coefficients[xxi] d_{31}, k_{31}, s_{11}^E, and ε_{33}^T exhibit a dependences opposite to $Q_{31}^{R/AR}$ (**Figure 4.34c-j**). All coefficients decrease continuously with increasing DC bias field along the polarization direction, which is in accordance with previous reports [54, 201, 238]. The slopes decrease at high DC bias, indicating the onset of a convergence. At low negative bias, the coefficients increase, but rapidly drop towards zero in the vicinity of the coercive field. The decrease of the coefficients and the increase of $Q_{31}^{R/AR}$ at positive DC bias fields indicate ferroelectric hardening; vice versa, the increase of the coefficients and the decrease of $Q_{31}^{R/AR}$ at negative DC bias field indicate ferroelectric softening. The coefficients vanish at the coercive field, due to an electric field-induced depolarization. Note that the impact on d_{31}, k_{31}, s_{11}^E, and ε_{33}^T is more pronounced in the soft compositions than in the hard compositions (**Figure 4.35b-e**), which is contrary to the behavior of $Q_{31}^{R/AR}$.

[xx] For comparison, the measurements have been carried out in air and insulating SF6 gas (1.29 kg/m³ and 6.63 kg/m³ density under standard temperature and pressure, respectively) between 0.01 – 2 bar pressure in the atmosphere chamber. A notable impact of the atmospheric conditions on the determined electromechanical coefficients has not been observed. It was concluded that viscosity friction according to Stokes' law [259] has a negligible effect.

[xxi] Note that the calculation of the coefficients involves the resonators's geometry and the static strain induced by the DC bias field must be consider. For example, to take into account the static change in the sample length, the calculation of elastic compliance (**Table 2.1**) is modified to $s_{11}^E = (4\rho f_R^2 l^2)^{-1} = (4\rho f_R^2 (l_0 + l_0 d_{31} E_{bias})^2)^{-1}$, where l_0 denotes the initial sample length and l the length under DC bias field. However, the influence of the static strain on the coefficients is in the range of 1 % and can usually be neglected.

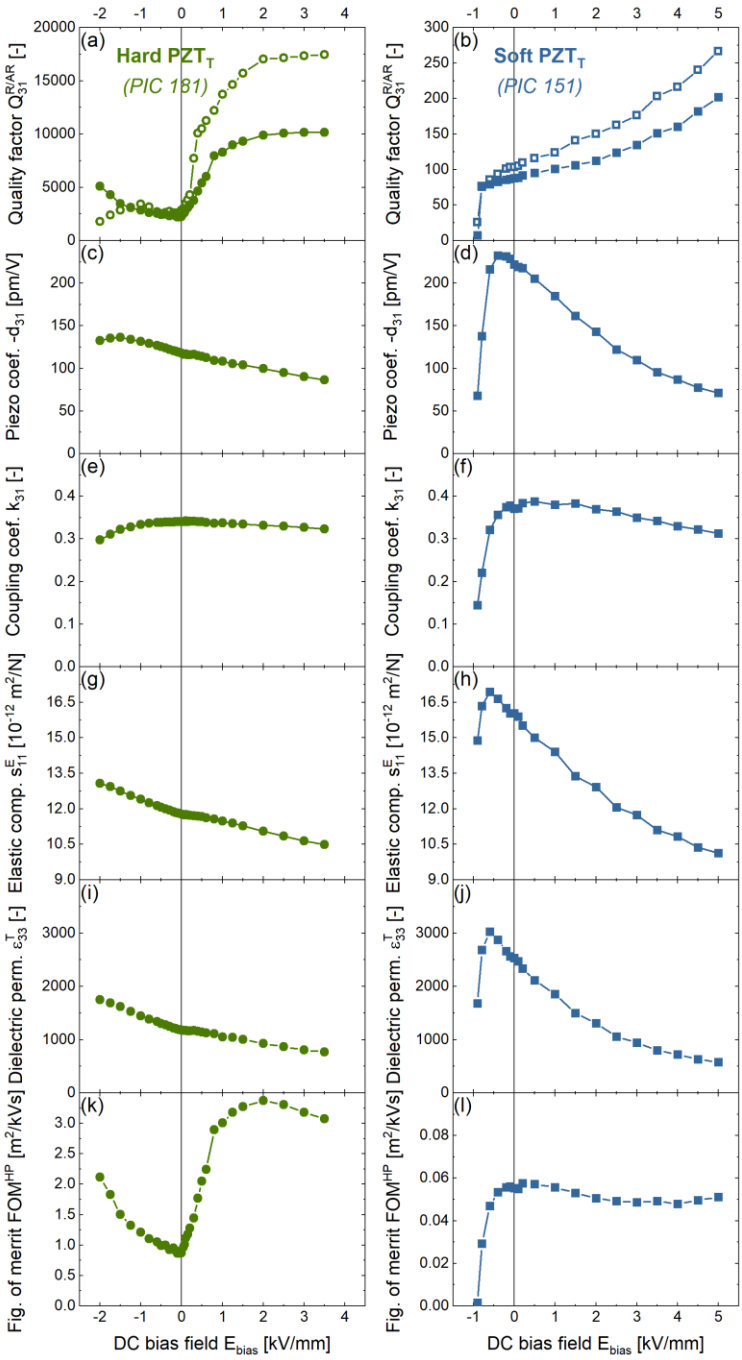

Figure 4.34. Electromechanical coefficients (a,b) Q_{31}^R (solid symbols) and Q_{31}^{AR} (open symbols), (c,d) d_{31}, (e,f) k_{31}, (g,h) s_{11}^E, (i,j) ε_{33}^T, and (k,l) high-power figure of merit (FOM^{HP}, **Equation (4.6)**) of hard PZT$_T$ (PIC 181) and soft PZT$_T$ (PIC 151) in the transverse (31) vibration mode as a function of DC bias field (E_{bias}) at 20 °C. Note the different scales between (a) and (b). Positive and negative field values denote the DC bias applied along and opposite to the polarization direction, respectively. The substantial increase of Q_{31}^R induces a significant increase of FOM^{HP} in hard PZT$_T$, while the Q_{31}^R increase on soft PZT$_T$ is entirely compensated by the decreasing d_{31}.

The difference between hard PZT$_T$ and soft PZT$_T$ is most prominently reflected in the evolution of FOM^{HP} (**Figure 4.34k,l**). The strong increase of Q_{31}^R and the simultaneously moderate decrease of d_{31} result in remarkably large FOM^{HP} values of hard PZT$_T$ induced by the positive DC bias field. The maximum appears at 2 kV/mm, where Q_{31}^R was found to saturate (**Figure 4.34a**). Interestingly, FOM^{HP} increases also at negative DC bias fields, due to increasing d_{31} and Q_{31}^R. The mechanistic reason will be elucidated below. On the other hand, positive DC

bias field has effectually no impact on the FOM^{HP} of soft PZT$_T$, since the increase of Q_{31}^{R} is entirely extinguished by the severe decrease of d_{31}. At negative DC bias fields the FOM^{HP} quickly drops to zero, due to the low coercive electric field and the induced depolarization.

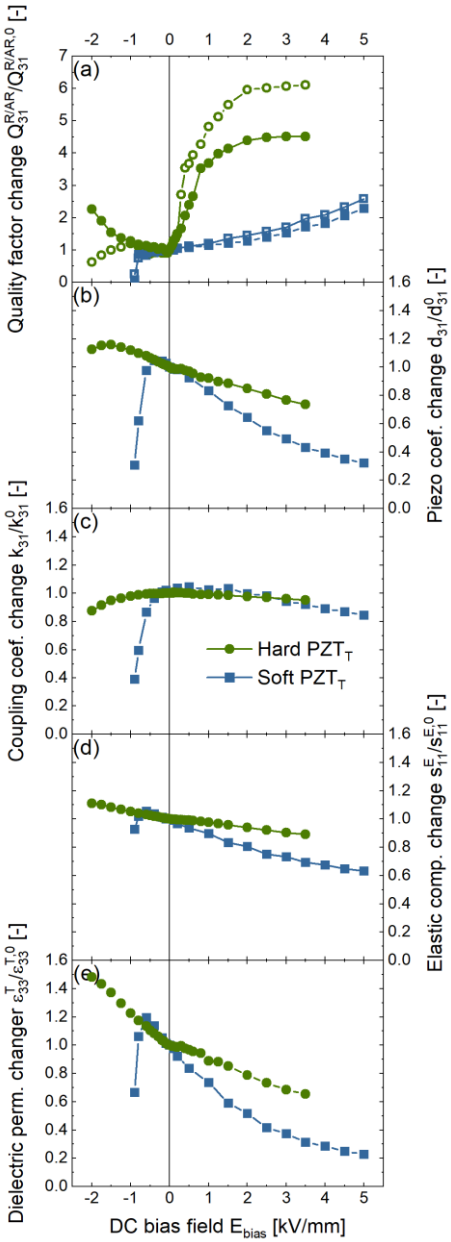

Figure 4.35. Relative change of the electromechanical coefficients (a) $Q_{31}^{R}/Q_{31}^{R,0}$ (solid symbols) and $Q_{31}^{AR}/Q_{31}^{AR,0}$ (open symbols), (b) d_{31}/d_{31}^{0}, (c) k_{31}/k_{31}^{0}, (d) $s_{11}^{E}/, s_{11}^{E,0}$, and (e) $\varepsilon_{33}^{T}/\ \varepsilon_{33}^{T,0}$ with respect to the zero DC bias condition of hard PZT$_T$ (PIC 181) and soft PZT$_T$ (PIC 151) in the transverse (31) vibration mode as a function of DC bias field (E_{bias}) at 20 °C. Positive and negative field values denote the DC bias applied along and opposite to the polarization direction, respectively. Hard PZT$_T$ is prone to a pronounced change of $Q_{31}^{R/AR}$, while in soft PZT$_T$ predominantly the other electromechanical coefficients reveal a susceptibility to the DC bias field.

4.5.2. Origin of the resonance-antiresonance quality factor ratio

The impact of the DC bias field on the electromechanical coefficients is first elucidated phenomenologically to address the origin of the increasing ratio between Q_{31}^{AR} and Q_{31}^{R} with increasing positive DC bias. From the constitutive piezoelectric **Equations (2.22)** and **(2.23),** and under the assumption that the resonating bar-shaped sample is a perfect insulator

exhibiting a displacement solely along its length, it was derived in Section 2.2.3 that the resonance quality factor can be approximated to be the inverse of the elastic loss (**Equation (2.45)**) [31]. These assumptions are reasonable at room temperature, small fields, and small vibration velocities, where dielectric loss, as well as width and thickness strains, are insignificant. Under these conditions, the antiresonance quality factor is determined by the compilation of the loss contributions from the piezoelectric, mechanical, and dielectric coefficients and expressed as (after **Equation (2.46)**)

$$\frac{1}{Q_{31}^{AR}} = \frac{1}{Q_{31}^{R}} - \frac{k_{31}^2}{1-k_{31}^2} tan\,\mu_{31}, \tag{4.19}$$

$$\text{with } tan\,\mu_{31} = tan\,\gamma_{11} + tan\,\delta_{33} - 2tan\,\phi_{31}.$$

The antiresonance quality factor is not independent of the resonance quality factor, but is determined by the coupling coefficient, the loss factor $tan\,\mu$, and the resonance quality factor itself. To track the interrelation of the two quality factors, a map of their ratio (Q_{31}^{AR}/Q_{31}^{R}) as a function of resonance quality factor and loss factor is displayed in contour plots in **Figure 4.36a,b**. Depicted are general ranges of large Q_{31}^{R} and correspondingly low $tan\,\mu_{31}$ values (**Figure 4.36a**) and low Q_{31}^{R} and large $tan\,\mu_{31}$ values (**Figure 4.36b**), respectively. The contour plots were calculated with k_{31}=0.34, which is about the coupling coefficient value of both PZT_T compositions at 20 °C and zero DC bias field (note that the changes of k_{31} under DC bias field are small, the influence on the contour plots is negligible). In addition, measured Q_{31}^{AR}/Q_{31}^{R} ratios of hard and soft PZT_T are marked in the contour plots, as a function of measured Q_{31}^{R} and calculated $tan\,\mu_{31}$ values (**Equation (4.19)**). Three specific regions can be distinguished, i.e., $Q_{31}^{AR} > Q_{31}^{R}$ (red color), $Q_{31}^{AR} \approx Q_{31}^{R}$ (light blue/yellow), and $Q_{31}^{AR} < Q_{31}^{R}$ (blue color). It is illustrated that the transition between the regions is steeper in the high-Q_{31}^{R} and high- $tan\,\mu_{31}$ regimes and shallow in the reverse case. It turns out that the large Q_{31}^{AR}/Q_{31}^{R} ratio in hard PZT_T is primarily the consequence of the overall larger Q_{31}^{R} values and significant Q_{31}^{R} increase upon positive DC bias field, since the $tan\,\mu_{31}$ loss factor values are comparable between hard and soft PZT_T and do not significantly change upon DC bias increase compared to Q_{31}^{R}. It can be deduced that the two quality factors are tightly coupled and cannot be considered independently, i.e., the rising Q_{31}^{AR}/Q_{31}^{R} ratio is not attributed to different mechanistic processes with dissimilar susceptibility to DC bias fields, but to their phenomenological interrelation.

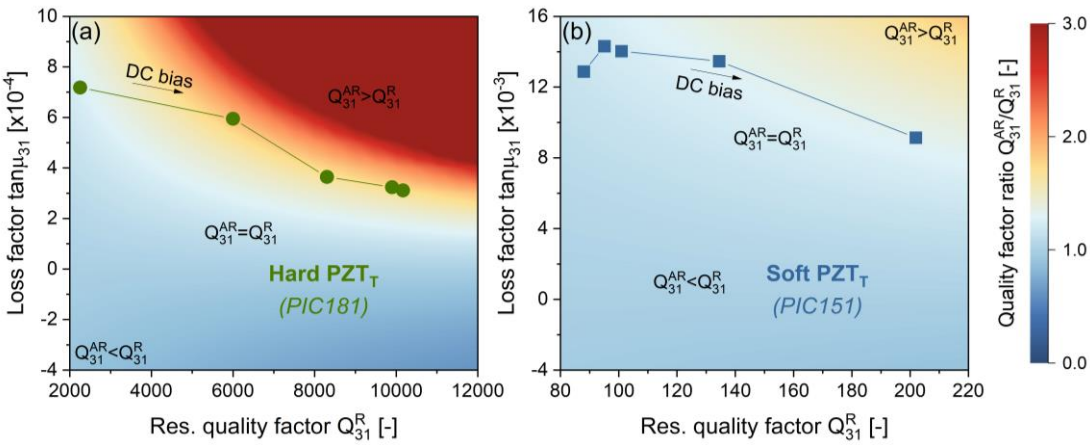

Figure 4.36. Contour plots of the resonance and antiresonance quality factor ratio (Q_{31}^{AR}/Q_{31}^{R}) as a function of resonance quality factor (Q_{31}^{R}) and loss factor ($tan\,\mu_{31}$) with a fixed coupling coefficient (k_{31}=0.34, **Equation (4.19)**), in (a) high Q_{31}^{R} and (b) low Q_{31}^{R} regime. Measured Q_{31}^{AR}/Q_{31}^{R} ratios of (a) hard PZT_T (PIC 181) and (b) soft PZT_T (PIC 151) are depicted in the contour plots.

4.5.3. Origin of the quality factor change with DC bias field

In order to reveal the origin of the observed Q_{31}^{R} (and coupled Q_{31}^{AR}) evolution under DC bias fields, the phenomenological description of the DC bias impact on the electromechanical loss is transferred to a mechanistic interpretation and is rationalized by following considerations: The applied DC bias field determines a point in the polarization and strain hysteresis loop of the sample in the polarized and aged state, at which a small AC electric field and dynamic mechanical stress are superimposed (illustrated schematically in **Figure 2.5** for zero DC bias). Starting from the remanent state, the positive DC bias field applied parallel to polarization direction induces domain switching, reversing the back-switching[xxii] after poling. The reduction of the Gibbs free energy for polarization directions along the applied electric field (Landau–Ginsburg–Devonshire theory [45, 46]) forces an elimination of all domains with unfavorable polarization vectors, leading to a growth of the domain size and reduction of domain wall density. In addition, following the same energetic argument, the DC bias field reduces the domain wall mobility by stabilizing the newly formed domain configuration and steepening the energy landscape, despite the increasing domain size and reduced domain wall density, which otherwise facilitate domain wall motion [62]. In a simplified representation, this can be described as an electric field-induced transition from a Rayleigh-like to a V-potential energy landscape [22, 94, 97]. Moreover, in case of acceptor-doped composition, the applied electric field accelerates the diffusion-controlled charge migration and defect-dipole reorientation, which additionally stabilizes the newly formed static domain configuration [239]. This is evidenced, for example, in **Figure 4.3g,i**, where the difference between maximum and remanent polarization/strain in the poled state (i.e., back-switching) is substantially reduced in hard PZT_T compared to soft PZT_T.

Upon application of the additional dynamic perturbation, i.e., applied small AC electric field and the emerging resonance mechanical stress, the coefficients $\varepsilon = {\partial P}/{\partial E}$, $s = {\partial S}/{\partial T}$, and $d = {\partial S}/{\partial E} = {\partial P}/{\partial T}$ are determined by the slope of the polarization/strain hysteresis loop at the point employed by the DC bias field (neglecting the frequency difference between large- and small-signal loops). The slope and thus the coefficients decrease with increasing DC bias field as a consequence of the domain stabilization. Furthermore, the hysteresis of the dynamic response reduces at large DC bias fields, implying reduced irreversible domain wall motion [57]. Hence, the increase of Q_{31}^{R} (and Q_{31}^{AR}) at positive DC bias fields is related to the immobilization of domain walls. This is supported by the simultaneous decrease of d_{31}, s_{11}^{E}, and ε_{33}^{T} and the fact that the decrease of these coefficients is more pronounced in the donor-doped than in the acceptor-doped PZT_T and PZT_R compositions, since domain wall motion has a more significant contribution to the electromechanical properties in soft ferroelectrics (Section 4.2.1). Primarily, it is the reduction of irreversible domain wall motion with its substantial out-of-phase component that leads to the increase of Q_{31}^{R}.

However, the correlation is not straightforward. Note that the applied DC bias fields are above the poling fields of the compositions (3 kV/mm for hard PZT_T and 2 kV/mm for soft PZT_T).

[xxii] Back-switching is a fluctuation process based on the energetic argument that the total domain wall free energy is determined by the difference between the wall energy per unit area and the product of temperature and entropy. Partial domain-switching to an unfavorable polarization direction increases the wall energy but also the entropy term, reducing overall the total free energy [54]. Defect-based domain wall pinning stabilizes the domain configuration and prohibits back-switching by increasing the wall energy per unit area.

Moreover, independent of the starting values, hard and soft PZT_T exhibit both very similar d_{31}, s_{11}^E, and ε_{33}^T values at large DC bias fields above 3.5 kV/mm and evidence a convergence of the coefficients to a constant value state. Convergence to the same values is, for example, also observed when approaching 0 K upon cooling, which has been related to a complete "freezing" of the extrinsic contributions [91]. Assuming that the intrinsic lattice contributions to the generated polarization/strain response are quantitatively similar in both compositions, the comparable residual coefficient values above 3.5 kV/mm indicate that the domain wall contribution (the only extrinsic contribution) has reduced to the same level in both compositions. Moreover, the convergence presumes that the properties in the range of maximum positive DC bias field are dominated by the intrinsic contributions. Yet, the Q_{31}^R values and the relative increase of Q_{31}^R reveal an enormous difference between hard and soft PZT_T. To elucidate the discrepancy, it must be recalled that d_{31}, s_{11}^E, and ε_{33}^T are determined by the magnitude of domain wall motion, whereas Q_{31}^R relays on the ratio between the in-phase and out-of-phase components. It can be deduced that the distinctly large Q_{31}^R values in hard PZT_T and their massive increase are associated with an efficient suppression of the out-of-phase component (i.e., irreversible domain wall motion) by a coupled DC bias field and defect-based stabilization of the newly formed domain configuration. Conductivity has no relevant impact of the Q_{31}^R evolvement, since the dielectric loss remains almost constant in the measured range (**Supplemental Figure 7.15**), indicating that the positive DC bias field does not reduce the conductivity. The magnitude of domain wall motion is also efficiently repressed in soft PZT_T; however, the flat potential and absent defect-based domain wall pinning still allow a substantial residual portion of out-of-phase domain wall motion.

An alternative explanation arises from the above-mentioned assumption that the intrinsic contributions dominate the polarization/strain response at large DC bias. In this case, inferior Q_{31}^R values in soft PZT_T can be related to extensive intrinsic loss. The origin is likely the lattice polarization rotation. A small ferroelectric crystal lattice distortion, i.e., in this case a small tetragonal distortion, such as was found in soft PZT_T (**Table 4.1**), is correlated with a shallow Gibbs free energy distribution according to the Landau–Ginsburg–Devonshire theory [45, 46]. The flat energy distribution facilitates the extension of the electric dipole in the lattice and promotes the rotation of the lattice polarization vector upon external perturbation [213]. An enhanced polarization rotation has already been suspected in soft PZT_T due to the pronounced deviation of the orientation-dependent lattice plane strains away from the polar axis towards a 45° angle in the polar representation (**Figure 4.12**). In single-domain single-crystals, an enhanced polarization rotation has been demonstrated to be accompanied by significant loss (out-of-phase component), markedly reducing the quality factor [102, 103]. Under these considerations, it can be deduced that enhanced susceptibility to polarization rotation and intrinsic loss are the reason for the inferior Q_{31}^R (and coupled Q_{31}^{AR}) values of soft PZT_T compared to hard PZT_T, even at large positive DC bias fields, where extrinsic contributions and loss are mostly extinguished. The rotation arises from the weak tetragonal lattice distortion, which is in turn determined by the Ti-Zr ratio of the compositions, while doping is not expected to have a noticeable impact on the distortion [43].

A strategy to confirm these mechanistic explanations of the DC bias impact would be to examine the presence of polarization/strain generating processes at large DC bias fields and compare them to the unbiased condition. Diffraction studies, such as proposed in Section 4.2, would be a reasonable experimental approach for such investigations. Studies on single- and multi-

domain single-crystals and extrapolation to poly-crystalline materials could be an alternative approach; however, the growth of crystals with these chemical compositions is challenging.

In theory, the polarization and strain responses to the electric field will become linear above a threshold value, leading to constant dielectric, mechanical, and piezoelectric coefficients. At this point, a saturated domain configuration and a purely intrinsic contribution are reached (intrinsic non-linearity is neglected). Under this condition, it would be possible to extract the $Q_{31}^{R/AR}$ values associated solely with the intrinsic loss of the poly-crystalline material and to compare it (with some limitations[xxiii]) to a multi-domain single-crystal of same composition. According to the P-E and S-E hysteresis loops (**Figure 4.3**) and the coefficients d_{31}, k_{31}, s_{11}^{E}, and ε_{33}^{T} (**Figure 4.24**), this state was not entirely reached yet under the applied measurement conditions. This state will be approached in subsequent studies, since it requires an enhancement of the dielectric breakdown strength of the materials. Following the above discussion, the threshold electric field is expected to be higher in soft compositions than in hard compositions, due to the missing assistance of defect-based domain wall pinning.

At negative DC bias fields, two processes are coupled. At low field values, the reverse DC bias field-effect appears, i.e., the field opposite to the polarization direction destabilizes the domain configuration, which facilitates (irreversible) domain wall motion and leads to enhanced d_{31}, k_{31}, s_{11}^{E}, and ε_{33}^{T} and reduced Q_{31}^{R} values. Reaching the coercive field, the sample depolarizes rapidly. In hard PZT_T, however, Q_{31}^{R} increases at negative DC bias field before depolarization and initiates a substantial increase of FOM^{HP}. The origin of this behavior is suspected to be related to a continuous rather than rapid depolarization process in hard PZT_T. The defect-stabilized domain configuration shifts the coercive electric field to larger negative values and spreads the depolarization process over a broader field range (**Figure 4.3**). The continuous depolarization with increasing negative DC bias fields occurs in terms of decreasing domain size, increasing domain wall density, as well as nucleation and growth of depolarized areas, which are electromechanically non-active. This configuration leads to significant mismatch stress and a so-called "self-pinning" effect of the domain walls [54]. At the same time, the polarization switching facilitates charge migration and defect-dipole reorientation, which are no longer localized at the domain wall or aligned along the polarization direction. This is evidenced by the simultaneously increasing dielectric loss (**Supplemental Figure 7.15**), which is conductivity-dominated in acceptor-doped compositions. As a consequence, Q_{31}^{R} increases while Q_{31}^{AR} decreases with the progressing depolarization upon increasing negative DC bias field (**Equation (4.19)**). A qualitatively equivalent evolution of Q_{31}^{R} and Q_{31}^{AR} has been reported during partial polarization of a PZT-composition starting from an unpolarized state [33].

4.5.4. Impact of experimental conditions on the DC bias dependence

PZT-based compositions are prone to a severe decrease of $Q_{31}^{R/AR}$ upon increasing vibration velocity with an especially large slope in the low vibration velocity range (**Figure 4.7** and **Figure 4.8**). The decrease is a potential error source for small-field measurements. The resonance impedance spectroscopy is usually conducted under constant driving AC electric field amplitudes (Section 3.1.1). The maximum vibration velocity appears thereby at the resonance and is determined by the applied field amplitude and the electromechanical coefficients

[xxiii] Due to the random orientation of grains in the poly-crystal and the intrinsic anisotropy, the determined values would represent an average intrinsic loss integrated over all possible orientations.

according to **Equation (2.48)**. Suppose the electromechanical coefficients undergo a change due to external perturbation, e.g., an additional DC bias field. Then the driving field amplitude requires an adjustment in order to maintain a constant (resonance) vibration velocity between measurements. In turn, the application of the constant field measurement conditions induces different vibration states, which can have an enormous impact on the measured Q_{31}^{R} values, due to the substantial change of Q_{31}^{R} as a function of vibration velocity (especially in the range of low vibration velocities).

Figure 4.37 schematically displays the situation of strong Q_{31}^{R} decrease, as it was found in the PZT compositions (**Figure 4.7** and **Figure 4.8**). An external parameter (DC bias field) will predominantly change the Q_{31}^{R} values but not the vibration velocity stability (evidenced above for chemical modifications and temperature). Therefore, the measurement conditions with constant field amplitude or constant vibration velocity will lead to different Q_{31}^{R} values determined as a function of the external parameter. The effect is expected to be smaller in (hard) compositions that reveal a threshold vibration velocity (e.g., hard PZT_T), in compositions with a stable Q_{31}^{R} evolution, or in (soft) compositions with small susceptibility of Q_{31}^{R} (or FOM^{HP} in general) to the external perturbation. The influence of the conditions is small for the determination of d_{31}, k_{31}, s_{11}^{E}, and ε_{33}^{T}, which generally have little vibration velocity dependence, especially in the range of low fields and/or low vibration velocities (**Figure 4.7** and **Figure 4.8**). Also the influence on Q_{31}^{AR} is negligible, due to the large impedance and inherently small vibration velocity ($v_1 \rightarrow 0\ m/s$) under small AC electric fields.

Therefore, it is proposed to perform the measurements under constant resonance vibration velocity to overcome this ambiguity. Hard PZT_T and soft PZT_T were measured under 0.05 m/s and 0.01 m/s, respectively. The driving AC field was adjusted after setting the DC bias field and ranged between 0.02-0.06 V/mm and 0.14-0.17 V/mm, respectively. On the other hand, PZT_R compositions were measured under constant AC field amplitude. The field was adjusted in the range between 0.15-0.95 V/mm only at zero DC bias field for a resonance vibration velocity of 0.03 m/s. Therefore, it is suspected that the measurement conditions could have influenced the DC bias field dependence of Q_{31}^{R} measured for the PZT_R compositions (**Supplemental Figure 7.14**). This is based on the observation that Q_{31}^{AR}, which is independent of the measurement conditions, reveals a dramatically larger increase than Q_{31}^{R}, especially in the hard PZT_R compositions, although both coefficients are phenomenologically interrelated.

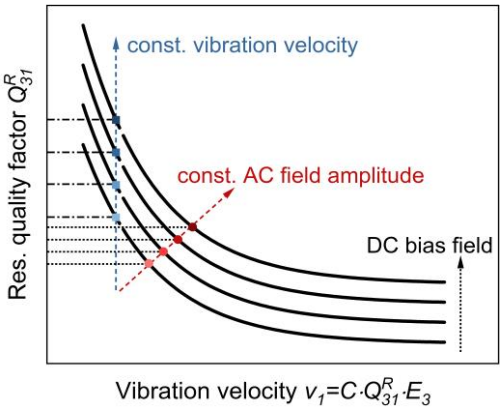

Figure 4.37. Schematic representation of typical resonance quality factor (Q_{31}^{R}) dependence of PZT-based compositions on the vibration velocity (v_1) at different DC bias fields. Is is assumed that the applied DC bias field influences the Q_{31}^{R} values without changing the vibration velocity stability. The dependence of Q_{31}^{R} on the DC bias field is different when the values are determined at equal vibration velocities or driving AC field amplitude.

4.5.5. Conclusions

Resonance impedance spectroscopy with superpositioned large DC bias fields is a useful approach to elucidate the phenomenological and mechanistic correlations between small-field electromechanical coefficients and their loss under resonance conditions. The quality factors $Q_{31}^{R/AR}$ demonstrated a remarkable increase upon applying DC bias fields along the poling direction, implying a strong hardening effect. d_{31}, k_{31}, s_{11}^{E}, and ε_{33}^{T} exhibited the opposite field dependence. In accordance with the previous results, both effects were attributed to the stabilization of the domain configuration and particular suppression of the out-of-phase components, primarily by inhibiting irreversible domain wall displacement. The stabilization is thereby most efficient if assisted by acceptor-defect-based domain wall pinning. An alternative explanation based on the intrinsic loss generation through polarization rotation was proposed as well, which needs to be confirmed in subsequent investigations, e.g., by diffraction studies.

Contraintuitivly, the impact on $Q_{31}^{R/AR}$ is much more prominent in acceptor-doped compositions, although the overall magnitude of domain wall motion and its contribution to the piezoelectric, mechanical, and dielectric coefficients is smaller. In contrast, the changes of d_{31}, k_{31}, s_{11}^{E}, and ε_{33}^{T} are distinctly larger in the donor-doped compositions. The same trend was discussed for chemical modifications and temperature as external parameters. It highlights the crucial need to consider the nature of the electromechanical response, i.e., the in-phase and out-of-phase components, as much as the overall magnitude. In consequence, only the acceptor-doped ferroelectrics (hard PZT_T) benefit from the DC bias field support in terms of significantly increasing FOM^{HP} values.

The extensive DC bias field capability of the utilized experimental setup enabled to determine a maximum FOM^{HP} in hard PZT_T. The maximum appeared at a comparably moderate DC bias field of 2 kV/mm (roughly the material's coercive field), which could be realized in selected applications. Therefore, it is the next step to implement an AC and DC electric field superposition in pulse drive measurements with burst excitation, in order to investigate the impact of DC bias fields also on the high-power stability of the electromechanical coefficients at large vibration velocities.

4.6. Mode dependence and anisotropy of the quality factors

Piezoelectric properties of ferroelectrics are anisotropic. Therefore, electromechanical coefficients are expressed as tensors in the constitutive equations with subscripts and superscripts depicting their directionality and mechanical/electrical boundary conditions (**Equation (2.8)-(2.9)**). Consistently, directionality and boundary conditions need to be accounted for loss as well (**Equations (2.36)-(2.38)**) [240]. Nevertheless, quality factors are commonly considered as isotropic coefficients, for example, in the European (EN 50324) [28, 241] or the IEEE (ANSI/IEEE Std 176–1987) [183] Piezoelectric Standardization, as well as in most industrial datasheets, although small-field measurements [173] and theoretical calculations [37] already revealed that $Q_{ij}^{R/AR}$ depend on the nature of coupling, i.e., on the dominant tensor indices and the mechanical/electrical boundary conditions. Consideration of this directionality is required for device design and plays a major role in performance enhancement. However, when it comes to high-power properties, current reports focus almost exclusively on the transverse length (31) vibration mode. Only few studies were done on the

radial (p) mode [135, 143, 157] and the longitudinal length (33) mode [152], even though the (33) mode is frequently used, for example, in ultrasonic transducers. These modes represent three of the five fundamental modes required to determine the ten independent electric, mechanical, and piezoelectric coefficients of a poly-crystalline piezoelectric ceramic with ∞m symmetry (Section 2.2.1).

Here, it is systematically investigated how the different vibration modes influence the individual electromechanical coefficients and their vibration velocity dependence. The study is conducted on hard PZT_T. All samples were cut and prepared from a single sintered block. This commercial material has a reliable chemical homogeneity to suppress sample-to-sample alternation in the study. The electromechanical coefficients are discussed with respect to the ferroelectric anisotropy and the vibrational strain distribution. The practical relevance is demonstrated by means of heat generation under constant drive conditions.

4.6.1. Resonance quality factors in transverse (31) and planar (p) vibration modes

The high-power resonance quality factors in the transverse (Q_{31}^R) and planar (Q_p^R) vibration modes are presented in **Figure 4.38a**, the corresponding sample geometries are depicted in **Table 2.1**. The measurement range was experimentally limited to 0.8 m/s; however, the majority of the quality factor decrease appears already in this low vibration regime (demonstrated on Q_{31}^R in **Figure 4.7a**) and carries the information on the mode dependency. The values obtained by the pulse drive measurement with burst excitation at low velocities are in good agreement with the values determined from small-field resonance impedance spectroscopy (star symbols in **Figure 4.38a**). Q_{31}^R and Q_p^R experience a rapid decrease with increasing vibration velocity, which has been discusses above for the transverse mode and reported on the planar mode in other PZT-based ferroelectrics [157]. While both curves exhibit a similar trend of Q_{ij}^R decrease, overall the Q_p^R values are lower than Q_{31}^R in the entire velocity range. This down-shift results from two convoluted effects: (1) A shape-difference of the strain distribution profiles, i.e., the difference between the one-dimensional linear vibration of the (31) mode compared to the two-dimensional radial vibration of the (p) mode. (2) And the intrinsic ferroelectric anisotropy, which originates from the contribution of different elastic compliance tensor elements and corresponding elastic loss.

In order to separate these two effects, the dimensionality is extracted first. To compare high-power properties of piezoelectric resonators, the electromechanical coefficients are determined with respect to the non-dimensional vibration velocity. Resonators of different sizes that exhibit the same vibration velocity are in equal strain states (**Equation (2.47)**), which in turn determines the electromechanical values. However, this assumption fails when comparing the (p) and (31) modes due to the radial or linear strain distribution, respectively. FEM models of the von Mises strain are depicted in **Figure 4.38d,e** to demonstrate the difference. The strain distributions along the traces (red lines in **Figure 4.38d,e**) were normalized to the center strain in the (31) resonator and are given in **Figure 4.38c**. The maximum strain in the (p) mode is considerably larger than in the (31) mode for all vibration velocities. For example, the difference at 0.6 m/s is about 37 % (**Figure 4.38c**). The larger strain results in lower Q_p^R values, which is mechanistically related to enhanced motion of ferroelectric/ferroelastic domain walls.

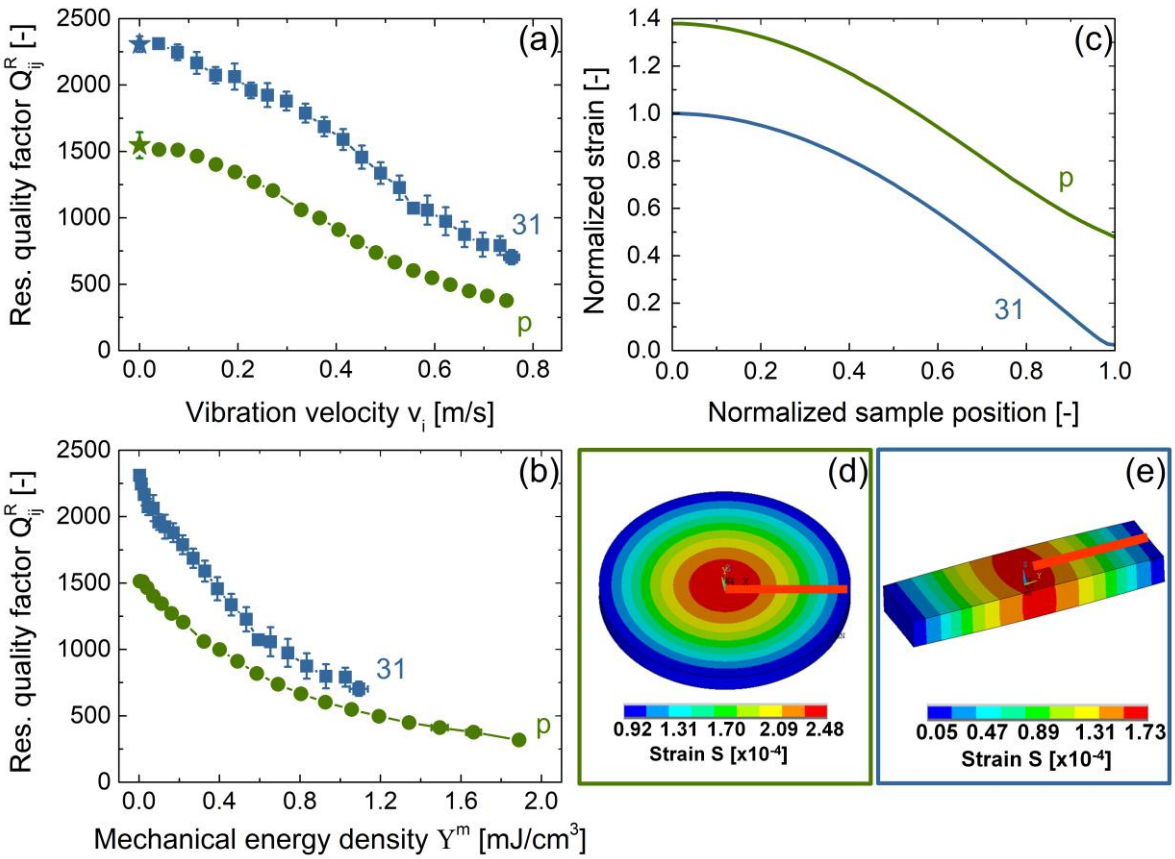

Figure 4.38. Resonance quality factors (Q^R_{31} and Q^R_p) of hard PZT$_T$ as a function of linear or radial (a) vibration velocity (v_i) and (b) mechanical energy density ($\Upsilon^{m,31}$ and $\Upsilon^{m,p}$) in the transverse (31) and planar (p) vibration modes. (c) FEM modeled von Mises strain distribution trace profiles for the (31) and (p) modes at 0.6 m/s edge vibration velocity, normalized to the maximum strain in the sample center in the (31) mode. (d,e) Corresponding 3D strain distribution models and traces (red lines).

In order to exclude the strain state influence, the Q^R_{31} and Q^R_p values must be contrasted to the mechanical energy density ($\Upsilon^{m,31}$ and $\Upsilon^{m,p}$), instead of the vibration velocity. The mechanical energy density can be expressed in terms of the maximum elastic energy, utilizing the non-linear tensorial expression of the elastic compliance, or in terms of the maximum kinetic energy, which is given for the two modes by [175]

$$\Upsilon^{m,31} = \frac{1}{4}\,\rho v_1^2 \text{ and} \tag{4.20}$$

$$\Upsilon^{m,p} = 0.3915\,\rho v_1^2. \tag{4.21}$$

Q^R_{31} and Q^R_p as a function of $\Upsilon^{m,31}$ and $\Upsilon^{m,p}$ are displayed in **Figure 4.38b**. Both resonance quality factors rapidly decrease with increasing mechanical energy density. Moreover, Q^R_p values still experience a down-shift with respect to Q^R_{31}. However, the down-shift in the proposed representation is attributed solely to the different values of the individual tensor components of the elastic compliance/loss and is not shadowed by the different vibration velocity distribution profiles anymore.

The phenomenological description of Q^R_{31} in Section 2.2.3 derived that, utilizing the constitutive **Equations (2.22)** and **(2.23)**, and the assumption that the resonator is a perfect insulator

exhibiting a displacement solely along its length, the resonance quality factor becomes equal to the inverse of the elastic loss (**Equation (2.45)**). The elastic loss accounts for the complex nature of the elastic compliance tensor elements [38] and considers that the evolving dynamic mechanical stress generates the majority of resonance strain. Utilizing the same derivations for the planar mode [39], the ratio between Q_{31}^{R} and Q_{p}^{R} can be expressed as

$$Q_R^p = \frac{\kappa_{11}-\kappa_{12}}{\kappa_{11}-\kappa_{12}\frac{tan\,\gamma_{12}}{tan\,\gamma_{11}}} \cdot Q_R^{31}, \text{ with} \tag{4.22}$$

$$\kappa_{11} = \frac{1+\sigma^2}{1-\sigma^2}\Omega_R^2 - (1-\sigma)^2, \tag{4.23}$$

$$\kappa_{12} = 2\sigma\left[\frac{\sigma}{1-\sigma^2}\Omega_R^2 + (1-\sigma)\right], \text{ and} \tag{4.24}$$

$$\Omega_R = \frac{\omega_p^R d}{2v_p^E}. \tag{4.25}$$

The parameters κ_{11}, κ_{12}, and Ω_R depend on the Poisson's ratio (σ), planar angular resonance frequency (ω_p^R), sample diameter (d), and radial sound velocity (v_p^E). $tan\ \gamma_{12}$ and $tan\ \gamma_{11}$ are the elastic loss of s_{12}^E and s_{11}^E and determine the relation between Q_{31}^R and Q_p^R according to (**Supplemental Figure 7.16**)

$$if\ \begin{Bmatrix} tan\ \gamma_{12} < tan\ \gamma_{11} \\ tan\ \gamma_{12} = tan\ \gamma_{11} \\ tan\ \gamma_{12} > tan\ \gamma_{11} \end{Bmatrix},\ than\ \begin{Bmatrix} Q_p^R < Q_{31}^R \\ Q_p^R = Q_{31}^R \\ Q_p^R > Q_{31}^R \end{Bmatrix}. \tag{4.26}$$

Note that $tan\ \gamma_{12}$ was previously reported to be smaller than $tan\ \gamma_{11}$ in PZT-based ferroelectrics [39, 240]. This is in agreement with the observed down-shift of Q_p^R compared to Q_{31}^R, in the entire probed vibration velocity or mechanical energy density ranges (**Figure 4.38a,b**). Moreover, the decrease of Q_{31}^R and Q_p^R with increasing mechanical energy density is quantitatively not the same for both vibration modes; while Q_{31}^R decreases by 70% between 0 and 1.1 mJ/cm³, the decrease of Q_p^R is only 64%. The difference might indicate that $tan\ \gamma_{12}$ exhibits a more pronounced increase with increasing mechanical energy density than $tan\ \gamma_{11}$.

4.6.2. Resonance quality factors in transverse (31) and longitudinal (33) vibration modes

The longitudinal (33) vibration, also denoted as stiffened mode, exhibits a one-dimensional displacement along the thickness (**Table 2.1**). This means that the displacement vector is parallel to the applied electric field and polarization, unlike the transverse (31) mode (unstiffened). Therefore, it was experimentally required to rotate the sample by 90° with the electroded faces towards the laser vibrometer, in order to conduct the pulse drive measurements (**Figure 3.2b**). In this configuration, the electrical connection to the circuit was established by thin Ag-wires attached to the electroded sample surfaces instead of the spring-loaded pins. Initial measurements in this arrangement revealed a small-signal Q_{33}^R value of 1422, which is almost half of the small-signal Q_{31}^R value of 2313 (filled star symbols in **Figure 4.39a**). With increasing vibration velocity, Q_{33}^R decreases and approaches the same value as Q_{31}^R above 0.55 m/s.

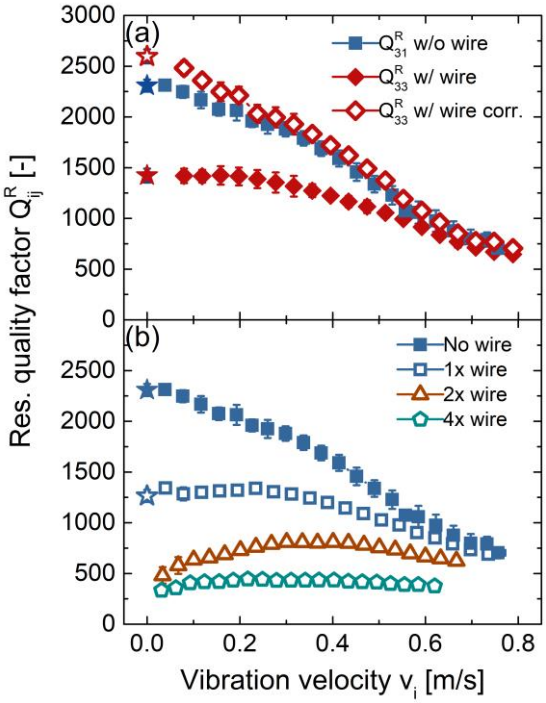

Figure 4.39. (a) Resonance quality factor of hard PZT$_T$ in transverse (31) mode (Q^R_{31}) measured without attached wire, in comparison to the resonance quality factor in longitudinal (33) mode (Q^R_{33}) with one wire attached to each side, and the corrected true Q^R_{33} values as a function of vibration velocity (v_i). (b) Q^R_{31} measured without (standard configuration), and with one, two, and four Ag- wires attached to each side of the surfaces in the vibration direction.

However, the low Q^R_{33} obtained in this initial configuration does not represent the true material response, but is influenced by the measurement condition. In order to demonstrate the experimental influence, several reference measurements using the (31) transducer geometry were performed. Different numbers of Ag-wires were attached to the non-electroded faces of the sample in the vibration direction (**Figure 3.2b**). Pulse drive measurements were carried out to examine the influence on the determined properties. Note that the attached wires were not electrically connected to the circuit. A drastic decrease of Q^R_{31} with increasing number of mounted wires demonstrates the influence of additional attached mass on the vibrating surface (**Figure 4.39b**). The impact is especially noticeable in the low vibration velocity regime. Simultaneously, the maximum achieved vibration velocity decreases, although the resonator driving electric field amplitude remains unchanged. Moreover, several alternative measurement configurations have been investigated, including different wire material, mass, and thickness, different attachment methods, and electrical conditions (short- or open-circuited wires). It was concluded that the influence has a mechanical rather than an electrical origin; however, the effect could not be avoided. It is assumed that the decrease of the Q^R_{ij} values is caused by the dissipation of vibrational energy into the attached wires and the adhesive.

Therefore, in order to compensate instead of eliminate the influence of the wires on the measured data, the Q^R_{31} measurements (**Figure 4.39b**) were used to determine a correction factor for the corresponding number of attached wires. This factor was applied to the initial Q^R_{33} result in order to extract the true Q^R_{33} values of the sample without wire influence (**Figure 4.39a**; open symbols). The corrected Q^R_{33} is quantitatively very similar to Q^R_{31} and exhibit an equal evolution throughout the entire vibration velocity range. This result is in agreement with the

conclusion of small-field studies [39], where no difference between Q_{33}^{R} and Q_{31}^{R} was observed for PZT-based ferroelectrics.

4.6.3. Dielectric, mechanical, and piezoelectric coefficients in the (31), (33), and (p) modes

The piezoelectric, mechanical, and dielectric coefficients (d_{31}, d_{33}, k_{31}, k_{33}, k_p, s_{11}^{E}, s_{33}^{E} and σ) of the three vibration modes were determined as a function of vibration velocity and are presented in **Figure 4.40**. It must be noted that the wires required for the measurement of the longitudinal (33) mode only influenced the Q_{33}^{R} values (see previous section), but had no influence on the other electromechanical coefficients; thus, no corrections were required. The reason is that those coefficients are affected mainly by the sample's mass, elastic compliance, and vibration velocity distribution, which are hardly changed by the thin wires, contributing less than 3% to the total mass of the samples.

All coefficients, with the exception of Poisson´s ratio σ, increase at large vibration velocity, which has been revealed above to be mechanistically correlated with an enhanced motion of ferroelectric/ferroelastic domain walls driven by the emerging dynamic mechanical stress. The increase of the coefficients in this low vibration velocity range accurately can be fitted by a quadratic expression (**Equation (2.56),** X: d_{31}, d_{33}, k_{31}, k_{33}, k_p, s_{11}^{E}, s_{33}^{E}, or ε_{33}^{T}). The expression has been derived from empirical [161] and non-linearity models [162, 178] for PZT-based ferroelectrics with particularly large Q_{ij}^{R} values. Thereby, ϑ is the quadratic proportionality constant indicating the coefficient´s stability under high-power drive. The fitting determines that d_{31}, k_{31}, and s_{11}^{E} exhibit quantitatively significant larger vibration velocity dependencies (larger ϑ values) than d_{33}, k_{33}, k_p, and s_{33}^{E} (**Figure 4.40**).

The quadratic expression resembles the observed threshold vibration velocity range around 0.4 m/s in hard PZT_T (Section 4.1.3), where the electromechanical coefficients reveal a distinct change in the slope of their vibration velocity dependence (**Figure 4.7**). The correlation appears to be valid predominantly in the low vibration velocity range of hard PZT_T; the vibration velocity dependence of the electromechanical coefficients in a broad vibration velocity range was shown to have a dominant linear component (**Equation (4.5)**), which also applies for the other compositions (**Figure 4.7** and **Figure 4.8**).

σ is the only coefficient that slightly decreases with increasing vibration velocity, indicating strain decoupling along different spatial directions. The reason is not clear yet and cannot be referenced to literature, since measurements of σ in resonance and dependence on vibration velocity have not been reported before. σ was determined only until 0.4 m/s due to the difficulties to measure the (p) mode in antiresonance, related to the large capacitance of the resonator.

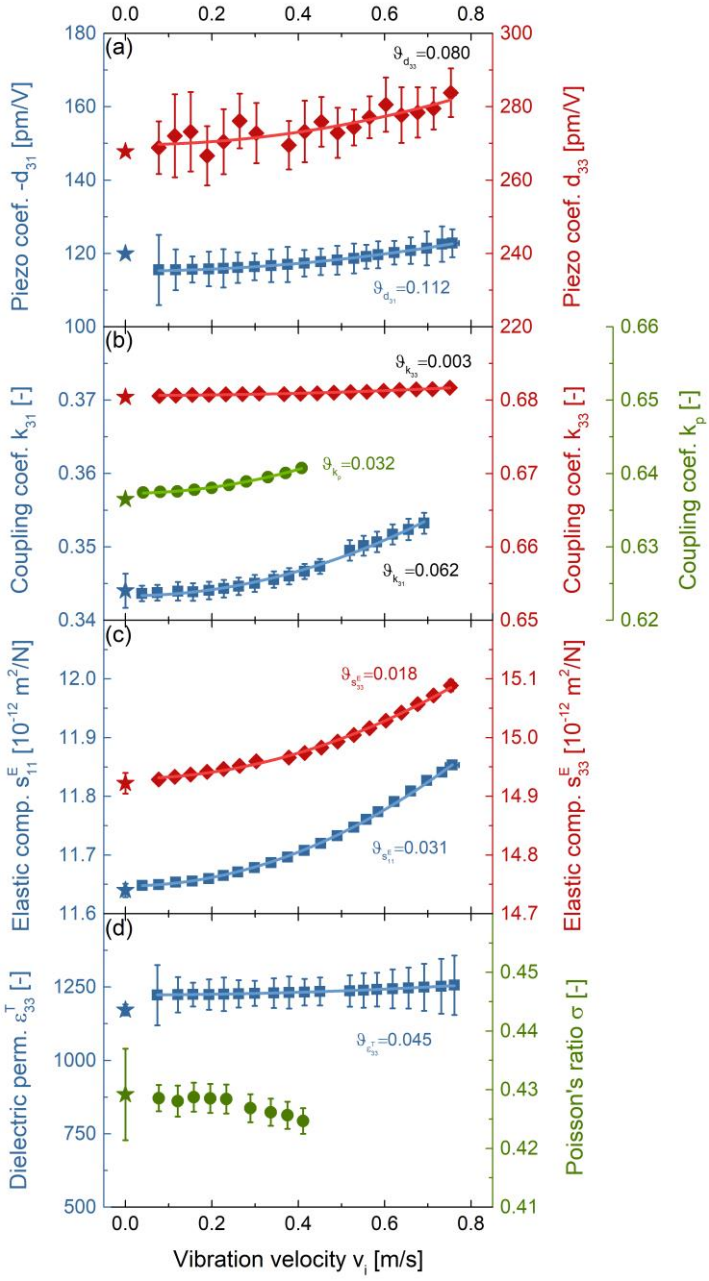

Figure 4.40. Electromechanical coefficients of hard PZT$_T$ in the transverse (31), longitudinal (33), and planar (p) modes as a function of vibration velocity (v_i): (a) Piezoelectric coefficients ($-d_{31}$ and d_{33}), (b) coupling coefficients (k_{31}, k_{33}, and k_p), (c) elastic compliance (s_{11}^E and s_{33}^E), (d) dielectric permittivity (ε_{33}^T), and Poisson's ratio (σ).

4.6.4. Mode dependent self-heating effects

In high-power applications, the piezoelectric element is usually driven continuously for a defined time period under constant AC electric field excitation amplitude. The field amplitude and the generated vibration velocity are limited by the evolving loss, which lead to heat generation through so-called "self-heating" effects. The heating induces severe changes of the transducer properties (Section 4.4) and is capable of initiating thermal depolarization of the ferroelectric material in case of overload. Heat generation through self-heating for the three vibration modes, (31), (33), and (p), is shown in **Figure 4.41** as a function of vibration velocity. Note that the measurements were performed under continuous drive of the resonator at constant vibration velocity until temperature stabilization. No significant temperature variation

was observed up to 0.4 m/s, which was denoted before as the threshold vibration velocity. Above that boundary, a considerable temperature rise was detected in the sample vibrating in the radial (p) mode. The temperature rise was significantly larger compared to the two other modes, which correlates to the lower Q_p^R values identified before in **Figure 4.38a**. On the other hand, the temperature profiles of the transverse (31) and longitudinal (33) modes are very similar, which confirms the observed similar values of Q_{31}^R and Q_{33}^R (**Figure 4.39a**). Noticeable temperature rise for these two modes starts at about 0.5 m/s, which marks a vibration velocity regime, where the Q_{ij}^R difference and the wire influence disappear.

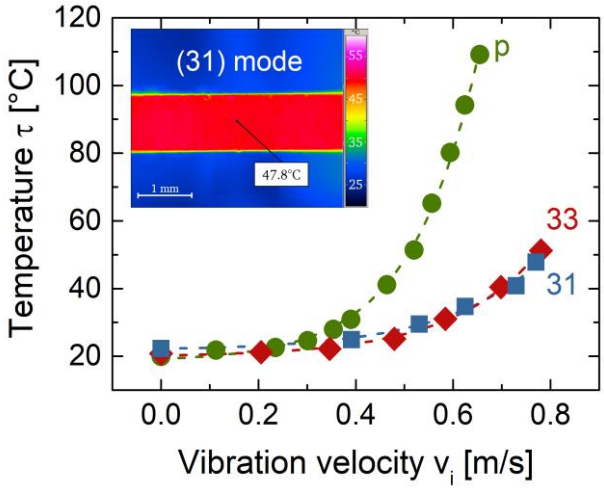

Figure 4.41. Stabilized sample temperature (τ) of hard PZT$_T$ in the transverse (31), longitudinal (33), and planar (p) vibration modes as a function of vibration velocity (v_i). The samples were driven continuously at the resonance frequency with constant AC electric field amplitude. Inserted is the infrared camera image of the (31) mode sample at 0.78 m/s.

4.6.5. Conclusions

The Q_{ij}^R values and their stability upon increasing vibration velocity are closely related to the utilized piezoelectric vibration mode. Thereby, the determined down-shift of Q_p^R in comparison to Q_{31}^R is related to the convoluted effects of two- or one-dimensional strain distribution profiles and the contribution of different elastic loss tensor elements. No significant difference has been observed between Q_{31}^R and Q_{33}^R. This means that measurement results of Q_{31}^R in the experimentally more convenient transverse (31) vibration mode, can be in first approximation reasonably transferred also to the longitudinal (33) vibration mode. On the other hand, coupling coefficients, elastic compliances, and piezoelectric coefficients of the (31) and (33) modes exhibited distinctly different evolutions at elevated vibration levels. Therefore, it is concluded that the vibration mode dependence should be considered carefully when a material's high-power properties are evaluated or materials are compared, which is most often neglected in literature. This is illustrated by heat generation measurements under continuous drive. The qualitatively same tendencies from the vibration velocity-dependent Q_{ij}^R evolution and temperature rise through self-heating confirm the vibration mode relation. Hence, considering anisotropy and nonlinear behavior in device design instead of extrapolation of the small-field values can contribute to enhanced performance, e.g., in terms of reduced heat generation and thus enhanced maximum power output.

5. Next-generation high-power ferroelectrics – Lead-free $(Na_{1/2}Bi_{1/2})TiO_3$-$BaTiO_3$

The second result chapter reports the high-power electromechanical behavior of $(Na_{1/2}Bi_{1/2})TiO_3$-$BaTiO_3$-based (NBT-BT) ferroelectric systems. Recent studies indicated that several NBT-based compositions exhibit a much more stable quality factor over a broader vibration velocity range than their $Pb(Zr,Ti)O_3$-based (PZT) counterparts [143, 173, 176]. Although the origin of this behavior is not understood yet, these findings have already resulted in first patents and commercial products [142]. Thereby, the development of these lead-free alternatives is not only triggered by the environmental concerns related to lead toxicity [124], but particularly by the potential to outperform lead-based ferroelectrics in specific high-power applications.

In this chapter, the dependence of the electromechanical coefficients on the vibration velocity is evaluated first. A comparison to the previously introduced PZT compositions highlights the inherently different high-power properties of the two material families. A combined electromechanical characterization and in-situ synchrotron diffraction study resolves the underlying mechanisms (Section 5.1). Afterward, temperature-dependent in- and off-resonance measurements are applied to examine the hardening and depolarization processes, which determine the operational range of the compositions (Section 5.2). This is followed by the investigation of the DC bias as external parameter tailoring the electromechanical properties (Section 5.3). The findings are elucidated under the mechanistic considerations introduced for PZT-based ferroelectrics and the relaxor-ferroelectric nature of these compositions. It allows, in the end, to draw a general conclusion on the sustainability of NBT-BT-based compositions as next-generation high-power ferroelectrics and the further requirements for their transfer into application.

Parts of Sections 5.1 were published in the journal article *"Origin of high-power drive stability in $(Na_{1/2}Bi_{1/2})TiO_3$-$BaTiO_3$ based piezoceramics"*, Slabki, M., Venkataraman, L. K., Rödel, J., and Koruza, J., Acta Materialia 227 (2022).

Parts of Section 5.2 were published in the journal article *"Thermal stability of the electromechanical properties in acceptor-doped and composite-hardened $(Na_{1/2}Bi_{1/2})TiO_3$-$BaTiO_3$ ferroelectrics"*, Slabki, M., Venkataraman, L. K., Rojac, T., Rödel, J., and Koruza, J., J Appl Phys 130 (2021).

5.1. High-power drive stability

The relaxor-ferroelectric solid solution NBT-BT transforms into a long-range polarized ferroelectric upon electric poling (Section 2.4.3), exhibiting tetragonal crystal structure (NBT-9BT) or a rhombohedral/tetragonal phase mixture (NBT-6BT). Especially the MPB composition reveals thereby a considerable electromechanical coupling but low quality factors. The most significant enhancement of Q_{ij} is obtained upon Zn^{2+} doping [113, 114] and composite formation with ZnO secondary phase [72, 75]. While the Zn^{2+} doping follows the acceptor-defect model previously explained for PZT, the second-phase hardening mechanism is related to strain incompatibility and mechanical mismatch stress induced between the ferroelectrically-switching NBT-BT and the non-ferroelectric ZnO phases (likely with an additional doping contribution) [75, 84].

Here, after an initial description of the microstructure and the ferroelectric characteristics, the evolution of the electromechanical coefficients at large vibration velocity is discussed. The inherent high-power properties of NBT-BT, as well as the impact of the different hardening approaches, will be evaluated, involving the microscale strain contributions. Primary focus will be on three selected and representative MPB compositions: unmodified (NBT-6BT), B-site substituted with 1 mole % Zn^{2+} (NBT-6BT-1Zn), and the composite with 0.1 mole-ratio of ZnO (NBT-6BT:10ZnO). The results are compared to NBT-9BT and NBT-9BT:20ZnO, the previously introduced state-of-the-art medium-hard PZT_T, and other lead-free ferroelectrics.

5.1.1. Crystallographic, microstructural, and ferroelectric characterization

The average XRD diffractograms (obtained after integration over the entire azimuthal range) of the three representative NBT-6BT compositions in the polarized ferroelectric state are compared in **Figure 5.1**. The splitting of the $\{111\}_{pc}$ and $\{200\}_{pc}$ pseudocubic reflections indicates rhombohedral and tetragonal lattice distortions, confirming the phase mixture that has been established for compositions with 6 mole% $BaTiO_3$ [113, 166]. Rietveld refinements of the polarized undoped NBT-6BT composition determined 19 % and 81 % phase fractions of the tetragonal *P4mm* and rhombohedral *R3c* phases, respectively [242]. Phase fractions of the modified compositions in the polarized state have not been resolved yet. However, the broadening and intensity ratio change of the $\{200\}_{pc}$ reflection split upon doping and composite formation indicate increasing tetragonal phase fractions as well as increasing tetragonal distortions (**Figure 5.1c)**. Both have also been observed in the unpolarized relaxor state [72, 113]. Impurities or secondary phases are not evident in NBT-6BT and NBT-6BT-1Zn, while distinct reflections appear in the NBT-6BT:10ZnO diffractogram (**Figure 5.1d)**. Those have been assigned to the introduced ZnO secondary phase, as well as a $TiZn_2O_4$ spinel phase that has likely formed during sintering [72].

The microstructures and grain size distributions of the representative NBT-6BT, NBT-6BT:10ZnO, and NBT-6BT-1Zn compositions are displayed in **Figure 5.2** (other compositions in **Supplemental Figure 7.17**). No secondary phases are observed in the unmodified and doped samples, while the NBT-6BT:10ZnO microstructure consists of isolated ZnO inclusions (red arrows in **Figure 5.2b**) embedded in the NBT-6BT matrix. In addition, a small amount of another secondary phase appears (blue arrow), which is attributed to the $TiZn_2O_4$ spinel phase.

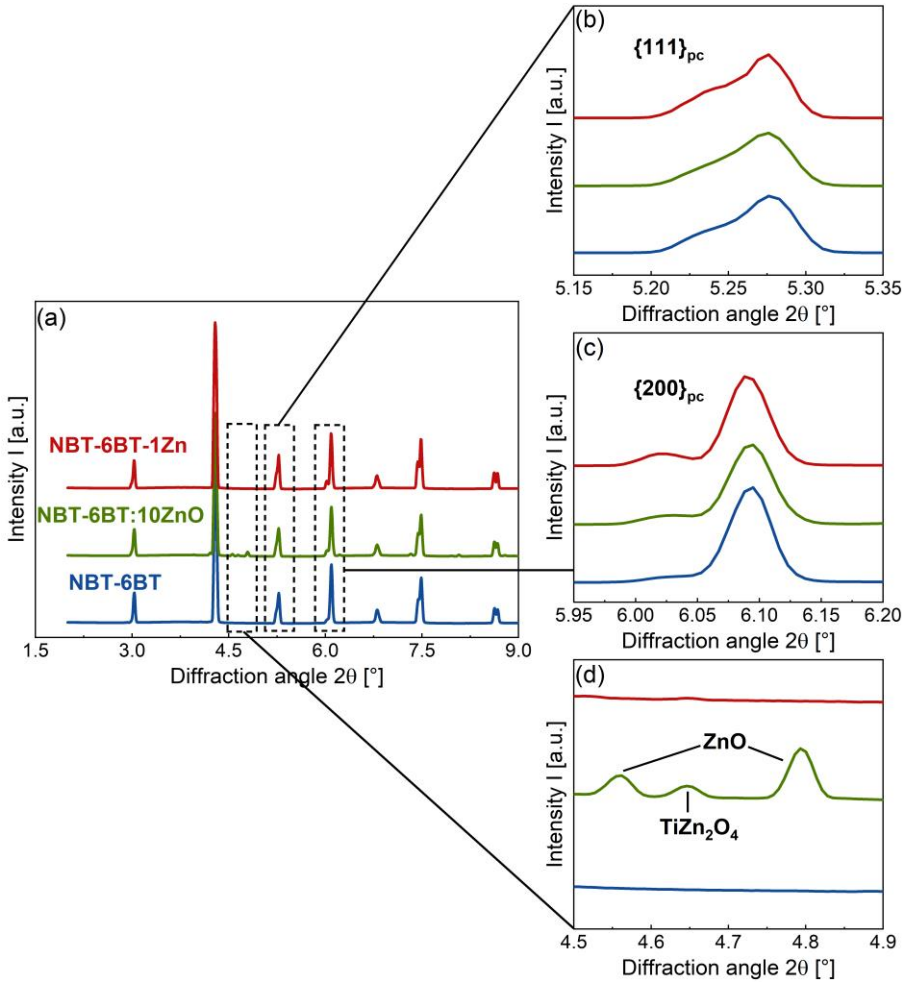

Figure 5.1. (a) Synchrotron diffractograms (λ=0.20673 Å) of the average crystal structure in the polarized ferroelectric state of unmodified NBT-6BT, Zn^{2+}-doped NBT-6BT-1Zn, and NBT-6BT:10ZnO composite. (b,c) Enlarged diffractogram ranges of $\{111\}_{pc}$ and $\{200\}_{pc}$ doublets demonstrate the mixed rhombohedral and tetragonal distortion. (d) Additional peaks in NBT-6BT:10ZnO originate from the introduced ZnO secondary phase and a formed $TiZn_2O_4$ spinel phase.

The average grain size and grain size distribution of the NBT-6BT phase increase by a factor of 2 in the composites and a factor of 4-8 in Zn^{2+}-doped samples, compared to the unmodified NBT-6BT (**Figure 5.2** and **Supplemental Figure 7.17**). It has been reported that a distinct increase in grain size correlates with enhanced thermal depolarization temperature (τ_d) and lower piezoelectric coefficient (d_{33}) values [171]. **Table 5.1** depicts the determined τ_d and d_{33} values of the NBT-BT compositions (will be discussed in the subsequent sections). In fact, such a trend is observed here; nevertheless, it is doubtful that the evolution of the values as well as the induced hardening and Q_{31}^R increase can be attributed to the grain size variation. For instance, although the average grain size increases by a factor of 2 in NBT-6BT-1Zn, as compared to NBT-6BT-0.5Zn, the changes in τ_d and d_{33} are only minor, below 6 %. Moreover, severe changes of the ferroelectric properties associated with modified domain configurations (a consequence of grain size variation) would only be expected in the sub-μm grain size range [243]. Therefore, the property evolution between the compositions will be assigned to the introduced modifications rather than the grain size dependence in the following analysis.

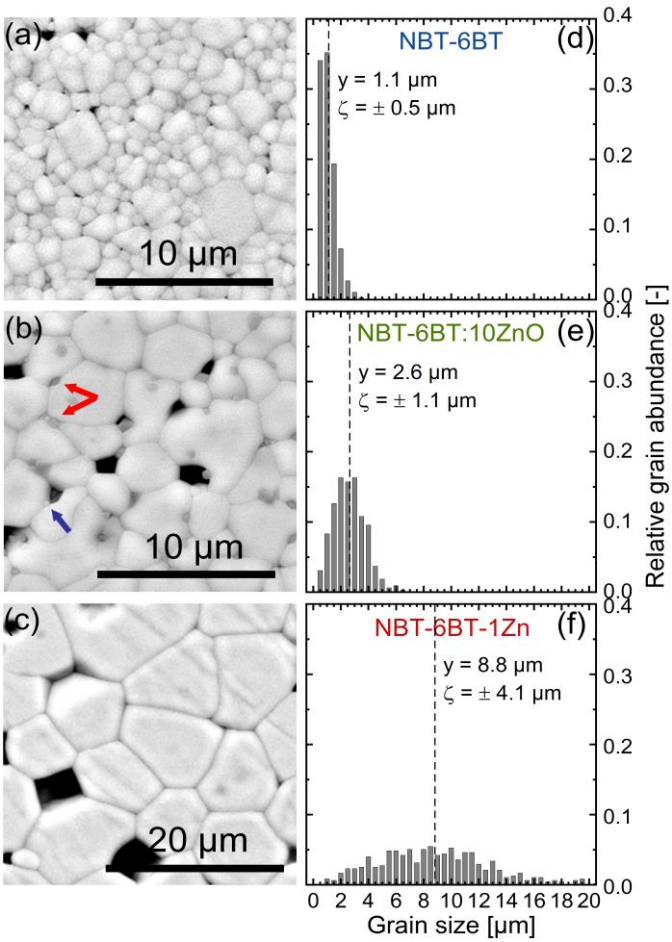

Figure 5.2. (a-c) Microstructures of unmodified NBT-6BT, Zn^{2+}-doped NBT-6BT-1Zn, and NBT-6BT:10ZnO composite determined by SEM. Arrows in (b) mark exemplarily inclusions of ZnO (red) and $TiZn_2O_4$ secondary phases (blue) in NBT-6BT:10ZnO. (d-f) Corresponding average grain size (y), size variance (ζ), and distribution. Note that only the NBT-6BT phase of NBT-6BT:10ZnO is represented in (e).

To evaluate the ferroelectric properties of the NBT-BT compositions, large-field bipolar P-E and S-E hysteresis loops were measured in the polarized and aged states (**Figure 5.3**). All compositions reveal square-shaped polarization loops and butterfly-shaped strain loops. The strain loops exhibit a distinct asymmetry after Zn^{2+}-doping and ZnO-composite formation. Moreover, the loops are shifted along the abscissa, evidencing the emergence of an internal bias field (E_{ib}) of 0.09 kV/mm, 0.30 kV/mm, and 0.41 kV/mm in NBT-6BT, NBT-6BT:10ZnO, and NBT-6BT-1Zn, respectively. Also the coercive fields (E_c) increase from 2.92 kV/mm in NBT-6BT to 3.04 kV/mm and 3.66 kV/mm in NBT-6BT:10ZnO and NBT-6BT-1Zn, respectively. The increasing asymmetry, internal bias fields, and coercive fields indicate ferroelectric hardening and domain wall clamping. The effect is stronger pronounced after Zn^{2+}-doping than after ZnO-composite formation, resulting in larger quality factor values (discussed later). Note that the internal bias field in NBT-6BT is comparable to those found for soft PZT_T and PZT_R, while the internal bias fields of NBT-6BT:10ZnO and NBT-6BT-1Zn are in the same range as those determined for medium-hard PZT_T and PZT_R (**Table 4.1** and **Table 4.2**). At the same time, the coercive fields of the NBT-6BT compositions are about a factor 3 larger than those of the PZT compositions. The large coercive fields in NBT-6BT indicate an inherent stability of the domain configuration and hindered domain wall switching.

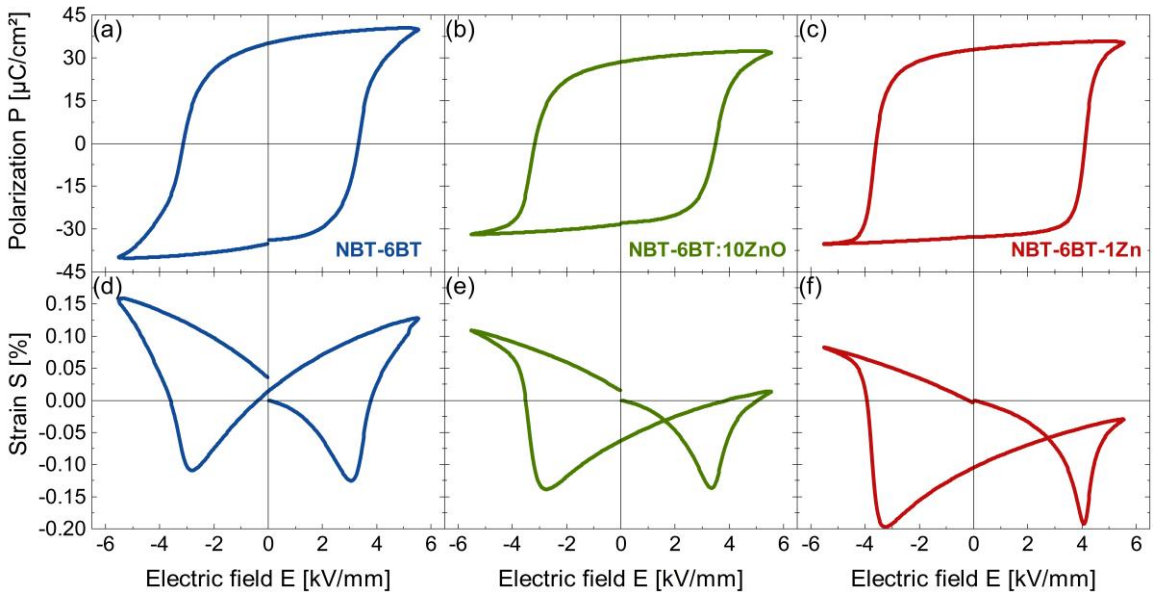

Figure 5.3. (a-c) Polarization (P) and (d-f) strain (S) hysteresis loops of unmodified NBT-6BT, Zn^{2+}-doped NBT-6BT-1Zn, and NBT-6BT:10ZnO composite in the polarized states as a function of applied bipolar electric field (E) at 1 Hz measurement frequency and 20 °C.

5.1.2. Electromechanical high-power properties

The high-power properties of the three representative NBT-6BT compositions in the transversal (31) vibration mode are depicted in **Figure 5.4** (further NBT-6BT and NBT-9BT compositions are displayed in **Supplemental Figure 7.18**). The electromechanical coefficients Q_{31}^{R}, Q_{31}^{AR}, d_{31}, k_{31}, s_{11}^{E}, and ε_{33}^{T} were determined as a function of vibration velocity at 20 °C by the pulse drive method with burst excitation. The small-field values of the coefficients were derived from resonance impedance spectroscopy and are denoted by star symbols in the figure and summarized in **Table 5.1**. It is essential to point out again that the discussion on the material's high-power properties must equivalently account for the values of the electromechanical coefficients as much as for their relative change or stability with increasing vibration velocity.

Unmodified NBT-6BT exhibits the lowest Q_{31}^{R} and Q_{31}^{AR} values in the range of 170 to 180. However, the values demonstrate an inherent stability and decrease moderately in a broad vibration velocity range (**Figure 5.4a**). After doping with 1 mole % Zn^{2+} $Q_{31}^{R/AR}$ values are approximately four-fold larger; the composite formation with 0.1 mole-ratio of ZnO achieves an almost two-fold increase. A further increase of the ZnO amount up to 0.4 mole-ratio in NBT-6BT has only a marginal additional effect (**Table 5.1**). The Zn^{2+}-doping reveals a more significant impact on the ferroelectric hardening of NBT-6BT than the introduction of the ZnO second phase, which agrees with the larger internal bias and coercive fields determined in **Figure 5.3**. Moreover, important is that the $Q_{31}^{R/AR}$stability is preserved or even slightly enhanced after doping as well as after composite formation (**Figure 5.4b,c**). The relative decrease of the resonance quality factor ($Q_{31}^{R}/Q_{31}^{R,0}$) is about 60 % at 3 m/s in all compositions, which is comparatively small, considering the generally strong sensitivity and dependence of $Q_{31}^{R/AR}$ coefficient on the vibration velocity[xxiv].

[xxiv] The $Q_{31}^{R/AR}$stability is a specific property of NBT-BT-based compositions. It is not a general feature of all lead-free or relaxor ferroelectrics (**Supplemental Figure 7.19**).

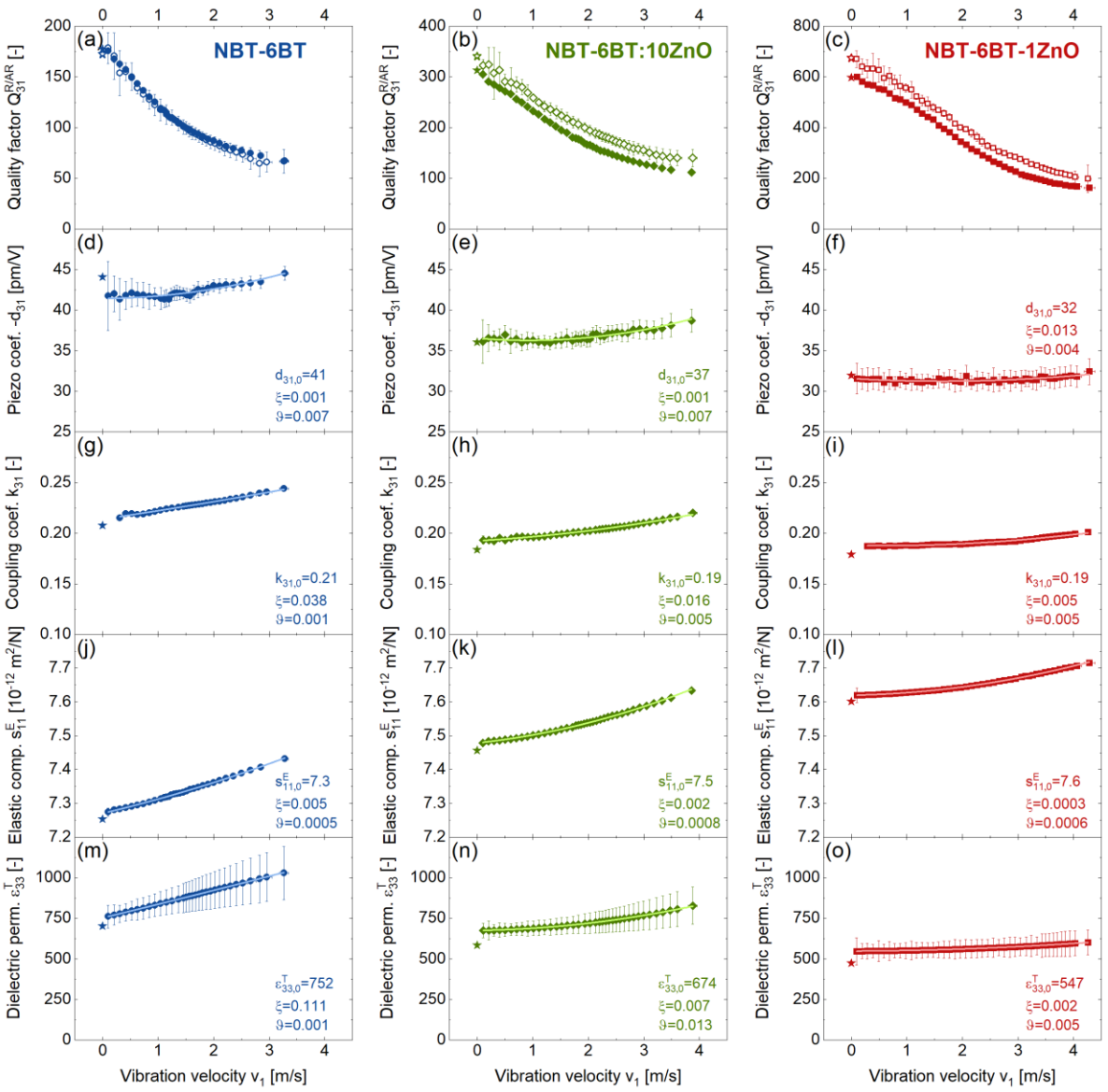

Figure 5.4. Electromechanical coefficients (a-c) Q_{31}^{R} (solid symbols) and Q_{31}^{AR} (open symbols; note the different scales), (d-f) d_{31}, (g-i) k_{31}, (j-l) s_{11}^{E}, and (m-o) ε_{33}^{T} of unmodified NBT-6BT, Zn^{2+}-doped NBT-6BT-1Zn, and NBT-6BT:10ZnO composite in the transverse (31) vibration mode at 20 °C as a function of vibration velocity (v_1). The data points denoted as stars at 0 m/s depict the small-field values determined from resonance impedance spectroscopy (**Table 5.1**). The electromechanical coefficients in (d-o) were fitted by a second-order polynomial (**Equation (4.5)**), intercept, linear (ξ), and quadratic (ϑ) coefficients are depicted in the figures. Note that NBT-6BT-1Zn was measured until fracture, while the maximum vibration velocity of the remaining NBT-BT compositions was experimentally limited by the maximum available electric field amplitude (i.e., driving voltage).

As expected for the ferroelectric hardening, the piezoelectric coefficients (d_{33} and d_{31}), the coupling coefficient, and the dielectric permittivity of NBT-BT-based composites and Zn^{2+}-doped samples decrease compared to unmodified NBT-BT, while the elastic compliance slightly increases (**Table 5.1**). The changes are probably also affected by the slight Zn-doping-induced shift of the MPB toward the NBT-rich side of the phase diagram (**Figure 2.14**) [144]. However, the variation of the coefficients is much smaller compared to the $Q_{31}^{R/AR}$ changes after modification. The effect also appears to be more pronounced in NBT 9BT than in NBT-6BT. Remarkably, the coefficients exhibit only a marginal increase upon increasing vibration velocity (**Figure 5.4d-o**). The increasing slopes (**Figure 5.3**) are only slightly larger in the unmodified NBT-6BT than in the modified compositions.

Table 5.1. Small-field electromechanical coefficients (Q_{31}^R, Q_{31}^A, d_{31}, k_{31}, s_{11}^E, ε_{33}^T) and high-power figure of merit (FOM^{HP}, **Equation (4.6)**) at 20 °C, determined by small-field resonance impedance spectroscopy. Piezoelectric coefficient (d_{33}) measured by Berlincourt meter. Depolarization temperature (τ_d) determined from temperature-dependent measurement of the inverse piezoelectric coefficient d_{33} (**Figure 5.11**) [169].

	Q_{31}^R [-]	Q_{31}^A [-]	d_{31} [pm/V]	k_{31} [-]	s_{11}^E [nm²/N]	ε_{33}^T [-]	FOM^{HP} [m²/kVs]	d_{33} [pC/N]	τ_d [°C]
NBT-6BT	177	172	44	0.21	7.3	700	0.036	140	99
NBT-6BT:10ZnO	312	340	36	0.18	7.5	584	0.051	128	133
NBT-6BT:40ZnO	349	325	31	0.14	7.1	740	0.050	95	130
NBT-6BT-0.5Zn	291	306	36	0.19	7.5	560	0.048	134	117
NBT-6BT-1Zn	597	674	32	0.18	7.6	472	0.086	127	120
NBT-9BT	96	88	43	0.15	7.0	909	0.019	120	150[86]
NBT-9BT:20ZnO	305	334	22	0.08	7.7	595	0.030	74	183[86]

5.1.3. X-ray diffraction analysis

The electromechanical properties of the NBT-BT compositions must be intimately related to the response of their crystallographic structure and microstructure to the applied electric field and evolving mechanical stress. In order to reveal the microscopic origin of the above-described stability of the electromechanical coefficients, the previously introduced combined high-energy in-situ diffraction study under resonance was conducted (Section 3.2). The experimental approach correlated the increasing strain contribution from non-180° domain wall motion in PZT with the increasing dielectric, mechanical, and piezoelectric coefficients, as well as the decreasing Q_{31}^R (Section 4.2.1). Although it was not possible to deconvolute the nature of the domain wall motion entirely, it could be rationalized that the increasing magnitude of domain wall motion must be correlated predominantly with an increasing out-of-phase component, which is the essential reason for the extrinsic loss increase and Q_{31}^R decrease.

The evolution of the diffraction peaks during field cycling is reconstructed in **Figure 5.5** for unmodified NBT-6BT at 1.1 m/s and NBT-9BT at 1.25 m/s (larger vibration velocities were experimentally not accessible). **Figure 5.5a,b** depicts the pseudocubic $\{111\}_{pc}$ and $\{200\}_{pc}$ reflections of the azimuthal 0°- and 90°-sections (**Figure 3.6**). The peak splitting identifies the above-introduced rhombohedral/tetragonal phase mixture in NBT-6BT and the mainly tetragonal distortion in NBT-9BT; the directional dependence confirms the texturing due to polarization. The time-dependent sinusoidal displacement of the diffraction intensities along the diffraction angle (2θ) evidences the lattice response to the external perturbation during the periodic resonance cycling (**Figure 5.5b,c,e,f**).

The lattice strains were determined from the change in lattice spacing, i.e., the 2θ displacement amplitude (**Equation (4.7)**); the non-180° domain wall motion was calculated from the domain switching fraction, i.e., the evolution of peak intensity interchange (**Equations (4.9)** and **(4.12)**). Please refer to Section 4.2.1 for details on the analysis and calculation procedure; the labeling of the utilized strain coefficients is summarized in **Table 4.5.** The derived lattice strains of different *hkl*-lattice planes ($S_{1,hkl}$), as well as the strains from domain wall motion ($S_{1,non-180°}$) in the transverse direction (x_1-direction) are displayed in **Figure 5.6** as a function of vibration velocity.

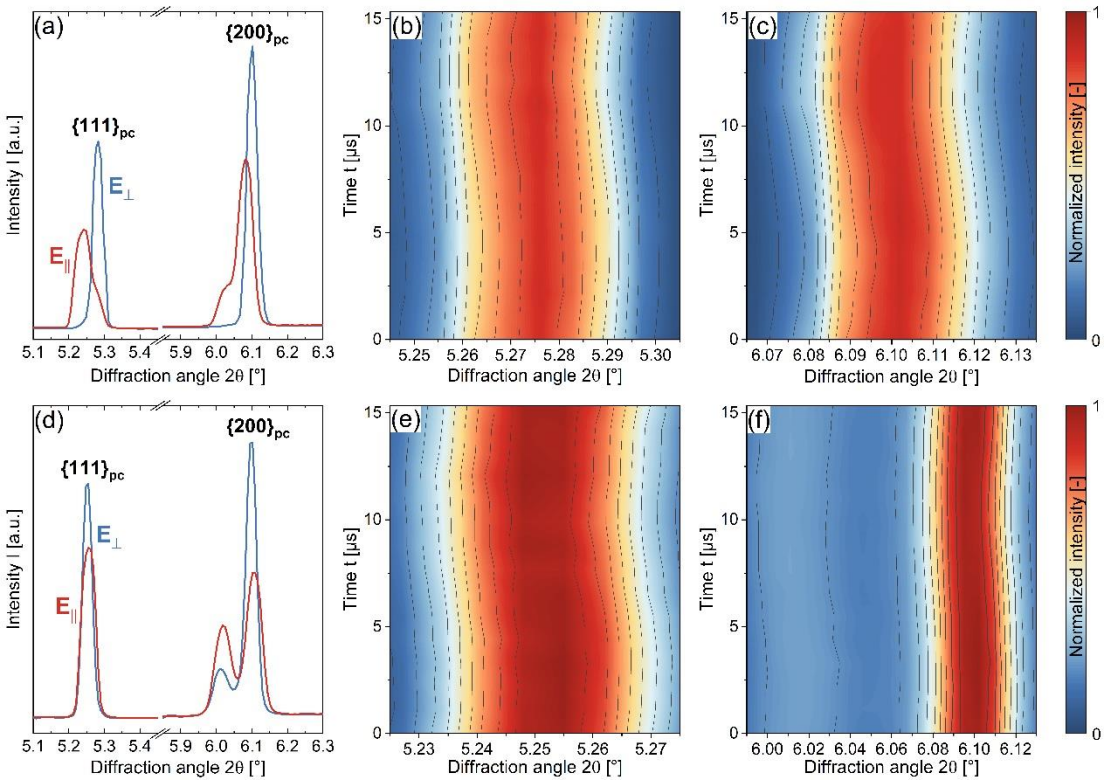

Figure 5.5. Diffractograms of polarized (a) NBT-6BT and (b) NBT-9BT featuring the $\{111\}_{pc}$ and $\{200\}_{pc}$ peaks parallel to the polarization and applied electric field direction and perpendicular to the applied field in the direction of largest strain amplitude in the transverse vibration mode (31). The $\{111\}_{pc}/\{11\bar{1}\}_{pc}$ and $\{002\}_{pc}/\{200\}_{pc}$ splitting depicts the rhombohedral/tetragonal phase mixture in NBT-6BT; NBT-9BT exhibited only a $\{002\}_{pc}/\{200\}_{pc}$ splitting of the tetragonal phase. The reconstructed diffractogram sections highlight the time-dependent evolution of the $\{111\}_{pc}$ and $\{200\}_{pc}$ peaks in (c,d) NBT-6BT and (e,f) NBT-9BT perpendicular to the applied electric field during the resonance vibration at 1.1 m/s and 1.25 m/s, respectively. The time scale depicts a single vibration cycle and represents all periodic cycles, during which the intensity was stroboscopically acquired and integrated.

All strain contributions increase upon increasing vibration velocity, indicating enhanced lattice distortion as well as enhanced domain wall motion. Remarkably, the domain wall generated strains in the rhombohedral and tetragonal phases of the NBT-6BT compositions are very similar. A significant dependence on the crystal structure is not observed. Considering that the strain contribution is determined by the product of non-180° domain switching fraction and the switching strain according to the lattice spacing (**Equations (4.11)** and **(4.12)**), the tetragonal phase reveals a larger distortion but a smaller switching fraction, while the rhombohedral phase exposes a smaller distortion but larger switching fraction. Moreover, it is important to note that the lattice strains are about one order of magnitude larger than the domain wall generated strains in all investigated compositions and the entire measurement range.

Since the compositions reveal a qualitatively similar evolution, the two unmodified samples NBT-6BT and NBT-9BT, were selected as representatives for the subsequent detailing of the strain ratios. The total lattice strain ($S_{1,lattice}$), the total strain from non-180° domain wall motion ($S_{1,non-180°}$), and the sum of both, i.e., the total microscopic strain determined from diffraction ($S_{1,XRD}$), are displayed in **Figure 5.7a,b.** For comparison, the macroscopic center strain ($S_{1,HPmax}$), measured with the laser vibrometer and calculated according to the strain distribution (**Figure 4.16c**), is plotted in the same figure.

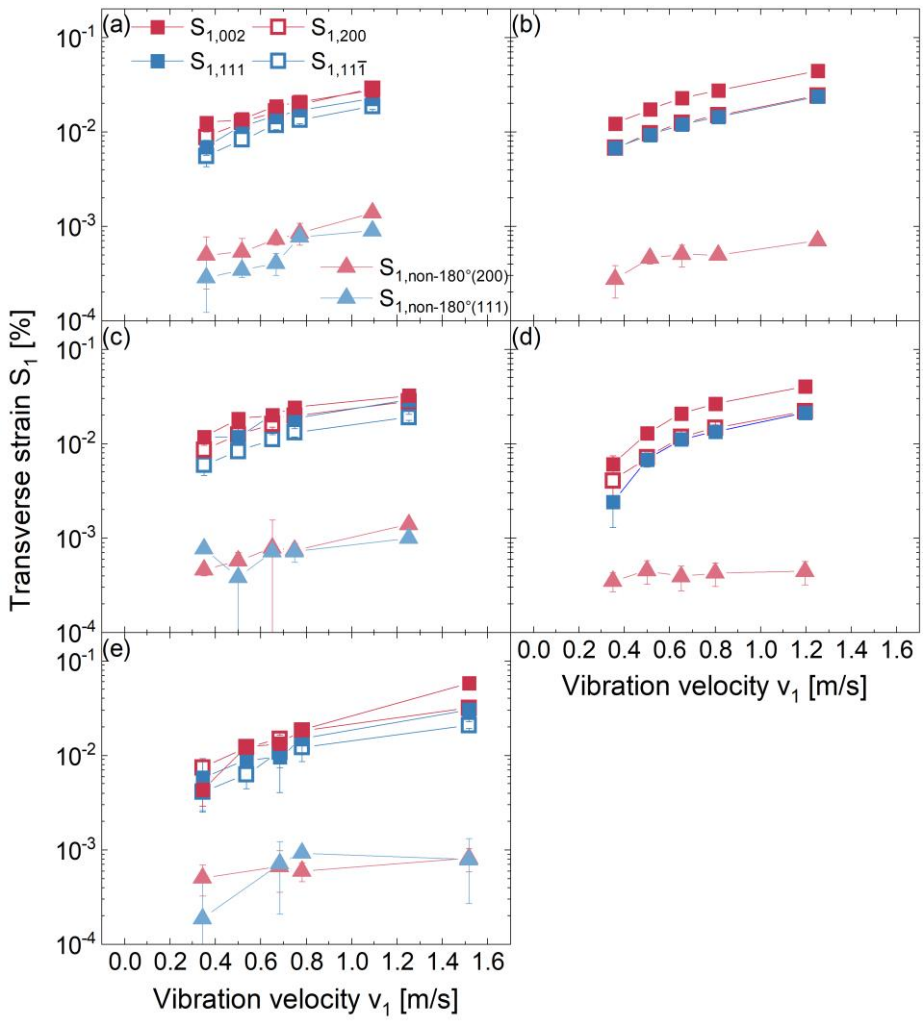

Figure 5.6. Lattice strains ($S_{1,hkl}$) of the $\{111\}_{pc}/\{11\bar{1}\}_{pc}$ and $\{002\}_{pc}/\{200\}_{pc}$ *hkl*-planes and strain contribution from rhombohedral/tetragonal non-180° domain wall motion ($S_{1,non-180°}$) in (a) unmodified NBT-6BT and (b) NBT-9BT, (c) NBT-6BT:10ZnO and (d) NBT-9BT:20ZnO composites, as well as (e) Zn^{2+}-doped NBT-6BT-1Zn as a function of edge vibration velocity (v_1) perpendicular to the applied field in the direction of the largest strain amplitude (transverse vibration mode (31)). Note that the strain-axis is logarithmic and the lattice strains are about one order of magnitude larger than the domain wall generated strains.

Note that for NBT-9BT all total strains were calculated considering a purely tetragonal phase, since no rhombohedral distortion was observed in the diffraction pattern[xxv]. On the other hand, NBT-6BT exhibits a mixture of 81 % rhombohedral and 19 % tetragonal phases [242]. Due to the presence of the phase mixture, the displayed domain wall motion strain is a weighted sum of the rhombohedral ($S_{non-180°(111)}$) and tetragonal contributions ($S_{non-180°(200)}$) according to their phase ratio (r)

$$S_{non-180°} = r_{200} \cdot S_{non-180°(200)} + r_{111} \cdot S_{non-180°(111)}. \tag{5.1}$$

Unfortunately, the phase mixture prohibited the calculation of the total lattice strain in NBT-6BT, which is therefore missing in **Figure 5.7a**. Due to the overlapping reflections of the two phases, strains of the individual lattice plains determined by Gauss fits cannot be assigned to the respective phase and require an additional full pattern refinement.

[xxv] A weak rhombohedral distortion was reported in the relaxor-state [244], but seems to disappear upon electric poling of NBT-9BT.

The results in **Figure 5.7a,b** reveal that the strain from domain wall motion is the inferior contribution to the total strain in both compositions. The total strain in NBT-9BT determined from diffraction agrees well with the macroscopically-measured strain ($S_{1,XRD} = S_{1,HPmax}$), evidencing the accuracy of the diffraction measurement (proven previously also for PZT_T in Section 4.2.1). Thus, the total strain values can be used interchangeably and the domain strain contribution can be expressed by the ratio $S_{1,non-180°}/S_{1,HPmax}$ given in **Figure 5.7c,d**. The domain wall contributions in both compositions are in the range of 3-5 %, which is considerably lower compared to soft and hard PZT_T, where contributions of 10-40% and 5-14% have been observed (**Figure 4.17**). Moreover, in contrast to PZT_T, the domain wall contributions remain comparatively constant over the investigated vibration velocity range (changes are below the detection limit of the applied experimental approach).

As a consequence, the comparison between PZT_T and NBT-BT implies that the main reasons for the stable Q_{31}^R response of NBT-BT-based compositions under high-power conditions originates from the lattice-dominant (intrinsic) strain response and only inferior and almost constant (extrinsic) domain wall contribution. However, the correlation is not straightforward and the magnitude of domain wall motion alone does not explain all observed effects. Note that even though the domain wall motion in NBT-BT turned out to be reduced, also the Q_{31}^R values are significantly smaller. A detailed discussion on the correlation is provided below.

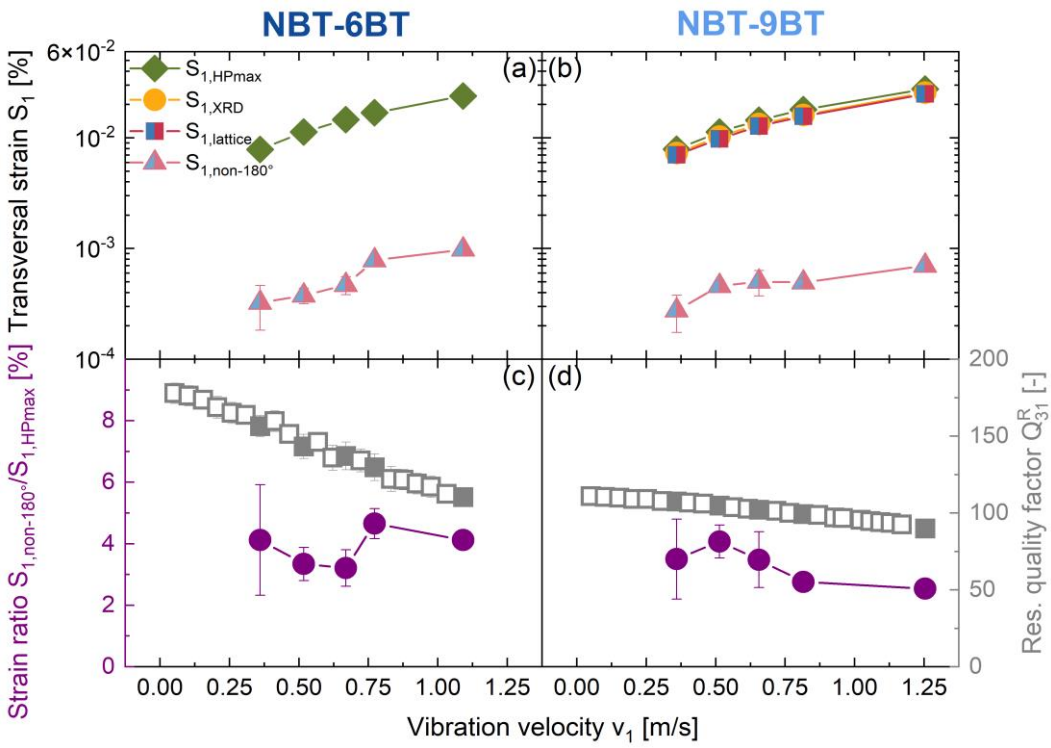

Figure 5.7. Total lattice strain ($S_{1,lattice}$), total strain from non-180° domain wall motion ($S_{1,non-180°}$), and total microscopic strain ($S_{1,XRD}$), determined from diffraction measurements, in comparison to the macroscopic maximum center strain ($S_{1,HPmax}$), determined from pulse drive measurements, for unmodified (a) NBT-6BT and (b) NBT-9BT as a function of edge vibration velocity (v_1) perpendicular to the applied field in the direction of the largest strain amplitude (transverse vibration mode (31)). Ratio of the strain contribution from non-180° domain wall motion to the total strain ($S_{1,non-180°}/S_{1,HPmax}$) in comparison to the resonance quality factor (Q_{31}^R) for unmodified (c) NBT-6BT and (d) NBT-9BT. Filled grey squares mark the vibration velocities at which the diffraction experiments were conducted.

5.1.4. Discussion and conclusions

NBT-BT-based ferroelectrics reveal fundamentally different high-power characteristics than PZT-based ferroelectrics. To emphasize the differences between the two material groups, representative compositions are contrasted in **Figure 5.8**. The medium-hard PZT_T features comparatively large Q_{31}^R values, but also a severe degradation with increasing vibration velocity, dropping by 80 % already at 1 m/s. Other hard- and soft-type PZTs with larger or lower Q_{31}^R values exhibit a similar degradation magnitude at even lower vibration velocities (**Figure 4.7** and **Figure 4.8**), which was described above as the main drawback for high-power applications. Ferroelectric hardening through Zn^{2+}-doping or ZnO-composite formation significantly increases the Q_{31}^R values of NBT-6BT, even exceeding those of medium-hard PZT_T. Zn^{2+}-doping reveals thereby a more pronounced effect; acceptor-doping with other elements (e.g., Mg^{2+}-doping) can potentially have a similar or even more significant impact. At the same time, NBT-6BT as well as NBT-9BT compositions reveal a much more stable Q_{31}^R at large vibration velocities. The values decrease by less than 30 % at 1 m/s and less than 60 % even at 3 m/s in all compositions (unmodified and modified). This emphasizes the inherently superior stability of NBT-BT in terms of the relative $Q_{31}^R/Q_{31}^{R,0}$ decrease, which is preserved even after a significant increase of the absolute Q_{31}^R values.

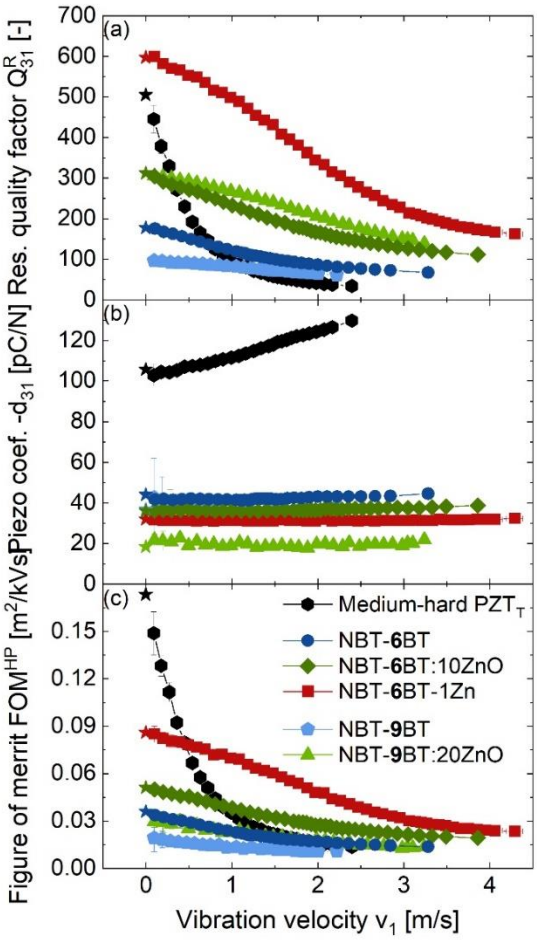

Figure 5.8. Electromechanical coefficients (a) Q_{31}^R, (b) d_{31}, and (c) high-power figure of merit (FOM^{HP}, **Equation (4.6)**) of different unmodified/modified NBT-6BT and NBT-9BT compositions compared to medium-hard PZT_T in the transverse (31) vibration mode at 20 °C as a function of vibration velocity (v_1). The data points denoted as stars at 0 m/s depict the small-field values (**Table 4.3** and **Table 5.1**). Note that NBT-6BT-1Zn and medium-hard PZT_T were measured until fracture, while the maximum vibration velocity of the remaining NBT-BT compositions was experimentally limited by the maximum available electric field amplitude (i.e., driving voltage).

The dielectric, mechanical, and piezoelectric coefficients, represented by d_{31} in **Figure 5.8**, are generally larger in PZT and exhibit a significant increase upon increasing vibration velocity in parallel to the decreasing $Q_{31}^{R/AR}$. This is mechanistically associated with an overall more pronounced extrinsic contributions to the generated strain and polarization, i.e., it correlates especially with a larger domain wall motion magnitude that further rises as increasing vibration velocities (Section 4.2.1). In contrast, the smaller and almost constant coefficients of the NBT BT compositions in the entire vibration velocity range are a consequence of reduced domain wall motion magnitude (despite the vicinity to the MPB) and an approximately constant contribution ratio to the generated strain at any vibration velocity. Both were directly evidenced by the in-situ XRD study (**Figure 5.7**).

Moreover, it turns out that the NBT-BT compositions also demonstrate clustering (**Figure 5.9**), as has been observed for the PZT compositions (**Figure 4.9**). From the phenomenological perspective, the compositional modifications, i.e., acceptor/donor doping or composite formation, influence the magnitudes of intrinsic and extrinsic loss contributions and in turn the $Q_{31}^{R/AR}$ values. However, the dependence of the loss on the rising vibration velocity and mechanical stress is primarily dictated by the inherent properties of the basic ferroelectric material and results in the observed clustering.

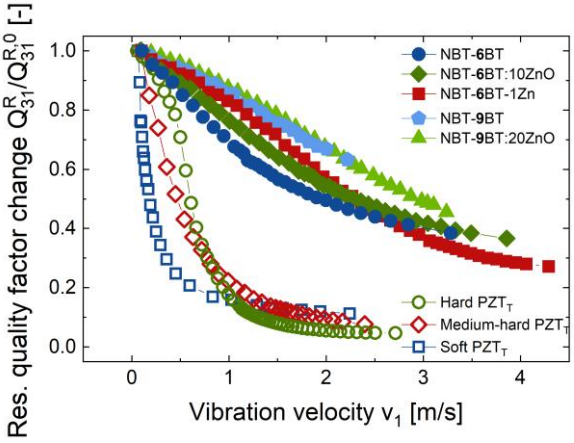

Figure 5.9. Relative change of the resonance quality factor ($Q_{31}^{R}/Q_{31}^{R,0}$) as a function of vibration velocity (v_1). The NBT-6BT and NBT-9BT compositions cluster, exhibiting a very similar Q_{31}^{R} change, determined by the properties of the basic material and independent of the small-field Q_{31}^{R} values, i.e., independent of modification-induced ferroelectric hardening/softening. Same clustering is observed in PZT, here represented by the tetragonal compositions.

Nevertheless, it is surprising that although the relative domain wall contribution in unmodified NBT-6BT is smaller than, for instance, in hard PZT_T (**Figure 5.7** and **Figure 4.17**), also the Q_{31}^{R} values are smaller. Moreover, the shallow but continuous decrease of Q_{31}^{R} in the NBT-BT compositions at large vibration velocity is not represented by an increasing domain wall strain contribution ($S_{1,non-180°}/S_{1,HPmax}$). Also, the two- to four-fold increase of Q_{31}^{R} after ZnO-composite formation and Zn^{2+}-doping is not reflected in a proportional decrease of the domain wall strain contribution. The ambiguity necessitates a further distinction of the loss nature or, in general, a consideration of the in-phase and out-of-phase components of the strain generating processes. Two hypotheses can be proposed to explain these observations following the current mechanistic understanding of intrinsic and extrinsic loss. (1) Due to the large coercive fields and stress in NBT-BT, and considering the polarization harmonics analysis discussed below (**Figure 5.17**), extensive irreversibility of the determined domain wall motion is unlikely. Also, the small and nearly unaltered ratio ($S_{1,non-180°}/S_{1,HPmax}$) hints toward a dominantly reversible

nature of the motion. In that case, the small Q_{31}^{R} values in unmodified NBT-BT represent a large and dominant out-of-phase component of the reversible motion. The out-of-phase component of reversible domain wall motion arises from the inertia and large effective mass of the domain walls [245]. The decrease of Q_{31}^{R} upon increasing vibration velocity or the increase upon chemical modification is in consequence an activated or inhibited out-of-phase contribution and altered ratio of the in-phase and out-of-phase components. (2) However, the fact that the intrinsic lattice contribution dominates the strain in NBT-BT raises doubts that the domain wall arguments entirely explain the Q_{31}^{R} behavior. It appears likely that Q_{31}^{R} in these materials is predominantly determined by a distinct intrinsic loss. The intrinsic loss originates from the rotation of the lattice polarization [102], which has been discussed in Section 4.5.3. The polarization rotation is promoted by the small ferroelectric (rhombohedral/tetragonal) lattice distortion in NBT-BT, which is associated with a shallow Gibbs free energy distribution according to the Landau–Ginsburg–Devonshire theory [45, 46]. Other than in PZT, the Zn^{2+}-doping and composite formation in NBT-BT were shown to influence the ferroelectric lattice distortion significantly, e.g., to increase the tetragonal c/a ratio [85, 113], which reduces the polarization rotation [213] and thus the intrinsic loss, leading to the increase of Q_{31}^{R}. Unlike the extrinsic loss from domain wall motion, the intrinsic loss is less dependent on the vibration velocity or external perturbations in general. This results in a stable Q_{31}^{R} evolution, albeit the (small-field) Q_{31}^{R} values in NBT-BT are below those of PZT due to the large intrinsic loss.

Irrespective whether Q_{31}^{R} is determined by the intrinsic or extrinsic loss, it is clear that the Q_{31}^{R} stability in NBT-BT benefits from the reduced domain wall mobility. In order to rationalize the reason for the inhibited domain wall motion, it is necessary to recall that the strain under resonance drive (lattice distortion and domain wall motion) is predominantly generated by the dynamic mechanical stress (tensile and compressive) evolving in the sample (Section 4.2.2). The applied electric field is small and acts only as a stimulus to produce vibration through electromechanical coupling. Assuming a linear elastic regime, the mechanical energy density during the one-dimensional transverse (31) vibration can be expressed as

$$\Upsilon_{31}^{m} = \frac{1}{4}\,\rho v_1^2 = \frac{1}{4}\pi^2 \frac{1}{2s_{11}^{E}} S_1^2 = \frac{\pi^2}{8}\frac{1}{s_{11}^{E}}\left(s_{11}^{E}T_1 + d_{31}E_1\right)^2, \tag{5.2}$$

which further reduces under the above assumption ($d_{31}E_1 \to 0$) to

$$\Upsilon_{31}^{m} = \frac{\pi^2}{8} s_{11}^{E} T_1^2. \tag{5.3}$$

The critical energy density for domain wall switching ($\Upsilon_{31}^{m,DWS}$) is reached when the mechanical stress becomes equal to the coercive stress T^c. The domain wall switching in PZT and NBT-BT is then correlated through

$$\Upsilon_{31}^{m,DWS}(NBT-BT) = \frac{s_{11}^{E}(T_1^c)^2(NBT-BT)}{s_{11}^{E}(T_1^c)^2(PZT)}\,\Upsilon_{31}^{m,DWS}(PZT). \tag{5.4}$$

The elastic compliance values derived in this study were in the range of 9.6 – 21.6·10^{-12} m^2/N for the PZT compositions and in the range of 7.0 – 7.8·10^{-12} m^2/N for the NBT-BT compositions, which is in fair agreement with the Young's moduli determined for hard PZT [217] and NBT-6BT [246, 247]. Coercive stress in the range of 49 – 180 MPa [164, 217] and 232 – 369 MPa [164, 248] were reported for PZT and NBT-BT materials, respectively. Inserting these values into **Equation (5.4)** returns domain switching energy densities being larger in NBT-BT than in PZT at least by a factor of 2. Consequently, it is expectable that sub-coercive

domain wall motion (bending and displacement) is significantly reduced in NBT-BT compositions, since the mobility scales with the coercive stress. The analysis of materials' high-power performance should thus inevitably include their mechanical properties, which is rarely done. Consideration of the coercive stress seems to be more pertinent than the coercive electric field.

To compare the overall performance of the NBT-BT compositions in comparison to PZT, their high-power figures of merit (FOM^{HP}) derived based on **Equation (4.6)** are considered in **Figure 5.8** (small-field values are listed in **Table 5.1**). The initially large FOM^{HP} values of medium-hard PZT_T rapidly decrease with increasing vibration velocity, dropping below those of NBT-6BT-1Zn and NBT-6BT:10ZnO values already in the low vibration velocity range at 0.46 m/s and 0.87 m/s, respectively. The FOM^{HP} obviously mimics the decrease of the Q_{31}^{R}, which is not equivalently compensated by the increase of d_{31}. This general observation highlights again the decisive role of a stable Q_{ij} for high-power materials. Particularly, the ZnO-composites and Zn^{2+}-doped compositions exhibit superior FOM^{HP} at large vibration velocity, emphasizing their potential to be transferred in high-power devices despite the comparatively low piezoelectric coefficients. Nevertheless, the importance of considering all electromechanical coefficients is highlighted exemplarily with the NBT-9BT composite, where the stability of Q_{31}^{R} cannot compensate for the low d_{31}, resulting in an overall low FOM^{HP}.

An additional benefit of the NBT-BT-based compositions is the ability to reach a significantly larger vibration velocity before mechanical fracture. Medium-hard PZT_T fractured at 2.6±0.3 m/s, the other PZT compositions fractured in the same or even lower vibration velocity range. In contrast, NBT-6BT-1Zn could be excited up to 4.4±0.2 m/s. All samples fractured in the center, in the plane perpendicular to the vibration direction (**Supplemental Figure 7.20**), which is the region of maximum dynamic (tensile and compressive) mechanical stress amplitude (**Equations (2.49)** and **(4.14)**) due to the sinusoidal stress distribution (**Figure 4.16c**) [14]. This results in a dynamic fracture strength of 63±7 MPa in medium-hard PZT_T and 128±6 MPa in NBT-6BT-1ZnO, which is in good agreement with the reported static fracture strength [248]. The larger mechanical resilience follows the about two-fold larger fracture toughness of NBT-BT compared to hard PZT [164] and is mostly independent of the BT content [248].

5.2. Temperature dependence of the electromechanical properties

Depolarization well below the benchmark temperature of 100 °C and a complicated depolarization mechanism, along with the intrinsically low electromechanical quality factor, are among the central deficits of NBT-6BT and related compositions. The narrow operational temperature range limits not only the external thermal loading, but also the maximum usable vibration velocity, since self-heating effects at large vibration velocities quickly terminate in thermal depolarization. Zn^{2+}-doping as well as ZnO-composite formation increase the quality factor and simultaneously substantially delay the thermal depolarization. Here, the influence of the modifications on the depolarization process and the origin of the delay are investigated. The behavior is related to the large-field ferroelectric characterization to elucidate the underlying mechanistic differences. Subsequently, the temperature evolution of the electromechanical coefficients is tracked up to the depolarization, reconstructing temperature-vibration velocity landscapes to define the resulting operational windows. Finally, the appearance of self-heating at different vibration velocities under continuous drive is correlated to the derived property landscapes to evaluate the performance of the materials. The study is

carried out on the three representative NBT-6BT compositions introduced above to expose the inherent differences between NBT-6BT and PZT compositions, and to differentiate between the chemical (Zn^{2+}-doping) and mechanical (ZnO-composite) hardening mechanisms.

5.2.1. Ferroelectric-to-relaxor transition and depolarization process

Thermal depolarization indicates an irreversible breaking of the long-range ferroelectric order and the coherence of the polarization directions in neighboring domains. The depolarization temperature (τ_d) denotes thereby the thermally-induced disappearance of macroscopic polarization that ultimately results in electromechanical coefficients being reduced to zero. The depolarization mechanisms of NBT-6BT are correlated to its complex electric field-temperature phase diagram and the relaxor-ferroelectric nature introduced in Section 2.3.5. A simplified schematic (**Figure 2.10**) represented the current understanding of the still disputed mechanistic processes based on the experimental data and the model of polar nano-regions (PNRs). Basically, the ferroelectric-to-relaxor transition temperature (τ_{F-R}) sets the natural upper limit to the depolarization boundary. The transition is associated with the breaking of the local coherence of neighboring dipole moments in the average structure. However, depolarization can be induced by several other processes. Therefore, τ_d can be lower, equal, or, in some cases, even slightly higher than τ_{F-R} (residual polarization), depending on the depolarization process.

The thermally-induced transition from the polarized ferroelectric state into the relaxor state (τ_{F-R}) is derived from the inflection point of the temperature-dependent real part of the relative dielectric permittivity (ε'_{33}) and the dielectric loss ($tan\,\delta$) at the thermal anomaly (**Figure 5.10a-c**; other compositions in **Supplemental Figure 7.21**). The τ_{F-R} increases from 98 °C in NBT-6BT to 131 °C in NBT-6BT:10ZnO and 115 °C in NBT-6BT-1Zn, which is in agreement with previous reports [83, 114]. Furthermore, ZnO-composites and Zn^{2+}-doped samples feature an additional low-temperature anomaly starting at 86 °C. The smaller low-temperature anomaly is best seen in the inverse $1/\varepsilon'_{33}$ representation and is highlighted by the shaded region in **Figure 5.10d**; the onset was determined from the 1st derivative of $1/\varepsilon'_{33}$ (T) (**Supplemental Figure 7.22**).

The thermal depolarization temperature (τ_d) is determined from the inflection point of the piezoelectric coefficient d_{33} measured in-situ during heating (**Figure 5.11a** and **Table 5.1**). Note that the polarization decrease in the depolarization vicinity sometimes occurs over a wide temperature range, particularly in NBT-based materials; thus, the τ_d is set at the temperature of the strongest polarization loss rate (inflection point) [13], although a residual polarization might still exist even at higher temperatures.

NBT-6BT exhibits an initial increase, followed by a sharp drop of d_{33} at 99 °C, while NBT-6BT:10ZnO and NBT-6BT-1Zn demonstrate a smaller increase of d_{33} and a delayed depolarization at 133 °C and 120 °C, respectively. Remarkably, the d_{31} coefficients reveal a significantly different temperature dependence (**Figure 5.11b**). d_{31} increases steadily in all compositions in the low-temperature regime to about 85 °C. At higher temperatures, $d_{31}$of unmodified NBT-6BT starts to decline before dropping to (almost) zero at 99 °C. On the other hand, in the two modified compositions, d_{31} decreases gradually above 85 °C, terminating in a final drop at the previously determined τ_d values. These temperature regimes of starting d_{31} decrease and terminating drop to zero coincide with the anomalies observed in the dielectric permittivity measurements (**Figure 5.10**).

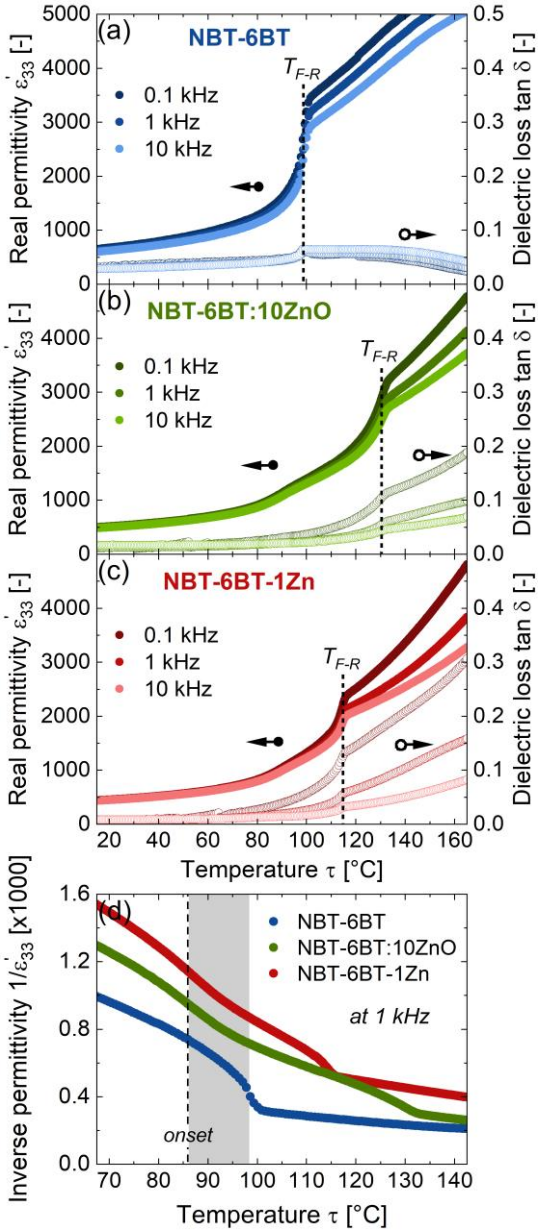

Figure 5.10. Temperature-dependent real part of the relative dielectric permittivity (ε'_{33}) and dielectric loss ($tan\ \delta$) of (a) unmodified NBT-6BT, (b) NBT-6BT:10ZnO composite, and (c) Zn^{2+}-doped NBT-6BT-1Zn in the polarized states. The inflection point at the thermal anomaly determines the ferroelectric-to-relaxor transition (τ_{F-R}). (d) Inverse of the permittivity real part ($1/\varepsilon'_{33}$) at 1 kHz for the three compositions in comparison. The grey-shaded region indicates the low-temperature anomaly observed in the temperature-dependent ε'_{33}; the dashed line marks the depolarization onset, determined from the 1st derivative of $1/\varepsilon'_{33}$ (τ) (**Supplemental Figure 7.22**).

The deviation between τ_d and τ_{F-R} are small for all compositions and within the experimental error range of about ±2 °C. Therefore, it is proposed that the characteristic temperatures of the individual compositions can be considered equal, which has also been concluded in previous electrical [113, 116] as well as structural [116] studies of undoped NBT-6BT. This means that the depolarization process is predominantly dictated by and directly terminates in the ferroelectric-to-relaxor transition, represented by state (V) in **Figure 2.10**. The absence of a distinct separation between τ_d and τ_{F-R}, as observed at least for undoped NBT-6BT in other studies [109, 111], might be induced by a more stable domain configuration, related, for example, to larger grain size. The grain size effect has been observed in NBT [171] as well as in $BaTiO_3$ [249] and $Pb(Zr,Ti)O_3$ [55].

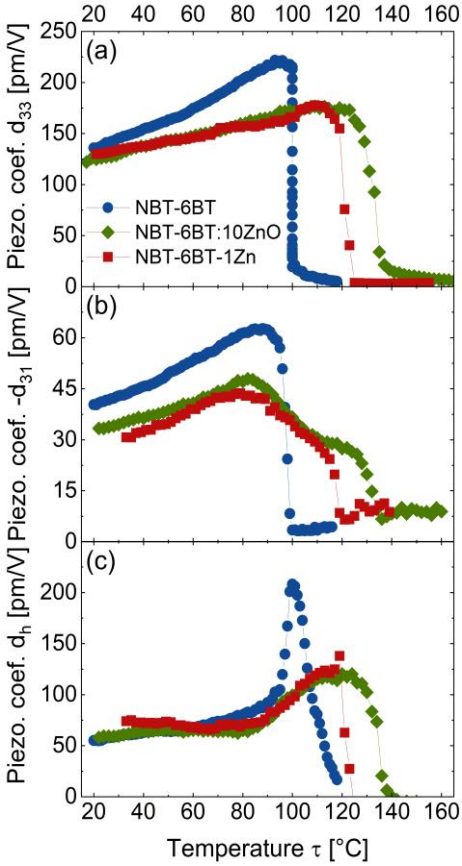

Figure 5.11. Temperature-dependent (a) longitudinal (d_{33}), (b) transverse (d_{31}), and (c) hydrostatic (d_h) piezoelectric coefficients in comparison between the representative NBT-6BT compositions. The inflection point of the d_{33} decrease determines the depolarization temperature. The coefficients reveal a decoupling above the depolarization onset.

Furthermore, Zn^{2+}-doping and even more ZnO inclusions efficiently stabilize the electromechanical response in terms of a depolarization delay to higher temperatures. τ_d increases by 21 °C and 34 °C, respectively, which is a significant improvement. However, the appearance of the first low-temperature anomaly at 86 °C suggests that although both types of modifications increase the τ_d ($=\tau_{F-R}$) values, they do not shift but rather spread the temperature range of thermal depolarization. This means that the actual depolarization onset remains at 86°C, nearly unchanged compared to unmodified NBT-6BT (**Figure 5.10a**). This specific onset temperature appears consistently in temperature-dependent XRD studies of unmodified and Zn^{2+}-doped NBT-6BT [114, 116]. Those identified the emergence of a pseudocubic phase in the temperature range between 80 – 90 °C, indicating the transition of the ferroelectric state into the ergodic relaxor state and demonstrating that the transition is a continuous process over a range of several °C rather than immediate. Here, the ε'_{33} anomaly, the increasing ε'_{33} and $tan\ \delta$ values, and the increasing frequency dispersion starting at 86 °C (**Figure 5.10**) indicate that the depolarization is induced by a starting gradual nucleation and growth of the non-polar ergodic relaxor phase (accelerated at higher temperatures), while the domain polarization texturing remains mostly unchanged (schematic in **Figure 2.10** (V)).

The broadening of the depolarization temperature range can be rationalized considering the intrinsically different τ_{F-R} values of the crystallographic phases in NBT-BT [112, 116, 118]. Experimental findings demonstrated that the tetragonal ferroelectric-to-relaxor transition is sharp upon heating. However, the transition is prone to temperature shifts under different

external conditions, such as applied external electric fields [112], altered domain configuration [118], or BT-content [116]. In contrast, the rhombohedral ferroelectric-to-relaxor transition is smeared out over a broader temperature range but remains nearly unchanged independent of external perturbation. In consequence, the modifications by Zn^{2+}-doping and ZnO inclusions likely result in a shift of the τ_{F-R} of the tetragonal phase, while the rhombohedral phase remains unaffected, resulting in the observed depolarization spreading.

Surprisingly, the depolarization process is associated with a decoupling of the d_{33} and d_{31} coefficients (**Figure 5.11**). The origin of this behavior is not entirely understood. Such decoupling is not observed in the τ_d vicinity of straight ferroelectrics [114], nor is it predicted in the Landau-Ginzburg-Devonshire theory framework [213], or has been previously reported for relaxor-ferroelectrics. However, comparable observations are often reported in piezoelectric two-phase materials [250, 251], where a piezoelectric powder is embedded in a non-piezoelectric matrix. The decoupling increases with a decreasing ratio of the piezoelectric phase. Following the above picture of the depolarization mechanism (**Figure 2.10** (V)), the material structure beyond the depolarization onset temperature (≈86 °C) can be interpreted as a two-phase structure with the residual polarized ferroelectric phase embedded in the recovered non-polar pseudocubic ergodic relaxor phase. Thereafter, it is hypothesized that the decrease of the d_{31} coefficient in the depolarization range is induced by the two-phase structure formation, while the thermally activated d_{33} simultaneously increases continuously until τ_d. From the application perspective, the decoupling opens up interesting advantages for the usage of these materials in directional ultrasonic transducers, demonstrated by an enhanced hydrostatic piezoelectric coefficient (d_h) in a widened temperature range (**Figure 5.11c**) [252]. The increasing anisotropy offers to reduce the propagation of parasitic modes other than the desired vibration mode.

5.2.2. Thermal impact on the small-field electromechanical coefficients

The evolution of the small-field electromechanical coefficients (Q_{31}^{R}, Q_{31}^{AR}, d_{31}, k_{31}, s_{11}^{E}) as a function of temperature was tracked by resonance impedance spectroscopy between -30 °C and the τ_d of the corresponding composition (**Figure 5.12**). The depolarization is featured by the disappearance of the (anti)resonance peaks from the impedance spectrum. The derived τ_d values are in good agreement with the off-resonance measurements (**Table 5.1**), albeit slightly lower (note the measurement step size of 5 °C). Unmodified NBT-6BT displays a steady decrease of $Q_{31}^{R/AR}$ with increasing temperature up to depolarization (**Figure 5.12a**). On the other hand, the modified compositions reveal an increase and subsequent decrease of $Q_{31}^{R/AR}$, with a maximum at about 30 °C, particularly pronounced in NBT-6BT-1Zn. NBT-6BT:10ZnO exhibits only a weak and broad increase and subsequent decrease, and overall the most invariant temperature behavior. Note that the evolution of $Q_{31}^{R/AR}$ with a distinct maximum in acceptor-doped NBT-6BT-1Zn is qualitatively very similar to the observed temperature-dependence of acceptor-doped PZT (**Figure 4.24** and **Figure 4.26**). The similarity indicates that the thermal properties of the acceptor-hardening are comparable in both material groups (despite different doping elements) and can be associated with the same mechanistic processes.

The temperature-dependences of d_{31} and k_{31} are similar in all NBT-6BT compositions (**Figure 5.12b,c**) and in good accordance with the off-resonance measurements of d_{31} (**Figure 5.11**). Both coefficients feature a continuous increase until the depolarization onset at

about 80 °C and a subsequent degradation until reaching the respective τ_d. Zn^{2+}-doping and ZnO-composite formation significantly extend the depolarization range. However, although τ_d increases, the onset of the depolarization is not shifted, as previously discussed in Section 5.2.1. The s_{11}^E increases continuously with increasing temperature in all compositions and does not resemble the temperature dependence of the other coefficients. The curves exhibit no anomaly at the depolarization onset (**Figure 5.12d**) and only a slight decrease in the vicinity of τ_d. It is remarkable that the depolarization onset impacts the temperature dependence of d_{31} and k_{31}, but not of $Q_{31}^{R/AR}$ and s_{11}^E.

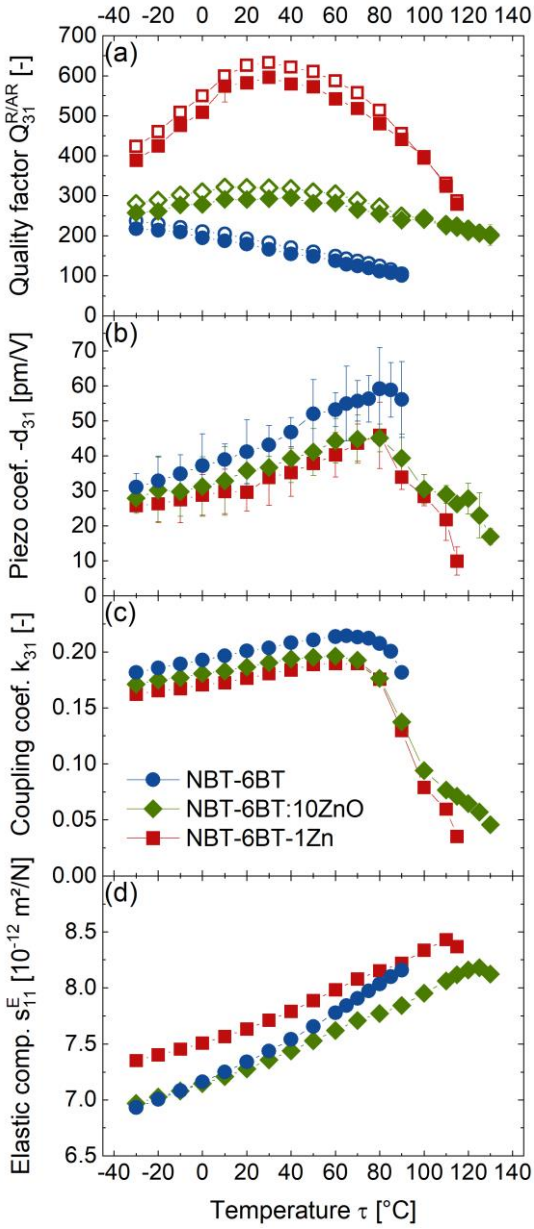

Figure 5.12. Small-field ($v_1 \rightarrow 0$ m/s) electromechanical coefficients (a) Q_{31}^R (solid symbols) and Q_{31}^{AR} (open symbols), (b) d_{31}, (c) k_{31}, and (d) s_{11}^E of unmodified NBT-6BT, Zn^{2+}-doped NBT-6BT-1Zn, and NBT-6BT:10ZnO composite in the transverse (31) vibration mode as a function of temperature (τ) during the first heating cycle after polarization. $Q_{31}^{R/AR}$ reveal a distinctly different temperature-dependent behavior than the other coefficients, indicating the simultaneous contribution of several processes to the thermal evolution of the coefficients.

Reversibility and degradation of electromechanical coefficients at elevated temperatures

To probe the degradation behavior of the modified NBT-6BT compositions above the depolarization onset, thermal cycling and time-dependent measurements of the electromechanical properties were carried out. The maximum temperature was set to 110 °C. The temperature is in the τ_d vicinity of both compositions, where a substantial degradation of the electromechanical coefficients with increasing temperature has been observed (**Figure 5.11** and **Figure 5.12**). The evolution of Q_{31}^R, d_{31}, and k_{31} in **Figure 5.13** evidences that all changes appearing above the depolarization onset are irreversible and the values do not recover upon cooling.

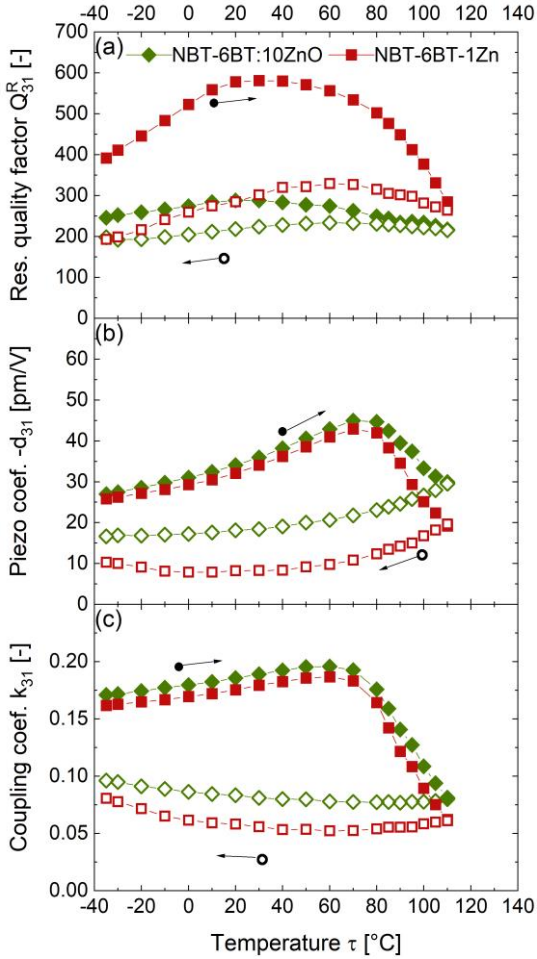

Figure 5.13. Small-field ($v_1 \rightarrow 0$ m/s) electromechanical coefficients (a) Q_{31}^R, (b) d_{31}, and (c) k_{31} of the transverse (31) vibration mode as a function of temperature (τ) during the first heating and cooling cycle after polarization. The maximum temperature of 110 °C is slightly below the depolarization temperature of Zn^{2+}-doped NBT-6BT-1Zn and NBT-6BT:10ZnO composite. The coefficients changes above the depolarization onset are irreversible.

In addition, the coefficients were tracked continuously for 12 h at the maximum temperature (**Figure 5.14**). Unmodified NBT-6BT exhibits no change of Q_{31}^R, while d_{31}, k_{31}, and s_{11}^E decrease by less than 10% and stabilized after 4 h. NBT-6BT-1Zn displays a decrease of Q_{31}^R by 8% and stabilized after 5 h. d_{31}, k_{31}, and s_{11}^E do not reveal a degradation. Interestingly, no changes are observed for NBT-6BT:10ZnO during the entire measurement time. The negligible time-dependence of the properties indicates that the processes in the materials, leading to the strong temperature-dependence of the electromechanical properties, particularly above the depolarization onset, are irreversible but also fast and thermodynamically stable.

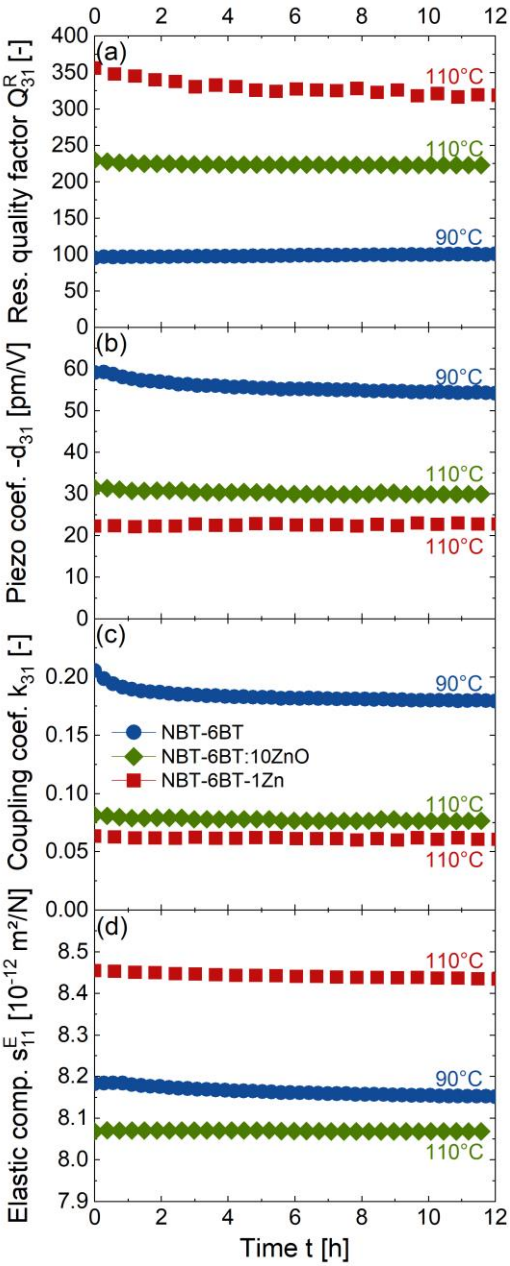

Figure 5.14. Time-dependent small-field (v_1→0 m/s) electromechanical coefficients (a) Q_{31}^{R}, (b) d_{31}, (c) k_{31}, and (d) s_{11}^{E} determined in the transverse (31) vibration mode by resonance impedance spectroscopy at a constant temperature in the vicinity of the depolarization temperature. The coefficients do not exhibit a time-dependent degradation.

5.2.3. Origin of the quality factor temperature dependence

It was elaborated above that the hardening mechanism based on the introduction of the ZnO second phase is not entirely understood yet. The explanation relies on the strain incompatibility and mismatch stress between the electromechanically active NBT-6BT and non-active ZnO phase. However, an additional Zn^{2+} acceptor-doping contribution cannot be excluded and it is difficult to separate the effects. NBT-6BT:10ZnO and NBT-6BT-1Zn demonstrated in **Figure 5.9** that the two hardening mechanisms based on doping or mechanical stress do not reveal different impacts on the high-power stability of the electromechanical coefficients. However, the stability is attributed to the properties of the basic ferroelectric material rather than to the modifications. On the other hand, Zn^{2+}-doping depicted a stronger influence on the values of the electromechanical coefficients, i.e., in terms of $Q_{31}^{R/AR}$ increase and decrease of d_{31} and k_{31}

(**Table 5.1**). Moreover, Zn^{2+}-doped compositions were reported to exhibit a much more pronounced low-frequency dispersion of the dielectric permittivity [75] and it was demonstrated here that the hardening approaches evidence different temperature dependencies, particularly in terms of Q_{31}^{R} evolution. Hence, clarifying the origin of the dissimilarity in the thermal properties of the compositions will contribute to the differentiation and understanding of the hardening mechanisms.

The small-field electromechanical coefficients of all NBT-6BT compositions exhibit very similar temperature dependencies, except for Q_{31}^{R} (**Figure 5.12**). Remarkable is especially the Q_{31}^{R} behavior in NBT-6BT-1Zn, i.e., the increase and subsequent decrease upon heating. The observed evolution is qualitatively similar to the temperature-dependence of Q_{31}^{R} in acceptor-doped PZT (**Figure 4.24** and **Figure 4.26**), indicating similar mechanistic processes (Section 4.4). Note that there is no evidence for a phase transition of NBT-6BT-1Zn in this temperature range and the behavior does not follow the trend of s_{11}^{E}. It appears that at least two contributions influence the observed temperature dependence of Q_{31}^{R}, exposed by the slope changing from positive to negative at about 30 °C. Based on the considerations derived for PZT, these contributions are related to the conductivity and the dielectric loss of the compositions. **Figure 5.15** depicts an enlarged section of the magnitude ($|\varepsilon_{33}|$), real (ε'_{33}), and imaginary (ε''_{33}) parts of the relative dielectric permittivity, as well as the dielectric loss ($tan\ \delta$) in the temperature range between -40 – 80 °C (derived from **Figure 5.10**). It is apparent that the temperature-dependence of Q_{31}^{R} is inversely correlated to the temperature-dependence of the dielectric loss (**Figure 5.15d**), which in turn is mainly influenced by the imaginary part of the dielectric permittivity. According to that, the decrease and subsequent increase of the dielectric loss in NBT-6BT-1Zn are associated with the previously mentioned low-temperature and high-temperature conduction processes, respectively. The conduction mechanism in that case is the ionic conductivity based on oxygen vacancy hopping. On the other hand, no considerable conductivity appears in unmodified NBT-6BT [253]. The small but continuous increase of the dielectric loss (**Figure 5.15d**) is therefore mechanistically related to the thermal activation of lossy intrinsic (e.g., polarization extension/rotation) or extrinsic (e.g., domain wall motion) processes, specifically it is related to the increase of their out-of-phase components. In consequence, the almost temperature-invariant stability of the dielectric loss in NBT-6BT:10ZnO (**Figure 5.15d**) confirms that the intrinsic and extrinsic loss contributions are constrained predominantly by the mechanical stress without introducing a significant conductivity. The thermal influence on the mechanical stress is expected to be negligible in the probed temperature range due to the low thermal expansion coefficients of NBT-6BT and ZnO [72]; hence, the ferroelectric hardening is not subjected to severe altering. The slight change of dielectric loss can be explained by the minor Zn^{2+} diffusion from the ZnO inclusions into the NBT-6BT lattice during sintering, inducing the same effect as in the doped compositions but to a distinctly lower extent.

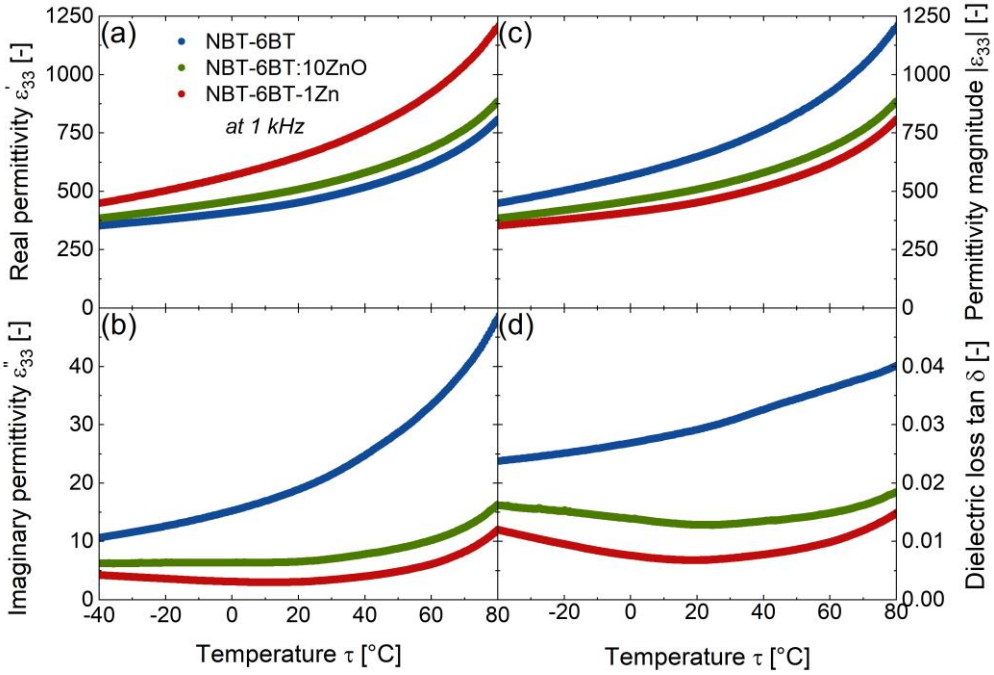

Figure 5.15. (a) Real part (ε'_{33}), (b) imaginary part (ε''_{33}), and (c) magnitude ($|\varepsilon_{33}|$) of the effective dielectric permittivity and the (d) dielectric loss ($tan\ \delta$) as a function of temperature (τ) of the three representative NBT-6BT compositions. The dielectric loss resembles inversely the temperature evolution of $Q_{31}^{R/AR}$ (**Figure 5.12**) and evidences its contribution to the small-field $Q_{31}^{R/AR}$ values.

Apart from the conductivity, also the thermal activation of domain wall motion has been discussed as an important contribution to the thermal properties. The role of domain walls in the NBT-BT-based compositions at elevated temperatures is deliberated in the following, considering the previous conclusion that $Q_{31}^{R/AR}$ in these compositions (at room temperature) are predominantly determined by intrinsic rather than extrinsic loss. The domain wall mobility and its nature were probed by temperature-dependent P-E and S-E hysteresis loops and harmonic analysis in the poled and aged states to evaluate whether the extrinsic influence increases at elevated temperatures. The hysteresis loops at elevated temperatures are demonstrated in **Supplemental Figure 7.23** and **Supplemental Figure 7.24**; the extracted coercive and internal bias electric fields are depicted in **Figure 5.16**. The average electric coercive fields decrease at higher temperatures in all compositions due to the thermal activation of the polarization switching process and the reduced lattice distortion. Also the asymmetry and shift along the abscissa determined for the NBT-6BT:10ZnO and NBT-6BT-1Zn in **Figure 5.3** decrease upon heating. The internal bias fields reveal two distinct temperature ranges: a decrease from 20 °C to 70 °C and an increase with an irregular trend above 80 °C (**Figure 5.16**, dashed line). The boundary between both regimes coincides with the onset of thermal depolarization (**Figure 5.10** and **Figure 5.11**). Decreasing coercive and internal bias fields evidence enhanced domain wall mobility and reduced pinning, due to the thermal activation of the domain wall displacement and the migration of oxygen vacancies. Moreover, the field values exhibit a more rapid decrease with temperature in NBT-6BT-1Zn than in NBT-6BT:10ZnO (although both field values are initially highest in NBT-6BT-1Zn at 20 °C), confirming the superior thermal stability of NBT-6BT:10ZnO due to the composite hardening approach, which is also likely the reason for the larger τ_d values. Moreover, it turns out that also in NBT-6BT:10ZnO both field values feature a thermally induced degradation, while Q_{31}^{R} exhibits a pronounced thermal-stability. The discrepancy points out again that the relationship between

the coercive and internal bias fields and Q_{31}^{R} is not as trivial as implicated in previous reports [143, 160]. Not only the magnitude but especially the character of domain wall mobility determine Q_{ij} and must be accounted, and the coercive stress appears to be the more pertinent parameter to predict the evolution of Q_{ij}.

Note that the hysteresis loops above the boundary at 80 °C indicate a mixed ferroelectric and ergodic relaxor phase state with a temperature-dependent phase ratio. Additionally, they evidence a pronounced conductivity. Both confirm the above-discussed depolarization process (Section 5.2.1) as well as the conductivity contribution to dielectric loss. Evidence are the evolving slim polarization loops, sprout-shaped strain loops with small negative strain, and the change of the remanent state before and after applying the electric field (**Supplemental Figure** 7.23 and **Supplemental Figure 7.24**), and the appearance of round hysteresis tips.

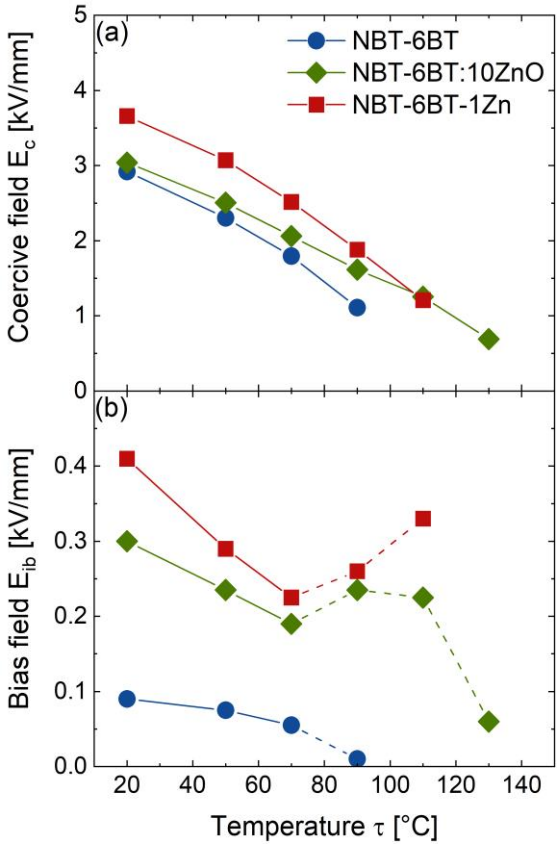

Figure 5.16. Temperature-depended (a) average coercive (E_c) and (b) internal bias (E_{ib}) electric fields of the three representative NBT-6BT compositions, determined from the minima in the strain hysteresis loops at 1 Hz (loops are depicted in **Supplemental Figure 7.23** and **Supplemental Figure 7.24**). The decreasing field values indicate a thermally activated enhancement of the domain wall motion.

Harmonic analysis of the weak-field polarization response was carried out to examine the character of the domain wall motion. Particularly, the amplitude of the 3rd polarization harmonic ($|P_3^{3rd}|$), the in-phase (P_3') and out-of-phase (P_3'') components, and the phase angle ($\delta^{3rd} = arctan\left(\frac{P_3''}{P_3'}\right)$) were determined as a function of electric field amplitude at different temperatures (**Figure 5.17** and **Supplemental Figure 7.25**). The higher harmonics amplitudes ($|P^n|$ with n>1) generally determine the nonlinearity of the polarization response, while specifically the third-harmonic P_3' and P_3'' are associated with in-phase (anhysteretic) and out-of-phase (hysteretic) nonlinear components of the non-lattice contributions, respectively; δ^{3rd}

determines their ratio [226]. Note that the remanent polarization of the poled samples remains mostly unchanged due to the subcoercive driving conditions ($E \leq E_c$) [97]. Generally, in relaxor-ferroelectrics, where a series of different mechanisms (e.g., domain wall motion, interface boundary motion, PNR dynamics) can contribute to the polarization response (Section 2.3.5), it is impossible to identify and deconvolute all contributions based on microscopic nonlinear harmonic analysis alone. However, considering the previous results, the similarity to the experimental data of hard and soft PZT, and the implications of the Rayleigh and V-potential model, it is assumed that the response is predominantly correlated with the domain wall contribution.

Qualitatively, all compositions exhibit similar behavior of the third-harmonic parameters. The $|P_3^{3rd}|$, P_3', and P_3'' amplitudes describe an electric field-dependent increase (**Figure 5.17** and **Supplemental Figure 7.25**); similarly, an increase in domain wall motion with increasing vibration velocity was observed in the diffraction study (**Figure 5.6**). The increase of the polarization amplitudes accelerates at elevated temperatures, which agrees with the decreasing coercive and internal bias fields (**Figure 5.16**), revealing thermally-activated nonlinear dynamic contributions to the polarization response. The third-harmonic phase angle evolves from around -180° at low electric fields towards -90° at large fields (**Figure 5.17d-f**). Considering that the analyzed NBT-6BT compositions feature hardening characteristics (**Figure 5.3**) and in analogy to the same behavior observed in hard PZT [97], this evolution can be interpreted as a transition from an anhysteretic (reversible) response towards a more hysteretic (irreversible) response with increasing electric field amplitude. The nonlinear anhysteretic-to-hysteretic transition, determined from the $\delta^{3rd}(E)$ inflection point, is lower in unmodified NBT-6BT (0.2 kV/mm) than in NBT-6BT:10ZnO (0.49 kV/mm) and NBT-6BT-1Zn (0.73 kV/mm). The shift of the anhysteretic-to-hysteretic transition to larger electric fields in the modified compositions demonstrates an effective suppression of the hysteretic nonlinear response by Zn^{2+}-doping and ZnO inclusions and correlates with the larger E_c, E_{ib}, and Q_{31}^R values, and the lower electromechanical coefficients. Note that the transition fields are significantly larger than the maximum driving electric field applied in the high-power resonance measurements, strengthening the argument of paramount reversible domain wall motion regime used in Section 5.1 to explain the evolution of the electromechanical coefficients. Most important is thereby that the evolution of $\delta^{3rd}(E)$ below the transition and the transition field values do not exhibit a significant temperature dependence. This means that the ratio between the anhysteretic and hysteresis or in-phase and out-of-phase components is field but not temperature dependent. This confirms in turn that the magnitude of domain wall motion increases with temperature; however, the contributions are equally thermally activated, so that their ratio and thus their influence on Q_{31}^R does not change with temperature. Above the transition fields, the evolution and the saturation values of δ^{3rd} remain temperature-independent in NBT-6BT and NBT-6BT:10ZnO, but disclose a strong temperature dispersion in NBT-6BT-1ZnO. In other words, the ratio between the hysteretic and anhysteretic components of the nonlinear polarization response strongly increases with temperature only in NBT-6BT-1Zn, providing an additional evidence for different domain stabilization mechanisms introduced by the ZnO second phase in contrast to Zn^{2+}-doping.

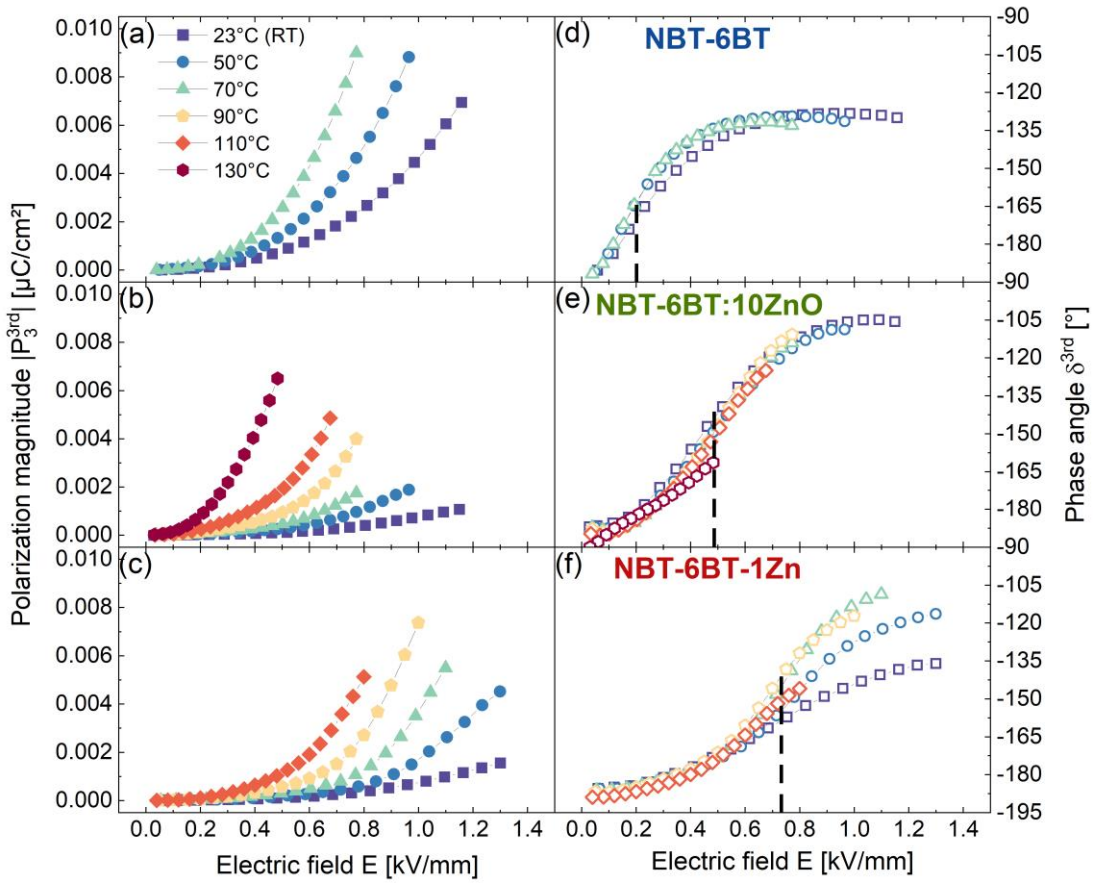

Figure 5.17. (a-c) Magnitude ($|P_3^{3rd}|$) and (d-f) phase angle (δ^{3rd}) of the 3rd-harmonic nonlinear polarization response as a function of the descending electric field amplitude (E) of unmodified NBT-6BT, NBT-6BT:10ZnO composite, and Zn^{2+}-doped NBT-6BT-1Zn in the polarized state and different temperatures. The dashed lines depict the anhysteretic-hysteretic transition (determined from the $\delta^{3rd}(E)$ inflection point). Please note that the maximum measured electric field was reduced at high temperatures due to the substantial decrease of E_c (**Figure 5.16**); thus, saturation values of δ^{3rd} could not be determined above 70 °C.

5.2.4. Thermal impact on the high-power electromechanical properties

The combined temperature and vibration velocity dependence of the electromechanical coefficients is summarized in property maps, yielding an overall property evaluation of the NBT-6BT compositions. Maps of Q_{31}^R, d_{31}, and FOM^{HP} in **Figure 5.18** (Q_{31}^{AR}, k_{31}, s_{11}^E, and ε_{33}^T are given in **Supplemental Figure 7.26**) were determined by pulse drive measurements at different temperatures; the results at the small vibration velocity end are in good agreement with the small-field resonance impedance measurements (**Figure 5.12**). Hence, all compositions exhibit the previously-observed continuous increase of d_{31} and k_{31} upon heating and the sharp drop (unmodified NBT-6BT) or continuous decrease (NBT-6BT:10ZnO and NBT-6BT-1Zn) above 90 °C. This behavior has been related to the ferroelectric-to-relaxor transition and the extended depolarization range. Notable is that the coefficients remain constant upon increasing vibration velocity at any temperature, even close to the depolarization temperature. The high-power measurements also confirm the different temperature dependences of Q_{31}^R observed in **Figure 5.12** for the compositions. However, despite the thermally induced changes, Q_{31}^R is remarkably stable upon increasing vibration velocity in all compositions and the entire temperature range, even close to depolarization. For comparison, **Figure 4.31** depicts the property maps for commercial hard PZTs, which exhibited substantial degradation of the electromechanical coefficients with both vibration velocity and temperature.

The compiled FOM^{HP} finally discloses the inherently stable and broad high-power operation window of NBT-6BT, which is demonstrated by the remarkably flat FOM^{HP} landscape. Moreover, both modifications increase the FOM^{HP} values and preserve the vibration velocity stability independent of the temperature. The NBT-6BT:10ZnO composite also demonstrates a reasonably flat FOM^{HP} landscape, evidencing the successful broadening of the temperature operational range and the capability of using the material well above 100 °C and even close to the depolarization temperature. On the other hand, Zn^{2+}-acceptor doping was revealed as the most effective approach to increase Q_{31}^{R} as well as FOM^{HP}. However, the introduced susceptibility to temperature variation is a notable drawback. The enormous thermal degradation of FOM^{HP} above the depolarization onset at about 90 °C makes the applicability of these compositions at elevated temperatures questionable.

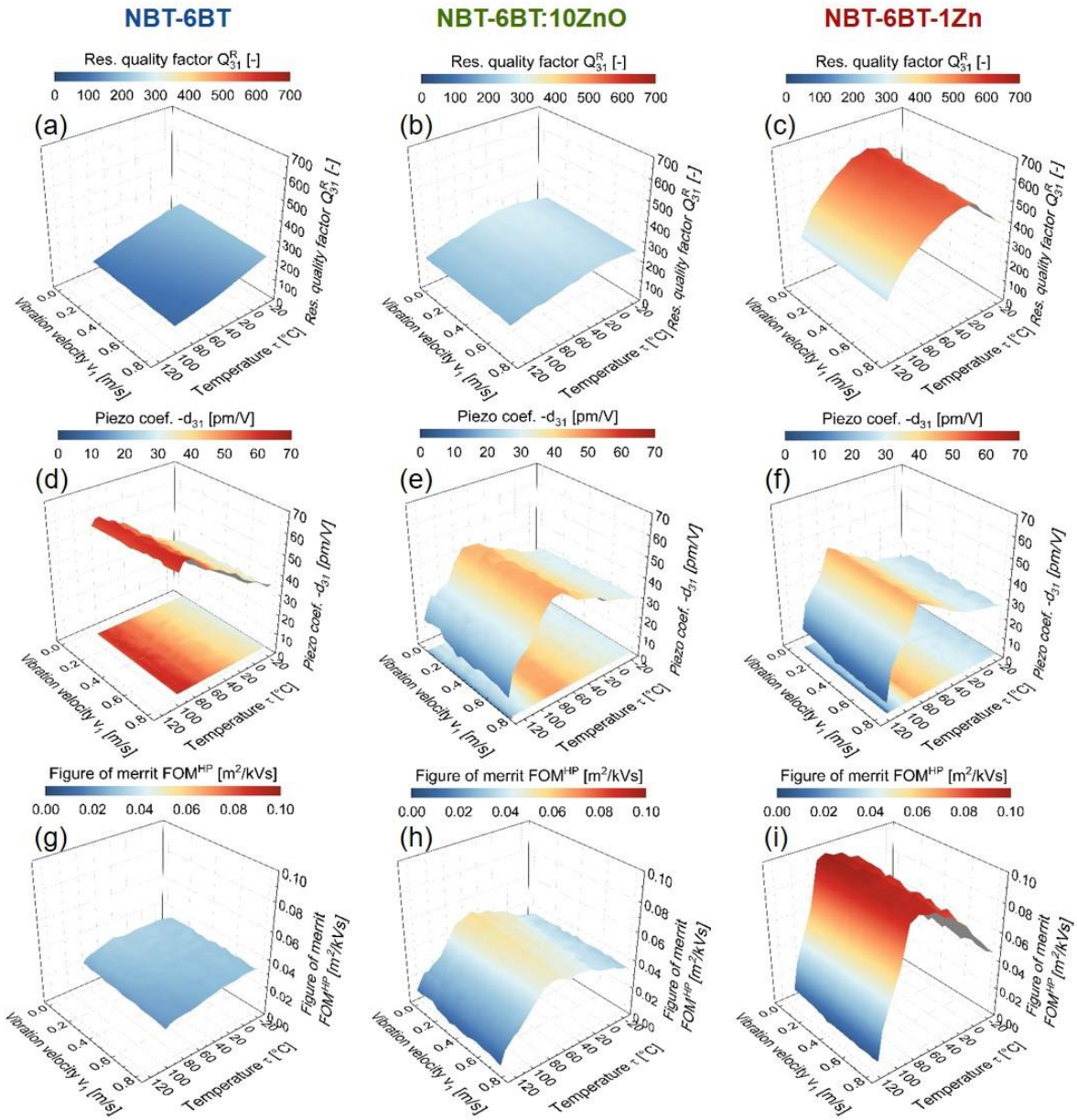

Figure 5.18. Temperature (τ) and vibration velocity (v_1) maps of the electromechanical coefficients (a-c) Q_{31}^{R}, (d-f) d_{31}, (g-i) s_{11}^{E}, and (j-l) FOM^{HP} of unmodified NBT-6BT, NBT-6BT:10ZnO composite, and Zn^{2+}-doped NBT-6BT-1Zn in the transverse (31) vibration mode. The variation of the coefficients with temperature and their stability upon vibration velocity at any temperature demonstrate that the thermal and vibrational impacts are decoupled.

Heat generation under continuous drive

The heat generation due to self-heating in the NBT-6BT compositions compared to the medium-hard PZT_T is depicted in **Figure 5.19**. The samples were driven at an ambient temperature of 20 °C continuously at different vibration velocities until the temperature of the samples stabilized. In medium-hard PZT_T, a considerable temperature rise sets in above 0.2 m/s. At that velocity, Q_{31}^R has already dropped down to about 70 % of the initial value (**Figure 4.7b**). The maximum measurement limit of 120 °C of the utilized IR camera is reached already at 0.64 m/s. Unmodified NBT-6BT displays a more gentle heat generation. Noticeable temperature increase starts at around 0.3 m/s. The maximum vibration velocity is limited to approximately 0.7 m/s, above which the temperature increase leads to the depolarization of the sample. NBT-6BT:10ZnO and NBT-6BT-1Zn reveal a very shallow temperature increase. The temperature barely exceeded 60 °C and 40 °C, respectively, at the highest experimentally accessible vibration velocity of 0.8 m/s. In general, the temperature profiles correlate with the $Q_{31}^R(\tau, v_1)$ and $FOM^{HP}(\tau, v_1)$ profiles of the samples discussed in **Figure 4.31** and **Figure 5.18,** with NBT-6BT-1Zn having the most stable and medium-hard PZT_T the least stable Q_{31}^R and FOM^{HP} values at large vibration velocity in that temperature range. However, it is expectable that NBT-6BT:10ZnO will outperform NBT-6BT-1Zn at further increasing vibration velocity and temperature due to the demonstrated superior stability above the depolarization onset, yielded by the property maps (**Figure 5.18**).

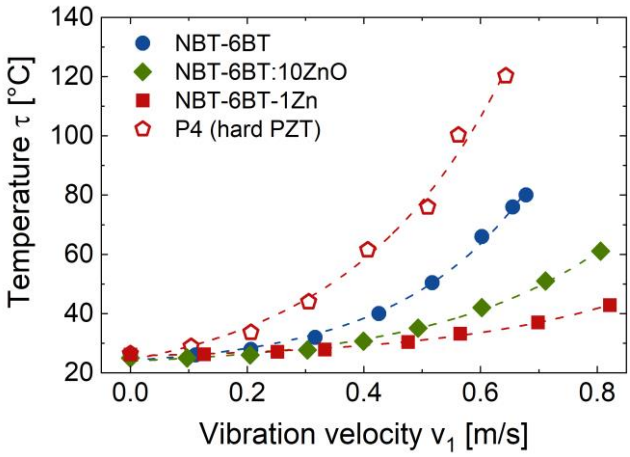

Figure 5.19. Vibration velocity (v_1) dependent temperature (τ) increase due to self-heating in transverse (31) vibration mode under continuous drive.

5.2.5. Conclusions

Zn^{2+}-doping as well as ceramic-ceramic composite formation with ZnO increase the depolarization temperature of NBT-6BT. The depolarization process terminates directly in the transition of the ferroelectric phase into the ergodic-relaxor phase without prior polarization detexturing; thus, the depolarization temperature increase is realized by the delay of the ferroelectric-to-relaxor transition temperature. However, the depolarization temperature and the ferroelectric-relaxor transition are not simply shifted to higher temperatures on average, but are smeared out over a wide temperature regime. Thereby, the onset temperature for depolarization remains unaltered at about 86 °C as in unmodified NBT-6BT, while the final depolarization occurs between 130 – 133 °C and 117 – 120 °C for the composites and the doped materials, respectively. The broadening discloses the decoupling of the piezoelectric d_{33} and

d_{31} coefficients in the depolarization region, which can be explained by a two-phase model, where the remanent textured ferroelectric phase is embedded in a growing ergodic-relaxor phase.

Zn^{2+}-doping most effectively increases the quality factors and the overall high-power figure of merit at ambient temperatures. However, the compositions become prone to thermal effects, displayed particularly by the quality factors' temperature dependence. Similar to acceptor-doped PZT, the temperature dependence arises from the thermally activated ionic conductivity rather than enhanced domain wall mobility. On the other hand, the NBT-6BT composite formation with ZnO inclusions leads to an overall minor increase of the quality factors, but the values are nearly temperature-invariant throughout the entire temperature range up to the delayed depolarization temperature. The thermal stability of the ZnO-composites supports the proposed hardening mechanism based on mechanical mismatch stress, which are not expected to alter remarkably in the probed temperature range.

Although the temperature has a noticeable influence on all electromechanical coefficients, the values remain stable upon increasing vibration velocity at any temperature and in all compositions. In accordance with the previous findings, the relative change of the high-power properties at large vibration velocities is determined by the basic ferroelectric material, decoupled from the thermal or compositional effects, which determine the absolute (small-field) values. The high-power stability of NBT-6BT-based compositions terminates, for example, in a reduced self-heating and enables the generation of significantly large vibration velocities even under continuous excitation.

5.3. Influence of DC bias field on the electromechanical properties

The effect of external DC bias fields on the electromechanical properties of PZT-based ferroelectrics in Section 4.5 demonstrated an enormous impact on the quality factors in acceptor-doped compositions, and on the piezoelectric, mechanical, and dielectric coefficients in donor-doped compositions. The changes were related to an effective immobilization of domain walls. Here, the impact of DC bias fields on the NBT-BT-based ferroelectrics is investigated. It is evaluated whether this external perturbation contributes to an additional ferroelectric hardening of the compositions, although predominantly the intrinsic rather than extrinsic contributions determine the electromechanical coefficients. The results should further enlighten the mechanistic differences between the two material groups.

5.3.1. Small-field electromechanical coefficients under DC bias field

Figure 5.20 displays the small-field electromechanical coefficients of unmodified NBT-6BT, NBT-6BT:10ZnO composite, and Zn^{2+}-doped NBT-6BT-1Zn as a function of the applied DC bias field. The coefficients were determined by resonance impedance spectroscopy utilizing the designed measurement system (Section 3.3). The measurements were conducted at a constant vibration velocity of 0.03 m/s for all compositions. Positive and negative field values denote the field applied along and opposite to the polarization direction, respectively. The ascending DC bias field branches are shown, from zero to maximum positive and from zero to minimum negative (depolarization) DC bias fields, respectively. The samples were prone to dielectric breakdowns during the frequency sweep at DC bias fields above 5 kV/mm; therefore, it was not possible to record the descending DC bias field branch in all cases.

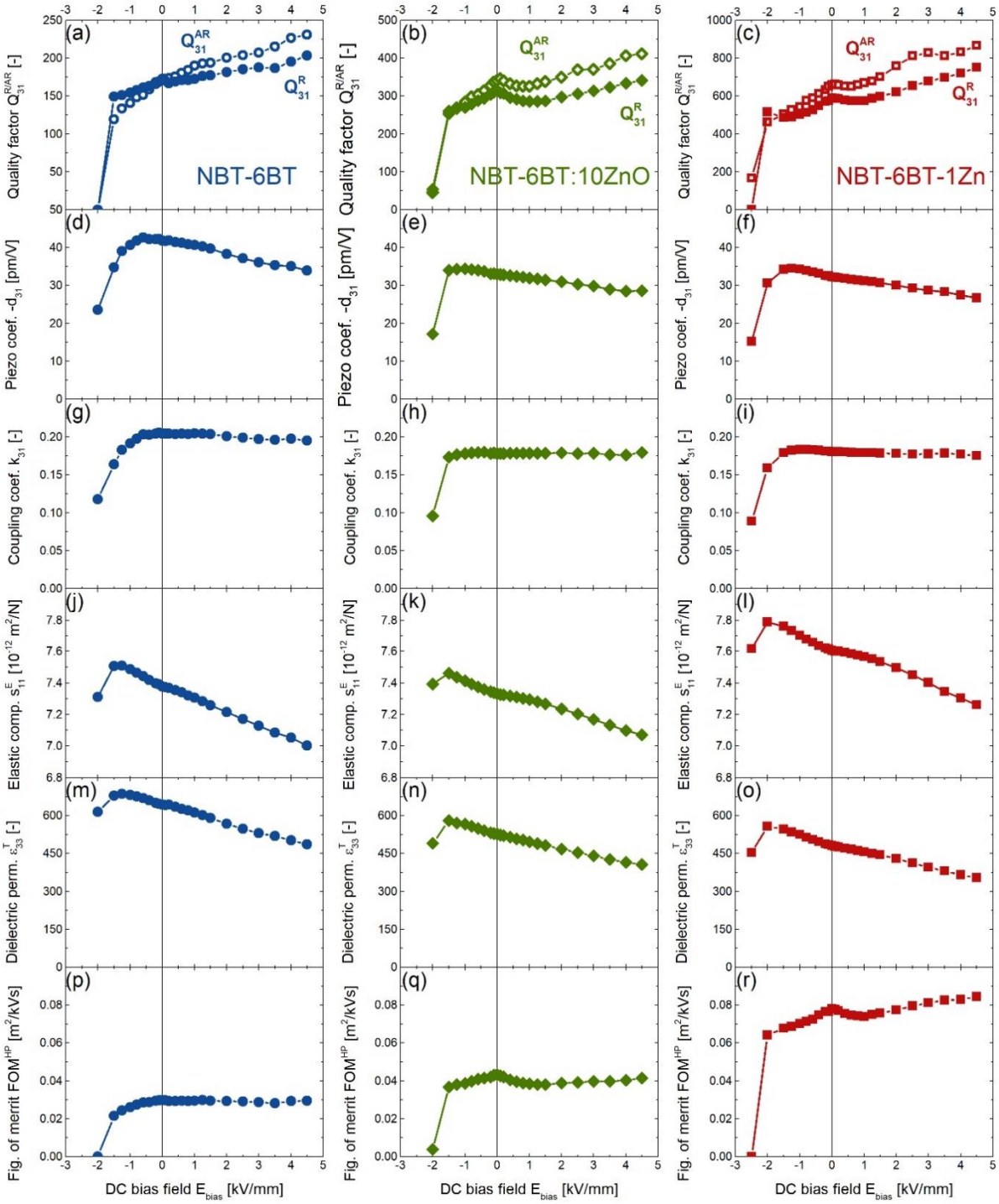

Figure 5.20. Electromechanical coefficients (a-c) Q_{31}^{R} (solid symbols) and Q_{31}^{AR} (open symbols), (d-f) d_{31}, (g-i) k_{31}, (j-l) s_{11}^{E}, (m-o) ε_{33}^{T}, and (p-r) high-power figure of merit (FOM^{HP}, **Equation** (4.6)) of unmodified NBT-6BT, NBT-6BT:10ZnO composite, and Zn^{2+}-doped NBT-6BT-1Zn in the transverse (31) vibration mode as a function of ascending DC bias field (E_{bias}) at 20 °C. Note the different scales in (a)-(c). Positive and negative field values denote the field applied along and opposite to the polarization direction, respectively. The marginal variation of the coefficients indicates a weak susceptibility of the compositions to the DC bias field.

The compositions reveal qualitatively very similar behavior with some important differences to the previously examined PZTs (**Figure 4.34** and **Supplemental Figure 7.14**). Q_{31}^{R} and Q_{31}^{AR} increase with increasing positive DC bias fields, demonstrating almost equivalent field dependence. The Q_{31}^{AR}/Q_{31}^{R} ratio changes only slightly, the largest increase of 15 % between zero

and maximum positive DC bias field appears in unmodified NBT-6BT. For comparison, the Q_{31}^{AR}/Q_{31}^{R} ratio change in the PZT compositions was in the range of 14-76 %.

The $Q_{31}^{R/AR}$ increase at large DC bias fields is linear. However, in NBT-6BT:10ZnO and NBT-6BT-1Zn the linear regime starts above about 1.5 kV/mm. In the low DC bias field range, $Q_{31}^{R/AR}$ of NBT-6BT:10ZnO and NBT-6BT-1Zn slightly decrease. The decrease is likely associated with the acceptor-defects, introduced purposely by Zn^{2+}-doping or unintendedly by diffusion from the ZnO second phase. During aging, the defects stabilize the domain configuration employed by the poling procedure, which is a time-dependent diffusion process. Application of small DC bias fields perturbates the configuration by dragging the domain walls apart from the defects, leading to slight ferroelectric softening, without introducing a prevalent DC bias hardening in turn yet. A related effect was reported in polarization harmonics measurements [97] and appears as well in the DC bias measurements of acceptor-doped PZT_T and PZT_R compositions upon ascending fields. The effect is not observed in unmodified NBT-6BT or donor-doped PZT. It evidences the above-discussed additional hardening contribution from parasitic Zn^{2+}-doping in the ZnO-composites. The effect vanishes upon descending DC bias fields, leading to a truly linear $Q_{31}^{R/AR}$ dependence throughout the entire field range in all compositions, i.e., the $Q_{31}^{R/AR}$ values in the linear regime are equal in the ascending and descending branches, the small hysteresis appears only in the low field regime.

It can be concluded that the overall $Q_{31}^{R/AR}$ increase upon positive DC bias field is comparatively small in all NBT-6BT compositions. The relative change expressed by $Q_{31}^{R}/Q_{31}^{R,0}$ and $Q_{31}^{AR}/Q_{31}^{AR,0}$ is almost equivalent between the compositions independent of the hardening approach (**Figure 5.21a**), resulting in a $Q_{31}^{R/AR}$ increase in the range of 9 – 27 % at maximum positive DC bias field. For comparison, the $Q_{31}^{R/AR}$ values increase by a factor of 2 – 6.1 (100 – 510 %) in the PZT_T compositions in the same DC bias field range (**Figure 4.35a**). At negative DC bias fields, $Q_{31}^{R/AR}$ values decrease and drop to zero in the vicinity of the depolarization fields, which is featured by the disappearance of the resonance/antiresonance peaks from the impedance spectrum.

The piezoelectric, mechanical, and dielectric coefficients d_{31}, k_{31}, s_{11}^{E}, and ε_{33}^{T} exhibit the opposite DC bias field dependence (**Figure 5.20d-o**). All coefficients decrease continuously with increasing DC bias field along the polarization direction. The influence of the DC bias field is almost identical independent of the hardening approach, which is exposed by the relative change of the coefficients in **Figure 5.21b-e**. The variation of the values between zero and maximum DC bias field is small, even compared to hard PZT_T (**Figure 4.35b-e**); k_{31} and s_{11}^{E} are nearly constant throughout the entire field range. The coefficients slightly increase at low negative DC bias fields, but rapidly drop towards zero due to an electric field-induced depolarization. Note that the depolarization induced by the DC bias field appears about 1 kV/mm below the coercive field of the compositions determined by P-E and S-E hysteresis loops (**Figure 5.3**). Akine shift of depolarization to lower field values was not observed for the PZT compositions.

The positive DC bias field has almost no impact on the FOM^{HP} values of the NBT-6BT compositions (**Figure 5.20p-r**). Only NBT-6BT-1Zn reveals a minor increase. Considering the relative change (**Figure 5.21f**), it can be concluded that FOM^{HP} is overall nearly constant and mostly independent of the DC bias in the entire field range.

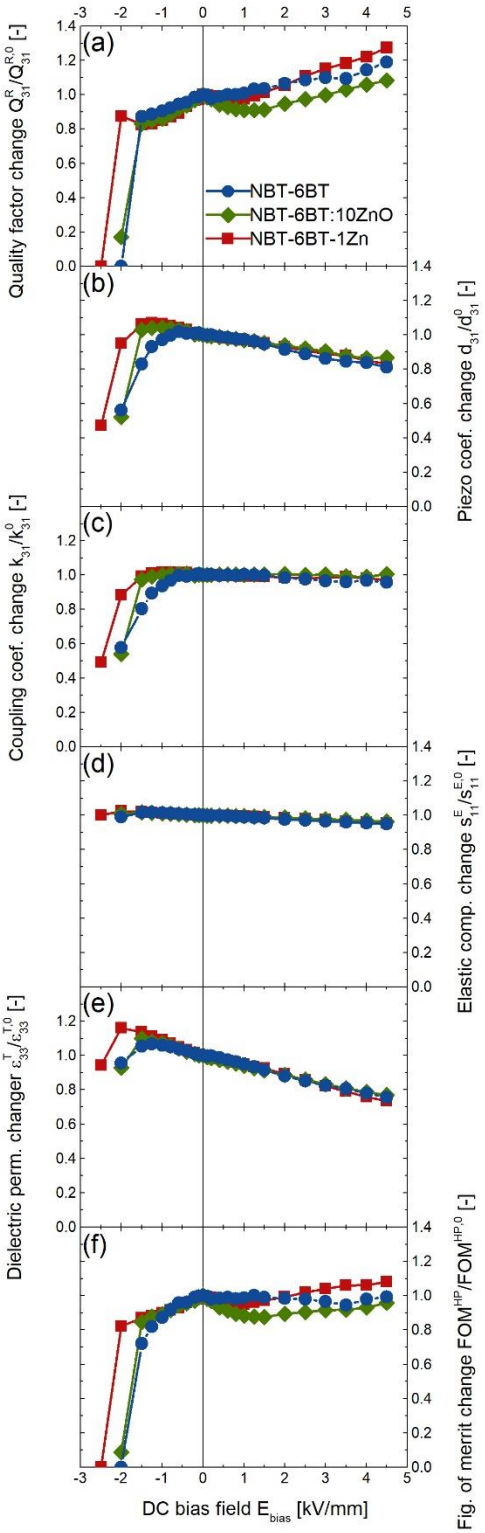

Figure 5.21. Relative change of the electromechanical coefficients with respect to the zero DC bias field condition (a) $Q_{31}^{R}/Q_{31}^{R,0}$, (b) d_{31}/d_{31}^{0}, (c) k_{31}/k_{31}^{0}, (d) $s_{11}^{E}/s_{11}^{E,0}$, (e) $\varepsilon_{33}^{T}/\ \varepsilon_{33}^{T,0}$, and (f) $FOM^{HP}/FOM^{HP,0}$ in unmodified NBT-6BT, NBT-6BT:10ZnO composite, and Zn^{2+}-doped NBT-6BT-1Zn in the transverse (31) vibration mode as a function of DC bias field (E_{bias}). Positive and negative field values denote the field applied along and opposite to the polarization direction, respectively. All compositions reveal an almost equivalent relative change of their coefficients, indicating the same mechanistic processes independent of the hardening approach.

5.3.2. Discussion and conclusions

The determined evolution of the electromechanical coefficients is overall in agreement with the proposed effect of DC bias field and the discussion put forward in Section 4.5, i.e., the decrease of the piezoelectric, mechanical, and dielectric coefficients and the increase of $Q_{31}^{R/AR}$ at positive DC bias fields imply ferroelectric hardening; vice versa, the increase of the coefficients and the decrease of $Q_{31}^{R/AR}$ at negative DC bias field indicates ferroelectric softening. However, the NBT-6BT compositions exhibit a considerably weaker susceptibility to the DC bias field than PZT.

The observed hardening is most likely related to the immobilization of domain walls, in common with the above-distinguished effect in PZT. But since the contribution of domain wall motion to the polarization/strain responses and to the generated loss (Section 5.1) is comparatively small, the immobilization has no significant impact on the electromechanical coefficients. Moreover, the domain wall contribution is quantitatively similar in all NBT-BT compositions (**Figure 5.6**), explaining the almost equal relative change of the coefficients.

Due to the insignificant domain wall contribution, the acceptor-doping exhibits no substantial influence, otherwise revealing an additional stabilization effect on the newly formed domain configuration under the DC bias field (increases the observed DC bias field hardening). In turn, a distinct difference between Zn^{2+}-doped, unmodified, and ZnO composites does not appear. The comparable impact of the DC bias field on the compositions independent of the applied modification further confirms that their properties are paramountly determined by the intrinsic mechanisms, which are significantly less influenced by the external perturbation than the extrinsic contributions dominating in PZT.

Note that the applied DC bias fields also affect the intrinsic properties and loss to a minor extent by disturbing the rhombohedral and tetragonal lattice distortions. Positive DC bias fields parallel to the polarization direction are expected to steepen the Gibbs free energy distribution according to the Landau–Ginsburg–Devonshire theory [45, 46] and to inhibit lattice polarization rotation. This leads to reduced intrinsic loss and increased quality factors, but also to smaller piezoelectric and dielectric coefficients. A considerable field-induced change of the rhombohedral/tetragonal phase fraction explaining the change of the coefficients is not expected after the initial polarization procedure [254]. The lattice effect is convoluted with the above-described influence of domain wall motion. However, it is evident that the impact on the intrinsic properties is insignificant, since the variation of the coefficients is small. Hence, it can generally be concluded that external conditions, including DC bias fields, vibration velocity, and temperature, have a significantly smaller influence on the NBT-BT compositions than on the PZT compositions. It aggravates the tuning of the properties but grants a stable operation under high-power conditions. The properties are ingrained by the intrinsic contributions, which can only be modified internally, for example, by doping or composite formation.

6. Summary and outlook

An experimental setup has been realized to perform pulse drive measurements of piezoelectric resonators with burst excitation at resonance and antiresonance frequencies. In combination with the three-stage procedure, the equipment overcomes the problem of beating and jumping effects and requires comparatively small excitation voltages to generate and measure large vibration velocities, excluding thereby the interference with self-heating effects. The design enables to carry out high-power measurements, determining the resonator's piezoelectric, mechanical, dielectric coefficients, and quality factors as a function of vibration velocity up to 10 m/s, at different temperatures in the range of -40 – 200 °C, and for various vibration modes (transverse, longitudinal, and radial). Referencing the measurements to standardized resonance impedance spectroscopy on the small-field end evidenced the setup accuracy and emphasized the non-linear evolution of the electromechanical coefficients, which necessitates the high-power characterization. Moreover, the equipment was combined with in-situ high-energy x-ray diffraction by synchronizing the high-frequency drive with short detector recording windows and stroboscopic intensity acquisition. This combination enabled a time-resolved observation of the strain contributions in resonance. It was proven that simultaneously measured macroscopic and microscopic strains are in excellent agreement. Additionally, a fully-integrated measurement setup has been realized to load piezoelectric resonators with superimposed AC excitation voltage and DC high-voltage bias under resonance conditions. The combination of two separate output amplifier stages and optimization feedback control algorithm allowed to overcome the problem of applying significant DC bias up to +/- 10 kV and constant AC voltage amplitude up to 10 V over a broad frequency range between 50 – 500 kHz on a sample with highly non-linear impedance in the range of 10^{-1} – 10^{6} Ω. The equipment enables to carry out piezoelectric resonance impedance spectroscopy under DC bias manipulation of the resonator, complying thereby with established Piezoelectric Standardization and ensuring appropriate protection of the device, resonator, and user. The functionality of the proposed setup was benchmarked against commercial impedance analyzers and reference equivalent circuits.

The amplified strain generation in piezoelectric resonance is a unique constitution determined by the resonator's piezoelectric, mechanical, and dielectric properties, as much as by the energy dissipation and generated loss, represented by the quality factor (Q_{ij}). The resonance performance of piezoelectric materials is thereby best expressed by accumulating the electromechanical coefficients to the derived high-power figure of merit (FOM^{HP}). This study raised awareness that two aspects of the FOM^{HP} necessitate being separated in order to evaluate high-power eligibility appropriately, i.e., the absolute (small-field) values on the one hand and the relative stability upon increasing vibration velocity on the other hand. The findings have consistently demonstrated that both aspects are predominantly dictated by the behavior of Q_{ij}, which is the most sensitive coefficient and prone to a substantial variation depending on internal and external parameters. However, at the same time, it turned out that the absolute values and the relative stability are not necessarily correlated. In fact, they are mostly independent and even associated with different mechanisms in certain cases.

The highest small-field FOM^{HP} values were determined in acceptor-doped (ferroelectrically hard) $Pb(Zr,Ti)O_3$ compositions on the Ti-rich tetragonal site of the phase diagram, evolving from large Q_{ij} values in combination with comparatively large piezoelectric coefficients.

However, the FOM^{HP} reveals a rapid decrease by more than 80 % already in the low vibration velocity range (<1 m/s). The decrease is associated with significant degradation of Q_{ij}, which is not equivalently compensated by the other electromechanical coefficients. The decrease appears qualitatively equivalent in all investigated compositions of the $Pb(Zr,Ti)O_3$ group, independent of the doping element and concentration (acceptor/donor), crystal structure (Zr/Ti ratio), grain size (domain size), or temperature (thermal activation), i.e., an increase of the absolute Q_{ij} values does not result in improved relative stability. Moreover, normalizing the vibration velocity dependence of Q_{ij} to the small-field values in terms of Q_{ij}/Q_{ij}^0 revealed a clustering of the relative Q_{ij} evolution throughout all compositions. The clustering manifests that the relative stability is primarily determined by the inherent properties of the ferroelectric matrix and, in contrast to the absolute values, mostly independent of chemical doping or other modifications.

Mechanistic origin of the Q_{ij} decrease and the concurrent increase of piezoelectric, mechanical, and dielectric coefficients is the increasing displacement of ferroelectric domain walls. Specifically, it is the enhanced contribution of the domain wall motion to the generated total strain compared to the lattice strain contribution. The motion is considered a loss-afflicted strain-generating process with a pronounced out-of-phase component relative to the driving force, due to the inertia and large effective mass of domain walls. The inverse correlation between Q_{ij} and the magnitude of domain wall motion was evidenced by the overlapping electromechanical and microstructural evolution as a function of vibration velocity (structure-property correlation) and supported by the opposite frequency dependence. Furthermore, it was determined that the vibration velocity and frequency dependence can be quantified by the proposed Rayleigh-like exponential and logarithmic expressions, respectively. It turned out that ferroelectrically hard and soft $Pb(Zr,Ti)O_3$ compositions reveal very similar attenuation coefficients (relative increase of domain wall motion contribution) despite exhibiting significantly different absolute strain contribution ratios. It was concluded that the attenuation is determined by the properties of the basic material and associated with the clustering of Q_{ij}. It is suggested to consider the attenuation coefficient as a general characteristic predicting the high-power stability of ferroelectric material groups.

The main driving force for the resonance strain is the dynamic mechanical stress emerging in the resonator, while the applied electric field only triggers the vibration. The observed domain wall motion is thus the lattice's response to the stress by periodically switching the polar axis away from the direction of maximum compression and into the direction of maximum tension. It follows that the stability of Q_{ij} associates with the coercive stress rather than the coercive field, which is inherently smaller in $Pb(Zr,Ti)O_3$-based compositions compared to $(Na_{1/2}Bi_{1/2})TiO_3$-$BaTiO_3$-based ferroelectrics. Furthermore, it was evidenced that the absolute values and the relative stability depend on the utilized vibration mode, which is related to different stress distribution profiles in the resonators and the contribution of different loss tensor components. It was demonstrated that accounting for the loss anisotropy (Q_{ij} as a tensor) and the direction dependence of the non-linear behavior can enhance the high-power performance, for example, in terms of reduced heat generation.

$(Na_{1/2}Bi_{1/2})TiO_3$-$BaTiO_3$ compositions possess, in general, inferior FOM^{HP}s than $Pb(Zr,Ti)O_3$. Nevertheless, selecting MPB-close compositions and introducing ferroelectric hardening was recognized to result in reasonably large values. The increase is primarily correlated with the

many-fold increase of Q_{ij}, which is most effectively attained by acceptor-doping with Zn^{2+}. Simultaneously, all $(Na_{1/2}Bi_{1/2})TiO_3$-$BaTiO_3$ compositions reveal an inherently superior relative stability that is preserved even after extensive ferroelectric hardening, i.e., the piezoelectric, mechanical, and dielectric coefficients are almost constant up to considerably large vibration velocities, while Q_{ij} exhibits only a moderate decrease. This leads to substantially higher FOM^{HP} values at large vibration velocities compared to state-of-the-art $Pb(Zr,Ti)O_3$, with a crossing point already in the low vibration velocity region. The pronounced stability in combination with profound fracture toughness and heat conductivity transforms into excellent high-power performance and enables the generation of large vibration velocities up to the range of 4 m/s with an essentially reduced self-heating. For comparison, $Pb(Zr,Ti)O_3$ compositions are basically limited to 2.5 m/s due to mechanical fracture and severe heat generation already at lower velocities.

The stability is an inherent property of $(Na_{1/2}Bi_{1/2})TiO_3$-$BaTiO_3$, which was confirmed again by the clustering of the normalized Q_{ij}/Q_{ij}^0 evolution. Mechanistic origin is the significantly lower contribution of non-180° domain wall motion to the generated strain and no evident increase of the contribution ratio with increasing vibration velocity, i.e., the strain generation has a predominantly intrinsic nature and results from lattice distortion. Both are most likely the consequence of the enormous coercive stress. The yet comparatively low (small-field) Q_{ij} values (e.g., unmodified NBT-6BT versus hard PZT_T) indicate a substantial contribution of intrinsic loss in addition to the usually-dominant extrinsic loss. The intrinsic loss was rationalized to originate from a pronounced lattice polarization rotation compared to the polarization extension, associated with a flat polarization potential according to the Landau-Ginzburg-Devonshire theory. Consequently, the relative stability relies on the lower dependence of the intrinsic loss on the vibration velocity. The increase of Q_{ij} after hardening (Zn^{2+}-doping and ZnO composite formation) correlates with reduced intrinsic loss through an enlarged ferroelectric lattice distortion (c/a ratio) and eventually a slightly reduced domain wall strain contribution, which has a significant impact on the highly sensitive Q_{ij} coefficient.

Furthermore, it was determined that the relative stability of FOM^{HP} is temperature independent for all investigated ferroelectrics, i.e., the above-discussed clustering appears also upon measurements at different temperatures, even close to the depolarization temperature of the $(Na_{1/2}Bi_{1/2})TiO_3$-$BaTiO_3$ compositions. On the other hand, the absolute values reveal a pronounced temperature dependence. Thereby, the electromechanical coefficients demonstrate distinctly different temperature behavior. The piezoelectric, mechanical, and dielectric coefficients exhibit a continuous change as a function of temperature, associated with the thermal activation of the total magnitude of lattice strain and domain wall motion, which was verified through structural, ferroelectric, and harmonic characterization. In contrast, Q_{ij} is almost temperature independent since it depends on the ratio of the in-phase and out-of-phase components instead of the total magnitude, which are equivalently thermally activated without a significant ratio change. An exception are acceptor-doped compositions with a pronounced non-continuous temperature alternation. However, in this case, the temperature dependence originates from the evolving dielectric loss associated with the generated oxygen vacancies and the thermally activated ionic hopping conductivity. This leads to the ambiguity that heavily acceptor-doped compositions reach exceptionally large Q_{ij} and FOM^{HP} values, but only in a narrow temperature window and are prone to substantial temperature variance.

A promising alternative is the second phase modified $(Na_{1/2}Bi_{1/2})TiO_3$-$BaTiO_3$ with ZnO inclusions at the grain boundaries. The ceramic-ceramic composite formation increases simultaneously the depolarization temperature and the Q_{ij} values. The depolarization process terminates directly into the transition of the ferroelectric phase into the ergodic-relaxor phase without prior polarization detexturing; thus, the depolarization temperature increase is realized by the shift of the ferroelectric-to-relaxor transition temperature and spreading of the depolarization process over a wide temperature range. These composites reach lower FOM^{HP} values than the Zn^{2+}-doped compositions; however, they possess almost temperature-independent properties, since the introduced mismatch stress does not contribute to conductivity. In combination with the inherent relative stability, the composites retain a broader temperature-velocity operation window. They are suggested to be more suitable for high-power applications under thermal load and/or pronounced self-heating.

Another approach to reach broad operation windows could be DC bias hardening. It was demonstrated that the superposition of the excitation load with a DC bias results in increasing Q_{ij} and decreasing piezoelectric, mechanical, and dielectric coefficients, which in total can terminate in enhanced FOM^{HP} values. The effect is most powerful in compositions with predominantly extrinsic loss, while it has only minor impact on compositions with dominant intrinsic loss. It is suggested that, for example, a reduction of the acceptor-doping concentration and simultaneous compensation of the reduced hardening by a superimposed DC bias has the potential to result in improved high-power properties in combination with enhanced temperature stability due to reduced parasitic conductivity loss.

In general, it can be concluded that ferroelectrics with excellent high-power properties in a broad temperature and vibration velocity range require a combination of large electromechanical coupling, efficiently inhibited out-of-phase components of the charge-displacing and strain-generating mechanisms, and a low conductivity implied by a significant activation energy. These requirements appear to be best achieved by MPB-compositions of ferroelectric systems with inherently large coercive stress, which are additionally non-chemically hardened by second phase formation or DC bias.

7. Supplemental material

7.1. Piezoelectric formalism

7.1.1. Extensive constitutive equations

The relations given in **Equations (2.8)-(2.12)** are usually referred to as (T,E)-type or intensive relations, indicating that only intensive, i.e., system size independent, variables and the corresponding coefficients are used. Intensive variables are preferably measured, since they are experimentally easier to access and control. However, from the physical point of view, the extensive variables S_j and D_j as well as the corresponding coefficients elastic stiffness c_{ij}, dielectric impermeability β_{ij}, and piezoelectric stiffness coefficient h_{ij}, are more fundamental. The (S,D)-type or extensive constitutive equations are expressed as [11]

$$T_i = c_{ij}^D S_j - h_{ij} D_j \text{ and} \tag{7.1}$$

$$E_i = \beta_{ij}^S D_j - h_{ij} S_j. \tag{7.2}$$

k_{ij} is determined by the electromechanical coefficients in multiple equivalent and physically interchangeable expressions, like

$$k_{ij}^2 = \frac{d_{ij}^2}{s_{ij}^E \varepsilon_{ij}^T} = \frac{h_{ij}^2}{c_{ij}^D \beta_{ij}^S}. \tag{7.3}$$

Thus, the intensive and extensive coefficients are interrelated through k_{ij} as

$$1 - k_{ij}^2 = \frac{c_{ij}^E}{c_{ij}^D} = \frac{s_{ij}^D}{s_{ij}^E} = \frac{\varepsilon_{ij}^S}{\varepsilon_{ij}^T} = \frac{\beta_{ij}^T}{\beta_{ij}^S}. \tag{7.4}$$

Subsequently, the relations between various physical coefficients emerge based on k_{ij}, which are required to formulate the resonance vibration of different vibration modes. Some of the relations utilized in the study are (utilizing the tensor abbreviation)

$$d_{nm} = \varepsilon_{np}^T g_{pm} = e_{np} s_{pm}^E, \tag{7.5}$$

$$h_{nm} = \beta_{np}^S e_{pm} = g_{np} c_{pm}^D, \text{ and} \tag{7.6}$$

$$\beta_{np}^S \varepsilon_{pm}^T = \Delta_{nm}, \tag{7.7}$$

where g_{np} is the piezoelectric voltage coefficient and e_{np} the piezoelectric stress coefficient. Note that the coefficients represent tensors of different ranks, therefore, the interchange is not trivial.

7.1.1. Equivalent circuit of the transverse (31) vibration mode

The admittance of a free bar resonator in transverse (31) vibration mode can be represented by an electric Butterworth-Van Dyke (BVD) circuit [30]. C_0 determines the off-resonance "clamped" capacitance, C_{d_n} and L_d denote the capacitance and inductance of the dynamic branches (**Supplemental Figure 7.1**). Multiple dynamic branches encounter higher harmonics of the vibration. The circuit elements are given by

$$C_0 = \varepsilon_{33}^T \frac{lw}{h}, \tag{7.8}$$

$$L_d = \frac{1}{\omega_{R_1}^2 C_{d_1}}, \text{ and} \tag{7.9}$$

$$C_{d_n} = p_n \frac{k_{31}^2}{1-k_{31}^2} C_0 \tag{7.10}$$

$$\text{with } p_n = \frac{8}{\pi^2}\frac{1}{n^2} \text{ and } \sum_n p_n = 1. \tag{7.11}$$

p_n is a scaling factor for the higher harmonics contribution and n represents odd integers.

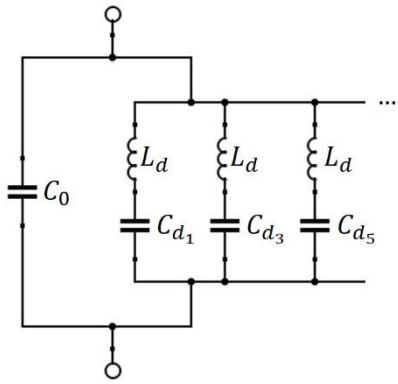

Supplemental Figure 7.1. Ideal equivalent electric circuit (loss-free) representing a piezoelectric resonator in transverse (31) vibration mode with a static (C_0) and multiple parallel dynamic ($L_d C_{d_n}$) branches.

The circuit reveals several resonance and antiresonance angular frequencies according to

$$\omega_{R_n}^2 = \frac{1}{L_d C_{d_n}} \text{ and } \omega_{AR_n}^2 \cong \frac{1}{L_d}\left(\frac{1}{C_{d_n}} + \frac{1}{C_0}\right). \tag{7.12}$$

The resonator's edge vibration velocity is proportional to the current amplitude in the circuit (specifically, to the dynamic branch current, but the static branch current is negligibly small). The proportionality is given by the force factor (A_{31}; **Equation (2.31)**), i.e., the force factor correlates the circuit elements with the electromechanical coefficients according to [11]

$$L_d = \frac{m}{2A_{31}^2}, \tag{7.13}$$

$$C_{d_1} = \frac{8}{\pi^2} A_{31}^2 s_{11}^E \frac{l}{4wh}, \text{ and} \tag{7.14}$$

$$C_0 = \frac{\pi^2}{8}\frac{1-k_{31}^2}{k_{31}^2}\frac{1}{\omega_{R_1}^2 L_d} = \frac{1}{L_d(\omega_{AR_1}^2 - \omega_{R_1}^2)}. \tag{7.15}$$

L and C_1 correspond to the coupled mass (m) and spring in the lumped mechanical model of the resonator.

7.1.2. Longitudinal vibration with k_{33} coupling

The derivation of the longitudinal (33) mode vibration (**Table 2.1**) assumes a large permittivity of the resonator, i.e., the depolarization field effect is small (valid assumption for most ferroelectrics). The electric and mechanical boundary conditions are given by [11]

$$\frac{\partial D_3}{\partial x_1} = \frac{\partial D_3}{\partial x_2} = 0 \text{ and } S_1 = S_2 = 0. \tag{7.16}$$

The corresponding constitutive piezoelectric relations are

$$T_3 = c_{33}^E S_3 - e_{33} E_3 \text{ and} \tag{7.17}$$

$$D_3 = \varepsilon_{33}^S E_3 + e_{33} S_3. \tag{7.18}$$

Inserting **Equation (7.17)** into **(7.18)** results in

$$T_3 = c_{33}^D S_3 - \frac{e_{33}}{\varepsilon_{33}^S} D_3 \tag{7.19}$$

$$\text{with } c_{33}^D = c_{33}^E + \frac{e_{33}^2}{\varepsilon_{33}^S} = \frac{c_{33}^E}{1-k_{33}^2}. \tag{7.20}$$

The admittance of the resonator is a sum of the static (Y_0) and dynamic (Y_d) contributions

$$Y = Y_0 + Y_d \tag{7.21}$$

$$\text{with } Y_0 = j\omega C_0 \tag{7.22}$$

$$\text{and } \frac{1}{Y_d} = \frac{1}{j\omega(-C_0)} + \frac{1}{\sum_{n_{odd}}^{\infty} \frac{1}{j\left(\omega L_d - {}^1/_{\omega C_{d_n}}\right)}}. \tag{7.23}$$

Opposite to the transverse (31) mode, the dynamic admittance Y_d contributes to the antiresonance, while both contribute to the resonance. A negative capacity $-C_0$ is introduced to the dynamic branch to encounter the depolarizing-field effect. The elements of the equivalent circuit (**Supplemental Figure 7.2**) are given by

$$C_0 = \varepsilon_{33}^S \frac{w^2}{h}, \tag{7.24}$$

$$L_d = \frac{1}{\omega_{AR_1}^2 C_{d_1}}, \text{ and} \tag{7.25}$$

$$C_{d_n} = p_n k_{33}^2 C_0 \tag{7.26}$$

$$\text{with } p_n = \frac{8}{\pi^2} \frac{1}{n^2}. \tag{7.27}$$

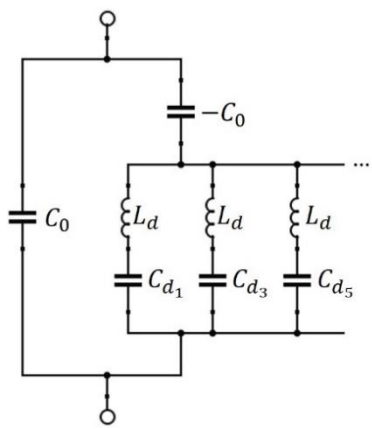

Supplemental Figure 7.2. Ideal equivalent electric circuit (loss-free) representing a piezoelectric resonator in longitudinal (33) vibration mode with a static (C_0) and multiple parallel dynamic ($L_d C_{d_n}$) branches. The negative capacity $-C_0$ accounts for the depolarizing-field.

The resonance and antiresonance angular frequencies are

$$\omega_{R_n}^2 \cong \frac{1}{L_d}\left(\frac{1}{C_{d_n}} + \frac{1}{-C_0}\right) \text{ and } \omega_{AR_n}^2 = \frac{1}{L_d C_{d_n}}. \tag{7.28}$$

The force factor (A_{33}) is

$$I_3 = A_{33} v_3 \text{ with } A_{33} = 2e_{33}\frac{w^2}{h}. \tag{7.29}$$

The circuit elements and the electromechanical coefficients correlate according to

$$L_d = \frac{m}{2A_{33}^2}, \tag{7.30}$$

$$C_{d_1} = \frac{8}{\pi^2} A_{33}^2 s_{33}^D \frac{h}{4w^2} = \frac{1}{\omega_{AR_1}^2 L_d}, \text{ and} \tag{7.31}$$

$$C_0 = \frac{\pi^2}{8}\frac{1}{k_{33}^2}\frac{1}{\omega_{AR_1}^2 L_d} = \frac{1}{L_d(\omega_{AR_1}^2 - \omega_{R_1}^2)}. \tag{7.32}$$

The coefficients k_{33}, s_{33}^E, and d_{33} are calculated from the measured quantities f_R, f_A, and A_{33} (**Table 2.1**).

7.1.3. Radial vibration with k_p coupling

The radial (p) vibration mode (**Table 2.1**) denotes the radial extension of a disc, which is basically equivalent to the transverse (31) mode with the difference that the vibration is two- instead of one-dimensional. The dimensionality can be encountered by considering the Poisson ratio (σ) in the formulations of the transverse mode and utilizing the cylindrical coordinate system to express the electric and mechanical boundary conditions according to [11]

$$T_3 = 0 \text{ and} \tag{7.33}$$

$$\frac{\partial E_3}{\partial x_1} = \frac{\partial E_3}{\partial x_2} = \frac{\partial E_3}{\partial r} = 0. \tag{7.34}$$

The emerging coupling coefficient (k_p) can be expressed as

$$k_p^2 \cong 2.51\frac{f_{AR}-f_R}{f_R} - \left(\frac{f_{AR}-f_R}{f_R}\right)^2 = \frac{2}{1-\sigma}\frac{d_{31}^2}{s_{11}^E \varepsilon_{33}^T} = \frac{2}{1-\sigma}k_{31}^2. \tag{7.35}$$

7.2. Resonance impedance spectroscopy

The most established method to determine small-field piezoelectric, mechanical, dielectric coefficients, and quality factors is the resonance impedance spectroscopy with *constant voltage* amplitudes over the entire frequency sweep (Section 3.1.1). The technique is typically included in commercial impedance analyzers and described in Piezoelectric Standardization (e.g., European (EN 50324) [28] or IEEE (ANSI/IEEE Std 176–1987) [183]). However, the method is limited to small vibration velocities due to several disturbing effects arising with increasing excitation voltages and velocities, respectively. The resonance region exhibits an evolving distortion that merges into impedance jumps and hysteresis depending on the sweep direction, i.e., rising or falling frequencies (**Supplemental Figure 7.3a,b**) [21, 255]. The distortion originates from the non-linearity of the electromechanical coefficients [24] and prohibits, for example, an accurate determination of $Q_{ij}^{R/AR}$ that requires symmetric and continuous impedance development around $f_{R/AR}$ (**Figure 3.1**) [12, 177, 181]. Moreover, the method requires a comparatively long measurement times of about 1 s at every frequency to achieve high accuracy, which is sufficient to induce notable resonator self-heating that additionally distorts the measured spectrum. The heating is especially pronounced in the resonance vicinity. For example, **Supplemental Figure 7.3c** shows the temperature development in soft PZT_T measured with a commercial impedance analyzer at a low velocity of 0.23 m/s in resonance of the transverse (31) mode.

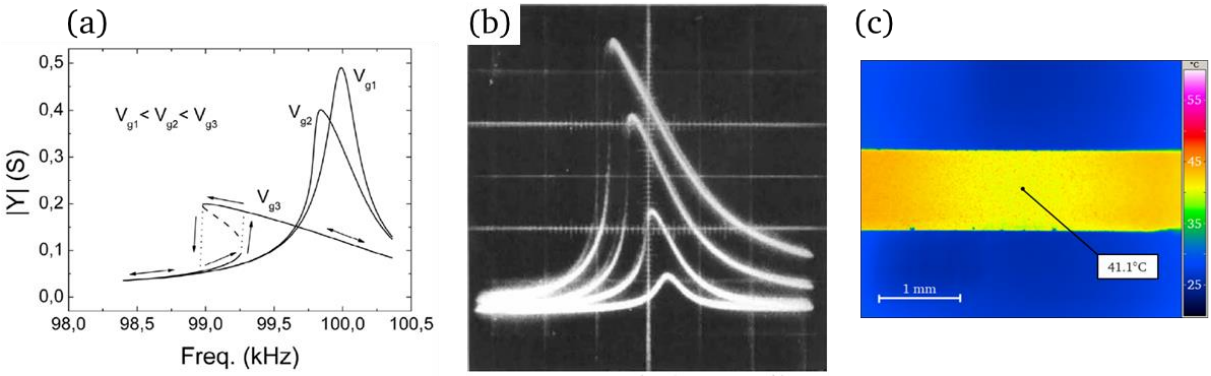

Supplemental Figure 7.3. (a) Schematic (reprinted by permission from IEEE [177] © 2007) and (b) measurement (reprinted by permission from Taylor & Francis [21] © 1982) of admittance ($|Y|$) hysteresis around resonance during rising or falling frequency sweep at different excitation voltage amplitude (V). The peak distortion prohibits a determination of the material's coefficients at high vibration velocities. (c) Temperature development in soft PZT_T (PIC 151) vibrating at 0.23 m/s and f_R during a frequency sweep with a commercial impedance analyzer (Alpha-A, Novocontrol Technologies) at 10 V/mm field amplitude (center T=41.1°C, surrounding T=23.4°C).

The distortion around resonance can be eliminated utilizing the *constant current* technique, a common variation of the constant voltage method [177, 180, 181]. Implementing a feedback loop, a current response of constant amplitude is generated by adjusting the excitation voltage continuously (**Supplemental Figure 7.4**). However, while a distortion at resonance is avoided, it appears instead at antiresonance, where the generated vibration is proportional to the applied voltage and not to the current response [256]. Moreover, the method is prone to pronounced heat generation and requires a high-frequency large AC voltage source to generate the set current amplitude around antiresonance, where the resonator resistance is usually considerably large.

Two alternative variations are the *constant vibration velocity* and the *constant input power* techniques [181]. A feedback loop is combined with a displacement sensor to adjust the excitation voltage amplitude and re-evaluate the generated displacement and current at every sweep frequency, keeping a pre-determined vibration velocity or power input constant. Due to the active control of voltage and current, resonance and antiresonance are measured without spectrum distortion [37]. Drawbacks are the requirement for a sophisticated feedback loop and a high-voltage/high-current source. Remaining handicap is the heat generation, which is even more pronounced since the measurement time is expanded by the computational time of the loop.

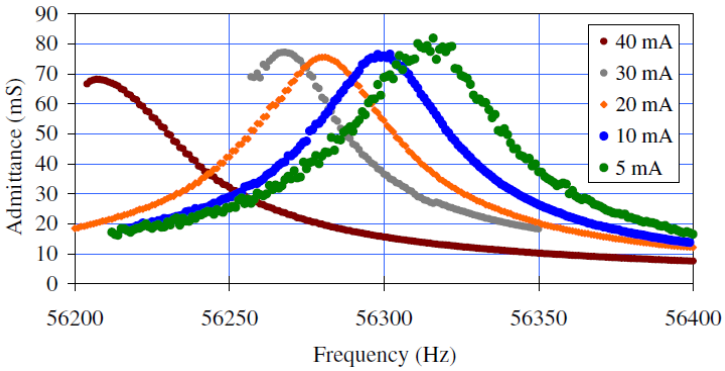

Supplemental Figure 7.4. Admittance as a function of frequency of a hard PZT ceramic resonator, measured at different current amplitudes using the constant current method (reprinted by permission from IOP Publishing [181] © 2009).

7.3. Supplemental tables

Supplemental Table 1. Samples geometries utilized for the three investigated vibration modes and the applied experimental methods.

Vibration mode	Geometry	Material group	Measurement methods
Transverse length (31) mode *(length x width x height) [mm]*	15x3x1	PZT	Electromechanical, dielectric, piezoelectric, and ferroelectric measurements
	20x3x1	NBT-BT	
	24x3x1	PZT & NBT-BT	Combined electromechanical and diffraction measurements
	8x1x1	PZT	Frequency-dependent electromechanical and diffraction measurement
	15x1x1	PZT	
	24x1x1	PZT	
	24x2x1	PZT	
	24x3x1	PZT	
	30x1x1	PZT	
Longitudinal length (31) mode *(length x width x height) [mm]*	2.4x2.4x6	PZT	Electromechanical measurements
Radial (p) mode *(diameter x height) [mm]*	15x1	PZT	Electromechanical measurements
	6x0.5	PZT & NBT-BT	Polarization harmonic measurements

7.4. Supplemental figures

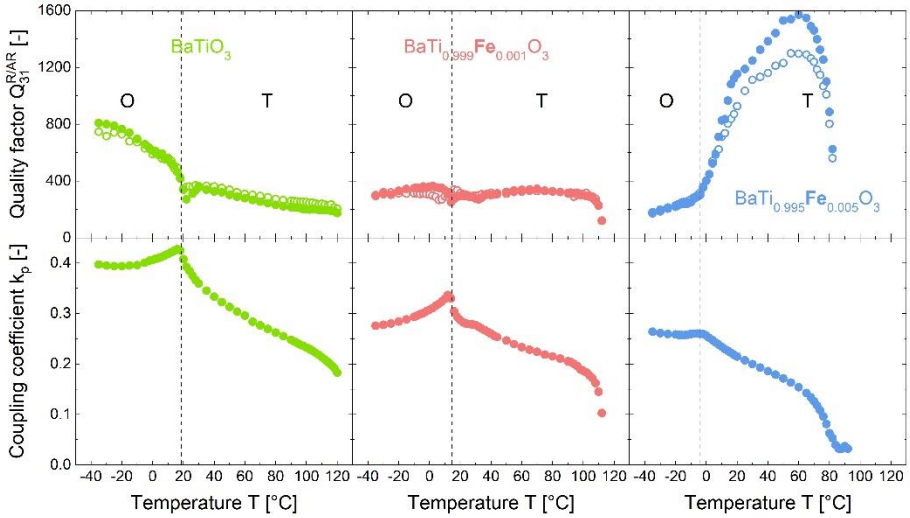

Supplemental Figure 7.5. Small-field (v_1→ 0 m/s) electromechanical coefficients Q_{p}^{R} (solid circles), Q_{p}^{AR} (open circles), and k_{p} of undoped and Fe-doped (0.1 mol% and 0.5 mol%) $BaTiO_3$ in the planar (p) vibration mode as a function of temperature (T) during the first heating cycle after poling. The dashed line separates the low-temperature orthorhombic (O) phase and high-temperature tetragonal (T) phase.

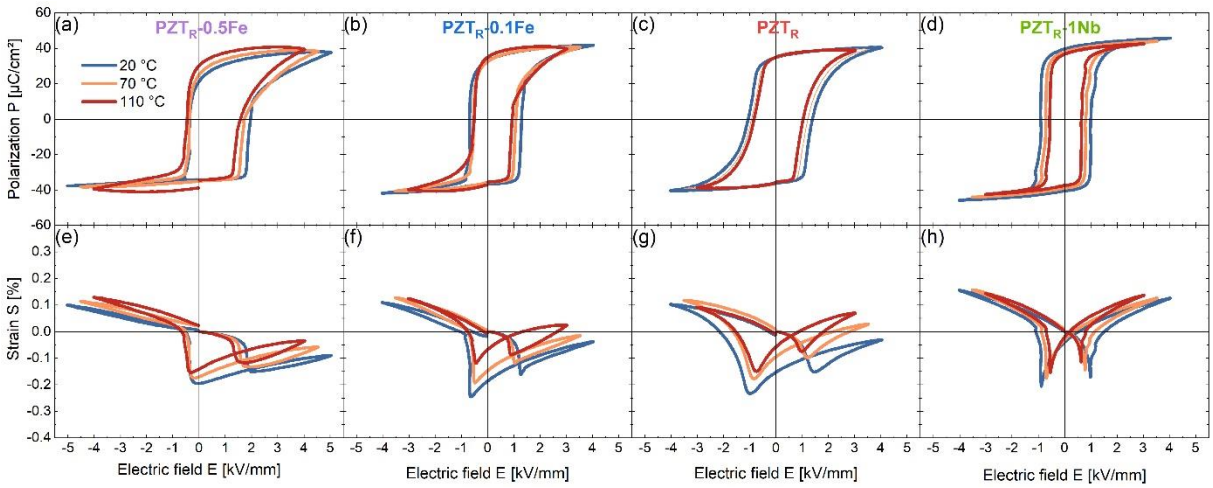

Supplemental Figure 7.6. Polarization (P) and strain (S) hysteresis loops as a function of applied 1 Hz bipolar electric field (E) of the four investigated PZT_R compositions in the poled state at different temperatures.

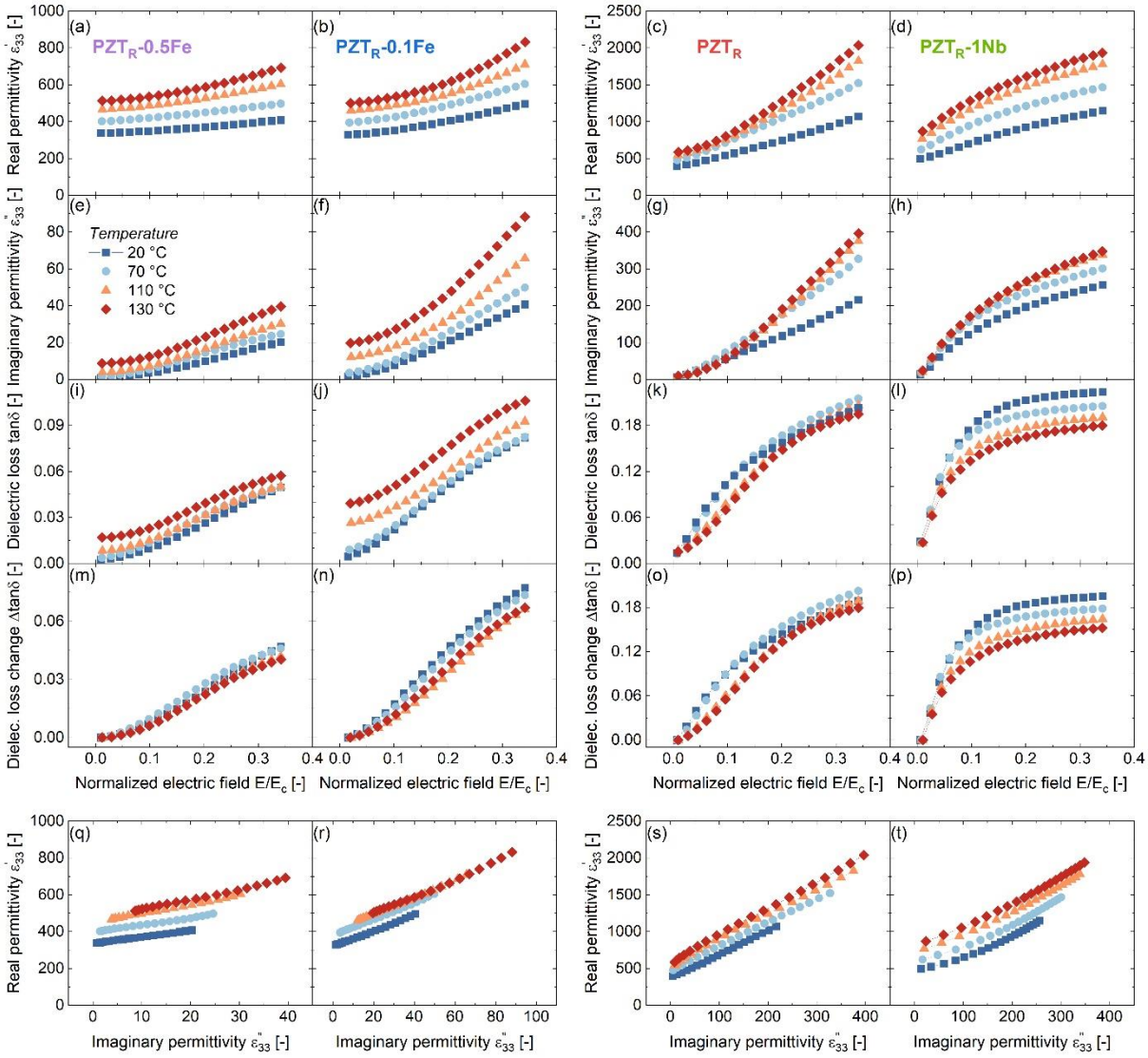

Supplemental Figure 7.7. (a-d) Real (ε'_{33}) and (e-h) imaginary (ε''_{33}) part of the relative dielectric permittivity as a function of descending electric field amplitude at different temperatures. The relative dielectric permittivity was determined in the complex form from the 1st-harmonic of the polarization response ($|P^{1st}| = \varepsilon_0|\varepsilon_{33}|E$). (i-l) Corresponding dielectric loss ($tan\delta$), determined from the ratio of the complex permittivity contributions ($tan\delta = \frac{\varepsilon''_{33}}{\varepsilon'_{33}}$), and (m-p) the relative change of the dielectric loss with respect to the zero field value ($\Delta tan\delta = tan\delta - tan\delta^0$). Shown are the four PZT$_R$ compositions in the poled state. The electric field amplitude was normalized to the corresponding coercive field (E/E_c) for comparability. (q-t) Resulting ε'_{33} – ε''_{33} relationships at the respective temperatures.

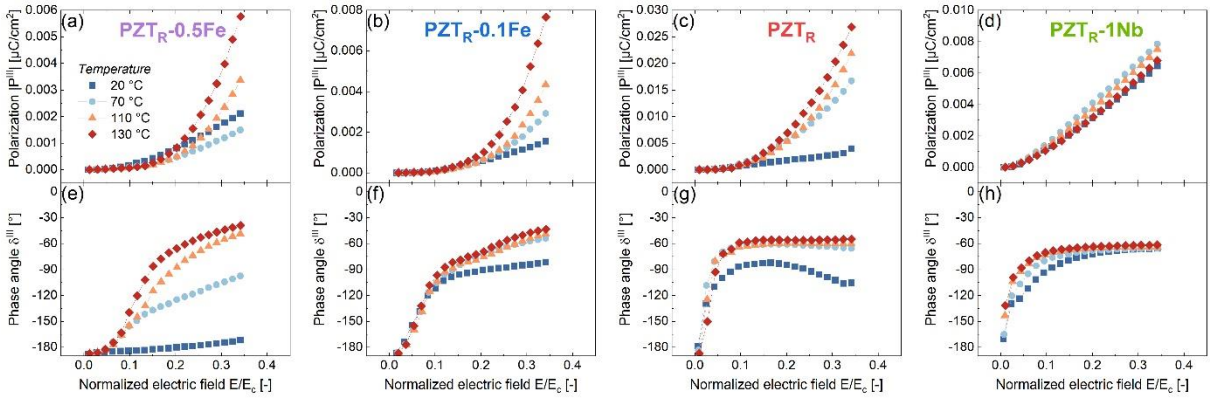

Supplemental Figure 7.8. (a-d) Polarization amplitude ($|P^{III}|$) and (e-h) phase angle (δ^{III}) of the third-harmonic nonlinear polarization response as a function of descending electric field amplitude at different temperatures. Shown are the four PZT$_R$ compositions in the poled state. The electric field amplitude was normalized to the corresponding coercive field (E/E_c) for comparability.

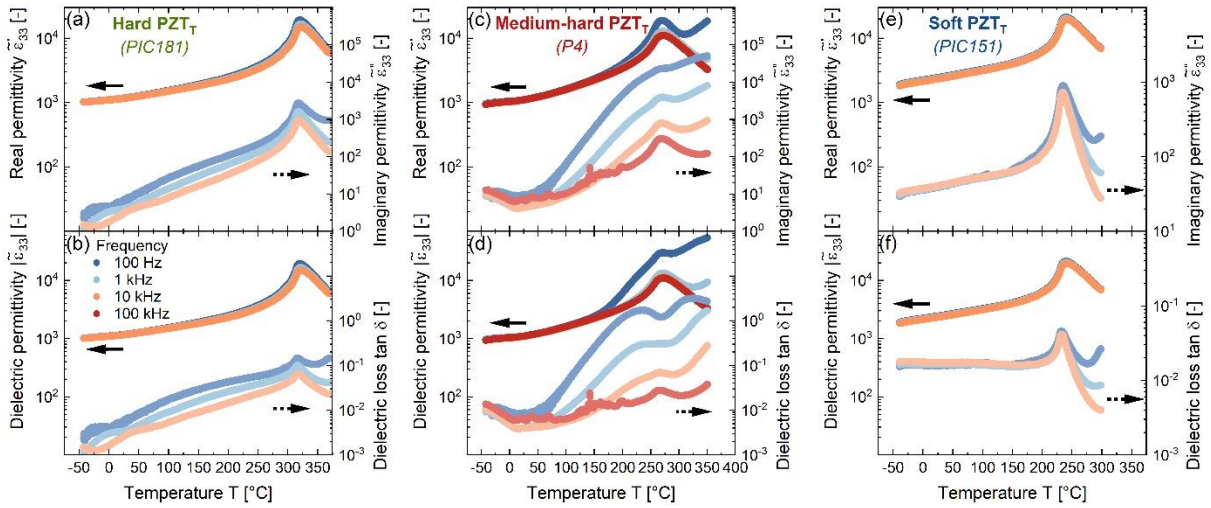

Supplemental Figure 7.9. Magnitude ($|\tilde{\varepsilon}_{33}|$), real ($\tilde{\varepsilon}'_{33}$), and imaginary ($\tilde{\varepsilon}''_{33}$) part of the effective dielectric permittivity and the dielectric loss ($tan\delta$) as a function of temperature (T) measured at different off-resonance frequencies for the three PZT$_T$ compositions.

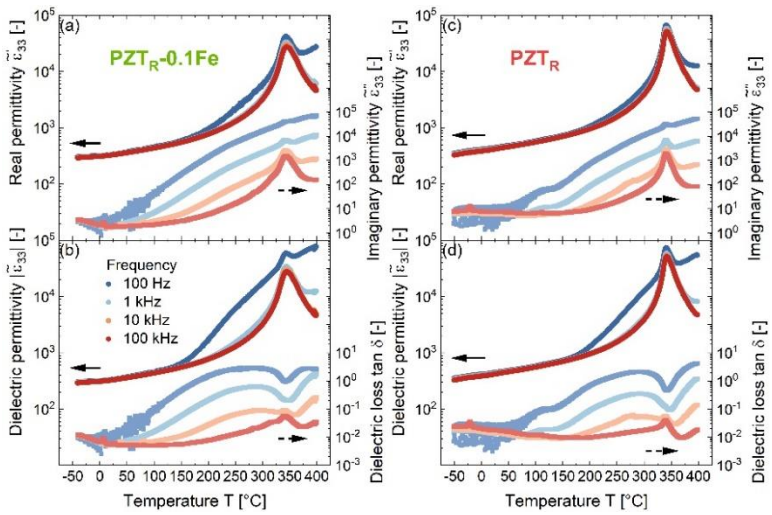

Supplemental Figure 7.10. Magnitude ($|\tilde{\varepsilon}_{33}|$), real ($\tilde{\varepsilon}'_{33}$), and imaginary ($\tilde{\varepsilon}''_{33}$) part of the effective dielectric permittivity and the dielectric loss ($tan\delta$) as a function of temperature (T) measured at different off-resonance frequencies for the acceptor-doped PZT$_R$-0.1Fe and undoped PZT$_R$.

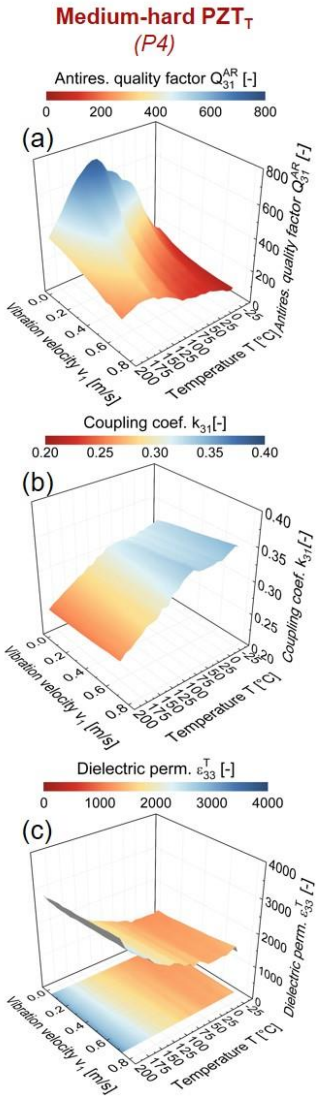

Supplemental Figure 7.11. Temperature (T) and vibration velocity (v_1) maps of the electromechanical coefficients (Q_{31}^{AR}, k_{31}, ε_{33}^T) of medium-hard PZT$_T$ (P4) in the transverse (31) vibration mode.

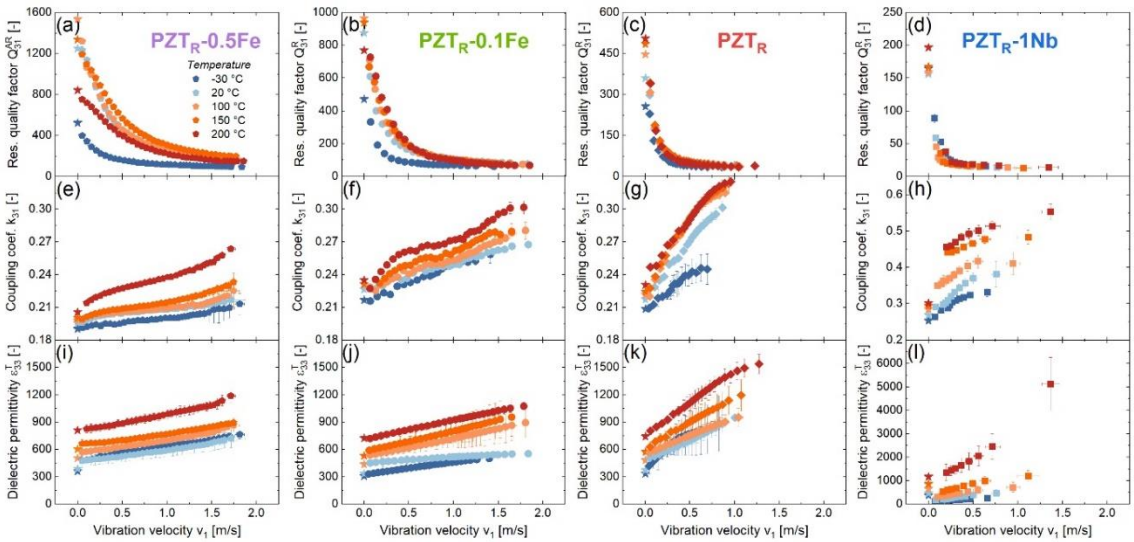

Supplemental Figure 7.12. Electromechanical coefficients (Q_{31}^{AR}, k_{31}, ε_{33}^T) of the four PZT$_R$ compositions in the transverse (31) vibration mode as a function of vibration velocity (v_1) at different temperatures. The data points denoted as stars at 0 m/s depict the small-field values determined from resonance impedance spectroscopy.

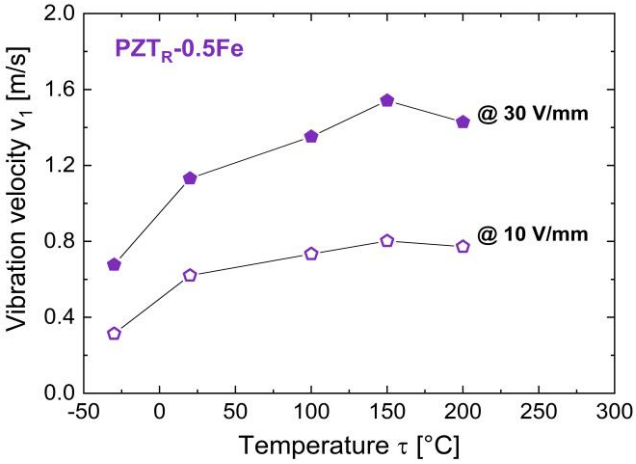

Supplemental Figure 7.13. Generated vibration velocity (v_1) in hard PZT$_R$-0.5Fe at different stabilized temperatures (τ) under continuous excitation with constant driving electric field amplitude of 10 V/mm and 30 V/mm.

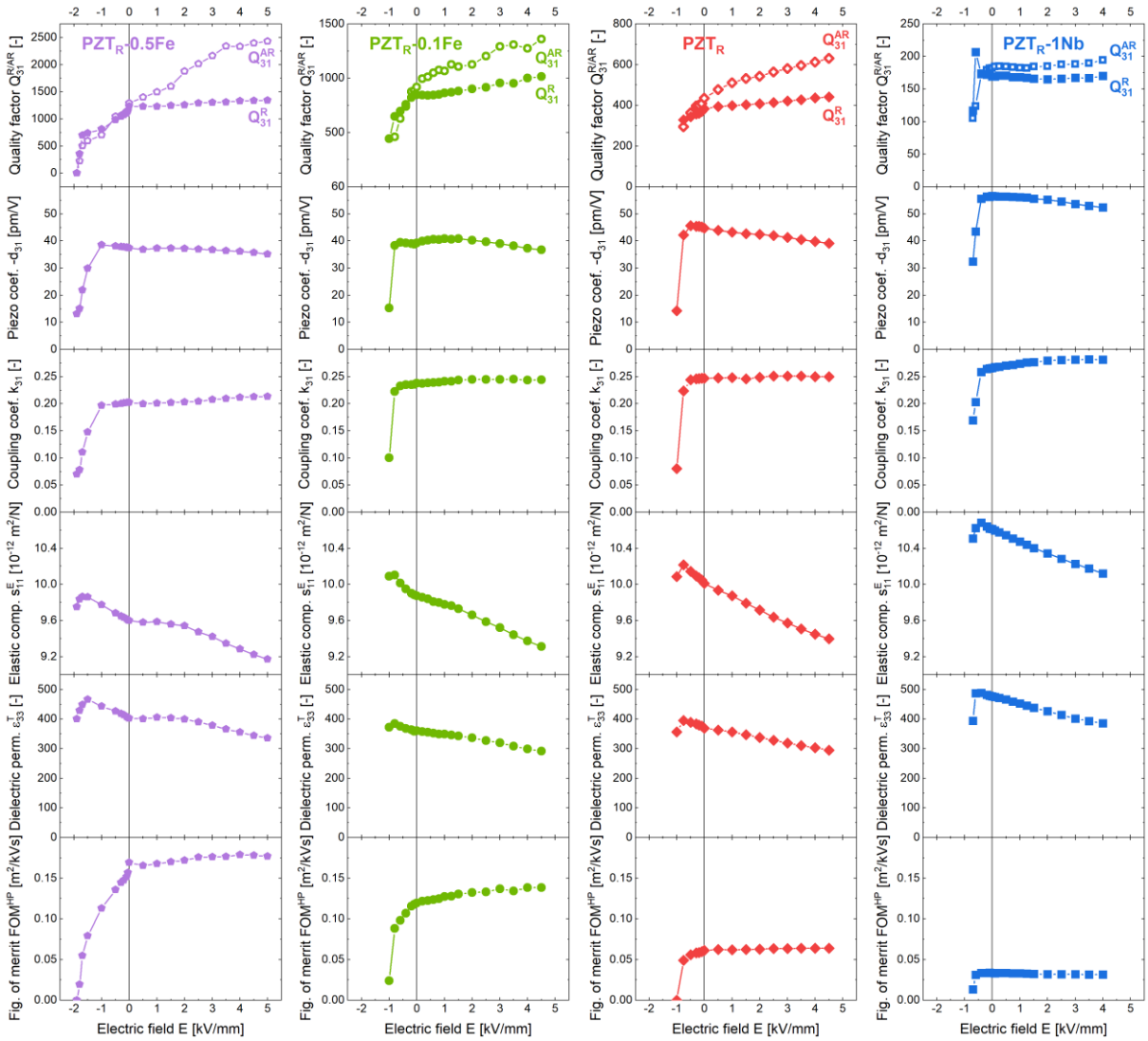

Supplemental Figure 7.14. Electromechanical coefficients (a,b) Q_{31}^R (solid symbols) and Q_{31}^{AR} (open symbols), (c,d) d_{31}, (e,f) k_{31}, (g,h) s_{11}^E, and (i,j) ε_{33}^T of the transverse (31) vibration mode as a function of DC bias field (E_{bias}) at 20 °C determined in the PZT$_R$ compositions (note the different scales in (a)-(b)). Positive and negative field values denote the field applied along and opposite to the polarization direction, respectively.

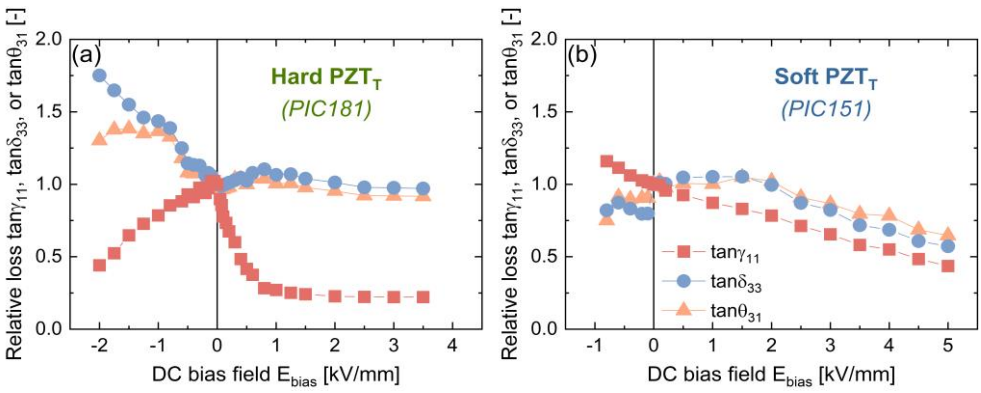

Supplemental Figure 7.15. Determined relative change of the mechanical ($tan\ \gamma_{11}$), dielectric ($tan\ \delta_{33}$), and piezoelectric ($tan\ \phi_{31}$) loss contributions in (a) hard PZT$_T$ (PIC 181) and (b) soft PZT$_T$ (PIC 151) as a function of applied DC bias field (E_{bias}) with respect to the zero DC bias field condition. The three contributions to the loss factor $tan\ \mu_{31}$ were deconvoluted assuming that the elastic loss is equal to the inverse of the measured Q_{31}^{R} (**Equation (2.45)**), that the resonance dielectric loss is equal to the off-resonance value (at 1 kHz, far below resonance the range), and that the piezoelectric loss can be calculated from the measured Q_{31}^{R}, Q_{31}^{AR}, k_{31}, and off-resonance $tan\ \delta_{33}$ values (**Equation (4.19)**) [38, 39].

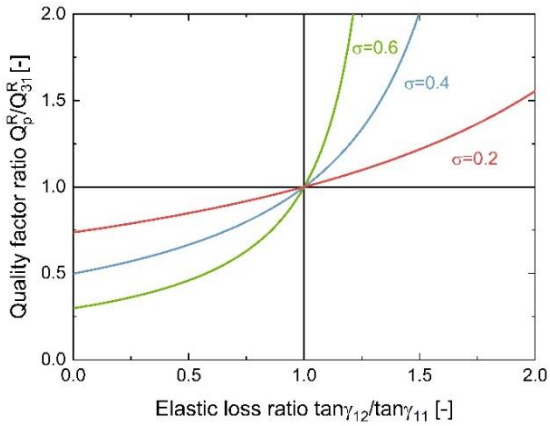

Supplemental Figure 7.16. Phenomenological dependence of the planar and transverse resonance quality factor ratio (Q_p^R/Q_{31}^R) on the elastic loss factor ratio ($tan\ \gamma_{12}/tan\ \gamma_{11}$) and the Poisson's ratio (σ) according to **Equation (4.22)**.

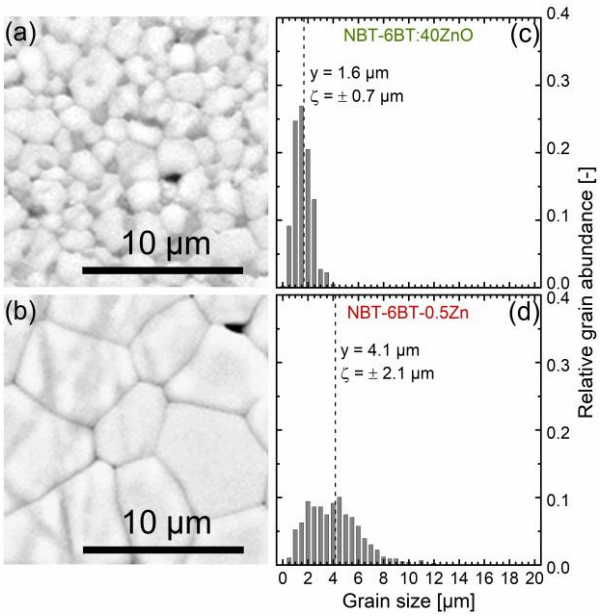

Supplemental Figure 7.17. (a,b) Microstructures of Zn^{2+}-doped NBT-6BT-0.5Zn and NBT-6BT:40ZnO composite determined by SEM. (c,d) Corresponding average grain size (y), size variance (ζ), and distribution (only the NBT-6BT phase in NBT-6BT:40ZnO).

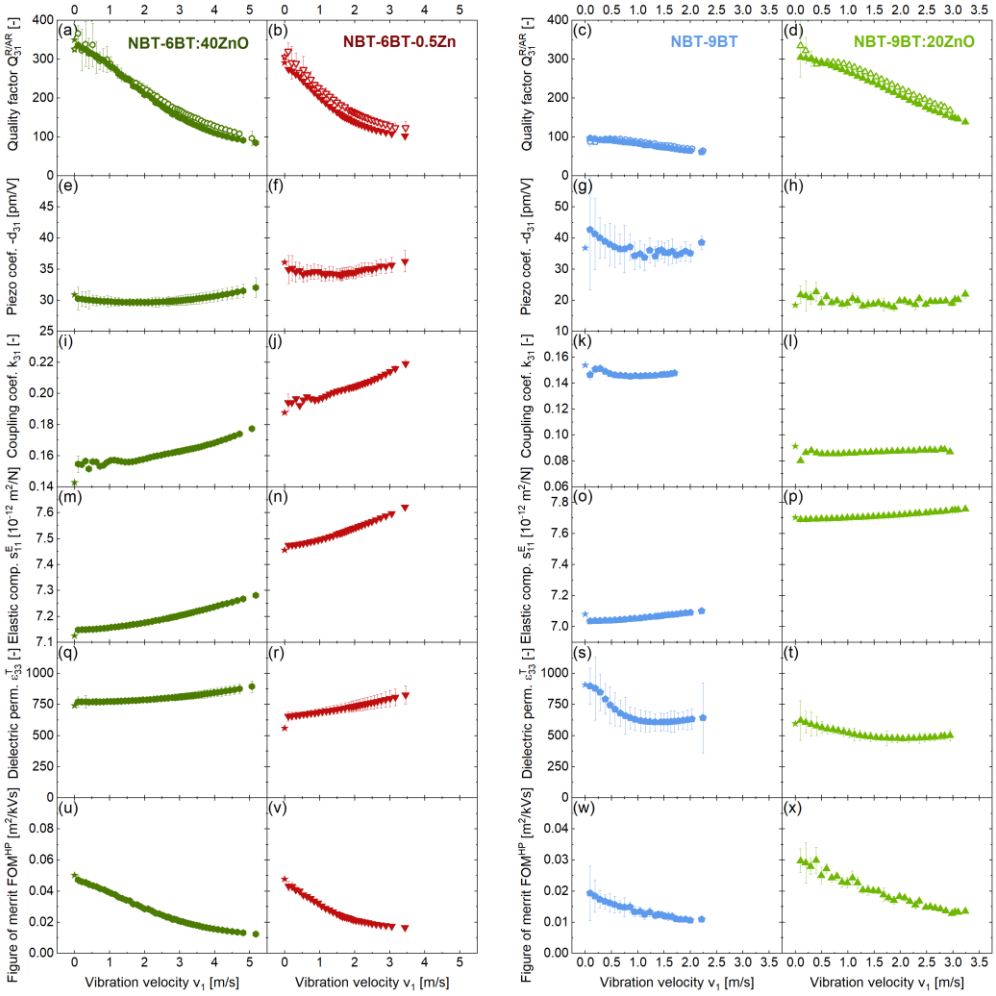

Supplemental Figure 7.18. Electromechanical coefficients (a-d) Q_{31}^{R} (solid symbols) and Q_{31}^{AR} (open symbols), (e-h) d_{31}, (i-l) k_{31}, (m-p) s_{11}^{E}, (q-t) ε_{33}^{T} of the transverse (31) vibration mode as a function of vibration velocity (v_1) at 20 °C for NBT-6BT:40ZnO composite, Zn^{2+}-doped NBT-6BT-0.5Zn, unmodified NBT-9BT, and NBT-9BT:20ZnO composite. The data points denoted as stars at 0 m/s depict the small-field values determined from resonance impedance spectroscopy (**Table 5.1**).

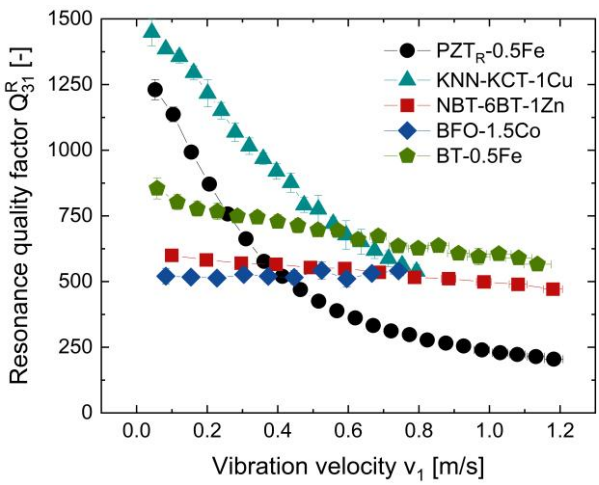

Supplemental Figure 7.19. Comparison of the resonance quality factors (Q_{31}^{R}) as a function of vibration velocity (v_1) in the transverse (31) vibration mode at 20 °C between several lead-based and lead-free acceptor-doped ferroelectrics. The comparisons include $Pb(Zr_{0.60}Ti_{0.40})_{0.995}Fe_{0.005}O_3$ (PZT_R-0.5Fe; [208]), $((K_{0.5}Na_{0.5})NbO_3)_{0.9862}(K_{5.4}Cu_{1.3}Ta_{10}O_{29})_{0.0038}(CuO)_{0.01}$ (KNN-KCT-1Cu; [136]), $(Na_{0.5}Bi_{0.5})_{0.94}Ba_{0.06}(Ti_{0.99}Zn_{0.01})O_3$ (NBT-6BT-1Zn; [72]), $BiFe_{0.985}Co_{0.015}O_3$ (BFO-1.5Co; [257]), and $BaTi_{0.995}Fe_{0.005}O_3$ (BT-0.5Fe; [258]). Referenced are the reports on the synthesis conditions.

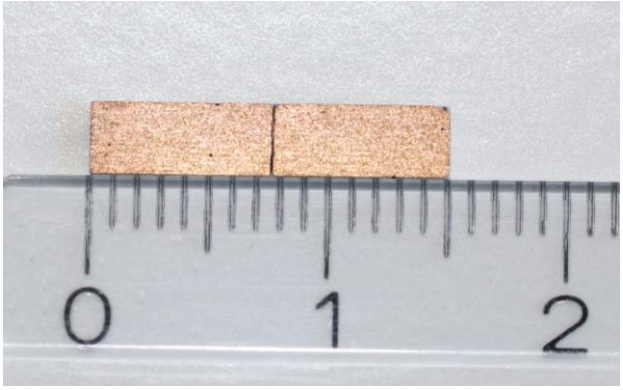

Supplemental Figure 7.20. Medium-hard PZT_T resonator fractured in the center at 2.6 m/s vibration velocity (maximum dynamic tensile stress amplitude 63 MPa).

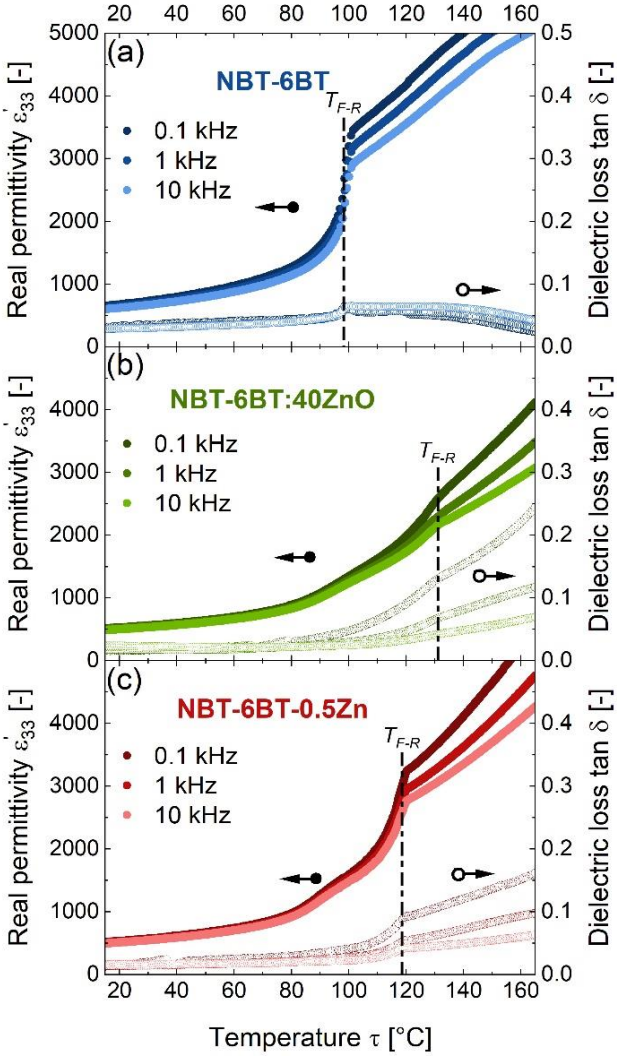

Supplemental Figure 7.21. Temperature-dependent real part of the relative dielectric permittivity (ε'_{33}) and dielectric loss ($tan\ \delta$) of (a) unmodified NBT-6BT, (b) NBT-6BT:40ZnO composite, and (c) Zn^{2+}-doped NBT-6BT-0.5Zn in the polarized states. The inflection point at the thermal anomaly determines the ferroelectric-to-relaxor transition (τ_{F-R}).

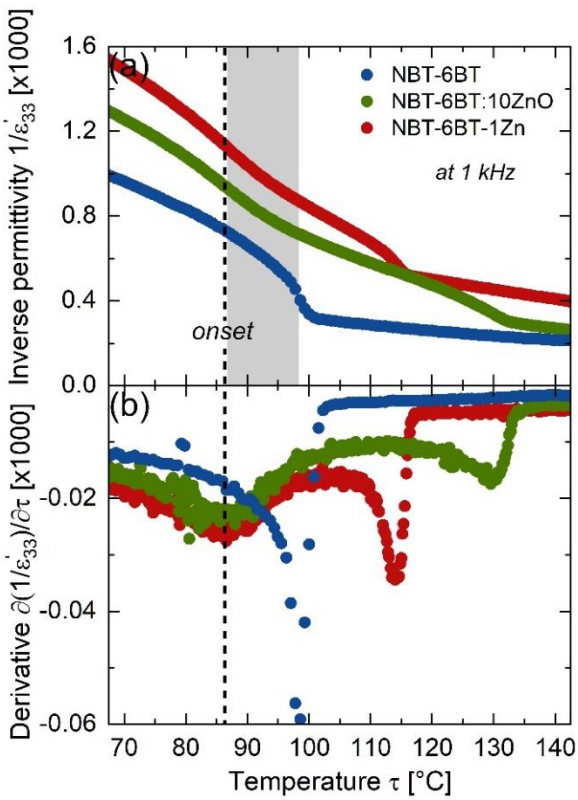

Supplemental Figure 7.22. Temperature-dependent (a) inverse of the permittivity real part ($1/\varepsilon'_{33}$) and (b) its derivative $\partial(1/\varepsilon'_{33})/\partial\tau$ for the unmodified NBT-6BT, NBT-6BT:10ZnO composite, and Zn^{2+}-doped NBT-6BT-1Zn in the polarized states at 1 kHz. The dashed line marks the inflection point for the two modified compositions and determines the depolarization onset; the grey-shaded region indicates the low-temperature anomaly observed in the temperature-dependent ε'_{33}.

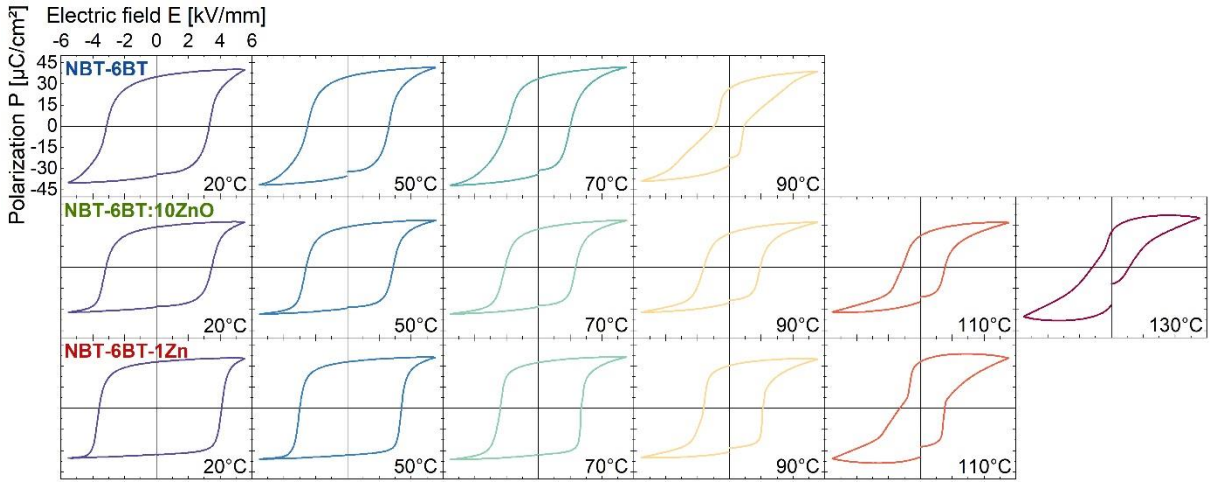

Supplemental Figure 7.23. Polarization (P) hysteresis loops of unmodified NBT-6BT, NBT-6BT:10ZnO composite, and Zn^{2+}-doped NBT-6BT-1Zn in the polarized states as a function of applied bipolar electric field (E) at different temperatures and 1 Hz.

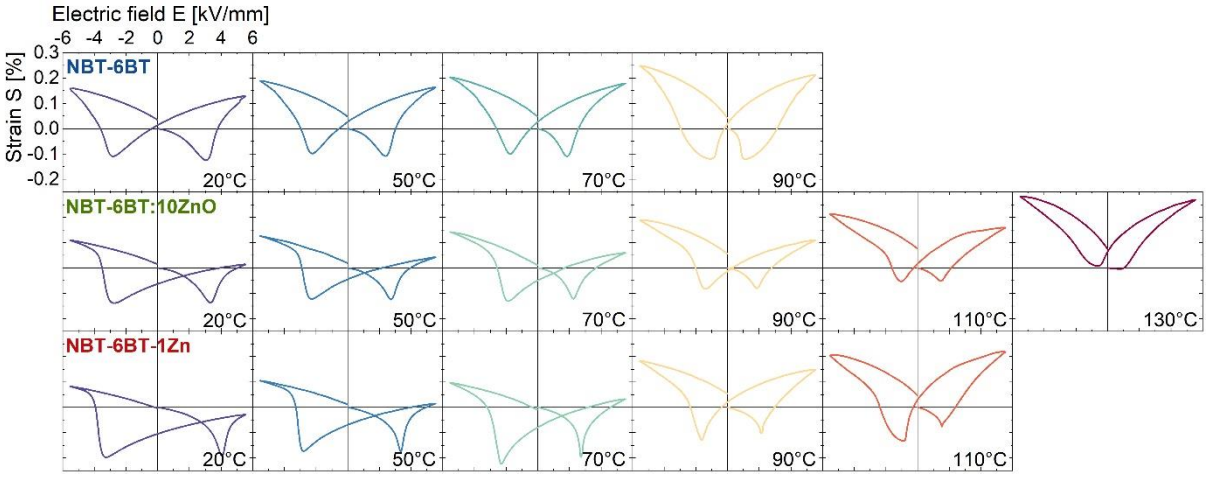

Supplemental Figure 7.24. Strain (S) hysteresis loops of unmodified NBT-6BT, NBT-6BT:10ZnO composite, and Zn^{2+}-doped NBT-6BT-1Zn in the polarized states as a function of applied bipolar electric field (E) at different temperatures and 1 Hz.

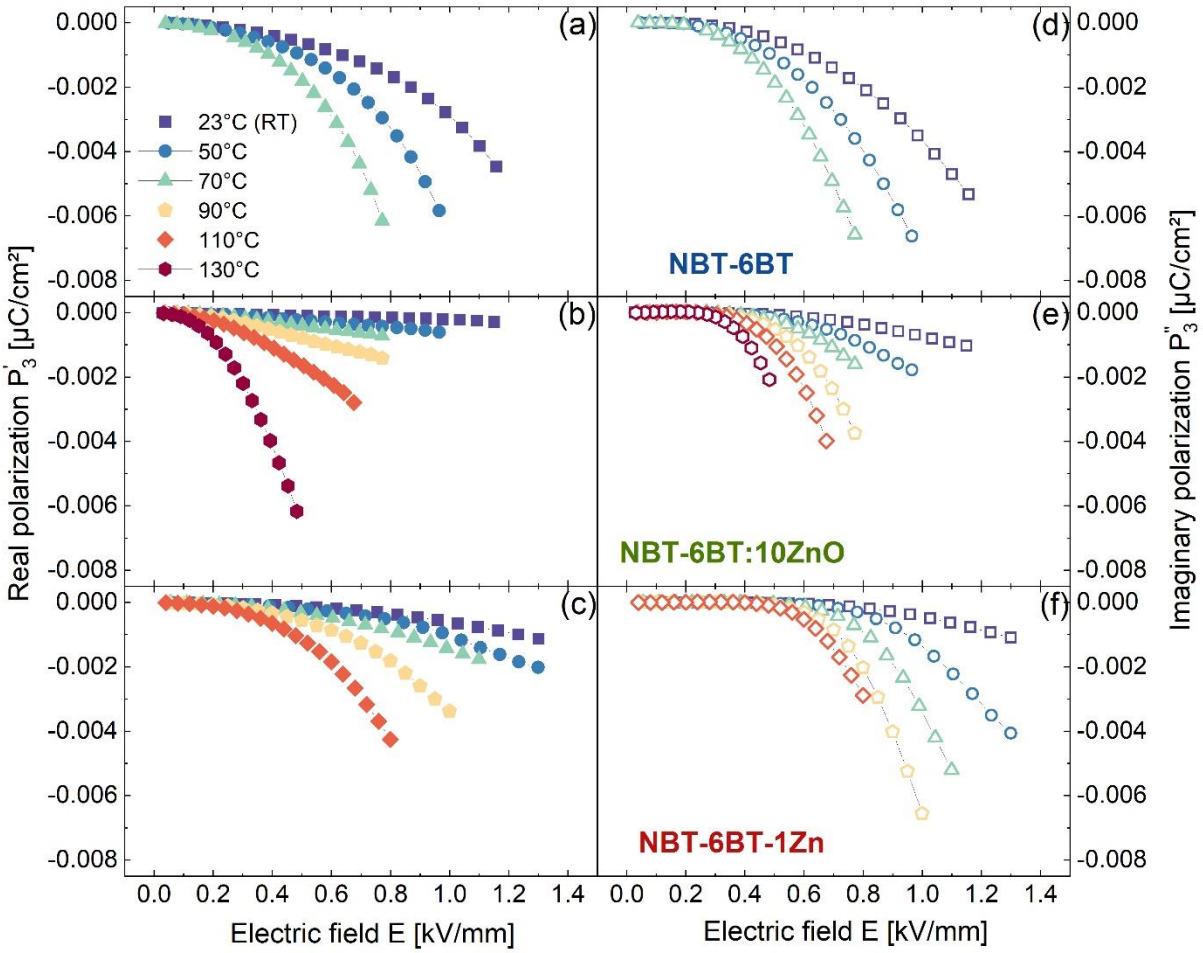

Supplemental Figure 7.25. (a-c) In-phase (P_3') and (d-f) out-of-phase (P_3'') amplitude of the 3rd-harmonic nonlinear polarization response as a function of the descending electric field amplitude (E) of unmodified NBT-6BT, NBT-6BT:10ZnO composite, and Zn^{2+}-doped NBT-6BT-1Zn in the polarized state and different temperatures.

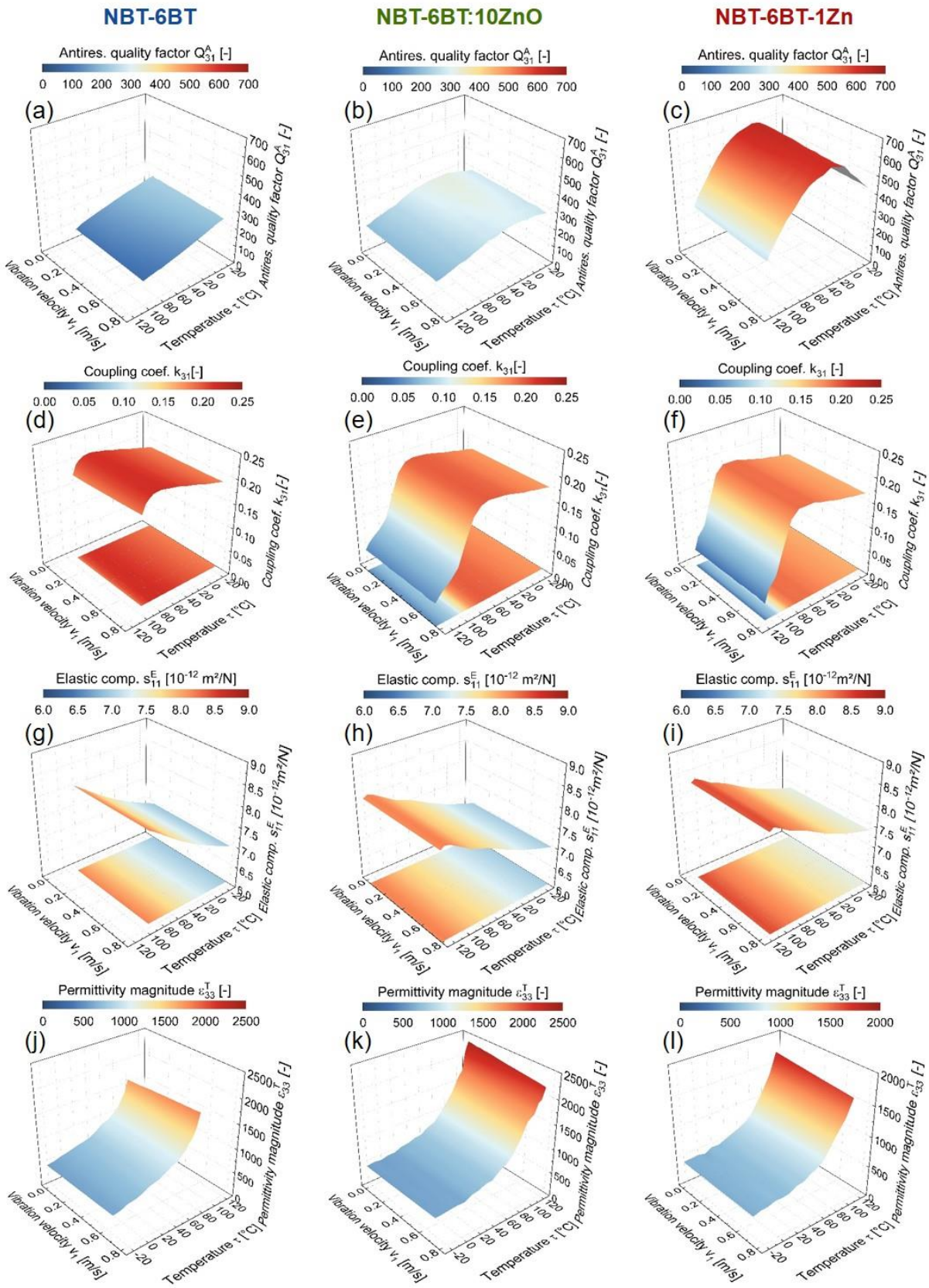

Supplemental Figure 7.26. Temperature (τ) and vibration velocity (v_1) maps of the electromechanical coefficients (a-c) Q_{31}^{AR}, (d-f) k_{31}, (g-i) s_{11}^{E}, and (j-l) ε_{33}^{T} of unmodified NBT-6BT, NBT-6BT:10ZnO composite, and Zn^{2+}-doped NBT-6BT-1Zn in the transverse (31) vibration mode.

References

[1] W. Heywang, K. Lubitz, W. Wersing, Piezoelectricity: Evolution and future of a technology, 1 ed., Springer Science & Business Media, Heidelberg (2008).

[2] M. Gagliardi, Materials with market value: Global ceramic and glass industry poised to reach $1 trilion, Am Ceram Soc Bull 96 (2017) 27-37.

[3] M. Gagliardi, Lead-free piezoelectric ceramics: Technologies and global opportunities (NAN063A) (2019).

[4] M. A. McEvoy, N. Correll, Materials that couple sensing, actuation, computation, and communication, Science 347 (2015) 1261689.

[5] K. Uchino, Advanced piezoelectric materials, 2 ed., Woodhead Publishing Limited, Cambridge (2017).

[6] K. Nakamura, Ultrasonic transducers: Materials and design for sensors, actuators and medical applications, 1 ed., Woodhead Publishing Limited, Cambridge (2012).

[7] S. Priya, High power universal piezoelectric transformer, IEEE T Ultrason Ferr 53 (2006) 23-29.

[8] S. Kumar, C. S. Wu, G. K. Padhy, W. Ding, Application of ultrasonic vibrations in welding and metal processing: A status review, J Manuf Process 26 (2017) 295-322.

[9] J. Jagannathan, N. T. Sanghvi, L. A. Crum, C. P. Yen, R. Medel, A. S. Dumont, J. P. Sheehan, L. Steiner, F. Jolesz, N. F. Kassell, High-intensity focused ultrasound surgery of the brain: Part 1-A historical perspective with modern applications, Neurosurgery 64 (2009) 201-210.

[10] W. P. Mason, Physical acoustics - Principles and methods, 1 ed., Academic press, New York (1964).

[11] T. Ikeda, Fundamentals of piezoelectricity, 1 ed., Oxford University Press, Oxford (1990).

[12] K. Uchino, J. H. Zheng, A. Joshi, Y. H. Chen, S. Yoshikawa, S. Hirose, S. Takahashi, J. W. C. De Vries, High power characterization of piezoelectric materials, J Electroceram 2 (1998) 33-40.

[13] S. Takahashi, S. Hirose, Vibration-level characteristics for iron-doped lead-zirconate-titanate ceramic, Jpn J Appl Phys 1 32 (1993) 2422-2425.

[14] M. Umeda, S. Takahashi, Y. Sasaki, K. Nakamura, S. Ueha, Vibration stress and temperature dependence of piezoelectric resonators with lead-zirconate-titanate ceramics, Electron Comm Jpn 2 83 (2000) 1-7.

[15] A. J. Moulson, J. M. Herbert, Electroceramics: Materials, properties, applications, 2 ed., John Wiley & Sons, Southern Gate (2003).

[16] L. Pardo, J. Ricote, Multifunctional polycrystalline ferroelectric materials: Processing and properties, 1 ed., Springer, Dordrecht (2011).

[17] M. E. Lines, A. M. Glass, Principles and applications of ferroelectrics and related materials, 1 ed., Oxford University Press, Oxford (2001).

[18] D. Damjanovic, Ferroelectric, dielectric and piezoelectric properties of ferroelectric thin films and ceramics, Rep Prog Phys 61 (1998) 1267-1324.

[19] J. F. Nye, Physical properties of crystals: Their representation by tensors and matrices, 2 ed., Oxford University Press, London (1967).

[20] V. E. Ljamov, Nonlinear acoustical parameters of piezoelectric crystals, J Acoust Soc Am 52 (1972) 199-202.

[21] H. Beige, G. Schmidt, Electro-mechanical resonances for investigating linear and non-linear properties of dielectrics, Ferroelectrics 41 (1982) 39-49.

[22] D. Damjanovic, M. Demartin, The Rayleigh law in piezoelectric ceramics, J Phys D Appl Phys 29 (1996) 2057-2060.

[23] S. P. Leary, S. M. Pilgrim, Harmonic analysis of the polarization response in $Pb(Mg_{1/3}Nb_{2/3})O_3$-based ceramics - A study in aging, IEEE T Ultrason Ferr 45 (1998) 163-169.

[24] R. Perez, A. Albareda, Analysis of nonlinear effects in a piezoelectric resonator, J Acoust Soc Am 100 (1996) 3561-3569.
[25] N. Aurelle, D. Guyomar, C. Richard, P. Gonnard, L. Eyraud, Nonlinear behavior of an ultrasonic transducer, Ultrasonics 34 (1996) 187-191.
[26] K. Ishii, N. Akimoto, S. Tashirio, H. Igarashi, Jump phenomena of current in piezoelectric-ceramic vibrators under high power conditions, J Eur Ceram Soc 19 (1999) 1157-1160.
[27] H. Shekhani, T. Scholehwar, E. Hennig, K. Uchino, Characterization of piezoelectric ceramics using the burst/transient method with resonance and antiresonance analysis, J Am Ceram Soc 100 (2017) 998-1010.
[28] Standards EN 50324-2, Piezoelectric properties of ceramic materials and components-Part 2: Methods of measurement–Low power (2002).
[29] M. Umeda, K. Nakamura, S. Ueha, The measurement of high-power characteristics for a piezoelectric transducer based on the electrical transient response, Jpn J Appl Phys 37 (1998) 5322-5325.
[30] K. S. Van Dyke, The electric network equivalent of a piezoelectric resonator, Physical Review 25 (1925) 895.
[31] A. V. Mezheritsky, Elastic, dielectric, and piezoelectric losses in piezoceramics: How it works all together, IEEE T Ultrason Ferr 51 (2004) 695-707.
[32] S. Hirose, M. Aoyagi, Y. Tomikawa, S. Takahashi, K. Uchino, High power characteristics at antiresonance frequency of piezoelectric transducers, Ultrasonics 34 (1996) 213-217.
[33] A. V. Mezheritsky, Quality factor of piezoceramics, Ferroelectrics 266 (2002) 277-304.
[34] D. Damjanovic, An equivalent electric-circuit of a piezoelectric bar resonator with a large piezoelectric phase-angle, Ferroelectrics 110 (1990) 129-135.
[35] G. E. Martin, Dielectric, elastic, and piezoelectric losses in piezoelectric materials, IEEE T Son Ultrason 22 (1975) 241-241.
[36] G. Arlt, Resonance-antiresonance of conducting piezoelectric resonators, J Acoust Soc Am 37 (1965) 151-157.
[37] K. Uchino, Y. Zhuang, S. O. URAL, Loss determination methodology for a piezoelectric ceramic: new phenomenological theory and experimental proposals, Journal of Advanced Dielectrics 1 (2011) 17-31.
[38] K. Uchino, S. Hirose, Loss mechanisms in piezoelectrics: How to measure different losses separately, IEEE T Ultrason Ferr 48 (2001) 307-321.
[39] Y. Zhuang, S. O. Ural, K. Uchino, Methodology for characterizing loss factors of piezoelectric ceramics, Ferroelectrics 470 (2014) 260-271.
[40] P. Gerthsen, K. H. Hardtl, N. A. Schmidt, Correlation of mechanical and electrical losses in ferroelectric ceramics, J Appl Phys 51 (1980) 1131-1134.
[41] S. Takahashi, Y. Sasaki, S. Hirose, Driving electric field effects on piezoelectric transducers, Jpn J Appl Phys 36 (1997) 3010-3015.
[42] K. Nakamura, Electrical evaluation of piezoelectric transducers, in: K. Nakamura (Ed.), Ultrasonic transducers: Materials and design for sensors, actuators and medical applications, Woodhead Publishing Limited, Cambridge (2012), pp. 264-276.
[43] B. Jaffe, W. Cook, H. Jaffe, Piezoelectric ceramics, 1 ed., Academic Press Limited, Cambridge (1971).
[44] A. Vonhippel, Ferroelectricity, domain structure, and phase transitions of barium titanate, Rev Mod Phys 22 (1950) 221-237.
[45] A. F. Devonshire, Theory of barium titanate - Part I, Philos Mag 40 (1949) 1040-1063.
[46] A. F. Devonshire, Theory of barium titanate - Part II, Philos Mag 42 (1951) 1065-1079.
[47] J. L. Jones, E. Aksel, G. Tutuncu, T. M. Usher, J. Chen, X. R. Xing, A. J. Studer, Domain wall and interphase boundary motion in a two-phase morphotropic phase boundary ferroelectric: Frequency dispersion and contribution to piezoelectric and dielectric properties, Phys Rev B 86 (2012) 024104.

[48] L. E. Cross, W. Heywang, Introduction, in: W. Heywang, K. Lubitz, W. Wersing (Eds.), Piezoelectricity: Evolution and future of a technology, Springer Science & Business Media, Heidelberg (2008), pp. 1-5.
[49] D. Damjanovic, Hysteresis in piezoelectric and ferroelectric materials, in: G. Bertotti, I. D. Mayergoyz (Eds.), The science of hysteresis, Oxford Academic Press, Oxford (2005), pp. 337-465.
[50] D. Berlincourt, Piezoelectric ceramics - Characteristics and applications, J Acoust Soc Am 70 (1981) 1586-1595.
[51] H. C. Cao, A. G. Evans, Nonlinear Deformation of Ferroelectric Ceramics, J Am Ceram Soc 76 (1993) 890-896.
[52] G. Arlt, H. Neumann, Internal bias in ferroelectric ceramics - Origin and time-dependence, Ferroelectrics 87 (1988) 109-120.
[53] T. J. Yang, V. Gopalan, P. J. Swart, U. Mohideen, Direct observation of pinning and bowing of a single ferroelectric domain wall, Phys Rev Lett 82 (1999) 4106-4109.
[54] Q. M. Zhang, W. Y. Pan, S. J. Jang, L. E. Cross, Domain-wall excitations and their contributions to the weak-signal response of doped lead zirconate titanate ceramics, J Appl Phys 64 (1988) 6445-6451.
[55] C. A. Randall, N. Kim, J. P. Kucera, W. W. Cao, T. R. Shrout, Intrinsic and extrinsic size effects in fine-grained morphotropic-phase-boundary lead zirconate titanate ceramics, J Am Ceram Soc 81 (1998) 677-688.
[56] G. Arlt, The influence of microstructure on the properties of ferroelectric ceramics, Ferroelectrics 104 (1990) 217-227.
[57] H. G. Baerwald, D. A. Berlincourt, Electromechanical response and dielectric loss of prepolarized barium titanate under maintained electric bias - Part I, J Acoust Soc Am 25 (1953) 703-710.
[58] H. Kungl, M. J. Hoffmann, Temperature dependence of poling strain and strain under high electric fields in LaSr-doped morphotropic PZT and its relation to changes in structural characteristics, Acta Mater 55 (2007) 5780-5791.
[59] D. J. Franzbach, Y. H. Seo, A. J. Studer, Y. C. Zhang, J. Glaum, J. E. Daniels, J. Koruza, A. Bencan, B. Malic, K. G. Webber, Electric-field-induced phase transitions in co-doped $Pb(Zr_{1-x}Ti_x)O_3$ at the morphotropic phase boundary, Sci Technol Adv Mat 15 (2014) 015010.
[60] A. Pramanick, A. D. Prewitt, J. S. Forrester, J. L. Jones, Domains, domain walls and defects in perovskite ferroelectric oxides: A review of present understanding and recent contributions, Crit Rev Solid State 37 (2012) 243-275.
[61] M. I. Morozov, D. Damjanovic, Charge migration in $Pb(Zr,Ti)O_3$ ceramics and its relation to ageing, hardening, and softening, J Appl Phys 107 (2010) 034106.
[62] D. Damjanovic, Contributions to the piezoelectric effect in ferroelectric single crystals and ceramics, J Am Ceram Soc 88 (2005) 2663-2676.
[63] P. Erhart, R. A. Eichel, P. Traskelin, K. Albe, Association of oxygen vacancies with impurity metal ions in lead titanate, Phys Rev B 76 (2007) 174116.
[64] H. Mestric, R. A. Eichel, T. Kloss, K. P. Dinse, S. Laubach, S. Laubach, P. C. Schmidt, K. A. Schonau, M. Knapp, H. Ehrenberg, Iron-oxygen vacancy defect centers in $PbTiO_3$: Newman superposition model analysis and density functional calculations, Phys Rev B 71 (2005) 134109.
[65] P. Erhart, P. Traskelin, K. Albe, Formation and switching of defect dipoles in acceptor-doped lead titanate: A kinetic model based on first-principles calculations, Phys Rev B 88 (2013) 024107.
[66] U. Robels, G. Arlt, Domain-wall clamping in ferroelectrics by orientation of defects, J Appl Phys 73 (1993) 3454-3460.
[67] A. S. Nowick, W. R. Heller, Dielectric and anelastic relaxation of crystals containing point defects, Adv Phys 14 (1965) 101-166.

[68] K. Carl, K. H. Hardtl, Electrical aftereffects in $Pb(Ti,Zr)O_3$ ceramics, Ferroelectrics 17 (1978) 473-486.
[69] V. S. Postnikov, V. S. Pavlov, S. K. Turkov, Internal friction in ferroelectrics due to interaction of domain boundaries and point defects, J Phys Chem Solids 31 (1970) 1785-1791.
[70] Y. A. Genenko, J. Glaum, O. Hirsch, H. Kungl, M. J. Hoffmann, T. Granzow, Aging of poled ferroelectric ceramics due to relaxation of random depolarization fields by space-charge accumulation near grain boundaries, Phys Rev B 80 (2009) 224109.
[71] A. Bencan, B. Malic, S. Drnovsek, J. Tellier, T. Rojac, J. Pavlic, M. Kosec, K. G. Webber, J. Rodel, D. Damjanovic, Structure and the electrical properties of $Pb(Zr,Ti)O_3$ - zirconia composites, J Am Ceram Soc 95 (2012) 651-657.
[72] L. M. Riemer, K. V. Lalitha, X. J. Jiang, N. Liu, C. Dietz, R. W. Stark, P. B. Groszewicz, G. Buntkowsky, J. Chen, S. T. Zhang, J. Rödel, J. Koruza, Stress-induced phase transition in lead-free relaxor ferroelectric composites, Acta Mater 136 (2017) 271-280.
[73] X. Wang, P. R. Ren, J. L. Wang, J. Q. Xu, Y. X. Xi, Multi-phase coexistence and temperature-stable dielectric properties in $BaTiO_3$/ZnO composite ceramics, J Eur Ceram Soc 40 (2020) 1896-1901.
[74] C. Zhao, S. Gao, T. Yang, M. Scherer, J. Schultheiß, D. Meier, X. Tan, H. J. Kleebe, L. Q. Chen, J. Koruza, J. Rödel, Precipitation hardening in ferroelectric ceramics, Adv Mater 33 (2021) 2102421.
[75] K. V. Lalitha, L. M. Riemer, J. Koruza, J. Rödel, Hardening of electromechanical properties in piezoceramics using a composite approach, Appl Phys Lett 111 (2017) 022905.
[76] D. A. Hall, A. Steuwer, B. Cherdhirunkorn, P. J. Withers, T. Mori, Micromechanics of residual stress and texture development due to poling in polycrystalline ferroelectric ceramics, J Mech Phys Solids 53 (2005) 249-260.
[77] D. A. Hall, A. Steuwer, B. Cherdhirunkorn, T. Mori, P. J. Withers, A high energy synchrotron x-ray study of crystallographic texture and lattice strain in soft lead zirconate titanate ceramics, J Appl Phys 96 (2004) 4245-4252.
[78] A. Pramanick, D. Damjanovic, J. E. Daniels, J. C. Nino, J. L. Jones, Origins of electro-mechanical coupling in polycrystalline ferroelectrics during subcoercive electrical loading, J Am Ceram Soc 94 (2011) 293-309.
[79] J. Y. Li, R. C. Rogan, E. Ustundag, K. Bhattacharya, Domain switching in polycrystalline ferroelectric ceramics, Nat Mater 4 (2005) 776-781.
[80] P. Keil, M. Trapp, N. Novak, T. Fromling, H. J. Kleebe, J. Rodel, Piezotronic tuning of potential barriers in ZnO bicrystals, Adv Mater 30 (2018) 1705573.
[81] T. Clyne, P. Withers, An introduction to metal matrix composites, 1 ed., Cambridge University Press, Cambridge (1995).
[82] K. V. Lalitha, C. M. Fancher, J. L. Jones, R. Ranjan, Field induced domain switching as the origin of anomalous lattice strain along non-polar direction in rhombohedral $BiScO_3$-$PbTiO_3$ close to the morphotropic phase boundary, Appl Phys Lett 107 (2015) 052901.
[83] J. Zhang, Z. Pan, F. F. Guo, W. C. Liu, H. P. Ning, Y. B. Chen, M. H. Lu, B. Yang, J. Chen, S. T. Zhang, X. R. Xing, J. Rödel, W. W. Cao, Y. F. Chen, Semiconductor/relaxor 0-3 type composites without thermal depolarization in $Bi_{0.5}Na_{0.5}TiO_3$-based lead-free piezoceramics, Nat Commun 6 (2015) 6615.
[84] Z. M. Fan, L. Zhou, T. H. Kim, J. Zhang, S. T. Zhang, X. L. Tan, Mechanisms of enhanced thermal stability of polarization in lead-free $(Bi_{1/2}Na_{1/2})_{0.94}Ba_{0.06}TiO_3$/ZnO ceramic composites, Phys Rev Mater 3 (2019) 024402.
[85] K. V. Lalitha, M. Hinterstein, K. Y. Lee, T. N. Yang, L. Q. Chen, P. B. Groszewicz, J. Koruza, J. Rödel, Spontaneous ferroelectric order in lead-free relaxor $Na_{1/2}Bi_{1/2}TiO_3$-based composites, Phys Rev B 101 (2020) 174108.
[86] L. K. Venkataraman, T. Frömling, J. Rödel, Role of matrix phase and electric field gradient in $Na_{1/2}Bi_{1/2}TiO_3$-$BaTiO_3$:ZnO composites, J Materiom (2021) 498-510.

[87] H. H. Krueger, D. Berlincourt, Effects of high static stress on piezoelectric properties of transducer materials, J Acoust Soc Am 33 (1961) 1339-1344.
[88] F. Rubio-Marcos, A. Del Campo, P. Marchet, J. F. Fernandez, Ferroelectric domain wall motion induced by polarized light, Nat Commun 6 (2015) 7594.
[89] D. A. Hall, Nonlinearity in piezoelectric ceramics, J Mater Sci 36 (2001) 4575-4601.
[90] B. Lewis, Energy loss processes in ferroelectric ceramics, P Phys Soc Lond 73 (1959) 17-24.
[91] Q. M. Zhang, H. Wang, N. Kim, L. E. Cross, Direct evaluation of domain-wall and intrinsic contributions to the dielectric and piezoelectric response and their temperature-dependence on lead-zirconate-titanate ceramics, J Appl Phys 75 (1994) 454-459.
[92] D. Damjanovic, M. Demartin, H. S. Shulman, M. Testorf, N. Setter, Instabilities in the piezoelectric properties of ferroelectric ceramics, Sensor Actuat a-Phys 53 (1996) 353-360.
[93] D. Damjanovic, M. Demartin, Contribution of the irreversible displacement of domain walls to the piezoelectric effect in barium titanate and lead zirconate titanate ceramics, J Phys-Condens Mat 9 (1997) 4943-4953.
[94] D. A. Hall, P. J. Stevenson, High field dielectric behaviour of ferroelectric ceramics, Ferroelectrics 228 (1999) 139-158.
[95] L. Rayleigh, XXV. Notes on electricity and magnetism.—III. On the behaviour of iron and steel under the operation of feeble magnetic forces, The London, Edinburgh, and Dublin Philosophical Magazine and Journal of Science 23 (1887) 225-245.
[96] D. Damjanovic, Logarithmic frequency dependence of the piezoelectric effect due to pinning of ferroelectric-ferroelastic domain walls, Phys Rev B 55 (1997) 649-652.
[97] M. I. Morozov, D. Damjanovic, Hardening-softening transition in Fe-doped $Pb(Zr,Ti)O_3$ ceramics and evolution of the third harmonic of the polarization response, J Appl Phys 104 (2008) 034107.
[98] D. Damjanovic, Stress and frequency dependence of the direct piezoelectric effect in ferroelectric ceramics, J Appl Phys 82 (1997) 1788-1797.
[99] D. A. Hall, Rayleigh behaviour and the threshold field in ferroelectric ceramics, Ferroelectrics 223 (1999) 319-328.
[100] U. Robels, C. Zadon, G. Arlt, Linearization of dielectric nonlinearity by internal bias fields, Ferroelectrics 133 (1992) 163-168.
[101] K. Härdtl, Electrical and mechanical losses in ferroelectric ceramics, Ceram Int 8 (1982) 121-127.
[102] G. Liu, S. J. Zhang, W. H. Jiang, W. W. Cao, Losses in ferroelectric materials, Mat Sci Eng R 89 (2015) 1-48.
[103] L. M. Zheng, R. Sahul, S. J. Zhang, W. H. Jiang, S. Y. Li, W. W. Cao, Orientation dependence of piezoelectric properties and mechanical quality factors of $0.27Pb(In_{1/2}Nb_{1/2})O_3$-$0.46Pb(Mg_{1/3}Nb_{2/3})O_3$-$0.27PbTiO_3$:Mn single crystals, J Appl Phys 114 (2013) 104105.
[104] E. I. Bondarenko, V. Y. Topolov, A. V. Turik, The role of 90-degrees domain-wall displacements in forming physical-properties of perovskite ferroelectric ceramics, Ferroelectrics Lett 13 (1991) 13-19.
[105] S. P. Li, W. W. Cao, L. E. Cross, The extrinsic nature of nonlinear behavior observed in lead zirconate titanate ferroelectric ceramic, J Appl Phys 69 (1991) 7219-7224.
[106] K. Uchino, J. H. Zheng, Y. H. Chen, X. H. Du, J. Ryu, Y. Gao, S. Ural, S. Priya, S. Hirose, Loss mechanisms and high power piezoelectrics, J Mater Sci 41 (2006) 217-228.
[107] L. E. Cross, Relaxor ferroelectrics: An overview, Ferroelectrics 151 (1994) 305-320.
[108] G. A. Samara, The relaxational properties of compositionally disordered ABO_3 perovskites, J Phys-Condens Mat 15 (2003) 367-411.

[109] W. Jo, J. Daniels, D. Damjanovic, W. Kleemann, J. Rödel, Two-stage processes of electrically induced-ferroelectric to relaxor transition in $0.94(Bi_{1/2}Na_{1/2})TiO_3$-0.06BaTiO, Appl Phys Lett 102 (2013) 192903.
[110] D. I. Woodward, R. Dittmer, W. Jo, D. Walker, D. S. Keeble, M. W. Dale, J. Rödel, P. A. Thomas, Investigation of the depolarisation transition in Bi-based relaxor ferroelectrics, J Appl Phys 115 (2014) 114109.
[111] E. M. Anton, W. Jo, D. Damjanovic, J. Rödel, Determination of depolarization temperature of $(Bi_{1/2}Na_{1/2})TiO_3$-based lead-free piezoceramics, J Appl Phys 110 (2011) 094108.
[112] E. Sapper, S. Schaab, W. Jo, T. Granzow, J. Rödel, Influence of electric fields on the depolarization temperature of Mn-doped $(1\text{-}x)Bi_{1/2}Na_{1/2}TiO_3$-$xBaTiO_3$, J Appl Phys 111 (2012) 014105.
[113] L. Kodumudi Venkataraman, T. Zhu, M. Pinto Salazar, K. Hofmann, A. Iqbal Waidha, J. C. Jaud, P. B. Groszewicz, J. Rödel, Thermal depolarization and electromechanical hardening in Zn-doped $Na_{1/2}Bi_{1/2}TiO_3$-$BaTiO_3$, J Am Ceram Soc 104 (2021) 2201-2212.
[114] L. Li, M. K. Zhu, K. L. Zhou, Q. M. Wei, M. P. Zheng, Y. D. Hou, Delayed thermal depolarization of $Bi_{0.5}Na_{0.5}TiO_3$-$BaTiO_3$ by doping acceptor Zn^{2+} with large ionic polarizability, J Appl Phys 122 (2017) 204104.
[115] J. Glaum, H. Simons, J. Hudspeth, M. Acosta, J. E. Daniels, Temperature dependent polarization reversal mechanism in $0.94(Bi_{1/2}Na_{1/2})TiO_3$-$0.06Ba(Zr_{0.02}Ti_{0.98})O_3$ relaxor ceramics, Appl Phys Lett 107 (2015) 232906.
[116] G. Das Adhikary, B. Mahale, B. N. Rao, A. Senyshyn, R. Ranjan, Depoling phenomena in $Na_{0.5}Bi_{0.5}TiO_3$-$BaTiO_3$: A structural perspective, Phys Rev B 103 (2021) 184106.
[117] W. Jo, R. Dittmer, M. Acosta, J. D. Zang, C. Groh, E. Sapper, K. Wang, J. Rödel, Giant electric-field-induced strains in lead-free ceramics for actuator applications - status and perspective, J Electroceram 29 (2012) 71-93.
[118] D. Schneider, J. Rödel, D. Rytz, T. Granzow, Orientation-dependence of thermal depolarization and phase development in $Bi_{1/2}Na_{1/2}TiO_3$-$BaTiO_3$ single crystals, J Am Ceram Soc 98 (2015) 3966-3974.
[119] J. Kling, W. Jo, R. Dittmer, S. Schaab, H. J. Kleebe, Temperature-dependent phase transitions in the lead-free piezoceramics $(1\text{-}x\text{-}y)(Bi_{1/2}Na_{1/2})TiO_3$-$xBaTiO_3$-$y(K_{0.5}Na_{0.5})NbO_3$ observed by in situ transmission electron microscopy and dielectric measurements, J Am Ceram Soc 96 (2013) 3312-3324.
[120] G. H. Haertling, Ferroelectric ceramics: History and technology, J Am Ceram Soc 82 (1999) 797-818.
[121] D. A. Berlincourt, C. Cmolik, H. Jaffe, Piezoelectric properties of polycrystalline lead titanate zirconate compositions, P Ire 48 (1960) 220-229.
[122] W. Wersing, Analysis of phase mixtures in ferroelectric ceramics by dielectric measurements, Ferroelectrics 7 (1974) 163-165.
[123] D. Berlincourt, Piezoelectric ceramic compositional development, J Acoust Soc Am 91 (1992) 3034-3040.
[124] A. J. Bell, O. Deubzer, Lead-free piezoelectrics - The environmental and regulatory issues, MRS Bull 43 (2018) 581-587.
[125] B. Noheda, J. A. Gonzalo, L. E. Cross, R. Guo, S. E. Park, D. E. Cox, G. Shirane, Tetragonal-to-monoclinic phase transition in a ferroelectric perovskite: The structure of $PbZr_{0.52}Ti_{0.48}O_3$, Phys Rev B 61 (2000) 8687-8695.
[126] Y. K. Gao, E. H. Chen, J. Ryu, K. Uchino, D. Viehland, Eu and Yb substituent effects on the properties of $Pb(Zr_{0.52}Ti_{0.48})O_3$-$Pb(Mn_{1/3}Sb_{2/3})O_3$ ceramics: Development of a new high-power piezoelectric with enhanced vibrational velocity, Jpn J Appl Phys 1 40 (2001) 687-693.
[127] H. J. Lee, S. Zhang, R. J. Meyer, N. P. Sherlock, T. R. Shrout, Characterization of piezoelectric ceramics and 1-3 composites for high power transducers, Appl Phys Lett 101 (2012) 032902.

[128] S. J. Zhang, R. Xia, L. Lebrun, D. Anderson, T. R. Shrout, Piezoelectric materials for high power, high temperature applications, Mater Lett 59 (2005) 3471-3475.
[129] D. Berlincourt, B. Jaffe, H. Jaffe, H. Krueger, Transducer properties of lead titanate zirconate ceramics, P Ire 47 (1959) 482-482.
[130] E. Boucher, D. Guyomar, L. Lebrun, B. Guiffard, G. Grange, Effect of (Mn,F) and (Mg,F) co-doping on dielectric and piezoelectric properties of lead zirconate titanate ceramics, J Appl Phys 92 (2002) 5437-5442.
[131] S. J. Zhang, J. Luo, W. Hackenberger, N. P. Sherlock, R. J. Meyer, T. R. Shrout, Electromechanical characterization of $Pb(In_{0.5}Nb_{0.5})O_3$-$Pb(Mg_{1/3}Nb_{2/3})O_3$-$PbTiO_3$ crystals as a function of crystallographic orientation and temperature, J Appl Phys 105 (2009) 104506.
[132] S. J. Zhang, F. Li, High performance ferroelectric relaxor-$PbTiO_3$ single crystals: Status and perspective, J Appl Phys 111 (2012) 031301.
[133] X. Q. Huo, S. J. Zhang, G. Liu, R. Zhang, J. Luo, R. Sahul, W. W. Cao, T. R. Shrout, Elastic, dielectric and piezoelectric characterization of single domain PIN-PMN-PT:Mn crystals, J Appl Phys 112 (2012) 124113.
[134] H. J. Lee, S. O. Ural, L. Chen, K. Uchino, S. J. Zhang, High power characteristics of lead-free piezoelectric ceramics, J Am Ceram Soc 95 (2012) 3383-3386.
[135] E. A. Gurdal, S. O. Ural, H. Y. Park, S. Nahm, K. Uchino, High power characterization of $(Na_{0.5}K_{0.5})NbO_3$ based lead-free piezoelectric ceramics, Sensor Actuat a-Phys 200 (2013) 44-46.
[136] H. S. Han, J. Koruza, E. A. Patterson, J. Schultheiss, E. Erdem, W. Jo, J. S. Lee, J. Rodel, Hardening behavior and highly enhanced mechanical quality factor in $(K_{0.5}Na_{0.5})NbO_3$-based ceramics, J Eur Ceram Soc 37 (2017) 2083-2089.
[137] Y. X. Liu, H. C. Thong, C. L. Zhao, Q. Liu, X. Y. Xu, K. Wang, J. F. Li, Influence of trace zirconia addition on the properties of $(K,Na)NbO_3$ solid solutions, J Mater Chem C 7 (2019) 6914-6923.
[138] X. H. Li, M. Jiang, J. Liu, J. L. Zhu, X. H. Zhu, L. H. Li, Y. Zhou, J. G. Zhu, D. Q. Xiao, Phase transitions and electrical properties of $(1-x)(K_{0.5}Na_{0.5})NbO_3$-$xBiScO_3$ lead-free piezoelectric ceramics with a CuO sintering aid, Phys Status Solidi A 206 (2009) 2622-2626.
[139] S. H. Park, C. W. Ahn, S. Nahm, J. S. Song, Microstructure and piezoelectric properties of ZnO-added $(Na_{0.5}K_{0.5})NbO_3$ ceramics, Jpn J Appl Phys 2 43 (2004) 1072-1074.
[140] Y. F. Chang, Z. P. Yang, L. L. Wei, B. Liu, Effects of $AETiO_3$ additions on phase structure, microstructure and electrical properties of $(K_{0.5}Na_{0.5})NbO_3$ ceramics, Mat Sci Eng a-Struct 437 (2006) 301-305.
[141] N. M. Hagh, K. Kerman, B. Jadidian, A. Safari, Dielectric and piezoelectric properties of Cu^{2+}-doped alkali niobates, J Eur Ceram Soc 29 (2009) 2325-2332.
[142] T. Tou, Y. Hamaguti, Y. Maida, H. Yamamori, K. Takahashi, Y. Terashima, Properties of $(Bi_{0.5}Na_{0.5})TiO_3$-$BaTiO_3$-$(Bi_{0.5}Na_{0.5})(Mn_{1/3}Nb_{2/3})O_3$ lead-free piezoelectric ceramics and its application to ultrasonic cleaner, Jpn J Appl Phys 48 (2009) 07GM03.
[143] M. Hejazi, E. Taghaddos, E. Gurdal, K. Uchino, A. Safari, High power performance of manganese-doped BNT-based Pb-free piezoelectric ceramics, J Am Ceram Soc 97 (2014) 3192-3196.
[144] D. Bremecker, K. V. Lalitha, S. Teuber, J. Koruza, J. Rodel, Influence of Zn^{2+} doping on the morphotropic phase boundary in lead-free piezoelectric $(1-x)Na_{1/2}Bi_{1/2}TiO_3$-$xBaTiO_3$, J Am Ceram Soc 105 (2022) 1232-1240.
[145] Q. Xu, M. Chen, W. Chen, H. X. Liu, B. H. Kim, B. K. Ahn, Effect of CoO additive on structure and electrical properties of $(Na_{0.5}Bi_{0.5})_{0.93}Ba_{0.07}TiO_3$ ceramics prepared by the citrate method, Acta Mater 56 (2008) 642-650.
[146] H. D. Li, C. D. Feng, W. L. Yao, Some effects of different additives on dielectric and piezoelectric properties of $(Bi_{1/2}Na_{1/2})TiO_3$-$BaTiO_3$ morphotropic-phase-boundary composition, Mater Lett 58 (2004) 1194-1198.

[147] H. C. Hu, M. K. Zhu, F. Y. Xie, N. Lei, J. Chen, Y. D. Hou, H. Yan, Effect of Co_2O_3 additive on structure and electrical properties of $85(Bi_{1/2}Na_{1/2})TiO_3$-$12(Bi_{1/2}K_{1/2})TiO_3$-$3BaTiO_3$ lead-free piezoceramics, J Am Ceram Soc 92 (2009) 2039-2045.
[148] M. S. Yoon, Y. G. Lee, S. C. Ur, Effects of co-doped CaO/MnO on the piezoelectric/dielectric properties and phase transition of lead-Free $(Bi_{0.5}Na_{0.5})_{0.94}Ba_{0.06}TiO_3$ piezoelectric ceramics, J Electroceram 23 (2009) 564-571.
[149] M. K. Zhu, L. Y. Liu, Y. D. Hou, H. Wang, H. Yan, Microstructure and electrical properties of MnO-doped $(Na_{0.5}Bi_{0.5})_{0.92}Ba_{0.08}TiO_3$ lead-free piezoceramic, J Am Ceram Soc 90 (2007) 120-124.
[150] S. Kawada, H. Ogawa, M. Kimura, K. Shiratsuyu, H. Niimi, High-power piezoelectric vibration characteristics of textured $SrBi_2Nb_2O_9$ ceramics, Jpn J Appl Phys 1 45 (2006) 7455-7459.
[151] H. Nagata, M. Seki, Y. Noumura, Y. Hiruma, T. Takenaka, High-power piezoelectric characteristics of nontextured bismuth layer-structured ferroelectric ceramics, Jpn J Appl Phys 50 (2011) 09ND05.
[152] Y. Noumura, Y. Hiruma, H. Nagata, T. Takenaka, High-power piezoelectric characteristics of $Bi_4Ti_3O_{12}$-$SrBi_4Ti_4O_{15}$-based ferroelectric ceramics, Jpn J Appl Phys 49 (2010) 09MD02.
[153] H. Ogawa, S. Kawada, M. Kimura, K. Shiratsuyu, Y. Sakabe, High-power piezoelectric characteristics of textured bismuth layer structured ferroelectric ceramics, IEEE T Ultrason Ferr 54 (2007) 2500-2504.
[154] B. S. Li, G. R. Li, S. C. Zhao, L. N. Zhang, A. L. Ding, Characterization of the high-power piezoelectric properties of PMnN-PZT ceramics using constant voltage and pulse drive methods, J Phys D Appl Phys 38 (2005) 2265-2270.
[155] S. Takahashi, S. Hirose, Vibration-level characteristics of lead-zirconate-titanate ceramics, Jpn J Appl Phys 1 31 (1992) 3055-3057.
[156] S. Tashiro, M. Ikehiro, H. Igarashi, Influence of temperature rise and vibration level on electromechanical properties of high-power piezoelectric ceramics, Jpn J Appl Phys 1 36 (1997) 3004-3009.
[157] S. O. Ural, Y. Zhuang, S. Tuncdemir, K. Uchino, Comparison of power density characteristics among disk and plate shaped piezoelectric devices, Jpn J Appl Phys 49 (2010) 021502.
[158] S. Hirose, Y. Yamayoshi, M. Taga, H. Shimizu, A method of measuring the vibration level dependence of impedance-type equivalent-circuit constants, Jpn J Appl Phys 30 (1991) 117-119.
[159] Y. Sasaki, S. Takahashi, S. Hirose, Relationship between mechanical loss and phases of physical constants in lead-zirconate-titanate ceramics, Jpn J Appl Phys 36 (1997) 6058-6061.
[160] Y. K. Gao, K. Uchino, D. Viehland, Time dependence of the mechanical quality factor in "hard" lead zirconate titanate ceramics: Development of an internal dipolar field and high power origin, Jpn J Appl Phys 1 45 (2006) 9119-9124.
[161] S. Takahashi, S. Hirose, K. Uchino, Stability of PZT piezoelectric ceramics under vibration level change, J Am Ceram Soc 77 (1994) 2429-2432.
[162] A. Albareda, P. Gonnard, V. Perrin, R. Briot, D. Guyomar, Characterization of the mechanical nonlinear behavior of piezoelectric ceramics, IEEE T Ultrason Ferr 47 (2000) 844-853.
[163] J. Suchanicz, A. Jezowski, R. Poprawski, S. Dacko, Thermal and dielectric behaviour of pure and doped $Na_{0.5}Bi_{0.5}TiO_3$ at low temperatures, Phys Status Solidi B 221 (2000) 789-795.
[164] K. G. Webber, M. Voegler, N. H. Khansur, B. Kaeswurm, J. E. Daniels, F. H. Schader, Review of the mechanical and fracture behavior of perovskite lead-free ferroelectrics for actuator applications, Smart Mater Struct 26 (2017) 063001.

[165] T. Takenaka, K. Maruyama, K. Sakata, $(Bi_{1/2}Na_{1/2})TiO_3$-$BaTiO_3$ system for lead-free piezoelectric ceramics, Jpn J Appl Phys 1 30 (1991) 2236-2239.
[166] R. Ranjan, A. Dviwedi, Structure and dielectric properties of $(Na_{0.50}Bi_{0.50})_{(1-x)}Ba_xTiO_3$: $0<x<0.10$, Solid State Commun 135 (2005) 394-399.
[167] C. Ma, H. Z. Guo, S. P. Beckman, X. L. Tan, Creation and destruction of morphotropic phase boundaries through electrical poling: A case study of lead-free $(Bi_{1/2}Na_{1/2})TiO_3$-$BaTiO_3$ piezoelectrics, Phys Rev Lett 109 (2012) 107602.
[168] W. Jo, J. E. Daniels, J. L. Jones, X. L. Tan, P. A. Thomas, D. Damjanovic, J. Rödel, Evolving morphotropic phase boundary in lead-free $(Bi_{1/2}Na_{1/2})TiO_3$-$BaTiO_3$ piezoceramics, J Appl Phys 109 (2011) 014110.
[169] M. Slabki, L. K. Venkataraman, T. Rojac, J. Rödel, J. Koruza, Thermal stability of the electromechanical properties in acceptor-doped and composite-hardened $(Na_{1/2}Bi_{1/2})TiO_3$-$BaTiO_3$ ferroelectrics, J Appl Phys 130 (2021) 014101.
[170] S. Prasertpalichat, D. P. Cann, Hardening in non-stoichiometric $(1-x)Bi_{0.5}Na_{0.5}TiO_3$-$xBaTiO_3$ lead-free piezoelectric ceramics, J Mater Sci 51 (2016) 476-486.
[171] D. K. Khatua, A. Mishra, N. Kumar, G. Das Adhikary, U. Shankar, B. Majumdar, R. Ranjan, A coupled microstructural-structural mechanism governing thermal depolarization delay in $Na_{0.5}Bi_{0.5}TiO_3$-based piezoelectrics, Acta Mater 179 (2019) 49-60.
[172] H. Muramatsu, H. Nagata, T. Takenaka, Quenching effects for piezoelectric properties on lead-free $(Bi_{1/2}Na_{1/2})TiO_3$ ceramics, Jpn J Appl Phys 55 (2016) 10TB07.
[173] Y. Hiruma, T. Watanabe, H. Nagata, T. Takenaka, Piezoelectric properties of $(Bi_{1/2}Na_{1/2})TiO_3$-based solid solution for lead-free high-power applications, Jpn J Appl Phys 47 (2008) 7659-7663.
[174] S. M. Denkhaus, M. Vogler, N. Novak, J. Rodel, Short crack fracture toughness in $(1-x)(Na_{1/2}Bi_{1/2})TiO_3$-$xBaTiO_3$ relaxor ferroelectrics, J Am Ceram Soc 100 (2017) 4760-4769.
[175] H. N. Shekhani, E. A. Gurdal, S. O. Ural, K. Uchino, Analysis of high power behavior in piezoelectric ceramics from a mechanical energy density perspective, arXiv preprint (2016) 1605.06685.
[176] Y. Doshida, H. Shimizu, Y. Mizuno, H. Tamura, Investigation of high-power properties of $(Bi,Na,Ba)TiO_3$ and $(Sr,Ca)_2NaNb_5O_{15}$ piezoelectric ceramics, Jpn J Appl Phys 52 (2013) 07HE01.
[177] A. Albareda, R. Perez, J. A. Casals, J. E. Garcia, D. A. Ochoa, Optimization of elastic nonlinear behavior measurements of ceramic piezoelectric resonators with burst excitation, IEEE T Ultrason Ferr 54 (2007) 2175-2188.
[178] Y. Y. Liu, R. Ozaki, T. Morita, Investigation of nonlinearity in piezoelectric transducers, Sensor Actuat a-Phys 227 (2015) 31-38.
[179] W. G. Cady, Piezoelectricity: An introduction to the theory and application of electromechanical phenomena in crystals, 1 ed., Dover Publications, New York (1946).
[180] S. Hirose, New method for measuring mechanical vibration loss and dielectric loss of piezoelectric transducer under high-power excitation, Jpn J Appl Phys 1 33 (1994) 2945-2948.
[181] S. O. Ural, S. Tuncdemir, Y. Zhuang, K. Uchino, Development of a high power piezoelectric characterization system and its application for resonance/antiresonance mode characterization, Jpn J Appl Phys 48 (2009) 056509.
[182] K. T. Chang, M. Ouyang, Open-circuit test of a PZT vibrator and its applications, Ultrasonics 41 (2003) 15-23.
[183] Standard ANSI/IEEE 176-1978, IEEE Standard on piezoelectricity (1978).
[184] J. F. Blackburn, M. G. Cain, Non-linear piezoelectric resonance analysis using burst mode: A rigorous solution, J Phys D Appl Phys 40 (2007) 227-233.

[185] M. Umeda, K. Nakamura, S. Takahashi, S. Ueha, Waveforms of the vibration velocity and the current of a piezoelectric transducer in the transient state, Jpn J Appl Phys 40 (2001) 5735-5739.
[186] K. Uchino, Piezoelectric actuators and ultrasonic motors, 1 ed., Kluwer Academic Publisher, Dordrecht (1996).
[187] M. J. Hoffmann, M. Hammer, A. Endriss, D. C. Lupascu, Correlation between microstructure, strain behavior, and acoustic emission of soft PZT ceramics, Acta Mater 49 (2001) 1301-1310.
[188] J. T. Reszat, A. E. Glazounov, M. J. Hoffmann, Analysis of intrinsic lattice deformation in PZT-ceramics of different compositions, J Eur Ceram Soc 21 (2001) 1349-1352.
[189] K. S. Lee, Y. K. Kim, S. Baik, J. Kim, I. S. Jung, In situ observation of ferroelectric 90 degrees-domain switching in epitaxial $Pb(Zr,Ti)O_3$ thin films by synchrotron x-ray diffraction, Appl Phys Lett 79 (2001) 2444-2446.
[190] J. L. Jones, M. Hoffman, J. E. Daniels, A. J. Studer, Direct measurement of the domain switching contribution to the dynamic piezoelectric response in ferroelectric ceramics, Appl Phys Lett 89 (2006) 092901.
[191] J. E. Daniels, T. R. Finlayson, A. J. Studer, M. Hoffman, J. L. Jones, Time-resolved diffraction measurements of electric-field-induced strain in tetragonal lead zirconate titanate, J Appl Phys 101 (2007) 094104.
[192] J. L. Jones, A. Pramanick, J. C. Nino, S. M. Motahari, E. Ustundag, M. R. Daymond, E. C. Oliver, Time-resolved and orientation-dependent electric-field-induced strains in lead zirconate titanate ceramics, Appl Phys Lett 90 (2007) 172909.
[193] J. E. Daniels, A. Pramanick, J. L. Jones, Time-resolved characterization of ferroelectrics using high-energy x-ray diffraction, IEEE T Ultrason Ferr 56 (2009) 1539-1545.
[194] G. B. Vaughan, R. Baker, R. Barret, J. Bonnefoy, T. Buslaps, S. Checchia, D. Duran, F. Fihman, P. Got, J. Kieffer, ID15A at the ESRF–a beamline for high speed operando X-ray diffraction, diffraction tomography and total scattering, J Synchrotron Radiat 27 (2020) 515-528.
[195] E. Zolotoyabko, J. P. Quintana, B. H. Hoerman, B. W. Wessels, Fast time-resolved X-ray diffraction in $BaTiO_3$ films subjected to a strong high-frequency electric field, Appl Phys Lett 80 (2002) 3159-3161.
[196] A. P. Hammersley, S. O. Svensson, M. Hanfland, A. N. Fitch, D. Hausermann, Two-dimensional detector software: From real detector to idealised image or two-theta scan, High Pressure Res 14 (1996) 235-248.
[197] B. D. Cullity, Elements of X-ray Diffraction, 1 ed., Addison-Wesley Publishing, Reading (1956).
[198] J. L. Jones, E. B. Slamovich, K. J. Bowman, Domain texture distributions in tetragonal lead zirconate titanate by X-ray and neutron diffraction, J Appl Phys 97 (2005) 034113.
[199] M. R. Daymond, The determination of a continuum mechanics equivalent elastic strain from the analysis of multiple diffraction peaks, J Appl Phys 96 (2004) 4263-4272.
[200] J. L. Jones, M. Hoffman, K. J. Bowman, Saturated domain switching textures and strains in ferroelastic ceramics, J Appl Phys 98 (2005) 024115.
[201] Q. M. Wang, T. Zhang, Q. M. Chen, X. H. Du, Effect of DC bias field on the complex materials coefficients of piezoelectric resonators, Sensor Actuat a-Phys 109 (2003) 149-155.
[202] P. Horowitz, W. Hill, The art of electronics, 3 ed., Cambridge University Press, Cambridge (2015).
[203] S. H. Nam, H. Rahaman, H. Heo, S. S. Park, J. W. Shin, J. H. So, W. Jang, Empirical analysis of high pressure SF_6 gas breakdown strength in a spark gap switch, IEEE T Dielect El In 16 (2009) 1106-1110.
[204] C. T. Kelley, Solving nonlinear equations with Newton's method, 1 ed., Society for Industrial and Applied Mathematics, Philadelphia (2003).

[205] P. K. Dixon, L. Wu, Broadband digital lock-in amplifier techniques, Rev Sci Instrum 60 (1989) 3329-3336.
[206] M. Otonicar, A. Bradesko, L. Fulanovic, T. Kos, H. Ursic, A. Bencan, M. J. Cabral, A. Henriques, J. L. Jones, L. Riemer, D. Damjanovic, G. Drazic, B. Malic, T. Rojac, Connecting the multiscale structure with macroscopic response of relaxor ferroelectrics, Adv Funct Mater 30 (2020) 2006823.
[207] S. Hashemizadeh, D. Damjanovic, Nonlinear dynamics of polar regions in paraelectric phase of $(Ba_{1-x},Sr_x)TiO_3$ ceramics, Appl Phys Lett 110 (2017) 192905.
[208] T. Rojac, S. Drnovsek, A. Bencan, B. Malic, D. Damjanovic, Role of charged defects on the electrical and electromechanical properties of rhombohedral $Pb(Zr,Ti)O_3$ with oxygen octahedra tilts, Phys Rev B 93 (2016).
[209] Standards EN 50324-1, Piezoelectric properties of ceramic materials and components-Part 1: Terms and definitions (2002).
[210] G. Picht, N. H. Khansur, K. G. Webber, H. Kungl, M. J. Hoffmann, M. Hinterstein, Grain size effects in donor doped lead zirconate titanate ceramics, J Appl Phys 128 (2020) 214105.
[211] D. M. Smyth, The defect chemistry of metal oxides, 1 ed., Oxford University Press, New York (2000).
[212] J. Y. Jo, S. M. Yang, T. H. Kim, H. N. Lee, J. G. Yoon, S. Park, Y. Jo, M. H. Jung, T. W. Noh, Nonlinear dynamics of domain-wall propagation in epitaxial ferroelectric thin films, Phys Rev Lett 102 (2009) 045701.
[213] M. Davis, M. Budimir, D. Damjanovic, N. Setter, Rotator and extender ferroelectrics: Importance of the shear coefficient to the piezoelectric properties of domain-engineered crystals and ceramics, J Appl Phys 101 (2007) 054112.
[214] A. Pramanick, J. E. Daniels, J. L. Jones, Subcoercive cyclic electrical loading of lead zirconate titanate ceramics II: Time-resolved x-ray diffraction, J Am Ceram Soc 92 (2009) 2300-2310.
[215] M. Hinterstein, M. Hoelzel, J. Rouquette, J. Haines, J. Glaum, H. Kungl, M. Hoffman, Interplay of strain mechanisms in morphotropic piezoceramics, Acta Mater 94 (2015) 319-327.
[216] S. Priya, D. Viehland, A. V. Carazo, J. Ryu, K. Uchino, High-power resonant measurements of piezoelectric materials: Importance of elastic nonlinearities, J Appl Phys 90 (2001) 1469-1479.
[217] M. Marsilius, K. G. Webber, E. Aulbach, T. Granzow, Comparison of the temperature-dependent ferroelastic behavior of hard and soft lead zirconate titanate ceramics, J Am Ceram Soc 93 (2010) 2850-2856.
[218] R. Gerson, Dependence of mechanical-Q and Youngs modulus of ferroelectric ceramics on stress amplitude, J Acoust Soc Am 32 (1960) 1297-1301.
[219] J. E. Garcia, R. Perez, D. A. Ochoa, A. Albareda, M. H. Lente, J. A. Eiras, Evaluation of domain wall motion in lead zirconate titanate ceramics by nonlinear response measurements, J Appl Phys 103 (2008) 054108.
[220] O. Kersten, M. Hofmann, G. Schmidt, Dielectric-dispersion of Mn doped ceramics, Ferroelectrics Lett 6 (1986) 75-80.
[221] U. Bottger, G. Arlt, Dielectric microwave dispersion in PZT ceramics, Ferroelectrics 127 (1992) 95-100.
[222] D. V. Taylor, D. Damjanovic, Evidence of domain wall contribution to the dielectric permittivity in PZT thin films at sub-switching fields, J Appl Phys 82 (1997) 1973-1975.
[223] S. N. Kallaev, G. G. Gadzhiev, I. K. Kamilov, Z. M. Ornarov, S. A. Sadykov, L. A. Reznichenko, Thermal properties of PZT-based ferroelectric ceramics, Phys Solid State 48 (2006) 1169-1170.
[224] G. Arlt, H. Dederichs, R. Herbiet, 90-degrees-domain wall relaxation in tetragonally distorted ferroelectric ceramics, Ferroelectrics 74 (1987) 37-53.

[225] H. Dederichs, G. Arlt, Aging of FE-doped PZT ceramics and the domain wall contribution to the dielectric constant, Ferroelectrics 68 (1986) 281-292.
[226] M. Morozov, D. Damjanovic, N. Setter, The nonlinearity and subswitching hysteresis in hard and soft PZT, J Eur Ceram Soc 25 (2005) 2483-2486.
[227] S. Srilomsak, W. A. Schulze, S. M. Pilgrim, F. A. Williams, Harmonic analysis of polarization hysteresis of aged PZTs, J Am Ceram Soc 88 (2005) 2121-2125.
[228] E. Barsoukov, J. R. Macdonald, Impedance spectroscopy: Theory, experiment, and applications, 3 ed., Wiley, Hoboken (2018).
[229] L. Jin, V. Porokhonskyy, D. Damjanovic, Domain wall contributions in $Pb(Zr,Ti)O_3$ ceramics at morphotropic phase boundary: A study of dielectric dispersion, Appl Phys Lett 96 (2010) 242902.
[230] V. Porokhonskyy, L. Jin, D. Damjanovic, Separation of piezoelectric grain resonance and domain wall dispersion in $Pb(Zr,Ti)O_3$ ceramics, Appl Phys Lett 94 (2009) 212906.
[231] R. Gerson, Dielectric properties of lead titanate zirconate ceramics at very low frequencies, J Appl Phys 31 (1960) 1615-1617.
[232] R. A. Eichel, H. Mestric, K. P. Dinse, A. Ozarowski, J. van Tol, L. C. Brunel, H. Kungl, M. J. Hoffmann, High-field/high-frequency EPR of paramagnetic functional centers in Cu^{2+}- and Fe^{3+}-modified polycrystalline $Pb[Zr_xTi_{1-x}]O_3$ ferroelectrics, Magn Reson Chem 43 (2005) 166-173.
[233] W. L. Warren, K. Vanheusden, D. Dimos, G. E. Pike, B. A. Tuttle, Oxygen vacancy motion in perovskite oxides, J Am Ceram Soc 79 (1996) 536-538.
[234] F. Cordero, F. Craciun, C. Galassi, Low-temperature phase transformations of $PbZr_{1-x}Ti_xO_3$ in the morphotropic phase-boundary region, Phys Rev Lett 98 (2007) 255701.
[235] D. E. Cox, B. Noheda, G. Shirane, Low-temperature phases in $PbZr_{0.52}Ti_{0.48}O_3$: A neutron powder diffraction study, Phys Rev B 71 (2005) 134110.
[236] G. Picht, V. Bouvier, S. Frank, J. Koruza, F. Felten, G. Lindemann, Ferroelastic properties of PZT: Characterization under compressive and tensile stress, finite-element simulation, and lifetime calculation, IEEE T Ultrason Ferr 65 (2018) 1542-1551.
[237] J. L. Butler, K. D. Rolt, F. A. Tito, Piezoelectric ceramic mechanical and electrical stress study, J Acoust Soc Am 96 (1994) 1914-1917.
[238] A. J. Masys, W. Ren, G. Yang, B. K. Mukherjee, Piezoelectric strain in lead zirconate titante ceramics as a function of electric field, frequency, and dc bias, J Appl Phys 94 (2003) 1155-1162.
[239] N. Balke, T. Granzow, J. Rodel, Degradation of lead-zirconate-titanate ceramics under different dc loads, J Appl Phys 105 (2009) 104105.
[240] M. Alguero, C. Alemany, L. Pardo, A. M. Gonzalez, Method for obtaining the full set of linear electric, mechanical, and electromechanical coefficients and all related losses of a piezoelectric ceramic, J Am Ceram Soc 87 (2004) 209-215.
[241] Standards EN 50324-3, Piezoelectric properties of ceramic materials and components-Part 3: Methods of measurement-High power (2002).
[242] A. Wohninsland, A.-K. Fetzer, R. Broughton, J. L. Jones, K. Lalitha, Structural and microstructural description of relaxor-ferroelectric transition in quenched $Na_{1/2}Bi_{1/2}TiO_3$-$BaTiO_3$, J Materiom (2022).
[243] D. K. Khatua, T. Mehrotra, A. Mishra, B. Majumdar, A. Senyshyn, R. Ranjan, Anomalous influence of grain size on the global structure, ferroelectric and piezoelectric response of $Na_{0.5}Bi_{0.5}TiO_3$, Acta Mater 134 (2017) 177-187.
[244] A.-K. Fetzer, A. Wohninsland, K. Hofmann, O. Clemens, L. K. Venkataraman, H.-J. Kleebe, Domain structure and phase evolution in quenched and furnace cooled lead-free $Na_{1/2}Bi_{1/2}TiO_3$–$BaTiO_3$ ceramics, Open Ceramics 5 (2021) 100077.
[245] G. Arlt, N. A. Pertsev, Force-constant and effective mass of 90-degrees domain-walls in ferroelectric ceramics, J Appl Phys 70 (1991) 2283-2289.

[246] X. Tan, E. Aulbach, W. Jo, T. Granzow, J. Kling, M. Marsilius, H. J. Kleebe, J. Rodel, Effect of uniaxial stress on ferroelectric behavior of $(Bi_{1/2}Na_{1/2})TiO_3$-based lead-free piezoelectric ceramics, J Appl Phys 106 (2009) 044107.
[247] F. Cordero, Elastic properties and enhanced piezoelectric response at morphotropic phase boundaries, Materials 8 (2015) 8195-8245.
[248] K. V. Lalitha, D. Isaia, W. Gong, C. F. Wu, Y. W. Li, J. Rodel, Deformation and bending strength of high-performance lead-free piezoceramics, J Am Ceram Soc 105 (2022) 3128-3132.
[249] G. Arlt, The role of domain-walls on the dielectric, elastic and piezoelectric properties of ferroelectric ceramics, Ferroelectrics 76 (1987) 451-458.
[250] H. Kara, R. Ramesh, R. Stevens, C. R. Bowen, Porous PZT ceramics for receiving transducers, IEEE T Ultrason Ferr 50 (2003) 289-296.
[251] R. Guo, C. A. Wang, A. K. Yang, Piezoelectric properties of the 1-3 type porous lead zirconate titanate ceramics, J Am Ceram Soc 94 (2011) 1794-1799.
[252] K. M. Rittenmyer, R. Y. Ting, T. A. Henriquez, Piezoelectric properties of calcium-modified lead titanate and its application in underwater transducers, J Acoust Soc Am 79 (1986) 2073-2076.
[253] S. Steiner, I. T. Seo, P. R. Ren, M. Li, D. J. Keeble, T. Fromling, The effect of Fe-acceptor doping on the electrical properties of $Na_{1/2}Bi_{1/2}TiO_3$ and $0.94(Na_{1/2}Bi_{1/2})TiO_3$-$0.06BaTiO_3$, J Am Ceram Soc 102 (2019) 5295-5304.
[254] N. H. Khansur, M. Hinterstein, Z. Y. Wang, C. Groh, W. Jo, J. E. Daniels, Electric-field-induced strain contributions in morphotropic phase boundary composition of $(Bi_{1/2}Na_{1/2})TiO_3$-$BaTiO_3$ during poling, Appl Phys Lett 107 (2015) 242902.
[255] K. Negishi, Jump phenomenon in resonance curve of ferroelectric ceramics, J Phys Soc Jpn 15 (1960) 534-534.
[256] M. Umeda, K. Nakamura, S. Takahashi, S. Ueha, An analysis of jumping and dropping phenomena of piezoelectric transducers using the electrical equivalent circuit constants at high vibration amplitude levels, Jpn J Appl Phys 1 39 (2000) 5623-5628.
[257] M. Makarovic, N. Kanas, A. Zorko, K. Ziberna, H. Ursic, D. R. Smabraten, S. M. Selbach, T. Rojac, Tailoring the electrical conductivity and hardening in $BiFeO_3$ ceramics, J Eur Ceram Soc 40 (2020) 5483-5493.
[258] K. N. Schuldt, H. Ding, J.-C. Jaud, J. Koruza, A. Klein, Influence of defects on the Schottky barrier height at $BaTiO_3/RuO_2$ interfaces, Phys Status Solidi A 218 (2021) 2100143.
[259] G. G. Stokes, On the effect of the internal friction of fluids on the motion of pendulums, Trans Cambridge Philos Soc 9 (1851) 8.

List of Figures

List of Tables

Acknowledgment

I was waiting impatiently for this opportunity to thank all people that paved my way over the last couple of years and without whom this work would not have been possible.

First and foremost, I would like to express my deep and sincere gratitude to my supervisor, mentor, and friend Prof. Dr. Jurij Koruza, who accompanied and navigated me throughout my entire academic career until now. You hired me as a HiWi shortly after coming to Darmstadt, supervised my Bachelor's and Master's theses, gave me the opportunity to conduct my PhD research, and sent me around the world for conferences, workshops, and research stays. Working with you was one of the main reasons for the career steps and decisions I have taken so far. Thank you so much for your tireless support, help, encouragement, guidance, and patience, which far exceeded your duties. It was a pleasure to work with you day in day out and to learn from you also beyond science. Thank you for the intense discussions (also those on the Mainz – Darmstadt trains on the way to work and back home), the ventured experimental approaches (especially when you entered the lab on a Friday afternoon), and your confidence to let me work independently and develop my ideas freely. It was a privilege to see you grow at the same time from postdoc to professor, I hope I contributed a little to the progress. Doubtless you will be successful and I wish you all the best.

I would like to thank Prof. Dr. Jürgen Rödel for giving me the opportunity to work for quite some time in a wonderful, well-organized, and well-equipped group at NAW. Thank you very much for your scientific and professional support, development, and trust. Moreover, I would like to thank Prof. Dr. Wolfgang Donner for reviewing this work, as well as Prof. Dr. Mario Kupnik and Prof. Dr. Robert Stark for their willingness to participate in the examination committee.

An essential part of the group organization and smoothness at NAW traces back to Gila Völzke. Thank you Gila for your work, for keeping all administrative problems away from the PhD students, and foremost, for your warm words and kind encouragement at any time of need. My greatest thanks also belong to Michael Weber, Daniel Isaia, and Patrick Breckner for their tremendous contribution and commitment designing and realizing all the experimental equipment. Thank you for being patient with me and for sharing your skills and knowledge. Essential parts of this work would not have been possible without you.

My greatest appreciation goes also to all the collaborators and colleagues with whom I was privileged to work during the past years: Prof. Dr. Tadej Rojac and Silvo Drnovšek from the Jozef Stefan Institute, Prof. Dr. John Daniel from the University of New South Wales, Dr. Stefano Checchia from the European Synchrotron Radiation Facility, Prof. Dr. Kentaro Nakamura and Dr. Jiang Wu from the Tokyo Institute of Technology, Prof. Dr. Hajime Nagata from the Tokyo University of Science, and Prof. Dr. Takeshi Morita from The University of Tokyo. Thank you for the fruitful discussions, the open and encouraging collaboration, and for kindling hosting me during the visits. Especially, I am incredibly thankful to Dr. Tomaz Kos from the Jozef Stefan Institute. You had a hard time explaining to me the basics of electrical engineering; nevertheless, you supported me vitally at any time and we constructed an excellent measurement system. Thank you so much.

I am also taking the opportunity to acknowledge all the colleagues and friends from the NAW group and MaWi department. Thank you for the time during work and after work, without you it would not have been such a great time. Particular gratitude belongs to Dr. Lalitha Kodumudi Venkataraman for supplying me with samples and discussing essential parts of this work, and to Dr. Lovro Fulanovic for providing the FEM modeling. Moreover, I would also like to thank the best office-mates ever, An-Phuc Hoang and Maohua Zhang. Thank you for the support and the open ears, I could not have wished for better friends sitting with me for three years in one room. This is what I will miss most. In addition, I would like to thank Marcel Sadowski, who accompanied me as a faithful friend from day one at the university until now. Without you I would not have come so far.

Finally, my deepest and sincerest thanks go to my parents and family for their unconditional support, inspiration, encouragement, and trust, no matter which way I took, and to my soulmate Darja for her love, endurance, and understanding.

Suffering is temporary, PhD is forever!

Publications

M. Slabki, J. Wu, M. Weber, P. Breckner, D. Isaia, K. Nakamura, and J. Koruza, Anisotropy of the high-power piezoelectric properties of $Pb(Zr,Ti)O_3$, J Am Ceram Soc 102 (2019) 6008-6017.

M. Slabki, L. K. Venkataraman, S. Checchia, L. Fulanovic, J. Daniels, and J. Koruza, Direct observation of domain wall motion and lattice strain dynamics in ferroelectrics under high-power resonance, Phys Rev B 103 (2021) 174113.

M. Slabki, L. K. Venkataraman, T. Rojac, J. Rödel, and J. Koruza, Thermal stability of the electromechanical properties in acceptor-doped and composite-hardened $(Na_{1/2}Bi_{1/2})TiO_3$-$BaTiO_3$ ferroelectrics, J Appl Phys 130 (2021) 014101.

M. Slabki, L. K. Venkataraman, J. Rödel, and J. Koruza, Origin of high-power drive stability in $(Na_{1/2}Bi_{1/2})TiO_3$-$BaTiO_3$ based piezoceramics, Acta Mater 227 (2022) 117703.

M. Slabki, T. Kos[xxvi], J. Petrovcic, D. Vrancic, G. Dolanc, and J. Koruza, Measurement system for piezoelectric resonance impedance spectroscopy under combined AC and high-voltage DC loading, submitted (2022).

D. Bremecker, **M. Slabki**, J. Koruza, J. Rödel, Characterization of the crystal structure, electrical and electromechanical properties of Mg-doped $0.94Na_{1/2}Bi_{1/2}TiO_3$-$0.06BaTiO_3$, submitted (2022).

Patent applications

T. Kos, **M. Slabki**, J. Petrovčič, and J. Koruza, Resonance spectrometer and method for determining characteristics of a device under test, European patent application number EP21217013.8 (2022).

[xxvi] T. Kos and M. Slabki are co-first authors.

Conference contributions

M. Slabki, M. Weber, P. Breckner, D. Isaia, and J. Koruza, Vibration mode dependence of the high-power piezoelectric properties of hard $Pb(Zr,Ti)O_3$, International Conference on New Actuators (Bremen, 2018).

J. Rödel, L. K. Venkataraman, **M. Slabki**, V. V. Shvartsman, D. C. Lupascu, M. Hinterstein, and J. Koruza, Second phase electromechanical hardening in alkaline bismuth titanate-based lead-free piezoceramics, European Conference on Applications of Polar Dielectrics (Moscow, 2018)

M. Slabki, L. K. Venkataraman, and J. Koruza, High-power electromechanical properties of $(Na_{1/2}Bi_{1/2})TiO_3$-$BaTiO_3$ based composites, Joint IEEE ISAF-ICE-EMF-IWPM-PFM Conference (Lausanne, 2019).

L. K. Venkataraman, **M. Slabki**, J. Koruza, and J. Rödel, Lead-free hard-type relaxor $(Na_{1/2}Bi_{1/2})TiO_3$-$BaTiO_3$ composites for high power applications, Electronic Materials and Applications (Orlando, 2019)

M. Slabki, S. Checchia, L. K. Venkataraman, J. Daniels, and J. Koruza, Characterization of electromechanical and structural parameters in piezoelectric resonance, Joint IEEE ISAF-ICE-EMF-IWPM-PFM Conference (Lausanne, 2019).

J. Koruza and **M. Slabki**, Piezoceramics for high-power drive: characterization, materials, and mechanisms, Reunion Nacional de Electroceramica (Castellon 2019).

M. Slabki, J. Daniels, and J. Koruza, Electromechanical and structural characterization of piezoceramics under high-power drive, Electronic Materials and Applications (Orlando, 2020).

M. Slabki, L. K. Venkataraman, S. Checchia, J. Daniels, and J. Koruza, Direct measurement of the intrinsic and extrinsic contributions to the dynamic piezoelectric response in ferroelectrics under high-power drive, Joint IEEE IFCS-ISAF Conference (virtual, 2020).

M. Slabki, L. K. Venkataraman, J. Rödel, and J. Koruza, High-power electromechanical properties of $(Na_{1/2}Bi_{1/2})TiO_3$-$BaTiO_3$ based piezoceramics composites, Electroceramics Conference (virtual, 2020).

D. Bremecker, L. K. Venkataraman, **M. Slabki**, J. Koruza, and J. Rödel, Processing and properties of $Na_{1/2}Bi_{1/2}TiO_3$-$BaTiO_3$:Al_2O_3 piezoceramic composites, Electroceramics Conference (virtual, 2020).

M. Slabki, L. K. Venkataraman, J. Rödel, and J. Koruza, High-power stability of $(Na_{1/2}Bi_{1/2})TiO_3$-$BaTiO_3$ and its ceramic-ceramic composites, Electronic Materials and Applications (virtual, 2021).

M. Slabki, L. K. Venkataraman, S. Checchia, J. Daniels, and J. Koruza, Characterization method for electromechanical and structural correlation in piezoceramics under high-power drive, DKG annual meeting (virtual, 2021).

M. Slabki, L. K. Venkataraman, T. Rojac, and J. Koruza, Temperature-dependent high-power electromechanical properties of $Na_{1/2}Bi_{1/2}TiO_3$-$BaTiO_3$ based composites, DKG annual meeting (virtual, 2021).

M. Slabki, C. Zhao, L. K. Venkataraman, T. Rojac, and J. Koruza, Temperature-dependence of the electromechanical quality factor in acceptor-doped ferroelectrics, Joint IEEE ISAF-ISIF-PFM Conference (virtual 2021).

J. Koruza and **M. Slabki**, Mechanisms defining the stability of hard-type piezoelectrics for high-power drive, International Conference on Advanced Electromaterials (virtual 2021).